Poly(lactic acid) filament filled with layered double hydroxide for fused deposition modelling; optimisation of additive fraction and material extrusion parameters

Philip de Bruin

CVD 800

31 July 2024

Poly(lactic acid) filament filled with layered double hydroxide for fused deposition modelling; optimisation of additive fraction and material extrusion parameters

by

Philip de Bruin
18017763

Supervisor: Prof. Frederick Johannes Willem Jacobus Labuschagné
Co-supervisor: Prof. Roelof Lodewyk Jacobus Coetzer

Submitted in fullfiment of the requirements for the degree
Master of Engineering (Chemical Engineering)
in the Faculty of Engineering, Built Environment and Information Technology
University of Pretoria
Republic of South Africa

CVD 800

31 July 2024

Poly(lactic acid) filament filled with layered double hydroxide for fused deposition modelling; optimisation of additive fraction and material extrusion parameters

Declaration and funding

The author, whose name appears on the title page of this dissertation, has complied with the University of Pretoria's Code of ethics for scholarly activities and has, in general, observed the principles of honesty, objectivity, the duty of care and fairness in giving credit and appropriate acknowledgement to the work of others.

This work was funded by M-ERA.Net MultiMat3 as part of a larger project.The author, whose name appears on the title page of this dissertation, declare that there is no conflict of interest pertaining to this work, and that no artificial intelligence was used during the writing process.

Ethics statement

The author, whose name appears on the title page of this dissertation, has obtained the required research ethics approval/exemption for the research described in this work.

The author declares that he have observed the ethical standards required in terms of the University of Pretoria's Code of ethics for Scholarly activities.

Data repository

All the raw data generated in this work is available in the open access data repository of the University of Pretoria with the DOI of 10.25403/UPresearchdata.24427819.

Acknowledgements

I always find it difficult to acknowledge people because in reality there are always many more people who deserve mentioning than who get acknowledged.

Nevertheless, I would like to thank Sappi for granting me a bursary which allowed me to pursue my Master of Chemical Engineering degree.

My supervisor, Prof Johan Labuschagné, guided me through all the hard work and broadened my perspective on all aspects of the research conducted as well as life and its challenges in general. My co-supervisor, Prof Roelof Coetzer, helped me with statistical analysis and concepts whenever I got stuck. To both of you, as well as all the staff and colleagues at the University of Pretoria who helped me during this time, thank you.

I also had the privilege of visiting the Leibniz Institut für Polymerforschung in Dresden, Germany, for two months to complete my research. The experience enriched me both personally and academically. To all involved during this time, thank you.

In a personal capacity my family, friends and wife, Lourene, supported me relentlessly through smooth sailing and frustrating times alike, which is no trivial task. Without this, the completion of this work would require significantly more personal effort. Thank you to all of you as well.

Saving the most important for last, I acknowledge the Creator of the universe, the God of Abraham, Isaac and Jacob, who gave me this potential, and the perseverance to harness it fully. *Soli Deo gloria.*

Poly(lactic acid) filament filled with layered double hydroxide for fused deposition modelling; optimisation of additive fraction and material extrusion parameters

Executive summary

The optimum layered double hydroxide (LDH) loading in poly(lactic acid) (PLA) filament, layer height, nozzle temperature and infill density levels were determined by statistically maximising the ultimate tensile stress of printed parts.

Fused deposition modelling (FDM) is a material extrusion additive manufacturing (AM) method. It allows the printing of complex parts with simple and relatively cheap equipment. After stereolithography, it is the most popular AM method. FDM parameters that influence a printed artefact most are layer height, nozzle temperature and infill density. PLA is a compostable polymer which can be synthesised from renewable sources. It is the most used polymer in FDM and is projected to continue dominating the 3D printing landscape. LDH is an anionic clay with a brucite-like structure. It contains carbonate anions in its interlayer, which can be exchanged with other substances, making it extremely versatile for various applications.

From a systematic literature review following preferred reporting items for systematic reviews and meta-analyses (PRISMA) guidelines it was shown that only one paper describes acrylonitrile butadiene styrene filament filled with LDH. This showed that filaments containing LDH for FDM purposes have scope for research. With PLA being the most popular FDM polymer, a second review using PRISMA guidelines were completed on PLA filled with LDH. No other review on LDH in PLA was found in the 87 articles considered.

A 2^{4-1} fractional factorial experiment was used to screen the four factors, and was augmented to fit quadratic models for the respective responses. These included ultimate tensile stress and load, elongation at break, Young's modulus and impact energy. A central composite design was used to verify the optimum conditions predicted by the derived models. The statistical design of experiments (DoE) considered the following ranges for LDH loading, layer height, nozzle temperature and infill density: 0 % to 10 %, 0.18 mm

to 0.42 mm, 190 °C to 220 °C and 10 % to 100 % respectively. Analysis of variance (ANOVA) was used to derive models and analyse the factors that affect the responses.

For tensile properties the optimum combination of factors were at lower levels of layer height, nozzle temperature and LDH loadings at 0.18 mm, 190 °C and between 0 % and 4 % respectively. Infill densities between 80 % and 100 % also yielded the maximum tensile properties. Impact properties did not vary statistically in this region either. Inconclusive results were observed for Young's modulus, and it is expected that another material extrusion parameter affects this response. Even though inferior in strength, parts could be printed with filament containing up to 10 % LDH.

It was shown that LDH_PLA filament can be made and that artefacts can be printed with FDM. Up to 4 % LDH can be printed without negatively affecting mechanical properties compared to pure PLA, and printing is still possible with LDH loadings as high as 10 %. Because substances can be intercalated into LDH for specific purposes, a legion of applications including medical, environmental and flame retardance applications are theoretically possible. The combination of the benefits of FDM and LDH can lead to tremendous advancements in a variety of fields. Since this is the first work reported on LDH_PLA filaments, further research and work is recommended. Development should focus on limiting degradation of PLA when making filled filament, achieving the required strengths for specific applications and testing the efficacy of intercalated substances after printing.

The proper use of statistics in research is highly recommended. It was shown that resources are wasted because statistics are not fully exploited, especially in the nature science and engineering establishments. Specifically, it is not necessary to have five or more replications for each experimental point in a statistically designed experimental programme, especially in the screening stage of a DoE. More research in the effect of slicing software on printed parts are also required. It was found that the fracture locations on printed tensile parts depended on the Ultimaker Cura slicer settings instead of the material.

Keywords: fused filament fabrication, FFF, MEX

Contents

List of Figures

List of Tables

Nomenclature

Symbols

A	area	m^2
H	hypothesis	
l	length	m
Q	quartile	
y	response	
E	Young's Modulus	MPa
F	force	N
H	enthalpy	
M	molecular mass	$\mathrm{kg\,kmol}^{-1}$
T	temperature	°C

Greek symbols

α	**(materials)** dominant crystallisation phase	
α	**(statistics)** type I error probability	
β	**(materials)** alternative crystallisation phase	
β	**(statistics)** type II error probability	
χ	**(materials)** degree of crystallisation	%
χ	**(statistics)** chi squared variable	
Δ	change in	
ϵ	**(mechanics)** elongation	%
ϵ	**(statistics)** random error	
γ	alternative crystallisation phase	
μ	mean	
σ	**(mechanics)** ultimate tensile strength	MPa

σ **(statistics)** standard deviation

σ^2 variance

ξ impact energy $\mathrm{kJ\,m^{-2}}$

Superscripts

$\hat{}$ normalised with respect to mass

$\prime$ metastable

Subscripts

$_0$ null

$_1$ alternative

$_c$ crystallisation

$_f$ fusion

$_g$ glass transition

$_m$ melting

$_n$ number

$_{cc}$ cold crystallisation

Abbreviations

4MC 4-methoxy chalcone

ca *circa*, which means approximately

e.g. *exempli gratia*, which means for example

i.e. *id est*, which means that is

status quo which means the existing state of affairs or the present situation

via which means by way of or by use of

vs *versus*, which means against or in contrast of

ABS acrylonitrile butadiene styrene

AM additive manufacturing

ANOVA analysis of variance

AO anti-oxidant

APP ammonium polyphosphate

APTES 3-triethoxysilyl-1-propanamine

BJ binder jetting

BPH 4-biphenyl acetic acid

CAD computer aided design

CCD central composite design

CF crystalline fraction

CJP colour jet printing

d2DGc dual 2D graphene LDH complex

DBS dodecylbenzenesulfonate

DDM dough deposition modelling

DED directed energy deposition

DMA dynamic mechanical analysis

DMAM dimethylacrylamide

DMF dextran magnetic LDH fluorouracil

DS dodecyl sulphate

DSC differential scanning calorimetry

EDX energy dispersive X-ray spectroscopy

EU European union

FA fumaric acid

FDM fused deposition modelling

FFF fused filament fabrication

FTIR Fourier transform infrared spectroscopy

GPC gas permeation chromatography

HPCP hexaphenoxycyclotriphosphazene

IFR intumescent flame retardant

ISO International Organisation for Standardisation

LDH layered double hydroxide

LDPE low denisty poly (ethene)

LMJ liquid metal jetting

LoF lack of fit

LOI limiting oxygen index

LS lignosulfonate

MAF mobile amorphous fraction

ME material extrusion

MFR melt flow rate

MJM multi jet modelling

MMT montmorillonite

MVR melt volume rate

OLLA low molecular mass PLA oligomers

P(NIPAMco-DMAM)-b-PLA triblock polymer containing PLA, PNIPAM and DMAM

PA phytic acid

PBAT poly(butylene adipate-co-terephthalate)

PBF powder bed fusion

PBS poly(butylene succinate)

PBSA poly(butylene succinate adipate)

PCL poly(caprolactone)

PEG poly(ethene glycol)

PEO poly(ethene oxide)

PEPA pentaerythritol phosphate

PET poly(ethene terephthalate)

pHRR peak heat release rate

PLA poly(lactic acid)

PLC poly(lactide-co-caprolactone)

PLDA poly(*d*-lactic acid)

PLGA poly(lactic-co-glycolic acid)

PLLA poly(*l*-lactic acid)

PMMA poly(methylmethacrylate)

PN polymer network

PNIPAM poly(N-isopropylacrylamide)

POM polarised optical microscopy

PPA phosphotungstic acid

PPC poly(propylidene carbonate)

pph parts per hundred

pPLA pure poly(lactic acid)

PRISMA preferred reporting items for systematic reviews and meta-analyses

PST poly(1, 4-butylene adipate-co-1,4-butylene succinate)

PVA poly(vinyl alcohol)

RAF rigid amorphous fraction

RGO reduced graphene oxide

RSM response surface methodology

SA sulfamic acid

SAXS small angle X-ray scattering

SDBS sodium dodecyl benzene sulfonate

SDS sodium dodecylsulfate

SDZ silver (I) sulfadiazine

SEC size exclusion chromatography

SEM scanning electron microscopy

SL sheet lamination

SLA stereolithography

SuA succinic acid

TEC triethyl citrate

TEM transmission electron microscopy

TGA thermogravimetric analysis

UV ultra violet

VP vat photopolymerisation

XRD X-ray diffraction

1 Introduction

Additive manufacturing (AM) has gained popularity recently. This may be ascribed to the ability to design and produce complex geometries, the simple and minimal equipment required, the flexibility to manufacture different designs without having to adjust equipment or procure additional resources as well as little to no material waste. There are also challenges associated with AM *e.g.* the materials that can be used, size limitations on parts, their final strength and imperfections. Long manufacturing times make AM unsuitable for mass production. (Mwema & Akinlabi, 2020) That being said, AM shows great potential, especially in rapid prototyping and the manufacturing of unavailable or niche, customised artefacts where mass production is not a consideration.

After stereolithography, fused deposition modelling (FDM) is the most used AM technology. The use of poly(lactic acid) (PLA) in FDM increased from 3 % in 2013 to 73 % in 2017, and it is projected to continue dominating the FDM landscape for the foreseeable future. PLA's industrial applications are limited due to its poor mechanical properties compared to petroleum based plastics. (Sandanamsamy *et al*, 2022) The popularity of PLA in FDM is a positive trend because it is a compostable polymer synthesised from renewable resources (Lim, Auras & Rubino, 2008; Valino *et al*, 2019).

Layered double hydroxides (LDHs) are clays with divalent and trivalent cation layers as well as anion interlayers ordered into an octahedral structure (De Roy *et al*, 1992; Forano *et al*, 2006). It has been used extensively as a filler in PLA for various applications with great success, but at the time of this work no literature was published on PLA filled with LDH in any FDM applications.

Two systematic literature reviews, Searches 1 and 2, using guidelines from preferred reporting items for systematic literature reviews and meta-analyses (PRISMA) were conducted. PRISMA guidelines ensure a transparent, unbiased approach and makes growing literature reviews possible (Page *et al*, 2021). Search 1 confirmed that no published research is available on any PLA filament filled with LDH for FDM purposes. Only one article discusses LDH in acrylonitrile butadiene styrene filament. Search 2 showed that a lot of work was completed on LDH in PLA, but no work was done for LDH filled PLA filament in FDM. The review highlighted the functionality of LDH in PLA and showed that no comprehensive review exists at the time of the search. The applications of LDH in PLA is already legion because of all the substances, like medicine or flame retardants, that can be intercalated into LDH before being compounded into PLA. Because PRISMA guidelines were used, conclusions are certain and indisputable. Since FDM allows the production of complex geometries the applications of tailored LDH in

PLA can be significantly expanded. Applications are however subject to part strength at required LDH loadings. Therefore the main aim is to generate useful information on the effect of LDH on PLA when FDM is used to manufacture parts, which can be used as a basis for further research on specific applications.

Because material extrusion parameters also affect the properties and strength of printed artefacts, the three FDM parameters that affect part strength the most are investigated as well. These are layer height, nozzle temperature and infill density. The scope is limited to finding the combination of the LDH loading, layer height, nozzle temperature and infill density levels at which the ultimate tensile stress will be a maximum.

Due to the vast number of factors and responses considered, it is near to impossible to conduct research without using statistics to its full potential. Factorial experimental designs is the most efficient way of investigating factors and their interactions and should replace conventional one factor at a time experiments in the scientific and engineering establishments (Montgomery, 2013).

Useful information on LDH filled PLA used in FDM will be collected with a statistical experimental design. As no information on this topic is available yet, impact and other tensile properties will be evaluated at each combination of factors tested to benefit future researchers. The material will be characterised extensively at each step of the process. This will give more insight into the effects of the respective factors. The same LDH loading at which the maximum ultimate tensile strength is found will be used to manufacture tensile specimens with injection moulding. This will be compared to the FDM specimens to see if FDM parts can compete with injection moulded parts.

Therefore, even though the main objective is to record observations on the strength of FDM manufactured parts using LDH filled PLA for future research, supplementary aims are to illustrate the use and benefit of conducting truly systematic literature reviews using PRISMA guidelines as well as illustrate the benefit of using a proper design of experiments.

2 Literature investigation

In order to determine if there is scope for polymeric filaments filled with LDH for FDM purposes, a systematic literature review was conducted, hereafter referred to as Search 1. Only one article was found, which was published within our research group. Because PLA is the most popular FDM polymer, a second systematic literature review (Search 2) was conducted to investigate LDH in PLA. No decent reviews on the topic existed at the time. The aim of Search 2 was to investigate the effect of LDH on PLA, the processing and manufacturing techniques used, and to identify the potential applications of the composite. The goal was to get extensive background on the composite to assist with the experimental design of making LDH filled PLA filament for the first time.

2.1 Systematic literature reviews

PRISMA provides guidelines and a checklist for completing systematic literature reviews. It ensures a transparent and unbiased approach is followed. It also eliminates the need for regular short reviews by making growing systematic reviews possible, which merely expand on a previous one as a field develops. (Page *et al*, 2021)

Using these guidelines, a systematic review was conducted to evaluate the development of LDH filled polymeric filaments used in FDM. Any LDH filled polymer was considered due to the novelty of the field. Search 1 considered four databases. Web of Science yielded three results for the search

> (("fused deposition modelling" OR "fused filament fabrication" OR "FDM" OR "FFF") AND ("layered double hydroxide" OR "LDH" OR "hydrotalcite"))

on 9 August 2022. None of these were eligible, because the LDH used in the abstracts referred to lactate dehydrogenase. Science Direct yielded no results on 2 August 2022 for the search

> ("fused deposition modelling" OR "fused filament fabrication" OR "FDM" OR "FFF") AND ("layered double hydroxide" OR "hydrotalcite" OR "layered clay") AND NOT ("lactate dehydrogenase")

Scopus yielded one result on 3 August 2022 for the search

> TITLE-ABS-KEY ((“fused deposition modelling” OR “fused filament fabrication” OR “FDM” OR “FFF”) AND (“layered double hydroxide” OR “LDH” OR “hydrotalcite” OR (“layered clay” AND “anionic”)) AND NOT (“lactate dehydrogen*”))

which was a duplicate of one of the Web of Science results. The other two papers did not appear in the results since the Boolean search could be more refined in Scopus. Google Scholar yielded 157 results on 2 August 2022 for the search

> (“fused deposition modelling” OR “fused filament fabrication” OR “FDM” OR “FFF”) AND (“layered double hydroxide” OR “LDH” OR “hydrotalcite” OR (“layered clay” AND “anionic”)) -“lactate dehydrogenase” -“field flow fractionation”

It was observed that Google Scholar does not limit its search to the title, abstract and keywords of literature, but also includes the body of the literature with its references, thus yielding many ineligible results. Only one eligible article was found in Google Scholar, and it was published within our research group in the Department of Chemical Engineering at the University of Pretoria.

Seeliger *et al* (2017) printed ABS filament compounded with indigo carmine and fatty acid intercalated layered double hydroxides. The dye was intercalated because LDH interacts more with polar polymer matrices, thus preventing its bleeding and plate out. Different ratios of fatty acid and dye was tested, and the authors found that the pure indigo carmine LDH compounded with ABS yielded the least amount of warping, with warping increasing as the fatty acid concentration in the LDH increased. They believe that this is due to the fatty acid reducing bed adhesion. Compared to pure ABS commercial filament, which showed the most warping, the pure indigo carmine LDH-ABS filament showed a 96 % reduction in warping, and a 97 % reduction in part shrinkage.

Another systematic review using PRISMA guidelines was conducted considering all literature on LDH filled PLA. In Search 1 it was found that Scopus is the best database to use. For Search 2 only the Scopus database were used, and 103 results were found on 16 August 2022 for the search

> TITLE-ABSKEY((“layered double hydroxide” OR “hydrotalcite” OR “LDH” OR (“layered clay” AND “anionic”)) AND (“polylactic acid” OR “poly(lactic acid)” OR “PLA”) AND NOT (“lactate dehydrog*” OR “LDH assay” OR “phospholipase” OR “lumbar disc herniation”))

Several results were still ineligible, *e.g.* two results that summarised the topics of all papers published in conferences, several medical papers using LDH in the context of lactate dehydrogenase and other papers that used the abbreviations in the search term for other words. After these ineligible results were removed 87 papers remained. Copolymers, polymer blends and any other application where PLA and LDH was discussed together was included, yielding a comprehensive review of the field. Many of the articles reviewed in the second review aimed to prove a specific application. Accordingly, the literature is discussed by sorting each paper according to the main application considered.

2.1.1 Flame retardancy

One of the popular applications for LDHs in PLA was flame retardancy. Twelve of the 87 papers were on this topic. Many of the authors managed to achieve a UL-94-V-0 rating.

Wang *et al* (2010) investigated the effect of 2 % dodecylbenzenesulfonate (DBS) modified ZnAl- and MgAl-LDHs combined with a flame retardant mixture (ammonium polyphosphate (APP), pentaerythritol and melamine cyanurate) in PLA. They found that the ZnAl-LDH performed better than the MgAl-LDH, and that it caused an intumescent char formation, which improved fire retardancy. The peak heat release rate (pHRR) was reduced by 58.5 % for the ZnAl-LDH filled PLA compared to the pure polymer.

Shan *et al* (2012) investigated the effect of 2 % NiFe-SDS (sodium dodecylsulfate), NiAl-SDS, and NiCr-SDS LDHs respectively with 8 % hexaphenoxycyclotriphosphazene (HPCP) on the flame retardancy of PLA. All samples attained a UL-94-V-0 rating, and from limiting oxygen index (LOI) values, the authors observed a slight decrease when HPCP was mixed with LDHs, which is ascribed to the formation of metal complexes. Char residues decreased in the following order: NiCr-SDS, NiAl-SDS and NiFe-SDS LDHs, indicating a decreasing thermal stability. The authors found that sample crystallinity followed a similar trend.

Ding *et al* (2015) modified NiAl-LDH with 2-carboxylethyl-phenyl-phosphinic acid and solution casted it into PLA films at 1 %, 5 %, 8 % and 10 %. Thermogravimetric analysis (TGA) results showed that the thermal stability of the PLA films decreased with increasing filler loading, and the authors suggested that this is due to the catalytic effect of the LDHs on degradation. Moreover, the authors also investigated the optical and flame retardant properties of the composite films.

Xueying *et al* (2015) developed an intumescent flame retardant (IFR) with silane coated APP and pentaerythritol phosphate (PEPA) with a corn starch carbon source. This IFR

was mixed into PLA with NiAl-LDH at 0.5 %, 1 %, 2 % and 3 %. They observed optimum flame retardancy at 2 % NiAl-LDH loading, with a UL-94-V-0 rating and the highest LOI. The authors confirmed that this loading shows the best synergy from heat release rates, and proposed that LDH catalysed char formation and improved its intumescence. They also tested the effect of a chitosan char source with silane coated APP and NiAl-LDH on PLA-PBS — poly(butylene succinate) — composites. The PBS was added to improve the matrix's mechanical properties, but the addition of NiAl-LDH reduced the ultimate tensile strength (σ) and the elongation at break (ϵ_b) of samples so that they were inferior to pure PLA. Nevertheless, flame retardancy also improved with NiAl-LDH loading.

Jin *et al* (2017) studied a new IFR (only called DTM by the authors) in combination with LDH and phytic acid intercalated LDH (PA-LDH) respectively, and their effects on PLA. They found that the PA-LDH was properly intercalated, although some defects were caused by the modification. Considering the morphology of the PLA compounds, the authors observed that DTM as well as DTM and PA-LDH dispersed well into the matrix, but that the DTM and LDH combination formed aggregates. They attributed the good dispersion of DTM and PA-LDH to the organic modification. The authors found that DTM combined with LDHs achieved a UL-94-V-0 rating, and also investigated the char morphology of samples. Lastly, from tensile tests, they observed that the addition of fillers reduced the mechanical properties of PLA. The PA-LDH-PLA did yield better properties than the LDH-PLA, and they suggested this is due to the better dispersion of the former.

Yan *et al* (2017) prepared LDH and sulfamic acid intercalated LDH (SA-LDH), which they melt compounded into PLA with an IFR. An UL-94-V-0 rating was obtained for PLA/IFR blends with both LDH and SA-LDH when these were incorporated at 1 % or more. The optimal LOI value was 48.7 % and was observed for the 1 % SA-LDH with 19 % IFR in PLA. This sample also had the best flame retardancy from cone calorimeter tests, with a reduction in the pHRR from 306.3 kW m^{-2} for neat PLA to 58.1 kW m^{-2}. The good performance of the sample was attributed to the formation of a stronger char and more of it. The authors concluded that the interaction between the SA-LDH and the IFR showed synergy in PLA. They found that the addition of the IFR and LDHs caused a decrease in both σ and ϵ_b, but SA-LDHs caused less deterioration in mechanical properties than pure LDH. Lastly, the authors showed that SA-LDH improved the crystallinity of the PLA by acting as a nucleating agent.

Shan *et al* (2018) investigated the effect of 1 %, 2 % and 3 % NiZnAl-SDS-LDH with 8 % HPCP on the flame retardancy of PLA. A UL-94-V-0 rating was observed for all samples. The authors found that the LDH and HPCP showed synergy due to increased char formation and catalysed esterification reactions.

Zhang *et al* (2018) intercalated phosphotungstic acid (PPA) into MgAl-LDH and melt compounded it as well as pure LDH into PLA along with an IFR. An UL-94-V-0 rating was obtained for PLA/IFR blends with both LDH and PPA-LDH at 1 % and more. The highest LOI value of 48.3 % was found for a sample containing 2 % PPA-LDH with 18 % IFR. From cone calorimeter tests, they witnessed a reduction in the pHRR from 306.3 kW m^{-2} for pure PLA to 40.1 kW m^{-2}. The performance of the PPA-LDH was attributed to the formation of a denser char. They found that the addition of the IFR and LDHs caused a decrease in both σ and ϵ_b, but that PPA-LDHs caused less deterioration in mechanical properties than pure LDH. Lastly, the authors showed that there is no significant change in molecular mass for the different samples, showing that drying the LDH samples limited the amount of degradation occurring by hydrolysis.

Tipachan *et al* (2020) blended SDS-LDHs and silica obtained from rice husks into PLA. Characterisation showed that the silica did not form a homogeneous blend with PLA, whereas the LDHs did. Mixtures of the two improved the PLA morphology. Although the SDS-LDH reduced PLA's thermal stability, and the silica increased it, combinations tended to decrease PLA's thermal stability compared to the neat polymer. However, combinations of fillers had a positive effect on char formation. The authors observed that the silica yielded higher LOI values than the LDHs in PLA, and that the highest LOI value recorded was at a 10 % LDH and 5 % silica concentration. Samples with only one type of filler could not achieve a UL-94-V-0 rating, in fact, only 10 % LDH and 3 % silica as well as 10 % LDH and 5 % silica PLA blends could attain the UL-94-V-0 rating. The combination of the two fillers yield a dense char on the composite surface and the authors concluded that there was synergy between the two fillers.

Wei *et al* (2021) synthesised graphene oxide, reduced graphene oxide (RGO), polyester functionalised graphene and a dual 2D graphene LDH complex (d2DGc). RGO and d2DGc contained MgAl-LDHs. These were then combined with PLA/PPC (poly(propylidene carbonate)) and PLA/PBS (poly(butylene succinate)) blends, and in some instances with MgAl-LDH. The fillers toughened the matrices and improved flame retardancy. Considering the LDH composites specifically, the authors observed a decrease in σ and an increase in ϵ_b for both PLA/PPC and PLA/PBS with 5 % RGO-LDH and 5 % d2DGc. Aggregates formed within the matrices with RGO-LDH composites, whilst the d2DGc composites achieved a homogeneous dispersion. The RGO filled matrices had lower flame retardancy compared to the d2DGc filled matrices, which the authors ascribed to the poor dispersion of the RGO fillers.

Dai *et al* (2022) intercalated APPs into yttrium doped MgAl-LDH (APP-YMgAl-LDH) and melt blended it into PLA at 5 %, 10 %, 15 %, 20 % and 25 %. They were able to achieve a UL-94-V-0 rating with 15 % filled PLA. From TGAs, the authors concluded

the filler increased the thermal stability of the PLA. The glass transition temperature (T_g) and the melting temperature (T_m) increased after the filler was added, whereas the cold crystallisation temperature (T_{cc}) decreased, indicating that the filler enhanced crystallisation. The mechanical properties of the compounds deteriorated as filler was added compared to pure PLA, and although they did increase again with filler loading, they never reached the properties of pure PLA.

Zhang *et al* (2022) investigated the effect of montmorillonite (MMT) on LDH-PLA blends, as well as IFR and LDH-PLA blends. The LDH was modified with SDS and the MMT with cetyl trimethyl ammonium bromide. The authors found that the addition of MMT improved the char stability formed by the systems, without altering the char formation mechanism. They concluded synergy between the respective fillers.

2.1.2 Medical applications

All articles pertaining to medical applications are related to drug release, although the specific application varies. Fifteen of the 87 papers were on this topic.

The following five authors did not investigate PLA, but rather one of its copolymers, poly(lactic-co-glycolic acid) (PLGA). Although strictly speaking this is not PLA, these articles are still included for completeness sake.

Chakraborti *et al* (2011) intercalated alendronate into MgAl-LDH (A-LDH) and manufactured PLGA films with A-LDH and tetracycline. They investigated the drug release from the films for guided tissue regeneration purposes and found that LDH allowed the controlled release of the alendronate. The authors suggested that this is favourable for periodontal treatment.

Chakraborti *et al* (2012) investigated the drug release of tetracycline, doxorubicin, 5-fluorouracil, vancomycin, sodium fusidate, and antisense oligonucleotides intercalated into MgAl-LDH from PLGA films. They performed *in vitro* release studies for each drug from the clay and found that doxorubicin and 5-fluorouracil released very slowly from the LDH, and therefore did not mix them into the films. The other drug intercalated LDHs in PLGA films showed controlled release, and the authors proposed that this may be beneficial for antibacterial applications.

Kim *et al* (2016) intercalated risedronate into ZnAl-LDH and prepared filled PLGA films to investigate its viability on theranostic plates. The authors concluded that the films are promising for X-ray diagnosis and bone repair applications, due to enhanced radiopacity and sustained drug release.

Ray *et al* (2017) intercalated methotrexate into MgAl-LDH and encapsulated the particles with PLGA. They investigated its antitumour efficacy on Balb/c nude mice, and found that the drug release efficiency and lack of toxicity makes the particles very promising for osteosarcoma applications.

Lastly, Pu *et al* (2020) intercalated danshensu into MgAl-LDH and compounded it into PLGA nanoparticles *via* a double emulsion solvent evaporation method. The authors investigated the drug release rates with *in vitro* studies, and also performed a hemolysis assessment. They found that intercalating the drug into LDH yielded a longer release time, and that it was compatible with human blood according to ISO standards.

Zhang, Jin & Gou (2016) also did not consider pure PLA. They synthesised P(NIPAM-co-DMAM)-b-PLA, a triblock polymer containing PLA, poly(N-isopropylacrylamide) (PNIPAM) and dimethylacrylamide (DMAM). They then made a dextran magnetic layered double hydroxide fluorouracil (DMF). They used these to make micelles with the PLA and drug loaded DMF forming the core, and the amide bonds the shell. The authors found that these micelles had good thermo and magnetic sensitivity, which could be beneficial for chemotherapeutic applications.

Zhou *et al* (2020) prepared a polymer network (PN) with 5 % MgAl-LDH and poly(lactide-co-caprolactone) (PLC) by using the LDH as an initiator with the monomers. The PN was the insoluble polymer. They found that the PN was superior in releasing Mg^{2+} ions to tissue culture plastic, and based on this and other results, they identified the PN as having potential for bone tissue regeneration applications.

Adepu, Luo & Ramakrishna (2021) intercalated biochanin A (bA) into MgAl-LDH *via* the coprecipitation (C) and ion exchange (I) methods, and encapsulated it with heparin tagged PLA-PEG — poly(ethene glycol) — copolymer, to synthesise a stent that is non-thrombogenic. A more controlled bA release was achieved for the LDH-C samples than for the LDH-I samples. After incapsulation, PLA-PEG-bA-LDH-C showed the best properties for stable drug release. The authors found that the heparin catalysed the polymer's degradation, increased its wettability and decreased its protein affinity. They also performed a hemolysis assay, and found that all samples were less than 5 %, making them non-thrombogenic. Stability tests showed that the bA-LDH-C is stable up to seven weeks. The authors also applied mathematical models to the release profiles of the different samples, and found that their filled polymer performed much better than other stents found in literature at the time.

The remaining authors investigated PLA, and not PLA forming part of a polymer blend or copolymer.

Dagnon *et al* (2009) manufactured poly(*l*-lactic acid) (PLLA) films with 1 %, 3 % and 5 % ibuprofen intercalated LDHs (I-LDH). They investigated the effect of the films on cell proliferation, and found that it inhibited smooth muscle cell proliferation effectively by controlled drug release. The Young's modulus (E) and σ of composites increased with filler loading, whereas the ϵ_b decreased. Optimum E and σ properties were observed for the 3 % film. The authors attributed their observations to the ability of the I-LDH to act as a nucleating agent for crystallisation as well as agglomeration of the I-LDHs in the matrix as loadings increase.

Similarly, Miao *et al* (2012) intercalated ibuprofen into MgAl-LDH, and electrospun 5 % filled nanofibres with poly(caprolactone) (PCL) and PLA respectively. The LDHs was properly dispersed in the matrices and had no significant effect on the electrospinning process. The authors observed that the drug release was slower from PLA fibres than from PCL fibres, and that the intercalated LDH filled matrices yielded much slower releases than the ibuprofen-polymer fibres. They proposed that the lower chain flexibility is responsible for the former observation, whereas the crystal structure of the LDH is responsible for the latter. They also investigated the effect of a hydrophilic enhancer, poly(oxyethene-boxypropylene-b-oxyethene), on LDH-PLA fibres, and found that it accelerated the ibuprofen release. The authors concluded that the different interactions between ibuprofen and fillers can be used to tailor products for drug delivery, wound healing and surgical implant applications.

San Román *et al* (2013) intercalated diclofenac, chloramphenicol and ketoprofen into ZnAl-LDH, and mixed this into PLA to make nanocomposites. They found that the drug release was drastically decreased when intercalated into LDH and compounded in the PLA matrix, yet appropriate drug concentrations were released, making it viable for implant applications.

Oyarzabal *et al* (2016) intercalated 4-biphenyl acetic acid (BPH) into LDH, and solvent casted 5 % PLA films. They investigated the effect of the drug and the drug intercalated LDH on the hydrolytic degradation of PLA. The BPH catalysed the hydrolytic degradation of PLA, while BPH-LDH initially limited degradation after which it was also accelerated. They proposed that this behaviour was due to retarded diffusion as well as an increase in hydrophilicity due to the LDH, followed by the BPH catalysation once the LDH barrier effect was reduced.

Benvenutti *et al* (2019) investigated the stability of 4-methoxy chalcone (4MC) in various PLGAs and PLAs, and found that 4MC plasticised the polymer matrices resulting in poor drug storage and recovery. The authors intercalated 4MC into stearate modified LDH, and then used this compound in PLA. This increased the drug storage and recovery, and

they proposed that further research be done in this regard.

Figueiredo *et al* (2020) electrospun poly(*d*-lactic acid) (PDLA) membranes containing naproxen intercalated Mg_4FeAl-LDH. The authors used two methods, (1) electrospinning PDLA and electrospraying naproxen separately layer by layer and (2) electrospinning PDLA and electrospraying naproxen simultaneously. Less aggregation for films manufactured *via* method 2 was observed and the tensile properties of the films depended more on its morphology than the LDH concentration. They observed that the drug release can be tailored by layer thickness in method 1, and that method 2 yields an intermediate drug release compared to the former method. Lastly, the authors proposed that these membranes can be applied as multi-functional dressings.

Malafatti *et al* (2020) intercalated silver (I) sulfadiazine (SDZ) into MgAl-LDH and electrospun a 2.5 % filled PLA scaffold. The filler was properly dispersed into the matrix and the latter remained amorphous. They found that LDH allowed the controlled release of SDZ, making the compound ideal for wound dressing applications. From an *in vitro* study, the authors found that the controlled release was safe for human cells whilst still maintaining its antimicrobial effect.

2.1.3 Environmental applications

The following articles investigated the use of PLA in applications that benefits the environment directly or indirectly. Many articles focused on the degradation of PLA, and the effect LDH has on the degradation rate. Eight of the 87 papers are discussed here.

Eili *et al* (2012) modified ZnAl-LDH with stearate and solution casted it into PLA nanocomposites with 1 %, 3 %, 5 %, 7 % and 10 % filler. The filler exfoliated well into the PLA matrix and the σ and E gradually decreased with filler loading. An optimum in ϵ_b was observed at 3 % with an increase of more than 600 %, after which the ϵ_b deteriorated with increased loadings. The authors believe this to be due to filler agglomeration. Lastly, the authors studied the effect of the filler on PLA's biodegradation for seven months in soil, and found that it stayed constant for all samples up to four months, after which it was significantly catalysed by the filler. They also considered the macrocomposite of only ZnAl-LDH in PLA, and found that it degraded slower than the stearate modified composites. The authors noted that the thermal stability of composites decreased with filler loading.

Amaro *et al* (2016) intercalated two anti-oxidants (AO), 3-(3,5-di-tert-butyl-4-hydroxyphenyl)propionic acid (IrganoxCOOH) and 6-hydroxy-2,5,7,8-tetramethylchroman-2-carboxylic acid (Trolox), into MgAl-LDH, and made PLA films at 0.5 % *via* solution mixing

and melt extrusion. The anti-oxidising ability of Trolox remained almost the same after intercalation, whereas the IrganoxCOOH almost doubled in its ability after intercalation into LDH. Although the AO-LDH filled PLA degraded more than AO filled PLA in thermo-oxidative tests, the LDH prevented migration of the AO. Moreover, the solution casted IrganoxCOOH-LDH filled PLA film experienced a loss in the number average molecular mass (M_n) of 35 % compared to pure PLA, which experienced a loss of 85 %, indicating that the AO-LDH still allows effective AO action.

Valentina *et al* (2017) investigated the effect of fumaric acid (FA) and LDH on PLA's degradation. They used a twin screw extruder to compound 3 % LDH, 3 % FA intercalated LDH (FA-LDH) and 1 % FA into PLA. From TGA and rheological analyses, the authors found that FA in PLA reduced the degradation of PLA, whereas FA-LDH-PLA showed no significant change in degradation compared to pure PLA, and that LDH-PLA degraded much more than pure PLA. From hydrolysis tests the only sample that had an improved stability compared to pure PLA was FA-LDH-PLA. The results were confirmed by gas permeation chromatography (GPC) and differential scanning calorimetry (DSC) analyses. The authors concluded that FA-LDH limited the degradation of PLA in its solid state.

In another work the same authors intercalated succinic (SuA), fumaric and ascorbic acid into MgAl-LDH, and compounded these into PLA at 3 % with a twin screw extruder. Valentina *et al* (2018) first compared the degradation caused by LDH-CO_3 and LDH-NO_3, and found that the latter caused less degradation. Thus, LDH-NO_3 and pure PLA was used to compare the acid intercalated LDHs. The acid intercalated LDHs caused less degradation in PLA than only LDH. This was confirmed by DSC and GPC analyses. The authors also determined the degradation kinetics of the respective samples. Finally, they observed the limitation of degradation by the acid intercalated LDHs through penetration tests and visual observation of samples. The authors concluded that SuA-LDH-PLA achieved the slowest degradation.

A few authors used compounds to prevent corrosion or to remove a pollutant from the environment.

Zeng *et al* (2015) coated a Mg alloy with ZnAl-LDH and a ZnAl-LDH-PLA composite to investigate its ability to prevent corrosion. The LDH formed a compact inner layer on the alloy and a more porous outer layer. The PLA formed a layer on top of the porous LDH layer in the composite. The authors found from potentiodynamic polarisation analysis that the corrosion current density decreased by three orders of magnitude for coated samples, from 33.7 μA cm^{-2} for the alloy, to 0.0679 μA cm^{-2} and 0.0120 μA cm^{-2} for the LDH and LDH-PLA coated alloy respectively. They attributed the latter result to the

LDH regenerating itself in the PLA composite, and confirmed this with further analyses. The authors proposed that the coatings prevent corrosion through ion exchange, forming a diffusion barrier and regenerating itself.

Sahithya, Das & Das (2016) synthesised MgFe-LDH-MMT nanocomposites, and made composites with chitosan, gum ghatti and PLA. They investigated the ability of composites to remove dichlorvos, and found that LDH-MMT-chitosan had the best ability, followed by LDH-MMT-gum ghatti, LDH-MMT and LDH-MMT-PLA. They focused more on the chitosan composite in further studies, where they fitted kinetic models and discussed the thermodynamics of the system.

Coiai *et al* (2018) intercalated fluorescein (flu) and cointercalated flu and dodecyl sulphate (DS) into MgAl-LDH. They also intercalated flu and DS into calcined LDH (cLDH) at two flu/(flu+DS) molar ratios of 1.34×10^{-2} and 1.34×10^{-3}, flu-DS-cLDH-1 and flu-DS-LDH-1 respectively. These fillers were solution mixed into PLA and low density poly(ethene) (LDPE) at 5 %. The flu-LDH sample did not show fluorescence emission and flu-DS-cLDH-1 had the best fluorescence, which was ascribed to flu agglomeration. Due to its higher concentration, flu-DS-cLDH-2 had the highest quantum yield. Moreover, the fillers dispersed much better in PLA than in LDPE. The thermal stability of PLA decreased whereas LDPE's did not change significantly. The fluorescence of filled polymers improved compared to the fillers in most cases, and more so in PLA. The quantum yield for flu-DS-cLDH-1-PLA increased the most, although flu-DS-cLDH-2 decreased in both polymers. The authors observed that the emissions of samples increased when exposed to a relative humidity of 99 %. LDPE composites showed a more dramatic increase. The observed change did however decrease in a second cycle. Nevertheless, the authors concluded that the composites might be used as on/off humidity indicators.

Lastly, Cheng *et al* (2022) used MgAl-LDH and 3-triethoxysilyl-1-propanamine (APTES) modified LDH to coat silver ion glass beads — AgB-LDH and A-AgB-LDH respectively — and melt blended it into PLA at 1 %, 3 % and 5 %. The fillers reduced PLA's thermal stability and changed the crystallisation from homogeneous to heterogeneous, forming more and smaller spherulitic crystals. The A-AgB-LDH caused a significant increase in PLA crystallinity from 2.88 % to 33.32 %, whereas the crystallinity of AgB-LDH-PLA did not vary significantly, indicating that APTES improved the compatibility of the filler with the polymer. The authors electrospun fibres, and found that the addition of the filler reduced fibre diameters, but also caused the formation of beads and a rough surface. The water contact angle increased with filler loading, and the best improvement was observed for 5 % A-AgB-LDH-PLA, with an increase from 86.7° to 109.3°. The oil philicity of PLA did not change significantly with filler loading, but the best oil absorption ratio was observed for 5 % A-AgB-LDH-PLA at 32 g g^{-1}. The authors showed that the membrane

retained its abilities after ten absorption-desorption cycles, and that it had a separation efficiency of 98.45 %. They also showed that the filler inhibits *Escherichia coli* growth, and concluded that A-AgB-LDH-PLA is ideal for separating oil from water.

2.1.4 Packaging applications

The following eleven articles out of the 87 papers considered mainly investigated the permeability of films, specifically for packaging applications. These applications vary between food, electronic and pharmaceutical packaging.

Katiyar *et al* (2010) prepared PLLA nanocomposites *via* ring opening polymerisation with MgAl-LDH and laurate modified MgAl-LDH (C_{12}-LDH) at 1 %, 3 % and 5 %. From GPC, the authors observed that the molecular masses of the PLA matrix decrease with increasing filler content. This is not due to the laurate but rather the Mg and Al present in the LDHs, which either terminated polymerisation early or caused degradation. Fillers increased thermal stability, albeit with a decrease in increased filler loading. DSC analyses showed that the filler increased the matrix's crystallinity. Finally, the authors found that C_{12}-LDH exfoliated in the PLA matrix, whereas LDH formed aggregates.

In another work, the same authors compared the effect of MMT and C_{12}-LDH in PLA for food packaging applications. Katiyar *et al* (2011) melt extruded films in two ways: (1) using self prepared masterbatches and diluting them and (2) loading fillers directly. From GPC results, the authors found that MMT did not cause significant PLA degradation, whereas LDH did. Using the masterbatch mitigated the degradation effect observed for LDH-PLA. Similarly, the LDH caused a much larger decrease in thermal stability compared to the MMT loaded PLA. From DSC analysis, the authors observed that LDH had a greater ability to nucleate crystallisation than MMT. Both fillers had a negative impact on the optical properties of films, and had an exfoliated and intercalated morphology, although the LDH did tend to form agglomerates as well. Lastly, LDH did not affect barrier properties, whilst *ca* 5 % of MMT reduced oxygen and water vapour permeability significantly.

Schmidt *et al* (2011) investigated the migration of LDH, tin, laurate and low molecular mass PLA oligomers (OLLA) from PLA films. They used a corotating twin screw extruder to melt blend C_{12}-LDH into PLA or to dilute a C_{12}-LDH-PLA masterbatch, which was prepared by ring opening polymerisation. The latter reaction used tin as catalyst. The total migration as well as specific migration of LDH, laurate, tin and OLLAs were below acceptable European Union (EU) specifications. They found that PLA hydrolysis, *i.e.*

degradation, occurred during migration tests, and proposed that this may be the reason why migration increased with C_{12}-LDH loadings.

Bugatti *et al* (2013) coprecipitated trihexyltetradecylphosphonium decanoate and trihexyltetradecylphosphonium dodecylsulfonate into MgAl-LDH, and coated PLA films with them. These coatings decreased the water permeability of PLA films by *ca* 35 %. The authors proposed that this is a good alternative method for food packaging, because it is much easier to manufacture than properly dispersed nano LDHs in a PLA matrix.

Demirkaya *et al* (2015) intercalated SDS into Mg_4AL_2-LDH and Mg_6Al_2-LDH, and solution casted PLA films with the pure and intercalated LDHs at 1 %, 3 %, 5 % and 10 %. SDS improved the dispersion of LDH in the PLA matrix, and Mg_4AL_2-LDH dispersed better than Mg_6AL_2-LDH. The SDS-LDH-PLA films decreased oxygen and water vapour permeability up to 23 % and 80 % respectively. An increase in surface energy and contact angles with increasing filler loading was observed. SDS-LDHs decreased PLA's thermal stability. Finally, the authors found from DMA analysis that 3 % SDS-LDH-PLA increased mechanical properties.

Yu *et al* (2016) dip coated PLA and poly(ethene terephthalate) (PET) films with a poly(vinyl alcohol) (PVA)-LDH coating. The LDH was synthesised in the presence of formamide to obtain single layer nanosheets. The lowest Mg/Al ratio of 2/1 as well as higher formamide concentrations benefited the formation of nanosheets. Lastly, the authors found that when PET and PLA films were coated with the LDH nanosheets, a significant reduction in oxygen and water vapour permeability occurs. These were 99.7 % and 77.5 % respectively.

Tipachan & Kajorncheappunngam (2017) solvent casted 1 pph, 3 pph, 5 pph and 7 pph LDH (Perkalite) into PLA with PEG as plasticiser. Filler agglomeration occurred at 5 pph and 7 pph in contrast to the intercalated morphology at lower loadings. A minimum in oxygen and water vapour permeability was observed in 3 pph LDH-PLA at reductions of 76 % and 44 % respectively, which the authors ascribed to the morphology observed.

Tipachan, Gupta & Kajorncheappunngam (2019) solution casted PLA films with SDS-MgAl-LDH and silica obtained from rice husk ash. They found that the silica was incompatible with PLA, whereas SDS-LDH was very compatible. A mixture of the two improved the compatibility of silica with PLA. The lowest water vapour permeability was for 3 % silica and 10 % SDS-LDH in PLA, which was ascribed to the morphology of the films and the particle characterisation of the fillers. This sample reduced the permeability by 67 % compared to neat PLA.

Lei *et al* (2020) prepared PA and copper II (Cu) and coated MgAl-LDH (CuPA-LDH)

with it. This compound was solution casted into PLA films at loadings of 0.5 %, 1 %, 3 % and 5 %. For CuPA-LDH loadings exceeding 1 %, the antibacterial rate of PLA composites exceeded 99.99 % and an increase in thermal stability was observed. DSC results showed an increase in crystallinity up to 1 %, from where a slight decrease was observed. Similarly, an optimum in σ and ϵ_b was observed at 1 % CuPA-LDH content, with a respective increase of 18.9 % and 53.0 %. Lastly, the authors found that a rapid decrease in oxygen permeability occurred up to 1 % (28 %), from where a slower decrease was observed from 1 % to 5 % (only 21 %). They found that this was due to agglomeration of the filler at higher loadings.

Mao *et al* (2022) coated MgAl-LDH with quercetin and copper (II) (queCu-LDH). They then made multilayered films consisting of biaxial PLA films, queCu-LDH-PVA films and catechol grafted chitosan (CS). Transparent films resulted, even though their UV absorption was increased. Furthermore, the mechanical properties of the composite film did not vary significantly, which was attributed to the relative thinness of the coating compared to the PLA film. The authors found that the copper yielded good antibacterial properties against *E. coli* and that the LDH decreased both the oxygen and water vapour permeability rates. They noted that the PVA plays a significant role in the latter observation.

Yang *et al* (2022) prepared an APTES modified LDH and solution casted PLA films at 0.1 %, 0.2 %, 0.5 %, 1 %, 5 %, 10 % 30 % and 50 % loadings. They found that serious agglomeration occurred at 30 % and 50 %. A decrease in both oxygen and water vapour permeability up to 10 % was observed, after which significant increases occurred, which was ascribed to the morphology of the films. The oxygen permeability decreased by more than 99 % for 5 % and 10 % filled PLA films, and by 94.1 % for the 10 % filled film. An increase in σ and decrease in ϵ_b was observed with increasing APTES-LDH loading. The authors found that the filler did not affect the biodegradation of the PLA films up to 10 %, but for 30 % and 50 % filler the biodegradation is significantly slowed.

2.1.5 Processing, characterisation and other properties

The vast majority of papers considered was on this topic. In fact, 36 of the 87 articles are reported below.

Chouzouri & Xanthos (2003) compared a synthetic polyester and biopolyester, poly(1, 4-butylene adipate-co-1,4-butylene succinate) (PST) and PLA respectively, by considering the effect of uncoated and stearic acid coated LDH on the properties of the compounds. PST compounds were prepared *via* solution and extrusion mixing, whereas PLLA com-

pounds were only prepared *via* solution mixing. Both polyesters were then compression moulded. The DSC data showed a decrease in the T_g and the T_m of 30 % LDH filled PLA, with the coated LDH yielding lower temperatures than the uncoated LDH. The authors proposed that the drop in T_g suggested a reduction in crystallinity, and therefore indicated degradation. TGA results showed that the coated LDH caused more instability than the uncoated LDH in PLA, especially at temperatures up to 300 °C. The uncoated LDH-PLA sample was placed in a phosphate buffered saline solution, and the authors observed from SEM images that the surface of the sample deteriorated significantly after 21 days. From this, they concluded that the degradation of filled PLA is more significant than that of filled PST.

Chiang & Wu (2008) intercalated PLA into MgAl-LDH, which was then used as a nanofiller in PLLA at 1 % and 3 % loadings. They confirmed that the PLA-LDH was exfoliated disorderly in the PLLA matrix. TGA results indicated that the thermal stability of the compound decreased with increasing LDH concentration. The authors proposed that Al and Mg catalysed PLLA depolymerisation.

In a later work, the same authors intercalated PLA into MgAL-LDH with a Mg/Al molar ratio of 2/1. This was once again used as a nanofiller in PLLA. Chiang & Wu (2010) confirmed PLA intercalation into the LDH, and that PLA-LDH was randomly dispersed and exfoliated within the PLLA matrix. The authors also included a detailed discussion on the storage modulus of the PLLA matrix, but unfortunately the data in their figures do not correspond to the data in their discussion, and therefore their results are not reported here. The authors however concluded once again that their observations showed that Mg and Al catalysed the depolymerisation of PLLA.

Zhao *et al* (2008) modified MgAl-LDH with DS and electrospun unwoven mats with 2 %, 5 %, 10 % and 15 % filled PLA respectively. The authors confirmed successful DS intercalation and the dispersion of LDH in the PLA matrix. They observed from SEM images that the 15 % DS-LDH-PLA fibres had knobs in, attributed to filler agglomeration. TEM analysis however confirmed decent dispersion of 15 % DS-LDH-PLA. From differential thermal analysis results, the authors concluded that LDH did not cause significant chain scission. The addition of LDH caused a loss in thermal stability. The authors noted this is unexpected due to no significant change in the molecular mass, and therefore proposed that the reduction in melting points are due to different crystallisation properties.

Ha & Xanthos (2009) intercalated trihexyltetradecylphosphonium decanoate (IL1), trihexyltetradecylphosphonium bis(2,4,4-trimethylpentyl) phosphinate (IL2) and trihexyltetradecylphosphonium hexafluorophosphate (IL3) into calcined and uncalcined LDHs and MMTs. Successful intercalation was confirmed. The respective clay compounds were

melt mixed with PLA at 5 %, and TGA results indicated that the LDH clays could be intercalated with up to three times the stoichiometric ratio of ILs, whereas the MMT becomes saturated at two times the stoichiometric ratio. Energy dispersive X-ray spectroscopy (EDX) results indicated that the anion of LDH-IL2 intercalated more as the stoichiometric ratio increased. Although smaller, the IL3 anion was observed in lower concentrations compared to IL2, suggesting anion size does not influence the degree of intercalation. The viscosity of PLA mixed with any of the clays decreased, and the IL1-LDH-PLA compound had a very large viscosity reduction. Accordingly, the authors suggested that IL1 acts as both a lubricant and degradant. The storage moduli of the samples confirmed the viscosity observations. TGA results of the PLA composites indicated that LDH-PLA composites have the lowest thermal stabilities, followed by modified MMT-PLA composites. Only the pure MMT-PLA compound had a higher thermal stability than neat PLA. This work was a conference article.

In a later published article, the same authors reported on the same work, and elaborated on some observations. Ha & Xanthos (2010) reported that FTIR results indicated that IL1 coated on the LDH surface, IL2 intercalated and coated the surface whereas IL3 neither intercalated nor coated the LDH. These results were confirmed by TGA analysis, which also indicated the thermal stability of the ionic liquids increased in the order: IL2, IL1, IL3. The authors tested for hydrophobicity by mixing clays in hexane-water mixtures and found that the IL2-LDH had the best hydrophobicity. PLA with modified MMT showed increased thermal stability compared to neat PLA, where the LDH filled PLA samples showed decreased thermal stabilities. The calcined LDH had a higher thermal stability than the normal LDH, followed by the IL-intercalated LDH-PLA compounds. DSC results did not show any significant changes in T_g. The addition of all clays resulted in a decrease in viscosity compared to neat PLA, with a very large decrease in viscosity for the IL2-PLA and IL1-LDH-PLA samples. The former is believed to be a plasticiser, whereas the latter is believed to act as both plasticiser and degradant.

Mahboobeh *et al* (2010) synthesised stearate-Mg_3Al-LDH and mixed it with PLA by solution casting at 1 %, 3 %, 5 %, 7 % and 10 % respectively. They found that the LDH was properly synthesised and exfoliated in the matrix. Tensile tests on the filled compound showed a general decrease in σ with filler loading and an optimum in ϵ_b between 1 % and 3 % of almost seven times the ϵ_b of pure PLA. SEM analysis of the fracture surfaces showed brittle behaviour. The authors proposed that LDH aggregates caused the decrease in σ, and that the fatty acid lubricated the matrix, thus causing the optimum in ϵ_b.

Zhou & Xanthos (2010) melt compounded 5 % MMT, LDH, calcined MMT and calcined LDH into PLLA and PLA respectively. They found the order of thermal stability of the

clays to be cMMT>MMT>cLDH≫LDH, and believe the calcined clays showed superior stability due to the absence of inter-layer water and surface metals, which catalyses degradation. The LDHs were better dispersed in the matrices than the MMTs and the former could be considered nanocomposites whereas the latter were microcomposites. The cMMTs showed less agglomeration than MMTs, and the authors suggested that this is due to the removal of water during calcination. They found that PLA and its composites degraded more rapidly than PLLA and its composites. Both LDHs and MMTs caused lower degradation rates than the pure polymers, and the LDHs caused lower degradation rates than the MMTs. The authors suggested this is due to the fillers' capability to absorb water and thus prevent degradation. Filled PLLA had even lower degradation rates for calcined clays than for uncalcinated ones, although PLA showed no difference between the two. The authors attributed this to PLA's higher water uptake ability. Degradation rates increased significantly at temperatures exceeding the T_g, and the authors proposed this is due to water being able to diffuse easier. Studying the morphology of samples, they concluded that degradation starts at the filler surface before propagating through the bulk of the matrix.

Gerds *et al* (2012) investigated the effect of several fillers on the degradation of PLA by considering the compound's molecular masses. Fillers were added at *ca* 5 %. The stability of PLA mixed with coprecipitated and reconstructed laurate modified LDHs, C_{12}-MgAl-LDH-$_{CP}$ and C_{12}-MgAl-LDH-C_R, as well as MgAl-LDH-CO_3 showed that the latter two decreased moderately, but the former decreased drastically. It was found that as the drying temperature of the LDHs increased, the degradation caused by C_{12}-MgAl-LDH-$_{CP}$ and MgAl-LDH-CO_3 both decreased, indicating that the presence of water plays a role in degradation. TGA results showed that the former has much less water than the latter, despite being the one with the most degradation, suggesting that metal catalysts also play a significant role in degradation. Magnesium and aluminium oxides and hydroxides, as well as lauric acid and sodium laurate were also compounded with PLA, and it was found that magnesium compounds and sodium laurate caused significant degradation. These are believed to act as catalysts for degradation, and the authors expect dispersion and contact surface to play a role. XRD indicated that the LDH fillers were properly dispersed and exfoliated, although MgAl-LDH-CO_3 filled PLA retained a MgAl-LDH-CO_3 characteristic peak. Low resolution SEM images suggest that the C_{12}-MgAl-LDH-$_{CP}$-PLA compound had the best dispersion and exfoliation. C_{12}-MgAl-LDH-$_{CP}$ was treated with phosphate, and it was shown that the treated LDH caused less degradation in PLA. Moreover, it increased the compound's thermal stability, and yielded low processing viscosity.

Livi *et al* (2012) prepared LDH-NO_3 and then surface modified it with 1 % trihexyltetradecylphosphonium decanoate (P1) and trihexyltetradecylphosphonium dodecylsulfonate (P2) respectively. These LDHs were compounded with PLA at 2 % loadings, and

then injection moulded. The LDHs were successfully synthesised, modified and intercalated, although agglomerates also formed. TGA results indicated that the modified LDHs had better thermal stability. Using the sessile drop method, the authors determined that the modification resulted in more hydrophobic surfaces, thus improving the LDHs affinity to PLA. TEM images of the compounds showed good dispersion in the matrix, although some tactoids formed. A decrease in the thermal stability of the PLA compound was observed from TGA analysis. The authors believe this to be due to the decanoate, dodecylsulfonate ions and interlayer water in decreasing order. Mechanical tests showed that E slightly decreased with the addition of LDHs, but that the ϵ_b increased more significantly, especially for the P2-LDH filled PLA. The ionic liquids had a plasticising effect on the matrix, with P2 the most plasticising.

Hennous *et al* (2013) prepared a lignosulfonate (LS) Zn_2Al-LDH, which they mixed into PLA, PBS and poly(butylene adipate-co-terephthalate) (PBAT) at 5 %. XRD of the filled polymers indicated intercalation into PLA and PBS, but not into PBAT. Similarly, the LDH increased the viscosity of the PLA and PBS, and lowered the viscosity of the PBAT. TGA results indicated an increase in thermal stability for PLA, followed by a slight increase for PBS, and largely exaggerated increase for PBAT. Finally, hydrophilicity was shown by the PBAT composite, but not the others.

McCarthy *et al* (2013) prepared pure PLA, stannous octoate PLA (PLA-St-Oct), stearic acid PLA, magnesium stearate PLA, aluminium stearate PLA and LDH-PLA. The latter was prepared with 1 %, 5 %, 10 %, 15 % and 20 % LDH loadings. The authors investigated the competing degradation and polymerisation effects of the LDH on the PLA. Synthesis was confirmed, and TGA results indicated that the optimum polymerisation occurred at 5 %. The authors suggested that degradation due to LDH increases at higher loadings, thus reducing the polymerisation. The LDH-PLAs contained a soluble (sol) and insoluble fraction. The former was analysed by GPC along with PLA, 2.5 % Mg-stearate-PLA and 2.5 % Al-stearate-PLA. The molecular masses of these samples were from smallest to highest PLA, 2.5 % Mg-stearate-PLA, 2.5 % Al-stearate-PLA and 5 % LDH-PLA-sol, where the latter had two peaks. The authors believe that two polymerisation processes along with a degradation process occurred in the chromatograph of the latter. Compared to other LDH loadings, 5 % LDH yielded the highest molecular mass, and as observed from the TGA results, degradation increased with LDH filler increase. The authors noted that the different fillers may have a different effect on the kinetics and chain lengths of the final polymer. Considering only 5 % LDH-PLA-sol, the authors observed the molecular mass distribution with reaction time. They found that the single peak splits into two at two hours, one at a lower and one at a higher molecular mass. Since the latter dominates, the authors proposed that a polymerisation mechanism prevails up to two hours when the spatial restriction of LDH is reduced. Then there is a second

polymerisation mechanism, which dominates a degradation mechanism. The authors also investigated how much of the LDH-PLA was soluble and insoluble, and found that the insoluble fraction increased up to 10 % before it decreased with increasing LDH loadings. They believe the decrease is due to monomer diffusion limitations. TGA results comparing the soluble and insoluble fractions of the LDH-PLA with some of the other samples indicated that the insoluble fraction contained some inorganic material and a lot of organic material, whereas the soluble fraction consisted of almost only organic material. Further chemical characterisation indicated that interlayer water and/or carbonates are present in the insoluble fraction, and that the insoluble fraction has a higher Mg/Al ratio than the soluble fraction. SEM analysis indicated that the insoluble fraction of LDH-PLA is a 3D network with LDH platelets dispersed within. The authors identified the organic material in the insoluble fraction as salt molecules (*e.g.* magnesium lactate, magnesium stearate and aluminium stearate) and stearate methene (believed to be PLA end groups). Based on all the results, the authors concluded that the LDH made it possible to form an ionomeric network in the PLA matrix.

Neppalli *et al* (2014) melt blended Dellite HPS, Dellite 43B and Perkalite at 3 % into PLA using a Barbender mixer. The former two fillers were pristine and modified MMTs, whereas the latter was a modified LDH. The HPS-PLA characterisation showed poor dispersion, whereas the modified clays dispersed much better. The Perkalite lammelar stacks were smaller than the 43B ones, and the authors proposed this is due to the LDHs being more fragile than the MMTs, thus breaking during processing. Moreover, it was observed from small angle X-ray scattering (SAXS) that the Perkalite PLA retained the PLA crystal lammellae the best, whereas the MMTs caused the lammellae order to be disrupted. Investigating the crystallisation kinetics with Avrami's method, the authors determined that the Perkalite is the only clay that exhibits a different crystallisation method. This explains why its crystallisation and crystallisation kinetics was the highest. The authors believe this is due to the Perkalite having more affinity to the PLA than the MMTs. Likewise, it was observed that the Perkalite caused the fastest and most detrimental degradation, although the MMTs also caused faster degradation than the neat PLA. The authors believe this is due to the better dispersion of the Perkalite, as well as its superior ability to exchange anions and form hydrogen bonds. This provides more surfaces at which degradation takes place, and increase the affinity to water, which degrades the polymer by hydrolysis reactions. The increased barrier properties of the clays are also believed to keep the water at the catalytic degradation sites for longer periods of time.

Scaffaro *et al* (2014) investigated the effect a single screw extruder (SSE), a counterrotating twin screw compounder (TSC) and a corotating twin screw extruder (TSE) had on the properties of filled PLA. Unmodified and modified Perkalites (LDHs) were mixed at

1 %, 2 % and 5 % into PLA. SEM analysis showed that the best dispersion was achieved by the TSE, followed by the TSC and the SSE. Moreover, modified LDH also improved dispersion in all extruders. The viscosities of all filled compounds were lower than the pure PLA regardless the type of extruder. The authors hypothesised that this is due to the LDH acting as a degradation catalyst. The modified LDHs caused more degradation than the unmodified LDHs, and the authors suggested that the modification agent enhanced degradation. In the frequency range investigated the pure PLA showed a Newtonian behaviour, whereas filled PLA showed non-Newtonian behaviour. The decrease in viscosity with filled PLA was most prominent in the TSE. Since the filler dispersed better, this could be due to more effective degradation catalysation. Comparing molecular masses determined by GPC, the authors confirmed the degradation hypothesis mentioned above. Tensile tests indicated a slight increase in E, but a decrease in both σ and ϵ_b with increasing LDH content. The modified LDH caused worse mechanical properties than the pristine LDH, although the authors suspected that the modified LDH was not properly modified. The overall results showed that a TSE was the best processing equipment, and a SSE the worst.

Scaffaro *et al* (2017) blended 5 % commercial LDH and organically modified LDH (mLDH) into PLA with a corotating twin screw extruder, and then reprocessed samples in a single screw extruder. From SEM analysis they observed that better dispersion was achieved for mLDH-PLA than LDH-PLA, and that dispersion improved with processing cycles for the former but worsened for the latter. The viscosity of PLA and LDH-PLA decreased with recycling, whereas the mLDH-PLA's viscosity increased up to the third recycle. The authors proposed this is due to the better dispersion of mLDH in PLA. The mLDH-PLA's viscosity also decreased from the third recycle onwards, which the authors ascribed to the degradation of the polymer. Filled PLA had a lower viscosity than pure PLA. The molecular mass of all samples decreased with recycling. In contrast, crystallinity increased with recycling and the largest increase was observed for mLDH-PLA. PLA and LDH-PLA experienced an increase in E and σ up to the third recycle, from where it deteriorated. The ϵ_b did not change significantly. mLDH-PLA had a different behaviour, with a small optimum in σ and ϵ_b after one recycle from where properties deteriorated rapidly. The reverse was observed for E. mLDH-PLA had the poorest tensile properties, followed by LDH-PLA and PLA. The authors concluded that degradation occurred with recycling, and that both LDH fillers catalysed degradation, especially as the material gets recycled more.

Teh *et al* (2014) modified MgAl-LDH with stearate and solution casted it at 0.5 %, 1 %, 1,5 %, 2 %, 3 %, 4 % and 5 % loadings into a PLA/PHB (10/90) blend. The authors selected the PLA/PHB ratio from tensile tests, which indicated that this ratio gave optimal mechanical properties. Optimum E and σ results were obtained at 1.5 %

filled blend, whereas ϵ_b was significantly lower than the unfilled blend. SEM and TEM analyses of the fracture surfaces indicated that the fillers caused a more brittle fracture as also noted by the mechanical properties.

Leng *et al* (2015) prepared MgAl-LDH modified with sodium dodecyl benzene sulfonate (SDBS) and melt mixed it into PLLA at 1 %, 3 %, 6 %, 9 % and 12 %. They found that the LDH was successfully modified, homogeneously dispersed and partially exfoliated in the PLLA. Size exclusion chromatography (SEC) showed that the molecular mass of the PLA compound decreased as the LDH content increased. The authors believe this was due to degradation catalysed by Mg and Al ions, as well as interlayer water. Using DSC and WAXS, the authors correlated the degree of crystallisation (χ) to the LDH concentration, and found that for the first and second heating cycles the critical LDH concentrations were *ca* 21 % and 14 % respectively. Cold crystallisation was believed to be completely suppressed beyond these concentrations. T_g was not significantly affected. Although a large increase in χ was observed with the addition of LDH, χ decreased with increasing LDH concentration. Dielectric spectroscopy indicated both prominent α- and β-relaxations as expected, but also revealed the following three phenomena: (1) an additional peak around 260 K increasing in intensity with LDH concentration, (2) a process around 310 K and (3) a process above the α-relaxation temperature, which increases in intensity with LDH concentration. The authors ascribed the first phenomenon to the increase in the polar SDBS concentration with the increase in LDH concentration, the second to the presence of both defects and rotational fluctuations of water molecules, and the last phenomenon to a shift in cold crystallisation, which was affected by the LDH concentration. The latter suggestion was based on a detailed inspection of the α-relaxation peaks, which were not significantly affected by the LDH concentration.

In a similar work, Leng *et al* (2017a) prepared NiAl-LDH modified with SDBS and melt mixed it into PLLA at 1 %, 3 %, 6 %, 9 % and 12 %. They compared results to the previous work completed by Leng *et al* (2015). Successful LDH modification and intercalation into PLA was confirmed. Comparison of SAXS and TEM results between the NiAl-LDH and the MgAl-LDH of Leng *et al* (2015) showed that the NiAl-LDH had an intercalated structure compared to the exfoliated structure of the MgAL-LDH. Moreover SEC indicated that NiAl-LDH-PLA had a larger decrease in molecular mass than MgAl-LDH-PLA. The authors suggested this is because Ni catalyses degradation more effectively than Mg. The degree of crystallisation as derived from DSC showed an optimum χ at 6 % NiAl-LDH-PLA. Extrapolation of the first and second heating cycles indicated critical concentrations where crystallisation is completely suppressed. The former is reported as *ca* 18 %, and although the latter is not numerically mentioned, it is lower than the former. Compared to MgAl-LDH, which showed a linear dependence of χ with LDH concentration, the NiAl-LDH had a parabolic dependence. The authors ascribed this to

differences in crystallisation kinetics and extent of dispersion. WAXS confirmed DSC results qualitatively. Dielectric spectroscopy clearly showed α and β-relaxations along with three other phenomena: (1) an additional peak around 237 K, (2) another process around 310 K and (3) a new peak formed from the broadening of the α-relaxation peak. The first observation is similar for both NiAl-LDH-PLA and MgAl-LDH-PLA, although shifted to a lower temperature. The authors ascribed these effects to the presence of SBDS and different interactions between Ni or Mg with PLA, as well as the different morphologies between the two LDHs. The second observation was ascribed to free volume faults and rotational fluctuations of water in the filler. The third phenomenon can be mistaken to be part of the α-relaxation, but the latter is not significantly affected by the LDH concentration. Rather, the authors proposed that the third observation is caused by conductivity and interfacial polarisation effects. The NiAl-LDH-PLA showed less dramatic peaks than the MgAl-LDH-PLA, which the authors ascribed to the different morphologies. Since NiAl-LDH was intercalated and MgAl-LDH was exfoliated in PLA, the former had less interfaces at, which charges may be blocked, and also less conductivity because of less free impurities — the authors believe the conductivity to be related to impurities within the LDHs.

Leng *et al* (2017b) also investigated the rigid amorphous fraction due to crystals ($\mathrm{RAF_{crystal}}$), the rigid amorphous fraction due to the filler ($\mathrm{RAF_{filler}}$), the crystalline fraction (CF) and the mobile amorphous fraction (MAF) of the composite prepared by Leng *et al* (2015). Due to the long halftime of the PLLA composite, the rigid amorphous fraction (RAF) of the composite can be determined from calorimetry because the crystallisation can be suppressed by high cooling rates. They used normal DSC and StepScan DSC to determine the respective fractions. They found that the melting enthalpy increased as filler was added to PLA, but then decreased with increasing filler loading, thus indicating the suppression of crystallisation. This allowed the estimation of the CF. Next, they determined the MAF from changes in the specific heat capacity at the T_g between the filled crystallised composites and pure amorphous PLA. This allowed the determination of the RAF. By comparing the same properties between the filled amorphous composites and pure amorphous PLA, the authors could determine $\mathrm{RAF_{crystal}}$ and $\mathrm{RAF_{filler}}$. The addition of 1 % LDH significantly increased the CF and significantly decreased the MAF of PLA. Increasing the LDH content to 12 % caused a further decrease in both the MAF and the CF. The $\mathrm{RAF_{filler}}$ increased almost linearly with LDH content, whereas the $\mathrm{RAF_{crystal}}$ stayed relatively constant. The authors noted that this seems to be unique to the LDH-PLA system.

Coiai *et al* (2017) modified MMT and LDH with PLA containing different end groups, namely ammonia chloride and sodium carboxylate respectively. Modification was confirmed. From DSC the authors observed that some of the intercalated PLA crystallised to

the metastable α' region instead of the normal α region, and that this was more evident for MMT composites. The PLA-MMTs and PLA-LDHs were then loaded into PLA at *ca* 1 % and 2 %. XRD and TEM showed that the filler was dispersed well within the PLA matrix, although some agglomerates were still observed on the TEM images. The LDH filled PLA had less aggregates than the MMT filled PLA. TGA results indicated that the PLA-NaCOOH intercalated LDH caused worse thermal properties. The authors also compared the effect of pure LDH in PLA *vs* PLA-NaCOOH intercalated LDH in PLA, and observed that the NaCOOH group caused PLA chain scission by hydrolysis. Further tests indicated that both the carboxylate and the LDH were responsible for this observation. In contrast, the MMT composites maintained their thermal stability. The number and weight average molecular masses of LDH filled PLA decreased substantially, whereas MMT filled PLA stayed relatively constant. This supported the observation that chain scission occurs in the LDH filled composites but not the MMT filled composites.

Hu *et al* (2018) exfoliated MMT and LDH separately with PLA, and confirmed proper exfoliation. They then hydrolysed the PLA from between the layers, allowing the MMT and the LDH to combine in different patterns depending on the mass ratios and the PLA hydrolysis. The layered structure of the MMT/LDH composite was confirmed by x-ray photoelectron spectroscopy. The authors showed with various optical analyses that for a PLA-MMT to PLA-LDH mass ratio smaller than one and larger than one, the so called head and tail of the train structures are LDH sheets and MMT sheets respectively. Controlling the hydrolysis also allowed manipulation of the final properties of the stacked clays.

Geng *et al* (2018a) intercalated amide ethylenediamine tetraacetic acid disodium salt in LDH (AE-LDH) and melt blended it into PLA with a double screw extruder at 0.05 %, 0.1 %, 0.3 % and 0.5 %. The compounds were then injection moulded into standard test specimens. The AE-LDHs exfoliated in the PLA matrix at a nanoscale and improved α-phase crystallisation. An increase in σ, ϵ_b and impact strength was observed up to 0.3 % AE-LDH-PLA, from where mechanical properties decreased again. The pure PLA had properties of 80.76 MPa, 18.47 % and 10.30 kJ m^{-2}, which increased to 84.15 MPa, 22.12 % and 19.81 kJ m^{-2} for the 0.3 % compound. The authors believed this was due to the LDHs improving crystallisation and strengthening intermolecular forces up to the point where there is too much filler after which agglomerates form, causing these phenomena to deteriorate at higher loadings. TGA and DSC results indicated an improvement in thermal resistance and crystallinity with an increase in LDH loading. Polarised optical microscopy (POM) showed that more spherulites formed in the LDH sample compared to pure PLA and that the total growth rate of crystals were faster, although individual spherulite growth was smaller due to impingement between spherulites. DMA results showed an increase in storage and loss moduli, as well as complex viscosity, with LDH

loadings up to 0.3 %, with a slight decrease at higher loadings as observed for the mechanical properties as well. The authors believed this was due to increased cross linking points restricting molecular motion, as well as hydrogen bonding between PLA and the amides in the LDH. Capillary rheological analysis coincided with the DMA results and showed a shear thinning pseudo-plastic behaviour with the viscosity for the filled polymer being higher than the neat one.

In a later work, the same authors synthesised a LDH-poly(methylmethacrylate) (PMMA) graft copolymer and melt blended it into PLA in a double screw extruder at 0.05 %, 0.1 %, 0.3 % and 0.5 %. Geng *et al* (2018b) found that the LDH-PMMA was well dispersed and exfoliated in the matrix, with crystals forming in the α-phase. Mechanical properties improved up to 0.3 %, after which they started decreasing again. For neat PLA and 0.3 % filled PLA the values of σ, ϵ_b and impact strength were 80.76 MPa, 17.47 % and 10.30 kJ m^{-2} as well as 85.32 MPa, 24.10 % and 15.42 kJ m^{-2} respectively. The authors proposed that this was due to enhanced crystallinity up to 0.3 %-LDH-PMMA, and that the decrease occurred due to agglomerates forming at higher LDH loadings. SEM analysis confirmed that the compound toughness increased, and that the LDH-PMMA could be responsible for additional energy dissipation mechanisms during impact tests. DSC tests showed that the heterogeneous LDH lowers the crystallisation activation energy, resulting in an increase of crystallinity from 5.21 % to 42.47 % for the 0.3 % sample. POM images showed that the total growth rate of crystals was larger for LDH filled samples due to more crystal nuclei forming. DMA results showed that the addition of LDH caused a lower T_g as well as a drop in storage modulus. It also indicated that the addition of LDH up to 0.3 % caused an increase in storage and loss moduli as well as complex viscosity, suggesting shear thinning behaviour. A slight drop is observed for higher LDH loadings. The shear thinning behaviour was confirmed with capillary rheology analysis.

In order to improve PLA's crystallisation, and thus its properties, Geng *et al* (2019) melt blended zinc oxide pillared LDH intercalated with SDS into PLA at 0.05 %, 0.1 %, 0.3 %, 0.5 % and 0.7 % loadings. The exfoliation and pillaring of the ZnO in the LDH was confirmed. They found that the ZnO-LDH-S had good UV absorption and antibacterial properties. Optimum mechanical properties were observed at 0.10 % ZnO-LDH-S, with an improvement in σ, ϵ_b and impact strength of 36 %, 39.83 % and 67.18 % respectively. This behaviour was ascribed to good compatibility at low LDH loadings, and the formation of aggregates at higher loadings, causing a decrease in performance. Impact test fracture surface analysis indicated a transformation from brittle to a tough fracture, assisted by the formation of oriented fibres in the matrix. TGA results showed an increase in thermal resistance with the filler. A reduction in the activation energy for crystallisation was observed from DSC analysis, and POM analysis showed that the LDH increased nuclei formation resulting in faster crystallisation and smaller spherulites. DMA indicated that

there was a reduction in T_g and that the storage modulus decreased as the filler loading increased. Moreover, the storage modulus and complex viscosity increased with LDH loading, and the viscosity showed shear thinning behaviour.

Geng & Zhen (2019a) also synthesised an amidated potassium hydrogen phthalate intercalated layered double hydroxide (AP-LDH) and melt blended it into PLA at 0.05 %, 0.1 %, 0.3 % and 0.5 %. They found that the filler was exfoliated within PLA with the formation of small aggregates, and that AP-LDH showed good anti-bacterial properties, especially against *E. coli*. Mechanical properties improved up to 0.3 %, after which they started decreasing again. Compared to neat PLA, 0.3 % filled PLA showed an improvement in σ, ϵ_b and impact strength of 5.57 %, 41.95 %, and 69.41 %, respectively. The authors proposed that the increase in mechanical properties was due to enhanced crystallinity and that the decrease occurs due to agglomerates forming at higher LDH loadings. SEM analysis on the impact test fracture surfaces indicated a transition from brittle to tough fracture, with fibres and rough surfaces observed for filled PLA. DSC results indicated an improvement in crystallinity due to a significant increase in the crystallisation enthalpy and lower transition temperatures. POM analysis indicated that LDH acted as a nucleating agent, forming more finer spherulite crystals and resulting in a faster overall growth rate. DMA results showed an increase in storage and loss moduli with filler loadings up to 0.3 %. The storage modulus was higher than the loss modulus, indicating a more dominant elastic system than a viscous system. The complex viscosity showed typical visco-elastic behaviour. The exfoliated nature of the LDH improved thermal stability through a more tortuous morphology, as shown by TGA results. Fitting non-isothermal TGA results to the Friedman model, the authors showed that the activation energy of thermal decomposition increased with filler loading.

The same authors mixed amidated benzoic acid intercalated LDH (AB-LDH) into PLA at 0.3 % and compared its properties with neat PLA. From DSC results, Geng & Zhen (2019b) showed a decrease in transition temperatures and an increase in the degree of crystallinity. POM analysis indicated more yet smaller spherulite crystals in the LDH sample than the neat PLA. An increase in σ, ϵ_b and impact strength of 12.83 %, 35.40 %, and 46.15 % respectively was observed. SEM images of the impact fracture surfaces indicate a brittle to tough fracture transition due to the increased crystallisation. Moreover, the LDH also absorbed UV radiation, thus improving the PLA's UV resistance. Fitting non-isothermal TGA data to the Friedman model, the apparent activation energy for degradation was found to increase with the LDH, thus indicating an increase in thermal stability. The authors also proposed a kinetic equation for the polymerisation reaction.

He (2019) investigated the effect of mixing MMT or LDH into PLA regarding its effect on crystallisation and the resulting effects. The author also briefly discussed poly(vinyl

acetate) formed by emulsion polymerisation with MMT.

Quispe-Dominguez *et al* (2019) prepared DBS-MgAl-LDHs and melt mixed them into PLA masterbatches (50 % LDH) *via* two methods, sonicated assisted masterbatch (SAM) and direct melt (DM) mixing. Thereafter 1.25 %, 2.5 % and 5 % LDH-PLA composites were prepared with a twin screw extruder. XRD and TEM analyses indicated that SAM achieved better dispersion than DM mixing, with the morphology being a combination of intercalated, exfoliated and tactoid structures. Larger and more agglomerates formed at higher loadings. TGA results showed that the thermal stability of samples decreased with increasing LDH loadings, and the SAM samples had superior thermal properties compared to the DM samples. DSC results indicated that the addition of LDH decreased the crystallinity of the compound, and that SAM achieved higher crystallinity than DM. The viscosity of samples increased with LDH loadings, and more so for the DM samples. The authors attributed their observations to the fact that the SAM mixing method achieved better dispersion than the DM mixing method.

Wang, Li & Liu (2019) made multilayered films consisting of separate aminolysed PLA, LDH and cellulose nanocrystal films. They mainly investigated the photoluminescent properties of the multilayered films, and found that the photoluminescent properties increased with the number of LDH-cellulose nanocrystal bi-layers, and that it retains its properties quite well even after bleaching. Moreover, they found that the tensile properties of aminolysed PLA was lower than that of pure PLA, although from ten bi-layers and more the tensile properties improved to such an extent that they were superior to that of pure PLA.

Delpouve *et al* (2020) modified LDH with hydrogenated fatty acids (O-LDH) and mixed this into PLA at 1 % and 2 %. Poly(butylene succinate adipate) (PBSA) was also compounded as a coupling agent with 1 % O-LDH filled PLA. This sample along with magnesium stearate modified PLA, processed PLA and neat PLA were used as references. The O-LDH was exfoliated in the PLA matrix, although some agglomerates were still observed. The crystalline domain increased with increasing annealing temperature. The authors suggested this is due to a larger amount of α-crystals, which are larger than the metastable α'-crystals that also formed. After annealing at 80 °C, the authors also noted that the lamellae thickness of crystals increased with filler loading, although this same trend was not noticed after annealing at 130 °C. The addition of filler promoted degradation as confirmed by both TGA and modulated temperature TGA. The lowest degradation temperatures were recorded for the 2 % O-LDH sample and the PBSA sample. The magnesium stearate sample, on the other hand, showed much better thermal stability. The authors believe this was due to less interfacial contact and less interaction with the PLA. Activation energies calculated from the TGA data also indicated that

degradation occurred differently under different atmospheres. The Mg and Al in the LDH is also believed to cause degradation. The authors observed that 1 % magnesium stearate filled PLA cold crystallised easier than neat PLA. Moreover, they reported that all fillers induced crystallisation, with the crystal type (α *vs* α') depending on the annealing temperature. They also noted that RAFs exist, and that these increased with O-LDH filler loading, and that PBSA had no effect on the fraction. The authors considered the mechanical properties of some samples. Generally, the O-LDH composites showed a reduction in σ and ϵ_b, and an increase in E for 1 % O-LDH, with a decrease again for 2 % O-LDH. The PBSA seemed to exaggerate the observations made. The magnesium stearate caused opposite observations. Annealing caused a reduction in σ and ϵ_b as well as an increase in E for all samples.

Mhlabeni, Pillai & Ray (2020) melt compounded 0.1 %, 0.5 % and 1 % LDH containing surface stearic acid functional groups (SaLDH) into a PLA/PBSA (80/20) blend. They observed from SEM analysis that PBSA formed droplets within the PLA matrix, which reduced in size up to 0.5 % SaLDH. They believe that the filler improved the dispersion of PBSA in PLA, although aggregates formed at higher loadings causing the filler to lose its effectiveness. TEM analysis confirmed this behaviour and the authors suggested that the clay mixes into the more viscous PBSA droplets during compounding, after which it diffuses to the PLA/PBSA interface due to its PBSA incompatibility. At lower loadings, the clay reduces interfacial tension and improves dispersion and miscibility, although the clay also dissolves into the PLA matrix at higher loadings, increasing its viscosity and thus the interfacial tension. Tensile tests showed that both the σ and ϵ_b increased with filler loading up to 0.5 % SaLDH, after which they decreased again. The same behaviour was observed for the thermal stability and the oxygen gas barrier properties of the compound. The authors proposed that this is due to the morphology as discussed above.

Liu *et al* (2021b) prepared Co, Ni, Cu and Zn MgAl-LDH as well as pure MgAl-LDH and confirmed successful synthesis with XRD. They melt blended it into PLA at 0.5 %, 1 %, 2 %, 4 % and 10 %. The addition of MgAl-LDH in PLA showed an optimum in tensile properties at 0.5 % with an increase in σ and ϵ_b from 36.89 MPa and 14.73 % to 43.46 MPa and 43.91 %. The impact strength and bending strength however deteriorated compared to pure PLA. The σ, ϵ_b and bending strength increased for the Co, Ni, Cu and Zn MgAl-LDH samples, whilst the impact strength decreased, with the CuMgAl-LDH filled PLA showing the best holistic properties. Adding a silane coupling agent to MgAl-LDH benefited the σ, ϵ_b and bending strength by plasticising the matrix. The oxygen index of PLA increased with MgAl-LDH loading from 0 % to 18.56 % for pure PLA to 10 % LDH. Moreover, the addition of the metals also benefited the oxygen index in the order Zn, Ni, Co and Cu from lowest to highest. The silane coupling agent did not show any significant effect on the oxygen index. DSC results indicated a decrease in T_g and

T_m, as well as an increase in crystallisation temperature (T_c) with increased MgAl-LDH loading. The metals caused a decrease in T_g from highest to lowest in the order Ni, Co, Zn and Cu. This indicated an increase in plasticisation.

Liu *et al* (2021a) prepared LDH and SDS modified LDH. They melt blended these into PLA at 0.5 %, 1 %, 2 %, 4 % and 10 % loadings. The addition of pure LDH resulted in a decrease in T_g and T_c but an increase in T_m. The authors did not find a general correlation between the temperatures and LDH loadings. The modified LDH showed a lower T_g and T_m but a higher T_c.

Monshizadeh *et al* (2021) modified LDH with 10 % triethyl citrate (TEC) and solution casted it as well as pristine LDH into PLA films at 2 % and 4 %. SEM and EDX analysis indicated that the TEC's plasticising effect enhances the LDH dispersion. The T_g and T_{cc} of pure and pristine LDH-PLA samples remained relatively constant, however the addition of TEC reduced these temperatures significantly. A bimodal melting curve also resulted for the latter two samples, and it was believed to be due to two crystal types induced by the lower T_{cc}. DSC scans indicated that the addition of LDH improved crystallisation, and that TEC samples crystallised during melt cooling. The crystallinity of LDH samples increased, and that of TEC-LDH samples increased significantly. The 4 % loadings yielded lower crystallinities than 2 % loadings. Tensile tests indicated that σ and ϵ_b decreased with filler loading for pristine LDH-PLA, whereas σ and ϵ_b decreased and increased respectively with TEC-LDH loading. Compared to pure PLA, the former showed an increase and decrease in σ and ϵ_b respectively, but a decrease and increase in σ and ϵ_b for TEC-LDH-PLA. The authors believed these effects were due to the plasticising effect of the TEC, as well as better dispersion at lower filler loadings. TGA indicated that the addition of both LDH and TEC-LDH improved the thermal stability of the PLA matrix.

Jilili *et al* (2022) mixed a thiolene and silane coupling agent surface modified ZnMgAl-LDH (LDH-B-OM) into PLA at 0.1 %, 0.3 %, 0.5 %, 0.7 % and 0.9 % called PLA1 to PLA5. Nanocomposite films were blow moulded. Mechanical tests indicated the optimum LDH-B-OM loading was 0.7 % (PLA4) yielding an increase in σ and ϵ_b from 36.47 MPa and 14.2 % for pure PLA to 46.99 MPa and 74.09 % respectively. Rheological tests indicated that PLA4 induced lower storage and loss moduli as well as complex viscosity over a range of angular frequencies, thus showing LDH-B-OM's plasticising nature. PLA crystallised easier under shear and the LDH-B-OM showed synergy for shear induced crystallisation. FTIR was used to confirm this by tracking the carbonyl group in the amorphous and crystal regions, and the Avrami equation was fitted to the IR spectra. The storage and loss moduli for PLA4 were lower than pure PLA at low degradation time, with a cross over at intermediate times and a slight increase in moduli for PLA4

over PLA at extended times. The same was observed for the complex viscosity, which also showed shear thinning behaviour. The authors believed the cross over suggested that the LDH-B-OM improved the thermal stability of the PLA. Relating degradation to complex viscosity and molecular mass as well as the carbonyl index measured by FTIR, the authors showed that the filler also mitigates thermal degradation.

Ozturk *et al* (2022) synthesised MgAl-LDH at 2/1 and 3/1 Mg/Al molar ratios. These were incorporated at 1 % and 2 % respectively into a 8 % PLLA/5 % poly(ethene oxide) (PEO)/chloroform mixture to produce electrospun fibres. The addition of MgAl-LDH caused a reduction in viscosity and surface tension as well as an increase in electrical conductivity, benefiting the electrospinning process. FTIR results indicated good interaction with the PEO and PLA matrix, thus resulting in amorphous and flexible nanofibres. SEM analysis showed that the filler allowed the fabrication of smooth and smaller diameter fibres. Tensile results indicated that no significant improvement resulted from adding 1 % MgAl-LDH, however a remarkable increase was observed for both the 2 % MgAl-LDH samples. From TGA results the authors noted that the Mg_3Al-LDH PLA/PEO composite decreased the PLA decomposition temperature, although it did not affect the PEO decomposition temperature. The authors believed this was due to the LDH-OH groups catalysing PLA degradation. TGA results confirmed that the 2 % MgAl-LDH filler reduced the decomposition temperature of the PLA, having no significant effect on the PEO. Nevertheless, the weight loss rate of the blend was faster than the filled blend. DSC results also showed that the melting temperatures of PLA and PEO was increased with increasing Mg_3Al-LDH content. Finally, the authors found that their XRD and TEM results correlate well with existing literature. They also used this to confirm the molar MgAl ratios quoted.

2.1.6 Review articles

Five of the 87 search results considered were literature review articles or book chapters. None of these were comprehensive in nature and they sporadically cited articles for a very specific application, of which most were already discussed, as summarised in Table 1. A few new articles were found in the reviews as detailed below.

Plackett (2011) summarised the developments in the applications of films and coatings. They cite only one article not already discussed, namely Ruiz-Hitzky *et al* (2010). They do not discuss PLA and LDH as a composite. Gong *et al* (2018) wrote a review article, and although they have an English abstract, the article could only be found in Chinese, and was not further considered. Mallakpour & Khadem (2018) discussed the status of biodegradable polymer LDH nanocomposites, but did not quote any new articles. Chat-

terjee, Bharadiya & Hansora (2019) reviewed the use of LDHs as bionanocomposites. One of the sections they addressed was LDH PLA nanocomposites. One new article was cited, namely Chatterjee & Hansora (2016), a book chapter on green polymer nanocomposites focusing on medical applications. No new articles were cited by the book chapter.

Rives *et al* (2014) summarised the use of LDHs in PLA for the purposes of controlled drug release. There were two new articles, namely Pan *et al* (2008) and Chiang, Chu & Wu (2011). Pan *et al* (2008) modified MgAl-LDH with SDS and melt blended it into PLLA with a single screw extruder. They found that the DS anion intercalated into the LDH, and that DS-LDH had an intercalated and partially exfoliated morphology in PLLA. The authors concluded that DS-LDH does not significantly affect the crystallisation or melting behaviour of PLA, but it does increase the rate of crystallisation. The DS-LDHs act as heterogeneous nucleating agents, resulting in a higher density of smaller spherulitic crystals. Chiang *et al* (2011) investigated the thermal degradation behaviour of the same samples prepared by Chiang & Wu (2010). The authors found from TGA results that an increase in filler loading caused a decrease in thermal stability. They proposed this is due to Mg and Al catalysing degradation, which they confirm from TGA results. They observed that the filler caused a decrease in activation energy.

Table 1: Summary of the articles cited by the review articles, which are already discussed in this review with the section where it was discussed.

Review	Section	Applicable articles cited
Rives *et al*, 2014	§ 2.1.1	Wang *et al*, 2010
	§ 2.1.2	Dagnon *et al*, 2009; Miao *et al*, 2012; San Román *et al*, 2013
	§ 2.1.3	Eili *et al*, 2012
	§ 2.1.4	Katiyar *et al*, 2010; Schmidt *et al*, 2011
	§ 2.1.5	Zhao *et al*, 2008; Chiang & Wu, 2010; Ha & Xanthos, 2010; Gerds *et al*, 2012
Mallakpour & Khadem, 2018	§ 2.1.1	Wang *et al*, 2010
	§ 2.1.1	Miao *et al*, 2012; San Román *et al*, 2013
	§ 2.1.5	Gerds *et al*, 2012
Chatterjee, Bharadiya & Hansora, 2019	§ 2.1.2	Dagnon *et al*, 2009; Miao *et al*, 2012; San Román *et al*, 2013
	§ 2.1.5	Hennous *et al*, 2013
Plackett, 2011	§ 2.1.4	Katiyar *et al*, 2011

2.1.7 Discussion

From Search 1 it is clear that polymeric filaments filled with LDH for FDM applications are completely undeveloped. Only one article could be found in this regard. It is recommended that further research be completed on LDH filled polymeric filaments for FDM applications.

Search 2 showed that most available literature on LDH and PLA concentrates on characterisation and general properties of compounds. Flame retardance, controlled drug release and permeability applications were the only subjects that have been developed in the field. Little literature was available on environmental applications, and a few articles discussed the removal of pollutants. It is suggested that general research on LDH filled PLA should be avoided, and that the composite should rather be researched for a specific application, e.g. FDM, pollutant filters *etc.*. Fields like controlled drug release, flame retardancy and packaging can also be developed further whilst keeping in mind what previous authors have already achieved.

It is clear that LDH has great potential as a functional filler. It does not necessarily increase the strength of parts significantly enough to be used for this sole purpose, but it allows for tailoring a final artefact. Because substances can be intercalated into LDH it has the potential of manufacturing parts that are highly flame retardant, that can diffuse medicine for customised situations and that can be used in environmental applications. The potential of useful applications can be expanded if it can be used in FDM, because of its ability to realise complex designs.

Contradicting results are reported about the effect of LDH on PLA, *e.g.* loadings at which optimum mechanical properties occur and thermal stability trends. This is most probably due to different grades of PLA and different compatibilisers used with LDH. It will also be worthwhile to conduct research on the effect of different PLA grades and LDH compatibilisers on properties of interest.

Figure 1 summarises the 87 articles reviewed by year and by topic. The field in general is quite new, starting only in 2003. Since then there was an increase in publications, although it seems as if they started to decrease again in 2019. It might be possible that the regulations and restrictions world wide due to Covid 19 might have caused this. Only some publications focused on specific applications, but the vast majority only considered general characterisation and properties. Clearly, there is much room for research on specific applications. In fact, it was determined that only six groups actively contributed to the field. This was done by considering connections between authors and co-authors who published three or more articles. With the versatility of LDH clearly demonstrated

by existing literature, new ideas and applications should be investigated. Lastly, no comprehensive review of LDH and PLA was found in literature. Therefore, this is the first review of its kind. Since the PRISMA guidelines were used, future reviewers may use this review as the base of a growing systematic literature review.

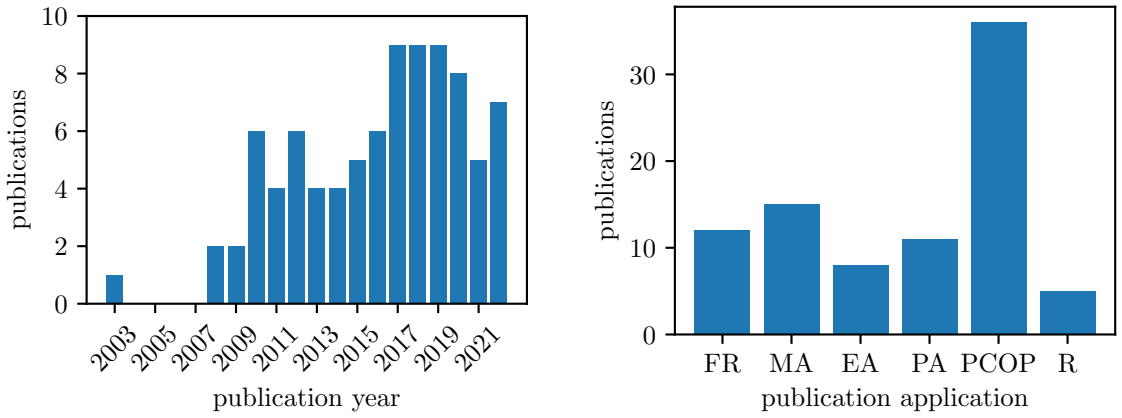

(a) Summary by year.

(b) Summary by application.

Figure 1: A summary of the 87 articles reviewed in the second systematic literature review by year and by application. Abbreviations in Figure 1b — FR: flame retardancy, MA: medical application, EA: environmental application, PA: packaging application, PCOP : processing, characterisation & other properties and R: reviews.

2.2 Materials

2.2.1 Poly(lactic acid)

PLA is a recent and actual research topic, since it is derived from renewable resources and it is compostable. Its products are therefore a favourable alternative to traditional plastic products, because it has the potential to reduce plastic waste in landfill sites and does not deplete fossil fuel resources. Its monomer is 2-hydroxypropionic acid (known colloquially as lactic acid), and exists as two enantiomers, namely *laevus* and *dexter* lactic acid (*l*- and *d*- lactic acid). Lactic acid from biological sources, *i.e.* renewable sources, exist mainly in the *laevus* form. Typically, crystalline PLA has a *laevus* content exceeding 90 %, with lower contents yielding amorphous PLA. PLA crystallises into the α, β and γ forms, with the former being the most stable. A reaction mixture with a high *l*-lactic acid content tends to form α crystals. Generally PLA has a good Young's modulus and strength but brittle characteristics. Within these constraints, it competes with petroleum based thermoplastics in a variety of applications. (Lim *et al*, 2008)

A variety of fillers have been researched for use in PLA manufacturing processes. For

FDM specifically a few examples include cellulose, carbon and metal based additives, continuous fibres, nanoclays and silica (Bardot & Schulz, 2020); commercial graphene nanocomposites (Prashantha & Roger, 2017); carbon and nylon glass fibres (Vinyas *et al*, 2019) and silicon (Vishal *et al*, 2022). The tensile properties recorded by two of the authors are summarised in Tables 2 and 3.

Table 2: Tensile properties determined by Prashantha & Roger (2017). 10GNC is an abbreviation for 10 m% graphene nanocomposite.

material	σ_b [MPa]	ϵ_b [mm mm^{-1}]	E [MPa]
PLA	31.6	0.026	1 827
10GNC-PLA	40.2	0.023	2 454

Table 3: Tensile properties determined by Vinyas *et al* (2019). 10CF and 30NGF are abbreviations for 10 m% carbon fibre and 30 m% nylon glass fibre respectively.

material	σ_b [MPa]	ϵ_b [mm mm^{-1}]	E [MPa]
PLA	46.66	0.000135	3 469.15
10CF-PLA	33.88	0.000213	1 591.35
30NGF-PLA	15.95	0.000067	2 403.19

Sandanamsamy *et al* (2022) thoroughly reviewed the use of PLA in FDM. Their main conclusions were that layer thickness, extrusion temperature, raster angle, nozzle diameter, infill pattern and nozzle temperature affect the mechanical properties of artefacts. The nozzle diameter and infill are more important, especially from a processing and cost optimising point of view. Infill density affects tensile properties and surface roughness significantly. Considering fillers, the authors found that carbon, plant and mineral based fillers comprised 43 %, 32 % and 25 % of PLA fillers in FDM respectively. The latter comprised of hydroxyapatite, ceramic and akermanite. They discussed the drawbacks of PLA, but highlight the growth trend of both FDM and PLA's use in FDM, and project further growth in future.

2.2.2 Layered double hydroxide

LDHs have divalent and trivalent metal cations in an octahedral structure, which form brucite-like hydroxylated layers. The layers have a positive charge due to the cations, which are counterpoised by carbonate and water molecules in between the layers. LDHs can be made from a variety of cations, such as Mg, Mn, Fe, Co, Ni, Cu, Zn and Ca divalent

cations as well as Al, Cr, Mn, Fe, Co, Ni and La trivalent cations. The generalised formula for LDH is

$$[{M^{II}}_{1-x}{M^{III}}_{x}\,(OH)_2][X^{m-}_{x/q}\,nH_2O]$$

where the charge of each layer is related to the substitution rate of the cations, x, and q refers to the charge of the anion. M^{II} and M^{III} are the divalent and trivalent cations and X^{m-} is the cation. LDHs can be tailored by exchanging the CO_3 anion with other anions. (De Roy *et al*, 1992; Forano *et al*, 2006) A graphical representation of the general structure of LDH is shown in Figure 2. The ability to intercalate anions of the user's choice and to adapt the cationic layers make LDHs extremely versatile.

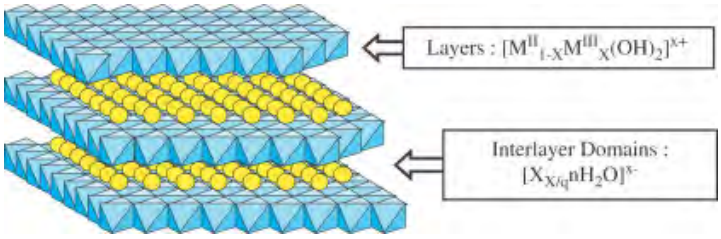

Figure 2: The general structure of LDH (Forano *et al*, 2006).

2.3 Additive manufacturing

To increase efficiency there is a large focus on automation and integrating information technology with physical systems and production. The Internet of Things and digital communications increased possibilities significantly, as did manufacturing processes by robots and AM. The latter is not necessarily ideal for mass production, but allows the manufacturing of complicated geometries as well as customisation of products and designs without changing production lines, workshop layouts or tools. As such, AM has already been employed in the aerospace and biomedical industries. (Dilberoglu *et al*, 2017)

AM mostly use polymers as the material of manufacturing, but stainless steel; aluminium, cobalt, nickel, shape memory alloys, titanium, textile and food materials and concrete have also been used (Dilberoglu *et al*, 2017). The general procedure to manufacture a part with AM is as follows: (1) design using a computer aided design (CAD) programme or 3D scan, (2) convert to an exchange format *e.g.* stl or 3mf file, (3) apply AM settings *e.g.* orientation, printing speed and other parameters, in a slicer software like Ultimaker Cura, (4) slice information into g-code, (5) print part, and (6) post processing. The last step is optional depending on final part requirements. (Gardan, 2016) Although stl files are the oldest and most used format for exporting CADs in the AM industry, they

have large file sizes and cannot detect errors. On the other hand, 3mf files are based on extensible markup language technology and addresses the problems associated with stl files. In addition to smaller files, 3mf files can also store additional information like material, texture and colour information. It is therefore the superior exchange format available. (Iancu, 2018)

2.3.1 Summary of additive manufacturing methods

There is a variety of AM methods, and they are based on laser, flash, extrusion, jet as well as lamination and cutting technologies.

Laser technologies include stereolithography (SLA), selective laser melting, selective laser sintering and direct metal laser sintering. In SLA, photosensitive resins are cured with light. This is typically used with polymers. It is the most used AM method. In the other methods, a powder is fused together using a laser. They were developed to allow the AM of metals. Flash technology was developed to allow faster production. It essentially works the same as SLA, but instead of only curing single lines or points it cures a whole layer at a time. (Gardan, 2016)

Extrusion technology includes FDM (also known as fused filament fabrication (FFF)), directed energy deposition (DED) and dough deposition modelling (DDM). It is relatively cheap compared to other extrusion technologies. DED is often used to repair or add metal material to an existing part and have several sub-technologies like Laser engineered net shaping, ion fusion formation and direct metal deposition. DDM work similar to FDM but with a dough in a syringe. It prints materials like silicone, chocolate, biopolymers and wood pulp. (Gardan, 2016)

Jet technologies include multi jet modelling (MJM), colour jet printing (CJP), prometal and liquid metal jetting (LMJ). MJM uses two photopolymers, one the actual part material and the other a soluble support gel. The latter is removed after printing using a water jet. Ultra violet light is used to cure the polymer deposited in droplets. It is accurate and yields smooth surfaces. CJP deposits a thin powder layer and then binds them together by inkjet printing. Metals, ceramics, silica and polymers have successfully been printed. Prometal uses stainless steel powder and binds it with a liquid binder. LMJ prints parts by jetting molten metal droplets that fuse together. (Gardan, 2016)

Laminated object manufacturing laminates papers layer by layer with a heat sensitive adhesive to form an object.Stratoconception cuts a sheet of material, *e.g.* wood, with a laser or milling device into individual layers or strata. These are then assembled into one object at the end with reinforcing pieces included in the design. (Gardan, 2016)

In recent reviews about AM, more standardised terms are being used. This is a positive development, because the AM community use different terms that are synonyms for the same technology. For example, FDM is also known as FFF, but the new standardised term is material extrusion (ME). The ISO and ASTM terms for the seven main technologies are vat photopolymerisation (VP), material extrusion, DED, powder bed fusion (PBF), binder jetting (BJ), material jetting (MJ) and sheet lamination (SL) (Du Plessis, Du Preez & Stefaniak, 2022; Mallikarjuna *et al*, 2023). Older terms are still very popular and often used in literature. For example, SLA is actually a trademark, but is often used instead of the official term: VP. DED and SL have remained unchanged, but PBF is the standard term for selective laser sintering and melting as well as direct metal laser sintering, BJ is the standard term for CJP and MJ is the standard term for MJM.

2.3.2 Fused deposition modelling

FDM is a form of AM in which a thermoplastic filament is melted by a print head and extruded onto a bed, printing an artefact layer by layer. The equipment is cheap compared to other AM methods and allows simple, rapid prototyping. (Ngo *et al*, 2018; Wong & Hernandez, 2012) After SLA, FDM is the most popular AM technique, because it is a relatively cheap method, which prints complex parts with accurate dimensions in a safe environment. A large selection of customised thermoplastic materials are readily available. (Sandanamsamy *et al*, 2022)

Printing parameters affect the final strength of a printed artefact. In a recent review, Syrlybayev *et al* (2021) concluded that optimisation of said parameters will differ from case to case depending on the application. Although the authors could not derive an empirical formula or correlation for part strength as a function of layer height, this parameter was considered to have the largest effect on a print's strength. It does however vary with filament material. The authors believe that nozzle temperature, also referred to as extrusion temperature, and infill density also affect part strength significantly. Similarly, Medibew (2022) reviewed the effect of FDM parameters on PLA parts specifically. They found that layer height affected part strength the most, followed by nozzle temperature, raster angle, infill density, infill pattern and lastly printing speed.

Figure 3 illustrates the basic concept of FDM, layer height and infill density. The general process where a thermoplastic filament is fed to the extruder is shown in Figure 3a. The filament enters a heating block, which melts the polymer and then passes through a nozzle before it is extruded on a bed. The latter is mostly heated as well, depending on the printer. The artefact is then printed layer by layer. Figure 3b illustrates layer height, and the concept of infill density is illustrated in Figures 3c and 3d. In these sketches,

lines have been used for infill density with an orientation of $\pm 45°$. Other orientations and infill patterns exist, *e.g.* triangular and hexagonal patterns. Typically, a few walls are printed against one another, as is also the case with the bottom and top layers. These form a shell around the infill that gives the artefact a solid outer surface. In the examples illustrated above, three walls are shown.

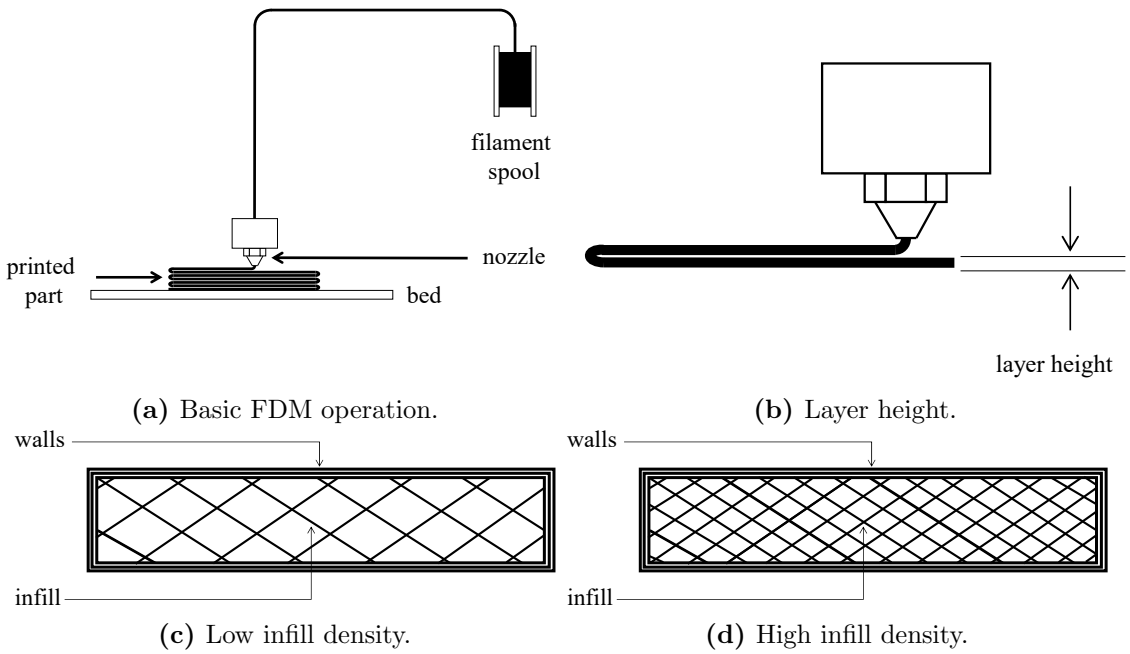

(a) Basic FDM operation.

(b) Layer height.

(c) Low infill density.

(d) High infill density.

Figure 3: Sketches giving and overview of how fused deposition modelling works and detailing some FDM parameters that has a significant effect on part strength.

Krajangsawasdi *et al* (2021) reviewed the effect of FDM parameters and various materials on the mechanical properties of final artefacts. Only neat and fibre reinforced polymers where considered. They concluded that printing speed does not have a drastic effect on tensile strength, but that it has to be balanced with material feed rate to prevent nozzle blockages as well as residual stresses between fillers and the polymer matrix. They found that a higher nozzle temperature allows chain randomisation between rasters, enhancing the mechanical properties of artefacts. However, nozzle temperatures should be well below the temperature at which the compound merely flows. A too high temperature lead to a change in material properties and poor print quality. Similarly, a bed and/or environmental temperature slightly below the glass transition temperature improves inter-raster fusion and part crystallinity. Upright build orientation was found to always be inferior to flat and on edge orientations, because the former depends on raster fusion whereas the latter depends on material strength. It seems as if material type plays a role in whether the flat or on edge orientation is superior. A $0°$ raster angle yields the best tensile, flexural and bending strengths, because the strength is tested in the same direction. This, however, makes artefacts very weak in the perpendicular

direction. For pure polymers, the ±45° raster angle was found to be superior, since it distributed loads evenly. Although trends fluctuate, fibre reinforced polymers are not necessarily strongest with either of these raster angles. Moreover, high raster width is recommended for improved tensile properties. Controversy exists in literature on the effect of raster thickness. Contour numbers and percentage infill are directly correlated to part strength, but the latter also causes higher manufacturing times. Nozzle geometry can be used to reduce swelling and thus improve mechanical properties, but can also increase manufacturing time and affect geometrical accuracy. PLA, acrylonitrile butadiene styrene (ABS), poly(propylene), polyamide, polyether ether ketone and polyethylenimine was reviewed by the authors, although PLA is by far the favourite material for FDM due to its low processing temperature and viscosity yielding good prints. However, ABS was found to be superior with fibre reinforcement despite its processing challenges, followed by polyethylene terephthalate glycol and PLA.

2.4 Injection moulding

Injection moulding is used for producing plastic products and dominates more than one third of the thermoplastic industry. A typical machine consists of a plasticising unit, clamping unit and a mould. A complete cycle consists of the following events. First the mould closes and molten material is injected into it, after which pressure is kept constant for some time. Then the screw turns in the extruder, filling it and melting the material for the next part. During this time the material in the mould cools, after which it opens and ejects the part. The process is repeated for each part made. The plasticising unit, which is also the injection unit, is similar to a single screw extruder, but is called a reciprocating screw extruder because the screw can slide in its barrel to store enough melt for injection into the mould. It melts the material and stores enough in the screw chamber to fill the mould, and provides the necessary holding pressure to prevent shrinkage. The clamping unit opens and closes the mould. The latter is specially designed for each product with a sprue and runner system, gate, and cooling and ejector systems. When properly designed, this yields optimal strength plastic parts without surface defects. (Osswald, 2017: 119-130)

2.5 Characterisation

2.5.1 Differential scanning calorimetry

Differential scanning calorimetry (DSC) is a quantitative thermal analysis method in which energy differences are measured. A thermogram indicating the heat flux *vs* temperature results. DSCs are used to determine the glass transition temperature, T_g, of a polymer, which is associated with a change in heat capacity, as well as other transition temperatures and their associated enthalpies. (Skoog, Holler & Crouch, 2018: 825-829) The degree of crystallinity, χ_c, of a sample can be determined from DSC results using Equation 1

$$\chi_c = \frac{\Delta H_f - \Delta H_c}{\Delta H_f^\circ} \tag{1}$$

with ΔH_f the enthalpy of fusion, ΔH_c the enthalpy of crystallisation and ΔH_f° the enthalpy of fusion of 100 % crystalline polymer (Delpouve *et al*, 2020; Leng *et al*, 2015; Geng *et al*, 2018b; Skoog *et al*, 2018). The latter can be taken as 93 J g^{-1} (Delpouve *et al*, 2020).

Zhang *et al* (2008) investigated the α and α' phases for PLLA specifically, and found that at T $\geq$ 120 °C the former phase forms whereas at at T $<$ 100 °C the latter forms. Based on WAXD results, the authors concluded that the α' phase discretely transforms to the α phase in a first order transition, instead of the continuous transition accepted before.

Delpouve, Saiter & Dargent (2011) investigated the effect of the l/d ratio of PLA on its crystallisation behaviour. They used the three phase model, which states that when semi-crystalline polymers crystallise, a crystalline, mobile amorphous and rigid amorphous phase forms. The RAF is the part of the amorphous phase that has restricted chain mobility due to its coupling to crystalline lamellae. PLA crystallises into a perfect crystal, the α phase, or into a less perfect crystal, the α' phase. The authors found that if isothermal crystallisation occurred at T $\geq$ 120 °C, the former phase results with a low RAF of around 10 %, whereas if it occurred at T = 80 °C the latter phase results with a higher RAF of around 35 %.

Righetti *et al* (2015) also investigated the α and α' phases for PLLA specifically, focusing on the differences in melting and crystallisation enthalpies of the two phases. They concluded that when DSC is done at general conditions, ΔH_m and ΔH_c includes an enthalpy associated with the conformation of the α' to the α phase, and therefore there is little accurate correlations in literature for estimating PLA enthalpies.

Delpouve *et al* (2020) used DSC in their analysis of PLA filled with a variety of fillers, including LDH. They observed a double melting peak for their compounds, which they ascribed to the conformational transition of the α' phase to the α one.

All the other authors in systematic literature review who mentioned DSC specifically in their tile, abstract or keywords either did not observe a double melting peak, or did not discuss the phenomenon. It seems as if the recognition of the metastable α' phase is relatively new.

2.5.2 X-ray diffraction

When X-radiation passes through a medium with highly regular scattering centres, and the wavelength is approximately the same as the distance between layers of atoms, the radiation gets diffracted. This is described by Bragg's law (Equation 2)

$$\mathbf{n}\lambda = 2d \sin\theta \tag{2}$$

with λ the wavelength, d the interplanar crystal distance and θ the angle. (Skoog *et al*, 2018: 279-280) X-ray diffraction (XRD) is used to study crystalline materials, more specifically the spacing and arrangement of atoms. It is also used in the identification of elements and compounds by comparing peaks at their 2θ positions to an empirical database. (Skoog *et al*, 2018: 294-297)

2.5.3 Fourier transform infrared spectroscopy

Fourier transform infrared spectroscopy (FTIR) is used to qualitatively identify organic functional groups from the absorbance spectra. Results may be ambiguous due to the overlap of group frequencies or variations in spectra due to sample preparation. Accordingly, results should be confirmed. Attenuated total reflectance (ATR) spectrometry is mostly used when working with polymers. (Skoog *et al*, 2018: 412-432)

Several authors have investigated the FTIR spectra of PLA and LDH. Their findings have been summarised in Table 4. The results reported by these authors compare quite well despite the different contexts of their research. Also added to the table are two references for distinguishing between stearic acid and stearate salts by identifying the respective peaks for $-\mathrm{COOH}$ and $-\mathrm{COO}^{-}$.

Table 4: FTIR results reported in literature for PLA and LDH.

Material	Group	Wavenumber / ν [cm^{-1}]	Reference
PLA	O–H stretching	3 444	Baltazar-y-Jimenez & Sain (2012)
	C–H stretching	2 995, 2 944	
	Absorbed water	1 640 - 1 635	
	CH_3 bending	1 453	
	C–H bending	1 382 - 1 362	
	C–O stretch	1 130	
PLA	C–H stretching	2 994	Geng & Zhen (2019b)
	C=O stretching	1 754	
	C–O–C stretching	1 182	
	C–O stretching	1 086	
PLA	C=O stretching	1 756	Ozturk *et al* (2022)
	CH_3 scissoring	1 454	
	C–O stretching	1 180	
	C–CH_3 stretching	1 045	
	C–COO stretching	868	
LDH	O–H stretching	3 460	Geng *et al* (2018b)
	CO_3^{2-} telescopic	1 385	
LDH	O–H stretching	3 519	Oyarzabal *et al* (2016)
	CO_3^{2-} stretching	2 922	
	interlayer water	1 644	
	CO_3^{2-} stretching	1 371	
	metal - oxygen modes	655	
LDH	O–H	3 500 - 3 200	Mhlabeni, Pillai & Ray (2020)
	C–O bonds in CO_3^{2-}	1 369	
Stearic acid	C=O bonds in COOH	1 703	Nguyen *et al* (2020)
and salts	COO^- from salt	1 552	
Stearic acid	C=O bonds in COOH	1 709	Shi, Rosa & Lazzeri (2010)
and salts	COO^- from salt	1 575	

2.5.4 Scanning electron microscopy

In scanning electron microscopy (SEM), a beam of electrons are impinged on the surface of a solid sample, and the backscattered electrons, secondary electrons and X-radiation is detected. From this data, the image is constructed. Samples are relatively large, with edges being several centimetres long. SEM works best with conductive samples, and non-conductive samples are sometimes coated with a conductive material, although the coating can obscure details of the surface. Polymers are not only nonconductive, but they may also thermally degrade, get damaged due to radiation or volatilise due to the high vacuum environment of the sample holder. Environmental SEM allows the sample to be placed in an environment with higher pressures and lower temperatures, avoiding problems associated with conventional SEM. A slight drop in resolution results. (Skoog *et al*, 2018: 553-558)

2.5.5 Dynamic mechanical analysis

Dynamic mechanical analysis (DMA) is a rheological test and its results are useful combined with thermal analyses (Menard, 2008: xi). By analysing the sample's response to an applied oscillating force, the viscosity and modulus of the material can be determined. Contrary to traditional tensile tests, DMA is completed over a range of frequencies and temperatures, yielding much more information on the sample's properties. DMA gives the complex viscosity, η^*, which may be correlated to steady shear viscosity, η, at low shear rates, as well as the complex, elastic and imaginary loss moduli (E^*, E' and E'' respectively). These moduli are not the same as Young's modulus, E, but they give a more detailed description of the material. E' shows the ability of the material to store or return energy, and E'' the ability to lose energy. The ratio of the two is exhibited as damping, and is known as $\tan\delta$.b(Menard, 2008: 1-12)

2.5.6 Polarimetry

Feng *et al* (2010) found that the *d* content of PLA copolymers and blends can be determined using polarimetry because the two enantiomers give the same magnitude optical rotation but with different signs. They found that results compared well with high performance liquid chromatography provided no fillers or monomer is present in the samples. They proposed Equation 3 to determine the d content (d %)

$$d\ \% = \frac{[\alpha]_{\mathrm{PLLA}} - [\alpha]_{\mathrm{PLA}}}{2[\alpha]_{\mathrm{PLLA}}} \times 100 \tag{3}$$

where $[\alpha]$ is the specific rotation of either pure l PLA (PLLA) or the PLA of interest respectively. The specific rotation can be calculated with Equation 4

$$[\alpha] = \frac{100\alpha}{lc} \tag{4}$$

with α the measured angle of rotation in °, c the concentration of the sample in g 100 mL^{-1} solvent and l the cuvette length in dm (Krüss Optronic GmbH, 2005).

2.5.7 Melt flow rate

ASTM D1238 (2023) and ISO 1133 (2022) describes how to determine the melt flow rate (MFR)— also known as melt flow index (MFI) — as well as the melt volume rate (MVR). In summary, a sample is forced through a capillary tube with a specific length by a load with a standard mass at a specific temperature. The mass, or volume, that passes through the tube in 10 minutes are reported as the MFR and MVR respectively. As such, the MFR gives an indication of the rheology of the sample, where the MFR is inversely proportional to the viscosity.

2.5.8 Oscillating rheology

Oscillatory rheometers can have different geometries, including cone plate, plate plate and concentric cylinder geometries. In each case the sample is placed in a small gap between the geometries, where the one is fixed and the other can be rotated. By rotating the one geometry at a constant shear rate or shear stress, the typical rheological parameters *i.e.* the storage and loss moduli, the complex viscosity and the damping factor, can be determined by measuring the variable responses of the material. Depending on the application, oscillatory rheometers can be used to complete amplitude, frequency, time and temperature sweeps. (Anton Paar GmbH, 2023)

The parallel plate rheometer is often used when measuring rheological properties for polymer melts of filled polymers. The gap between the one stationary and the other rotating plate is normally 1 mm to 2 mm for 25 mm diameter discs. As long as the ratio of the particle diameter to the gap between the plates are much smaller than one, the rheological properties measured are accurate. A draw back of the parallel plate rheometer is that viscoelastic materials tend to leave the gap at high shear rates and that the flow in the gap is heterogeneous. (Carreau, De Kee & Chhabra, 2021: 110-111)

2.5.9 Thermogravimetric analysis

TGA is an analytical method where a sample is heated in a controlled atmosphere and its mass is measured as a function of time and temperature. Temperature is normally increased linearly. TGA is used to study various physical processes but are mainly employed for decomposition studies in polymer science. It is also useful for determining moisture content. The derivative of mass loss is useful because it can be used to identify transitions in the thermogram that is not easy to distinguish. Often TGA is coupled with FTIR or mass spectrometers to allow the identification of the TGA products. (Skoog *et al*, 2018: 820-823)

2.5.10 Tensile testing

ASTM D638 (2022) and ISO 527 (2019) describe how the tensile properties of plastics should be determined. The stress, strain and Young's Modulus of the specimen can be determined from the measurements made. According to both standards, five specimens should be tested that break within the claws of the strainmeter, and do not break due to some fault in the specimen. The dimensions between the standards differ for the test specimen, as do the recommended testing speeds. Both standards agree well on the testing procedure. The stress, σ, is given by

$$\sigma = \frac{F}{A} \tag{5}$$

with F the force or load and A the cross sectional area. The strain is calculated with

$$\epsilon = \frac{\Delta l}{l} \tag{6}$$

with Δl the change in length of the specimen and l the original length. Young's modulus is determined in the elastic region of the test, where the graph of σ *vs* ϵ yields a straight line, as the slope of said line, *i.e.*

$$E = \frac{\Delta \sigma}{\Delta \epsilon} \tag{7}$$

2.5.11 Charpy impact testing

ASTM D6110 (2018) and ISO 179 (2010) describe how Charpy impact tests should be conducted. The impact energy required to break the specimen is calculated from a mechanical energy balance. The standard requires that a specimen breaks completely, and the notch should be placed on the opposite side from, which the pendulum strikes. The size of the specimen can differ according to requirements or limitations, but the size of the notch is fixed. The standard suggests reporting the energy per width, although the energy per surface area may also be reported. At least five specimens should be tested and if possible, ten or more samples are suggested.

2.6 Statistical experimental design

Experiments are conducted to determine the effect of a factor or several factors on a response. Different levels of a factor is tested in order to observe its effect. Some people with a lot of knowledge on a system use a best guess approach, guessing levels and factors, and using the response to guess the next set of variables for an experiment. There is no way for such an experimenter to know if the best possible solution was found. One factor at a time experiments are probably most widely in use, but they do not provide any information on the interaction between factors. Factorial experiments are the most efficient designs for getting the most information with the least amount of runs. Despite this, the number of experiments become quite large with an increasing number of factors and levels. Other methods, like fractional factorial experiments, can still provide good information for relatively few experiments in such cases. (Montgomery, 2013: 1-8)

The general factorial design has levels a, b, c *etc.* for factors A, B, C *etc.*, with n replicates of each experiment. Main effects are the effect of a change in the level of a single factor on the response. An interaction occurs when the effect of a change in the level of a factor differs at different levels of the other factors. When interactions are very large, they tend to make the main effects insignificant. (Montgomery, 2013: 183-186)

2.6.1 Basic statistics

When conducting experiments noise, or experimental error, due to variances in responses under the same conditions are observed. Box and whisker plots are useful to quickly visualise the distribution of observed responses, since it displays the minimum, maximum, median as well as the lower and upper quartiles on a single graph. They also typically indicate outliers, defined by Tuckey's test.

Tuckey (1977) suggested a method using whiskers to define outliers using the lower and upper quartiles, Q_1 and Q_3 of a data set and a constant, k, as shown in Equation 8. Should the data point in question fall outside these whiskers when $k = 1.5$, it is an outlier, and if it falls outside these whiskers when $k = 3$, it is far out. The former value is for k is most widely used.

$$[Q_1 - k(Q_3 - Q_1), Q_3 + k(Q_3 - Q_1)] \tag{8}$$

Probability distributions show the probability structure of a variable, and can be discrete or continuous. From these the mean (μ) and variance (σ^2) can be retrieved. Statistics are conclusions from samples without any unknowns, but sample statistics are used as estimators. Good estimators are unbiased and have minimum variance. The normal distribution is regularly encountered with the probability distribution

$$f(y) = \frac{1}{\sigma\sqrt{\pi}} e^{-\left(\frac{1}{2}\right)\left[\frac{y-\mu}{\sigma}\right]^2}; \qquad -\infty < y < \infty \tag{9}$$

where $-\infty < \mu < \infty$ and $\sigma^2 > 0$, and is denoted by $y \sim N(\mu, \sigma)$. The F distribution is given by

$$h(x = F_{u,v}) = \frac{\Gamma\left(\frac{u+v}{2}\right)\left(\frac{u}{v}\right)^{\frac{u}{2}} x^{\frac{u}{2}-1}}{\Gamma\left(\frac{u}{x}\right)\Gamma\left(\frac{v}{2}\right)\left[\frac{ux}{v}+1\right]^{\frac{u+v}{2}}}; \qquad 0 < x < \infty \tag{10}$$

where

$$F_{u,v} = \frac{\frac{\chi_u^2}{u}}{\frac{\chi_v^2}{v}} \tag{11}$$

with u and v the degrees of freedom for each χ^2 variable. An F-value can be calculated with Equation 12

$$F = \frac{\sigma_u^2}{\sigma_v^2} \tag{12}$$

with the σ^2 the two sample variances. This is then compared to the F-distribution to reject or fail to reject the null hypothesis. (Montgomery, 2013: 25-36)

Statistics are based on null hypotheses, and these can be set up in different ways. One of the most common options is to state that two sample means are equal, *i.e.* $H_0 : \mu_1 = \mu_2$.

The alternative hypothesis would be that they are not, *i.e.* $H_1 : \mu_1 \neq \mu_2$. Two kinds of errors can be made in hypothesis testing, namely that H_0 is rejected when actually true and that H_0 is not rejected when actually false. These are referred to as types I and II errors respectively. The probabilities of these errors are called α and β, where the former is called the significance level of the test. On a specified α, the applicable distribution can be used to determine whether the null hypothesis is accepted or rejected. Alternatively, a p-value may be reported. The p-value indicates the smallest α that would lead to the rejection of H_0, and therefore anyone who interprets the results can apply them on any significance level acceptable to themselves. The different tests, or distributions, are used to reject or fail to reject the null hypothesis. (Montgomery, 2013: 36-40)

2.6.2 Analysis of variance

Analysis of variance (ANOVA) is frequently used in situations that would require repeating several t tests. For a data set of one factor with several levels ANOVA can be used to test multiple null hypothesis simultaneously, *i.e.*

$$\begin{aligned} &H_0 : \mu_1 = \mu_2 = \cdots = \mu_a \\ &H_1 : \mu_i \neq \mu_j \quad \text{for at least one pair } (i, j) \end{aligned} \tag{13}$$

If the effects model is used — *i.e.* $\mu_i = \mu + \tau_i$, where μ is the overall mean and τ is the i^{th} treatment effect — Equation 13 can be written as

$$\begin{aligned} &H_0 : \tau_1 = \tau_2 = \cdots = \tau_a = 0 \\ &H_1 : \tau_i \neq 0 \quad \text{for at least one pair } i \end{aligned} \tag{14}$$

Then the model for a single factor experiment would be

$$y_{ij} = \mu + \tau_i + \epsilon_{ij} \tag{15}$$

where ϵ_{ij} is a random error component. ANOVA can be used to accept or reject the null hypothesis using the F-test. If the H_0 of no difference in treatment means hold true, the F-test is

$$F_0 = \frac{SS_{\text{treatments}}/a-1}{SS_E/N-a} = \frac{MS_{\text{treatments}}}{MS_E} \tag{16}$$

with SS and MS the sum of squares and mean sum of squares of the treatments and error respectively, with a total of a treatments and n observations per treatment, and accordingly $N = an$ total observations. The parameters $a-1$ and $N-a$ represent the degrees of freedom of the respective sum of squares, and if $F_0 > F_{\alpha,a-1,N-a}$, H_0 must be rejected. The p-value can also be calculated from the F-test, and is often reported when a programme is used to calculate the ANOVA. (Montgomery, 2013: 68-80)

For a general factorial design, with a, b, c *etc.* levels of factors A, B, C *etc.*, and n replicates, $abc\cdots n$ experiments will be conducted. ANOVA may be employed to conduct hypothesis tests on main effects and interactions. (Montgomery, 2013: 206)

The adequacy of a model is checked by considering the residuals, which will be structureless or random if the model is adequate. The normality assumption is checked by creating a normal probability plot, with the residuals on one axis, and their theoretical normal probability on the other. If this plot forms a general straight line, the assumption is justified. To check the independence assumption, residuals are plotted in time order. If a tendency of positive or negative residuals result, the assumption is violated. Typically, a model is adequate when the order of experiments is randomised, and when an experimenter with the same skill conducts all the experiments. Lastly, the residuals can be plotted against the values predicted by the model. If no obvious pattern results, the model is adequate. (Montgomery, 2013: 80-84)

2.6.3 Regression analysis

Once the statistical analysis has been completed, an empirical model is often required. This is done by regression analysis, where a first or higher order equation is fitted to the data. The lowest order polynomial that fits the data adequately will be the simplest and therefore the best model. (Montgomery, 2013: 89-90) For an experiment with k factors, a first order equation is

$$y = \beta_0 + \beta_1 x_1 + \beta_2 x_2 + \cdots + \beta_k x_k + \epsilon \tag{17}$$

Interaction terms can be added, *e.g.* the interaction between x_1 and x_2 can be included by adding the term $\beta_{12} x_1 x_2$, as well as quadratic terms, which yields a response surface model, *e.g.*

$$y = \beta_0 + \beta_1 x_1 + \beta_2 x_2 + \beta_{12} x_1 x_2 + \beta_{11} x_1^2 + \beta_{22} x_2^2 + \epsilon \tag{18}$$

The method of least squares is used to minimise the sum of the errors by varying the β parameters. (Montgomery, 2013: 449-462)

Similar to ANOVA analysis, the adequacy of regression models have to be confirmed. This can also be done with residual plots. Other procedures can be used too, *e.g.* the scaled residuals and the predicted residual sum of squares methods. (Montgomery, 2013: 470)

2.6.4 The 2^k factorial experiments

Often it is not known which factors affect a response of interest. It is then useful to conduct screening experiments to determine which factors affect the response significantly. Factorial experiments with k factors and two levels are convenient for this purpose, and are called 2^k factorial designs. In such experiments, levels are referred to as low and high. Modelling can be done in coded or actual variables, where the former refers to using -1 and +1 for levels, and the latter refers to using the actual values. (Montgomery, 2013: 233-238) Coded variables show the relative importance of all design factors, which may be lost when actual variables are used (Montgomery, 2013: 292). The general approach for such experiments are to estimate effects and set up a full model containing all interactions. This model is then tested with ANOVA, and based on the results the model is simplified to only include statistically significant main effects and interactions. The model is then checked for adequacy, and finally results are interpreted. When many factors are investigated, the number of experiments increases rapidly. As a result, single replicates are often used. The risk of fitting the model to noise or an outlier is greatly reduced by choosing a large level range for each factor, and is most often not a concern. This is done within bounds where the response is expected to be linear by the researcher. In other words, factor levels should not be selected to yield very small ranges for screening experiments, especially if single replications are used. If determined that h factors are insignificant, any unreplicated 2^k factorial can be reduced to a 2^{k-h} factorial with 2^h replicates for $h < k$. (Montgomery, 2013: 253-268)

To test whether a first order model is sufficient, centre points are added at the 0 points of all factors (i.e. halfway between the -1 and +1 levels). If the difference in the averages of the factorial responses and the centre points averages are small, quadratic effects are negligible. If not, more experiments are required to calculate the additional regression coefficients. This is normally done with central composite designs (CCD), where axial

runs are added to the factorial design. Contrary to other runs, centre points should be collected in an orderly fashion, evenly spread out from the start to the end of the programme. When plotted against time, the responses at the centre will indicate if responses drifted with time. Replicating a few centre points can be used to quantify the experimental error. (Montgomery, 2013: 285-289)

Fractional 2^k designs are often employed when resources are limited in order to reduce the number of experiments conducted. The success of such designs are based on three ideas: (1) the sparsity of effects principle, which assumes that a system is likely to be primarily dependent on main effects and low order interactions, (2) the projection property, which describes how fractional factorial designs can be projected into replicated designs in a subset of significant factors and (3) sequential experimentation, which indicates the possibility of folding fractional factorial designs into full factorial designs. A 2^{k-p} design is a $1/2^p$ fraction of the design. Consider for example a half fraction design, where $p = 1$. The design may be constructed by first writing down the full factorial for a 2^{k-p} design. The generator $I = ABC \cdots K$ is solved in order to add the missing columns so that the k^{th} factor has the signs of the product $ABC \cdots (K-1)$. Any interaction can be used for the generator, but the highest interaction gives the best resolution. In general, a design has a resolution R if no p factor effect is aliased with another effect with $R - p$ factors; resolution is indicated with a Roman numeral subscript. Changing the sign of the generator gives the other half fraction of runs, called the alternate fraction. The positive generator yields the principal fraction. The procedure for the half fraction design of a 2^3 factorial design is illustrated in Table 5 and Figure 4. Any fractional factorial design of resolution R can be projected to a full factorial with $R - 1$ factors. This is evident from Figure 4, which can easily be projected to a full 2^2 design. If enough information is not available, the other half of the design can be run as well, and the full factorial be retrieved as a blocked experiment. This may also be thought of as a confirmation experiment, although so many runs are not required if a sufficient model was obtained. In the latter case, any of the points not included in the half factorial can be run, and compared to the model prediction. If no serious discrepancies are observed, the model is sufficient. If this is not the case, it is worthwhile to run the other half of the factorial design. It is important to select a fractional factorial design so that the highest possible resolution is achieved. (Montgomery, 2013: 320-342)

Table 5: The outline of the 2^{3-1} factorial design (Montgomery, 2013: 324).

	Full 2^2 factorial		2^{3-1}_{III}; $I = ABC$			2^{3-1}_{III}; $I = -ABC$		
Run	A	B	A	B	C $= AB$	A	B	C $= -AB$
1	-	-	-	-	+	-	-	-
2	+	-	+	-	-	+	-	+
3	-	+	-	+	-	-	+	+
4	+	+	+	+	+	+	+	-

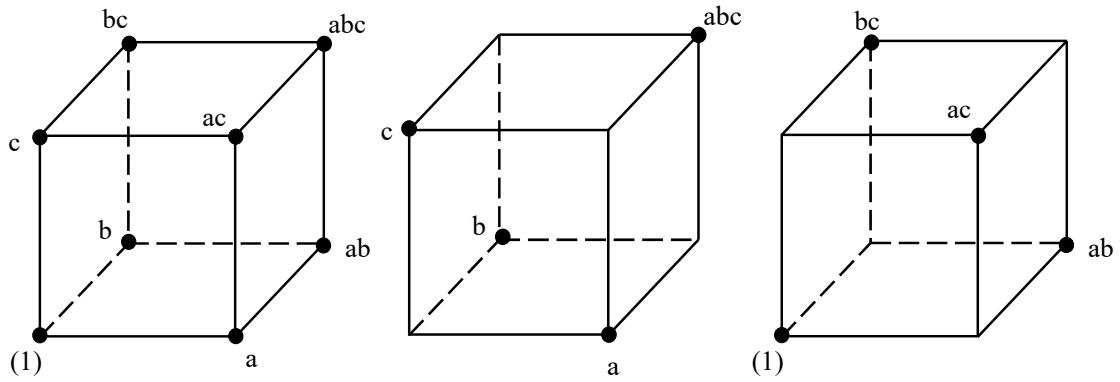

(a) Full 2^3 factorial design. **(b)** Principal fraction. **(c)** Alternate fraction.

Figure 4: Visual representation of a full 2^3 factorial experiment along with its principal and alternative half fractions (Montgomery, 2013: 322).

2.6.5 Response surface methodology

Response surface methodology (RSM) is typically used in optimisation studies. RSM use first and/or second order models, and although the true functional relationship over the entire space of factors is unknown, they usually approximate the relationship between the response and the inputs over small design regions very well. If curvature is confirmed, a second order model can be used to determine the optimum.

The estimated second-order model is

$$\hat{y} = \hat{\beta}_0 + \sum_{i=1}^{k} \hat{\beta}_i x_i + \sum_{i=1}^{k} \hat{\beta}_{ii} x_i^2 + \sum_{i<j} \hat{\beta}_{ij} x_i x_j \tag{19}$$

which can be rewritten in matrix notation as

$$\hat{y} = \hat{\beta}_0 + \mathbf{x}'\mathbf{b} + \mathbf{x}'\mathbf{B}\mathbf{x}$$

$$\text{with} \quad \mathbf{x} = \begin{bmatrix} x_1 \\ x_2 \\ \vdots \\ x_4 \end{bmatrix} \quad \mathbf{b} = \begin{bmatrix} \hat{\beta}_1 \\ \hat{\beta}_2 \\ \vdots \\ \hat{\beta}_4 \end{bmatrix} \quad \text{and} \quad \mathbf{B} = \begin{bmatrix} \hat{\beta}_{11} & \hat{\beta}_{12}/2 & \cdots & \hat{\beta}_{1k}/2 \\ & \hat{\beta}_{22} & \cdots & \hat{\beta}_{2k}/2 \\ & & \ddots & \\ \text{sym.} & & & \hat{\beta}_{kk} \end{bmatrix} \tag{20}$$

from which the stationary points can easily be derived by equating the first derivative of Equation 20 with respect to all the factors to zero, *i.e.*

$$\mathbf{x}_s = -\frac{1}{2}\mathbf{B}^{-1}\mathbf{b} \tag{21}$$

Substituting Equation 21 into Equation 20 yields

$$\hat{y}_s = \hat{\beta}_0 + \frac{1}{2}\mathbf{x}_s'\mathbf{b} \tag{22}$$

which can be used to predict the stationary point. (Montgomery, 2013: 478-500)

Fitting response surfaces can be facilitated by the proper choice of experimental design. If the first order model

$$y = \beta_0 + \sum_{i=1}^{k} \beta_i x_i + \epsilon \tag{23}$$

is of interest, orthogonal first order designs are perfect, since they minimise the variance of the regression coefficients. Simplex designs, which are shapes with $k + 1$ vertices in k dimensions can be used, but the 2^k factorial designs, or fractions thereof, are also suitable. In the case of the latter, centre points are required to estimate the experimental error and test for curvature. CCDs are most popular for fitting second order models. The distance of the axial points from the design origin, δ, and the number of centre runs, n_C, are important. The choice of δ can be made to ensure that the design is rotatable, which means that the variance of $\hat{y}$ is constant at a fixed distance from the design centre. If n_F is the number of factorial points, $\delta = (n_F)^{0.25}$ will yield a rotatable design. Such a design have to include at least three to five centre runs. Other designs also exist, *e.g.* the Box-Behnken, centred central composite, equiradial, and small composite designs. If necessary, blocking may be used, but preferably experiments should be blocked

orthogonally. Sometimes, constraints on an experimental region necessitate the use of other experimental designs. In such cases designs can be generated using various optimal criteria, *e.g.* D-, G-, A- and V-optimal criteria. (Montgomery, 2013: 500-522)

3 Experimental

3.1 Materials

DHT - 4A® supplied by Kisuma Chemicals B. V. with magnesium aluminium hydroxide carbonate as the main ingredient (CAS no. 11097-59-9) was used as received, and is further referred to as LDH. Note that the LDH have been coated with less than 4 % fatty acid salts (C16 to C18).

PLA granules with a MFR of 3 g 10min^{-1} and 8 g 10min^{-1} at 190 °C and 210 °C (2.16 kg, ISO 1133-A) were used as received from SA Filaments, who redistributed Luminy® LX175. It has a d content of 4 %, melting and glass transition temperatures of 155 °C and 58°C, a tensile strength and modulus of 45 MPa and 3 500 MPa, strain at break below 5 % and an impact energy below 5 kJ m^{-2} respectively. The processing recommendation was drying for four to six hours at 85 °C and processing between 170 °C and 210 °C.

3.2 Processing equipment

Compounding LDH into PLA was done with a TX28P (Taiwan) corotating twin screw extruder. The compounder was fitted with screws from CFAM (South Africa) consisting mainly of kneading elements assembled in such a way to also pump the melt through the extruder. Compounding was done between 60 % and 75 % motor load, and strands were cooled in a water bath at room temperature and granulated with a chipper (China).

The 1.75 mm filament was extruded in a Friend Machinery (China) single screw extruder. The feedstock in the hopper was at 60 °C and the filament was cooled in a water bath at room temperature.

FDM was done on Creality Ender 6 3D printers (China) with 0.6 mm brass nozzles.

Injection moulding was done on an Arburg Allrounder 270 S 400 70 with a screw diameter of 18 mm. ISO 527 Type 1A tensile specimens were made. Dosing, packing and cooling times were 1.63 s, 22.40 s and 25.0 s respectively, and the cycle time was 54 s. Melt and mould temperatures were set to 190 °C and 20 °C. The melt temperature was changed to 185 °C for the 10LDH_PLA material. A speed of 45 mm s^{-1} was used over a dosing displacement of 76 mm, and the switchover point was at 8.7 mm and 9 mm for pure and

filled PLA respectively. The hydraulic pressures at the switchover point was recorded as 57 bar, 52 bar and 46 bar for 0LDH_PLA, 2LDH_PLA and 10LDH_PLA.

3.3 Analytical instruments

DSC was done with a Perkin Elmer DSC 4 000. Calibration was done with zinc and indium standards. Samples were heated at 10 °C min^{-1} from 20 °C to 200 °C in a nitrogen atmosphere (19.8 mL min^{-1}). Samples were first heated, then cooled and finally heated a second time. Five samples were run for each LDH loading.

FEGSEM was done with a Zeiss 540 Ultra Plus using an electron high tension (EHT) voltage of 1.00 kV.

DMA was done with a Perkin Elmer DMA 8 000. A temperature scan from 30 °C to 130 °C at a rate of 2 °C min^{-1} was used whilst measuring frequencies at 0.1 Hz, 1 Hz, 10 Hz and 100 Hz.

XRD was done with a Bruker D2 Phaser with Cu Kα radiation ($\lambda = 1.45060$ Å) generated at 30 kV and 10 mA. A scanning rate of 0.02° min^{-1} over a 2θ range of 5° to 70° was used, with a Lynxeye detector and a 4.99° position sensitive detector.

ATR-FTIR was done on a Bruker alpha. Thirty-two scans were averaged for each run, and each scan was done from 4 000 cm^{-1} to 400 cm^{-1}.

Tensile tests were done on a Ametek Lloyd LRX plus 5 kN universal testing machine. In accord with the ISO 527 standard, a speed of testing of 1 mm min^{-1} and a 50 mm extensometer (SANS) was used to test Type 1A specimens.

Impact tests were done on a Zwick D - 7 900 machine with a 4 J hammer and a 225 mm long pendulum. In accord with the ISO 179 standard, Type 1A specimens was tested.

Polarimetry was completed with a Krüss P3002RS automatic digital polarimeter using 1 g solute 100 mL^{-1} solvent concentrations and a cuvette with a length of 1.1 dm.

Oscillatory rheology was done on an Ares G2 parallel plate rheometer with stainless steel plates (diameter 25 mm). Sample discs where prepared with injection moulding having a thickness of 2 mm. A gap between 1.5 mm and 1.7 mm was used. For time sweeps an angular frequency of 1 rad s^{-1} and strain of 10 % was used over 30 min at 190 °C. For frequency sweeps a temperature of 170 °C were used with frequencies from 600 rad s^{-1} to 0.6 rad s^{-1} at the following logarithmic intervals: 538 rad s^{-1}, 379 rad s^{-1}, 239 rad s^{-1},

151 rad s^{-1}, 95 rad s^{-1} and 60 rad s^{-1}. All samples were tested in nitrogen conditions and were preheated for *ca.* seven minutes.

Melt flow rate measurements were made with a Göttfert MI-4 machine with a melt temperature of 170 °C, 190 °C and 210 °C and a 2.16 kg mass.

TGA was done on a TGA/DSC 3+ Von Mettler Toledo from 30 °C to 800 °C at a rate of 10 K min^{-1} with air flowing at 40 mL min^{-1}.

3.4 Software

The slicer software used was Ultimaker Cura (version 5.2.2.). Statistical analyses were completed in JMP® (version 17.0.0).

3.5 Planning

The main purpose of the experiments is to determine whether LDH has a positive effect on the ultimate tensile stress and mechanical properties of PLA parts manufactured by FDM, and to observe how it influences printability. PLA was chosen because it dominates the FDM landscape and is projected to continue doing so (Sandanamsamy *et al*, 2022). The ultimate tensile stress was selected because it is a popular measure of part strength, and it is a more intuitive parameter than one like Young's modulus. Elongation at break was not selected, because it was already known that the material is brittle. Even though and optimum for σ will be found, impact and all tensile properties will be investigated to yield a holistic set of results regarding the overall strength of specimens.

Although there is no literature on LDH filled PLA filaments for FDM, literature discussing LDH in PLA in other applications showed that many properties are affected by the crystallinity that changes due to competing effects. Since LDH acts as a nucleating agent, it varies the crystallinity, and as a result also many other properties, *e.g.* viscosity, transition temperatures *etc.*. It is expected that the crystallinity data, and other characteristic properties, will be required in order to explain observations in the tensile properties. Samples will be analysed with XRD, FTIR, SEM, DSC and DMA at every step of the process.

The material extrusion factors that affect the strength of FDM parts the most are the layer height (A), extrusion temperature (B) and infill percentage (C) (Sandanamsamy *et al*, 2022; Syrlybayev *et al*, 2021; Medibew, 2022; Krajangsawasdi *et al*, 2021). The LDH

loading (D) will also have an effect on strength and printability. In fact, it is expected that at some high loading the filament will not even be able to print.

It is believed that the factors of interest interact so much that a non-linear model will be required. The response surface methodology will be followed, with an initial screening test determining which factors affect the response significantly. Sequential experimentation will then be used to gain enough information until a sufficient model can be fitted to data points. After finding the optimum from this model, and confirming its adequacy, the mechanical properties will be compared with a traditional manufacturing process, injection moulding.

Due to the standards requiring at least five test specimens for a tensile property, the number of runs required for each experiment increases drastically with each additional factor. If a full 2^4 factorial experiment is conducted for the screening test with five replications per experimental point, 80 runs will be required just for screening. In order to preserve resources, a 2^{4-1} fractional factorial experiment will be conducted, with centre points as illustrated in Figure 5. The coded variables are shown in Table 6. All runs, including replications, will be completely randomised. Centre points will be evenly distributed with five replications at the start, in the middle and at the end of the programme respectively.

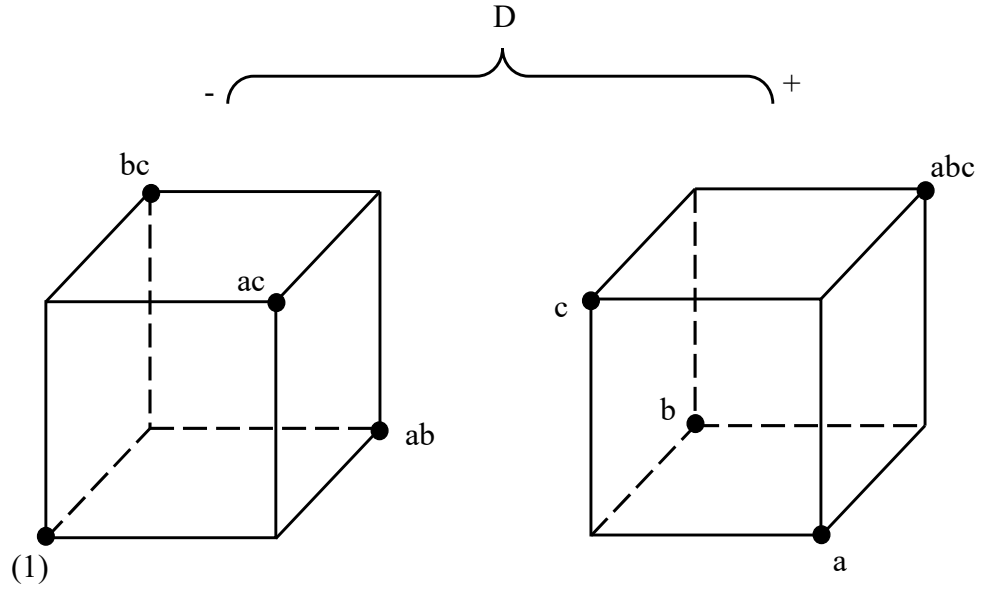

Figure 5: Graphical representation of the 2^{4-1}_{IV} screening experiment shown in Table 6.

The actual variables corresponding to the coded ones are given in Table 7. Although no formal guidelines are available in the academic literature, the FDM community (suppliers, hobbyists, home printers *etc.* (Lütkemeyer, 2023; Zuza, 2023)) suggests that layer height should be between 25 % and 75 % of the nozzle diameter. Instead of working on these extreme values, 30 % and 70 % is rather used to narrow the range a little and avoid printability issues. The printing temperatures are based on the most used printing

temperatures of PLA in literature (Sandanamsamy *et al*, 2022). These values are subject to change, since the effect of the filler on the glass and melting temperatures of the compound is unknown, and might be adjusted based on DSC measurements. The infill percentage was selected to be as broad as possible, but not on the extreme values of 0 % and 100 %, for the same reasons mentioned along with the choice of layer height. The LDH loadings were selected based on the ranges seen in the systematic review.

Table 6: The half fraction 2^4 experiment with resolution IV to be used for screening the factors A, B, C and D.

	Full 2^3 factorial			2^{4-1}_{IV}, I = ABCD			
Experiment	A	B	C	A	B	C	D = ABC
1	-	-	-	-	-	-	-
2	+	-	-	+	-	-	+
3	-	+	-	-	+	-	+
4	+	+	-	+	+	-	-
5	-	-	+	-	-	+	+
6	+	-	+	+	-	+	-
7	-	+	+	-	+	+	-
8	+	+	+	+	+	+	+

Table 7: The values for the low and high levels of the screening experiment.

	A [mm]	B [°C]	C [%]	D [mass %]
low level	0.18	190 [a]	10	2
high level	0.42	220 [a]	90	10
centre point	0.30	205 [a]	50	6

[a] subject to change based on DSC results

From these results, it will be possible to determine which factors influence σ the most. If a factor is found to not affect the response in a statistical significant way, it will be excluded from further experimentation, and the design will fold into a full 2^3 factorial design. If the runs do not provide enough information to make conclusions, the other half of the factorial will also be completed, or specific runs will be added in a sequential manner.

Once the factors have been screened, it is expected that the fractional factorial experiment can be used as a starting point for the response surface method. If additional runs are required, they will be completed at this point. As soon as the region of the optimum is determined, a CCD will be used to verify the predicted optimum point and provide more

information on the area surrounding it. The FDM optimum will then be compared to the same specimens prepared by injection moulding which will indicate how the different processing techniques affect the tensile properties.

The process will include compounding a modified LDH into PLA in a twin screw compounder. Both materials will be obtained commercially and used as received. The compounded strands will be granulated, after which a filament suitable for use in a FDM printer will be extruded using a single screw extruder. The filament will be used to print specimens *via* FDM. Some of the granules fed to the filament extruder will be kept for use in injection moulding to allow a comparison between the two very different techniques. The LDH and the pure PLA, as well as all intermediate and final products will be thoroughly characterised.

3.6 Methods

Filaments were prepared by compounding LDH into PLA using the twin screw compounder. Before compounding the PLA was dried overnight at 50 °C. The LDH was not dried, since it is hydrophobic. The required masses of LDH and PLA were weighed and thoroughly mixed by hand before it was fed to the compounder. The strands from the compounder were chipped into granules and dried again overnight at 50 °C before producing filament in the single screw extruder. The filament was made with a diameter ranging between 1.72 mm and 1.76 mm and was named as follows: XXLDH_PLA, where XX indicates the mass percentage of LDH added into the PLA. The filament was then analysed by XRD, SEM, FTIR, DMA and DSC. The latter was used to fix the temperatures used in printing tensile and impact specimens.

Specimens were drawn in Fusion 360 and exported as a .3mf file, as shown in Figure 6. This was then imported into Ultimaker Cura to slice into g-code for use with the printers. An infill orientation of ±45° was always used and parts were printed flat as depicted in Figure 6. Table 8 summarises important settings that were set for all parts sliced. The same printer was used throughout the experiments for printing tensile and impact specimens respectively.

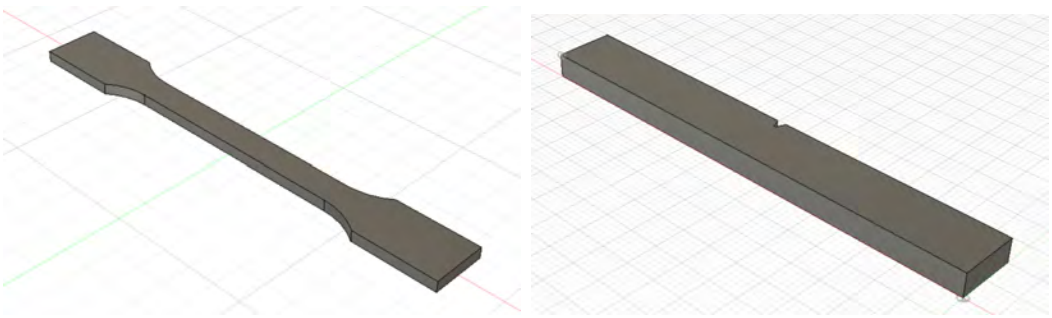

(a) Tensile ISO 527 Type 1A specimen. **(b)** Impact ISO 179 Type 1A specimen.

Figure 6: The CAD drawings of the ISO standards used for preparing the tensile and impact Type 1A specimens. Note that the two figures do not have the same scale.

Table 8: The Ultimaker Cura settings that were changed from the standard profile and kept constant for all the other prints.

Main setting	Sub setting	Option	Unit
Walls	Wall line count	3	
Walls	Z seam alignment	Random	
Top/bottom	Top layers	3	
Top/bottom	Bottom layers	3	
Infill	Infill pattern	Lines	
Infill	Randomise infill start	✓	
Infill	Infill before walls	✓	
Material	Build plate temperature	60	°C
Speed	All printing speeds	50	mm s^{-1}
Speed	Enable acceleration control	✓	
Speed	All acceleration control	1 500	mm s^{-2}
Support	Generate support	✓	
Support	X/Y distance	0.5	mm
Build plate adhesion	Build plate adhesion type	Brim	

3.6.1 Screening experiment

A half factorial experiment was conducted with four factors: layer height, nozzle temperature, infill density and LDH loading. The high and low values selected are shown in Table 9, along with the centre values. Centre points were included in order to investigate experimental drift and variance throughout the experiment, due to the random order in which the other experimental runs were conducted. The eight experiments conducted for the screening experiment are shown in Table 10, and the order of runs are given in Table 11. Five replications of each experiment were done. Samples where named as follows: se_XX, where XX refers to the run number in Table 11.

Table 9: The values of the low, high and centre levels for the four factors used in the screening experiment.

level	layer height [mm]	nozzle temperature [°C]	infill density [%]	LDH loading [mass %]
low	0.18	190	10	2
high	0.42	220	90	10
centre	0.30	205	50	6

Table 10: The levels of the eight respective experiments used in the screening experiment.

experiment	layer height [mm]	nozzle temperature [°C]	infill density [%]	LDH loading [mass %]
0	centre	centre	centre	centre
1	low	low	low	low
2	high	low	low	high
3	low	high	low	high
4	high	high	low	low
5	low	low	high	high
6	high	low	high	low
7	low	high	high	low
8	high	high	high	high

Table 11: The random order in which each of the eight experiments (exp) and the centre runs (c) of the screening experiment were conducted.

run	exp	run	exp	run	exp	run	exp	run	exp	run	exp
1	0	11	4	21	3	31	6	41	2	51	0
2	0	12	6	22	8	32	4	42	6	52	0
3	0	13	2	23	5	33	1	43	4	53	0
4	0	14	8	24	6	34	7	44	7	54	0
5	0	15	1	25	1	35	5	45	5	55	0
6	2	16	7	26	0	36	4	46	6		
7	2	17	8	27	0	37	8	47	1		
8	3	18	3	28	0	38	7	48	5		
9	8	19	4	29	0	39	3	49	7		
10	2	20	5	30	0	40	1	50	3		

3.6.2 Augmented screening experiment

The screening experiment was augmented with an I-optimal algorithm for reasons explained in § 4.2.3. Replications were not added, save for the centre points and for one experiment. The levels of the augmented screening experiment are shown in Table 12, and the order of these are given in Table 13.

Table 12: The levels of the second block of the respective experiments used in the augmented screening experiment.

Experiment	Layer height [mm]	Nozzle temperature [°C]	Infill density [%]	LDH loading [mass %]
9	high	high	low	high
10	high	low	38	centre
11	0.37	201	low	low
12	centre	high	low	centre
13	low	203	15	high
14	low	high	high	high
15	centre	high	low	centre
16	0.26	low	42	high
17	high	197	72	high
18	high	high	high	low

Table 13: The random order in which each of the experiments (exp) and the centre runs (c) of the augmented screening experiment were conducted.

run	exp	run	exp	run	exp	run	exp
56	0	61	0	66	0	71	10
57	9	62	13	67	15		
58	10	63	0	68	16		
59	11	64	14	69	17		
60	12	65	0	70	18		

3.6.3 Central composite design experiment

From the augmented screening experiment results it is clear that factors A and B does not affect the response as much as factors C and D, as will be discussed in § 4.4. Thus layer height and nozzle temperature were excluded as factors in the CCD, and kept constant at the optimum conditions recorded in said section. Further reducing said factors introduces serious printing difficulties. The levels for C and D were selected as follows. The model predicted an increase in tensile stress with an increase in infill density. Therefore the maximum infill density of 100 % is expected to yield the strongest specimens. This was selected as a limit, and the symmetrical lower limit of 80 % was selected so that the previous optimum of 90 % is still within the new experimental region. In order to compare filled PLA with pure PLA, one of the limits of the CCD was selected as 0 % LDH loading. A symmetrical higher limit of 4 % was chosen to still have the previous optimum of 2 % in the new experimental region. The levels are summarised in Table 14. Three repeats for each level was conducted, and the random order of runs are shown in Table 15.

Table 14: The levels of the respective experiments used in the CCD.

Experiment	Infill density [%]	LDH loading [mass %]
1	90	2
2	82.9	0.6
3	97.1	0.6
4	82.9	3.4
5	97.1	3.4
6	90	0
7	90	4
8	80	2
9	100	2

Table 15: The order in which the experiments of the CCD was completed.

run	exp	run	exp	run	exp
1	2	11	5	21	3
2	2	12	1	22	3
3	9	13	7	23	2
4	4	14	7	24	1
5	6	15	5	25	6
6	3	16	1	26	6
7	4	17	8	27	8
8	1	18	4	28	1
9	9	19	7	29	9
10	1	20	5	30	8

4 Results and discussion

4.1 Pure PLA characterisation

A few basic characterisations were completed and compared to the PLA's accompanying data sheet. A very important parameter was the *d*-content, because the morphology of the PLA is greatly dependent on its concentration. The PLA used in this work and pure PLLA (Schultzer L100H) — used as reference — were dissolved in chloroform at 1 g 100 mL^{-1}. Seven polarity measurements of each solution was taken, and the average angle of rotation of these were used to calculate the specific rotation using Equation 4 as -136.8° and -133.8° respectively. Using Equation 3, this yields a *d*-content of 1.1 %, which is a little lower than that given in the data sheet. Nevertheless, a crystalline PLA is expected.

The DSC results of the second heating showed a glass transition, cold crystallising and melting temperature of 61.12 °C, 116.14 °C and 151.37 °C respectively, which compares quite well with the data sheet. The second heating curve can be seen in Figure 7a along with the FTIR spectra in Figure 7b which is typical of PLA. The melt flow rate results are summarised in Table 16. These are significantly higher than the values reported in the data sheet.

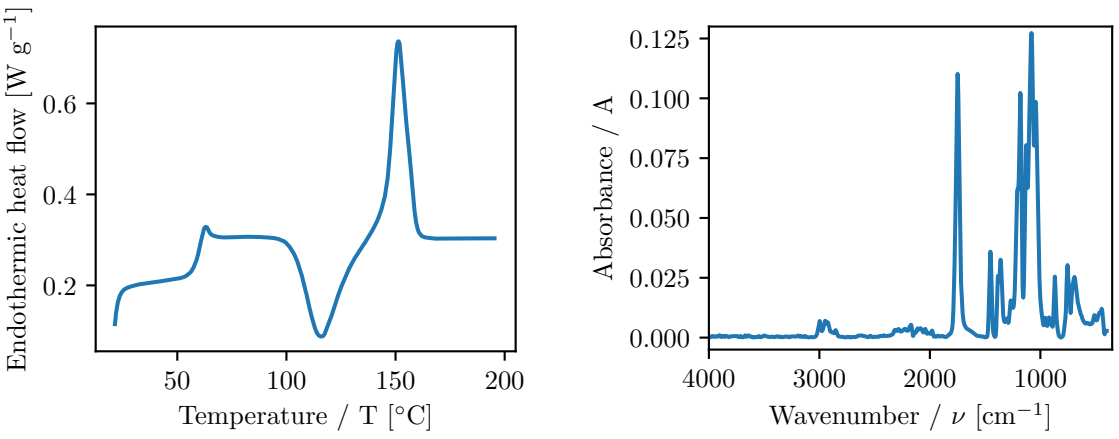

(a) DSC. **(b)** FTIR.

Figure 7: The second heating curve of pPLA determined with DSC as well as its FTIR spectra.

Table 16: The MFR results of the pure PLA granules as received from SA Filaments at various melt temperatures using a 2.16 kg mass.

Temperature °C	MFR g $10min^{-1}$	MVR cm^3 $10min^{-1}$
170	4.21	3.71
190	12.17	11.08
210	35.62	32.23

4.2 Screening experiment

All auxiliary information for the screening experiment is in Appendix A. These include repeats for characterisations, visualisation of outliers, ANOVA tables, images of test specimens and average properties of test pieces which were not absolutely necessary for discussing the results.

4.2.1 Filament

The 2LDH_PLA and 6LDH_PLA filaments were compounded at 180 °C, but the 10LDH_PLA filament was compounded at 165 °C, as summarised in Table 17. These temperatures were used because the samples bubbled at higher temperatures, not allowing a strand to be pulled through the cooling bath. The processing temperatures used in making the filament are also shown in Table 17. Similar to the compounding, temperatures had to be lowered with increasing LDH loading. It is proposed that the bubbling at higher clay loadings is due to the increase in shear forces experienced by the compound. Considering that the thermocouples are located on the barrel and heating bands, it is probable that the melt temperature increases due to the shear contribution, but that it is not picked up by the thermocouples. It is also possible that the bubbles are due to water forming due to decomposition or the breaking of the hydroxide groups in the LDH, although this is less likely at these temperatures.

The DSC results of the filaments are summarised in Figure 8. The second heating runs are shown. These were compiled from the data of five repeats of each filament and pure LDH, available in Appendix A. Good repeatability was achieved. The most obvious difference between increasing LDH loadings was the formation of a double melting peak with an increasing clay loading. The first endotherm peak is the melting of the α' phase followed by a small exotherm due to the conformation of the α' phase to the α phase and then ending with a final endotherm peak as the α phase melts completely. A clear glass transition and cold crystallisation exotherm can be distinguished before the melting

Table 17: The processing temperatures used in compounding the LDH into PLA and in manufacturing the filament used in the screening experiment.

sample	compounding	filament extruder			
		first zone	second zone	third zone	die
	[°C]	[°C]	[°C]	[°C]	[°C]
2LDH_PLA	180	170	180	180	180
6LDH_PLA	180	155	155	155	160
10LDH_PLA	165	145	150	150	150

peak for all polymer samples. The melting temperatures do not vary as drastically as the adjustments required during processing, and these cannot be attributed to the LDH loading affecting the compounds' melting properties. This confirms that the melt has a higher temperature than recorded by the extruder thermocouples. There are no phase transitions in the DSC curves of the pure LDH. The slight increase that is observed in heat flow is believed to be due to surface moisture evaporating, since samples where not dried before analysis.

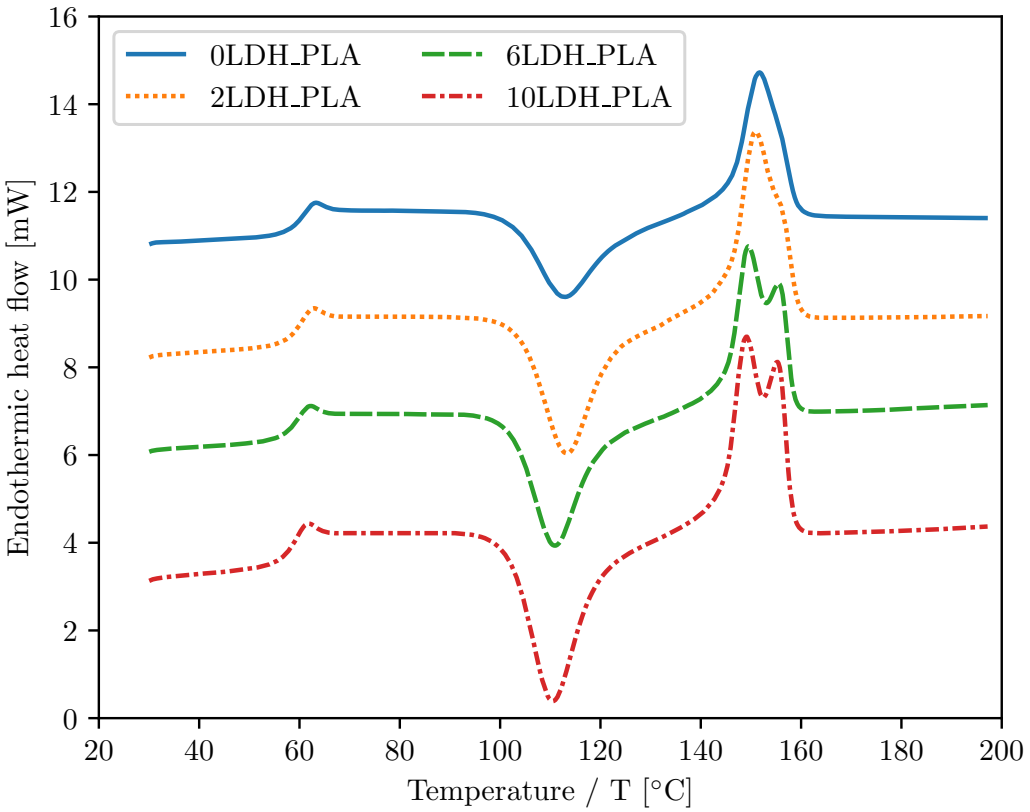

Figure 8: Representative DSC results of the second heating cycle of the filament made for use in the screening experiments compiled from Figure A.1.

From the DSC analysis ΔH_c and ΔH_f were calculated from the areas under the peaks. The T_g was taken as the half extrapolated heat capacity. The T_c was recorded as the trough temperature, and the T_m as the first peak temperature. The interested reader may follow the procedure of recording the above in the appendix (Figure A.2). No crystallisation occurred during the cooling cycle in the DSCs. From running an ANOVA on the runs within a set of five samples for a specific clay loading, it was determined that no property differed statistically significantly on a 95 % confidence interval. Figure 9 shows all these properties as a function of the LDH loading in violin plots — Yi (2023). Each graph is enlarged to show more detail. An ANOVA showed that all these properties differ in a statistically significant manner between the different LDH loadings. This is especially true for T_g, T_c and T_m. Even though differences are statistically significant, they are not really of practical importance in the FDM application. All the transition temperatures varied between 2 °C and 4 °C for the different loadings, which does not drastically affect the printing process. The transition temperatures decreased with LDH loading, even when no shear was used during melting, as is the case in DSC. It is believed that this phenomenon is observed due to the different crystallisation behaviour when LDH is present in the matrix, because it acts as a nucleating agent. It is possible that a larger amount of the matrix is present in the rigid amorphous fraction trapped between the filler and crystallised regions, which become mobile as temperatures increase, thus causing easier phase transformations. Both the drop in T_c and the increase in ΔH_c shows that the LDH acted as a nucleating agent. There is no clear trend in ΔH_f, and it does not vary much. The degree of crystallisation is negative, which is concerning. It is believed that the reason for this is not a mistake, but rather a phenomenon particular to PLA. This is discussed in more depth in §4.6. In summary, the enthalpies measured are highly dependent on the DSC parameters used, and different enthalpies were recorded for the same samples when different conditions were used. Moreover, the small exotherm between the melting peaks might also be the cause of negative degrees of crystallinity, because the area under the curve includes the endothermic melting peak and the exothermic conformational trough. No crystallisation occurred during cooling between the first and second heating runs for any of the samples.

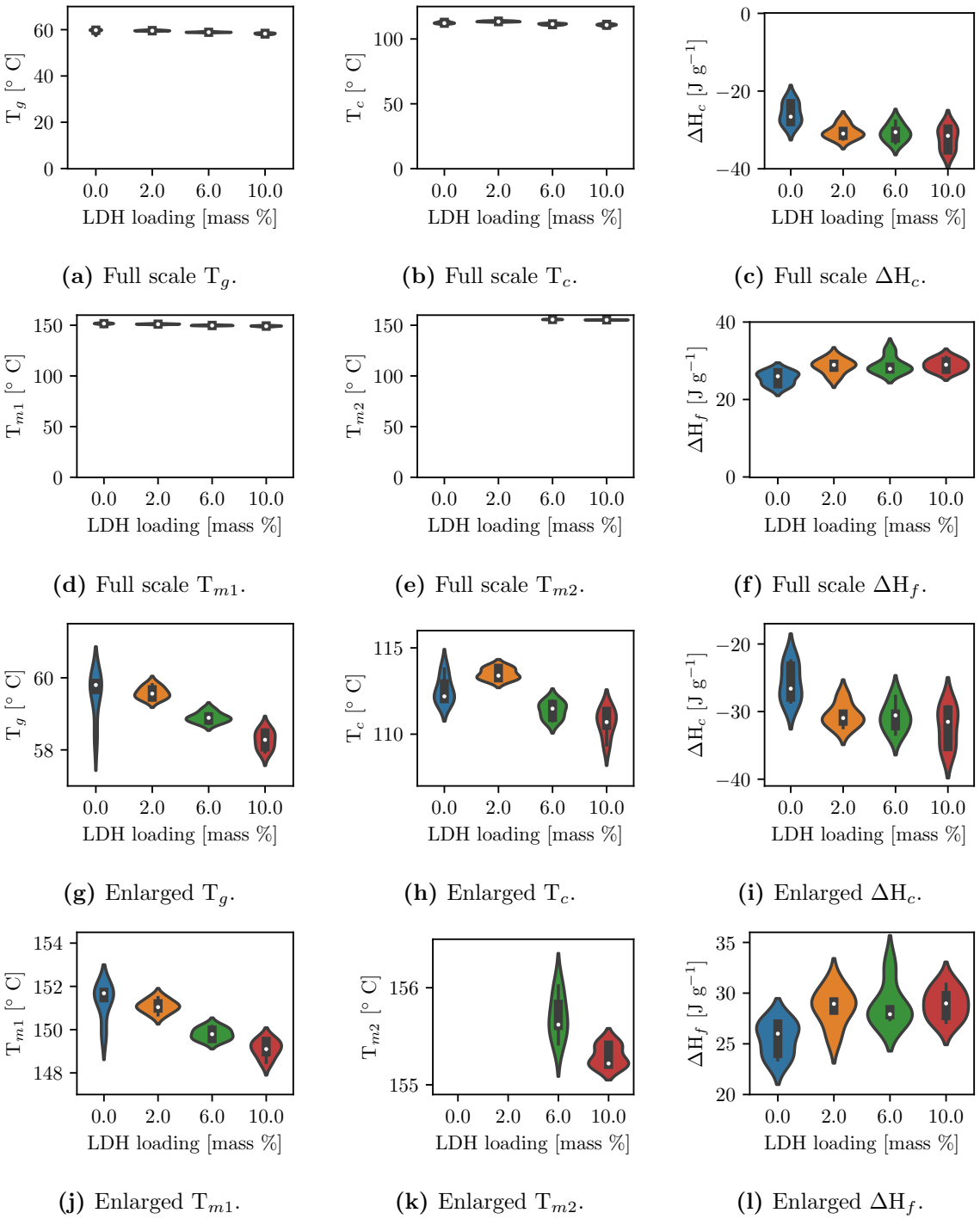

(a) Full scale T_g. **(b)** Full scale T_c. **(c)** Full scale ΔH_c.

(d) Full scale T_{m1}. **(e)** Full scale T_{m2}. **(f)** Full scale ΔH_f.

(g) Enlarged T_g. **(h)** Enlarged T_c. **(i)** Enlarged ΔH_c.

(j) Enlarged T_{m1}. **(k)** Enlarged T_{m2}. **(l)** Enlarged ΔH_f.

Figure 9: The average properties of the respective filaments made for the screening experiment as determined from DSC.

The XRD results of the filament produced for the screening experiments as well as the pure LDH are shown in Figure 10. For all the composite samples, the broad peak observed for pure PLA filament centred at *ca.* 20° remains, but as the LDH loading increases, the peaks observed for pure LDH powder develop until all of them are clearly visible for 10LDH_PLA. From left to right these are located at the general 2θ locations of 12°, 24°, 35°, 40°, 47°, 31°, 63° and 67°. These results confirm that LDH was successfully compounded into PLA, and that the amount of LDH increases for each filament made.

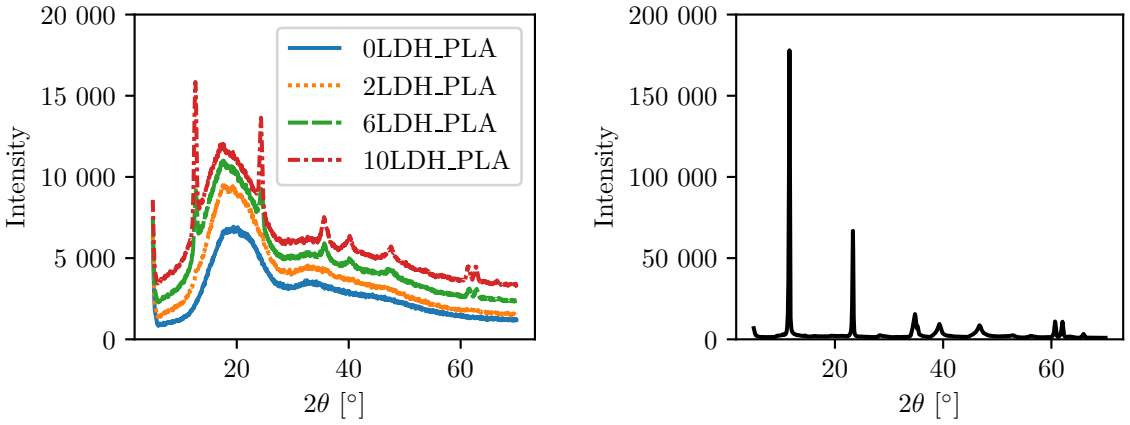

(a) LDH. **(b)** LDH.

Figure 10: The XRD results of the filament made for use in the screening experiments as well as the pure LDH powder and pure PLA filament.

The FTIR results of the filaments and LDH are given in Figure 11. This was compiled from the five repeats completed for each sample. Good repeatability was achieved, with peak locations remaining constant and only peak heights varying slightly. The pure PLA filament's spectra, 0LDH_PLA, compares well with literature. The broad band between 3 750 cm^{-1} and 3 200 cm^{-1}, although not very clear, is ascribed to the bending vibrations of the C−H groups. The peaks located between 2 994 cm^{-1} and 2 855 cm^{-1} are due to the stretching vibrations of the C−H groups. The peaks at 1 747 cm^{-1}, 1 180 cm^{-1} and 1 083 cm^{-1} are caused by the stretching vibrations of the C=O, O−C−O and C−O groups respectively whereas the peak at 1 453 cm^{-1} is caused by CH_3 bending and scissoring. The spectra of the pure filament also compares very well to that of the pure PLA before processing. All peaks deviate less than 3 cm^{-1} and have the same shape. Similarly, the pure LDH powder's spectra compares well to literature. The peaks at 3 412 cm^{-1} and 1 363 cm^{-1} are ascribed to the O−H and CO_3^{2-} stretching vibrations, and the peak at 653 cm^{-1} is ascribed to the metal-oxygen modes. The peak at 1 568 cm^{-1} is ascribed to the COO^- group which confirms that the LDH particles are coated with fatty acid salts and not fatty acids. The peaks of both the PLA and LDH are visible in the spectra of composite filaments. The most significant indications proving successful compounding are the increasing OH (3 412 cm^{-1}), fatty acid salt COO^- (1 568 cm^{-1}) and metal-oxygen

mode (653 cm^{-1}) peaks. The LDH peak observed at 444 cm^{-1} can also be observed in the compounds. All the PLA peaks are also still clearly visible in the compounds, as expected.

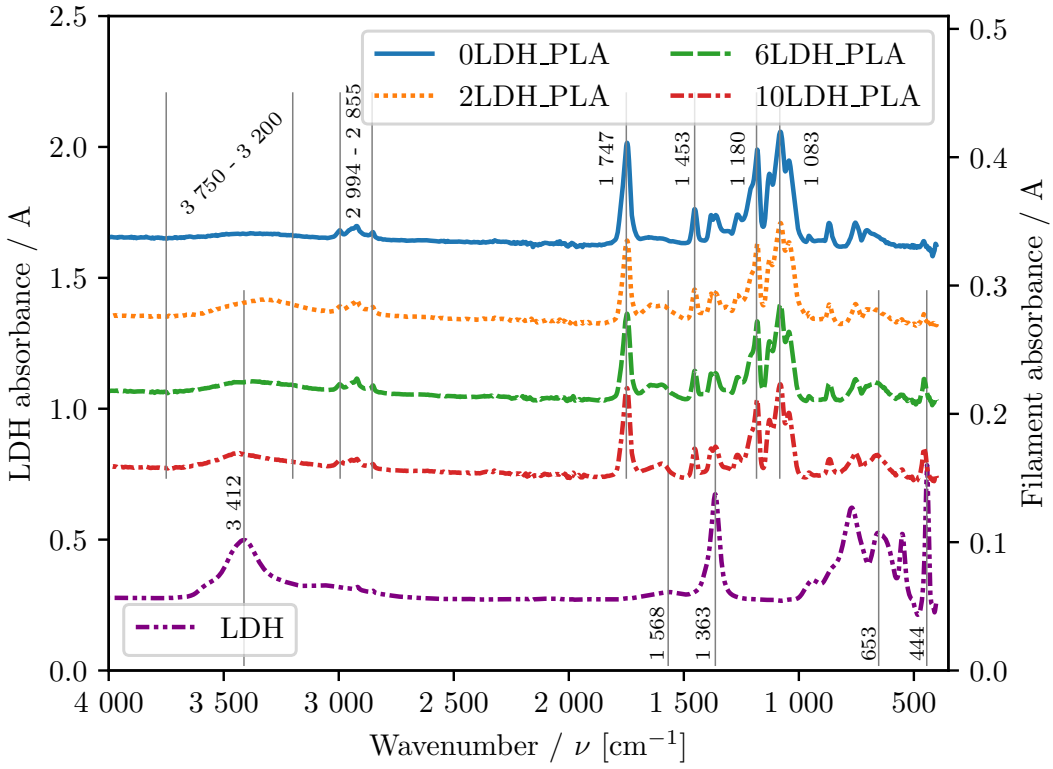

Figure 11: Representative FTIR results of the filament made for use in the screening experiments and the pure LDH compiled from Figure A.3.

The SEM analysis is given in Figure 12. Magnifications of 500×, 5 000× and 80 000× are shown. It is very clear from the 5 000× and 80 000× magnifications that the clay was dispersed evenly in the matrix, and that it did not form large agglomerates. Some small agglomerates do form with a few particles clumped together, but there are also ample particles that are completely isolated from one another in the matrix. The increase in clay particles can also be observed between the different clay loadings. Considering that the LDH was compounded into the PLA as received these results are favourable. Should LDH be compounded into PLA on a commercial scale, DHT - 4A® would be an ideal option since it compounds well and with ease. It might even have a material cost advantage. Additionally, it seems as if the filler can be classified as a microfiller, due to particles varying between 50 nm and 400 nm. Of course, agglomerates are larger, but there are none that reach the scale of 1 μm.

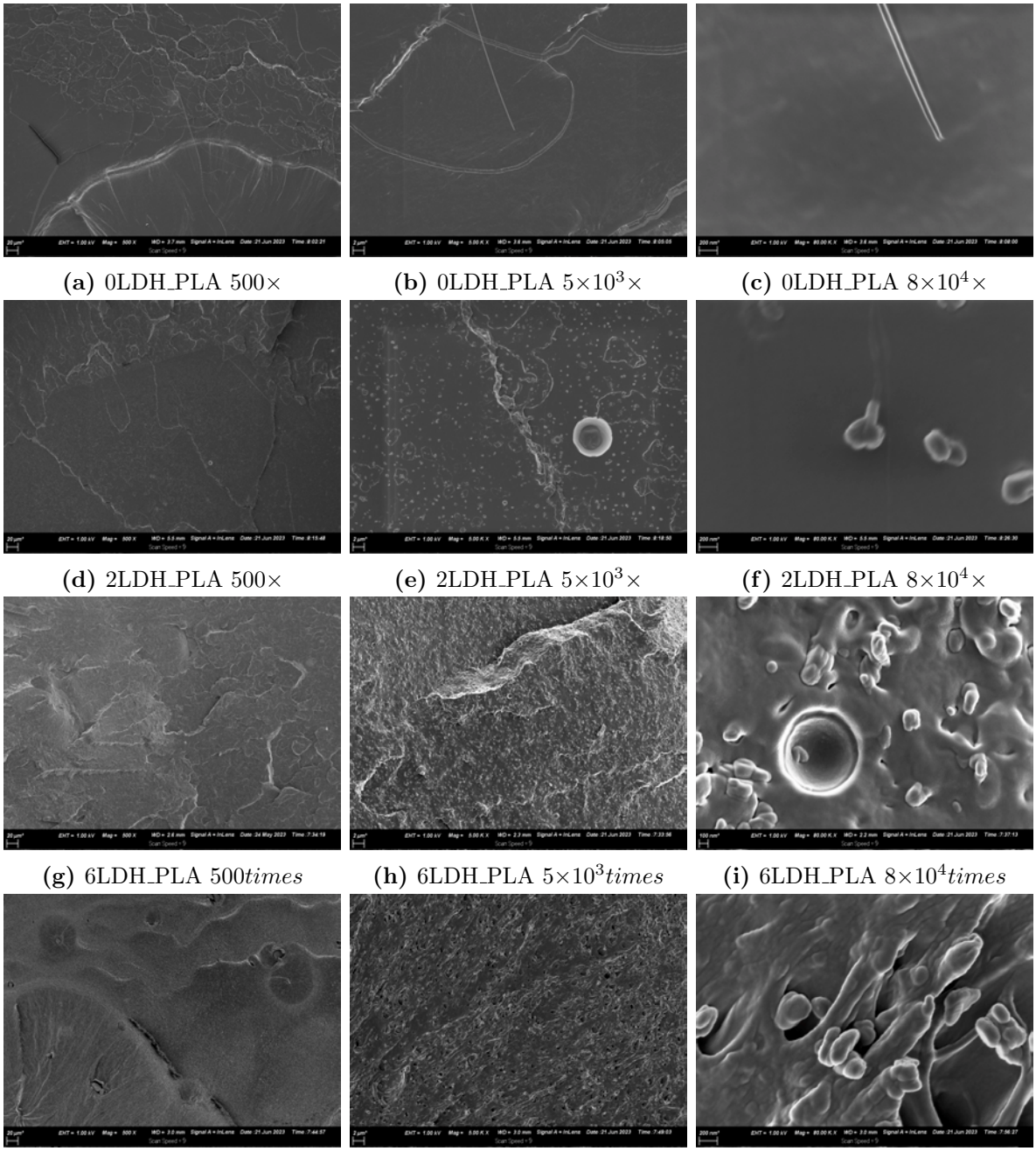

(a) 0LDH_PLA 500× **(b)** 0LDH_PLA 5×10^3× **(c)** 0LDH_PLA 8×10^4×

(d) 2LDH_PLA 500× **(e)** 2LDH_PLA 5×10^3× **(f)** 2LDH_PLA 8×10^4×

(g) 6LDH_PLA 500$times$ **(h)** 6LDH_PLA 5×10^3$times$ **(i)** 6LDH_PLA 8×10^4$times$

(j) 10LDH_PLA 500× **(k)** 10LDH_PLA 5×10^3× **(l)** 10LDH_PLA 8×10^4×

Figure 12: The SEM results of the filament made for use in the screening experiments as well as the pure PLA filament.

All the characterisation methods used indicated that LDH was successfully compounded into PLA. Some interesting behaviours were observed, including but not limited to the effects on the phases and their transition as a function of LDH loading, as well as the good dispersion of the LDH without the assistance of additives.

4.2.2 Tensile test samples

Figure 13 shows the broken tensile test specimens. The same samples before testing is available in Appendix A. Although all samples were printed in a random order for statistical purposes, the samples are grouped according to experimental runs instead, allowing visual comparison between samples. There are no visual differences between all the centre runs as is evident from Figure 13a to Figure 13c. The different parameters did have an effect on print quality. Experiments 3 and 8 had a poor print quality. This seems to be due to the high clay loading and the high printing temperature. At lower loadings, the temperature did not show this effect as drastically, and *vice versa*. The print quality of Experiments 4 and 7 were poorer compared to the others. The common factor between the four experiments is the high level printing temperature. The clay acted as an opacifier at higher loadings. The 2 % samples were more translucent regardless the infill used, whereas the higher loadings appeared white. The 10 % samples were more white than the 6 % ones. These differences were more apparent on the samples before they were tested.

All samples broke in a brittle manner. Most parts broke toward the end of the narrow section, with the exception of samples se_21, se_34 and se_46, which broke more or less in the middle, as shown in Figures 13f, 13i and 13j. None of these form part of the same experiment, and therefore the observation cannot be attributed to any of the experimental factors, *i.e.* LDH loading, percentage infill, nozzle temperature or layer height. Care was taken to insert the side on which the arrow is located into the top clamp of the tensile machine. However, when removing samples from the printing bed and writing the sample number with the arrow, the orientation changed between samples, *i.e.* the side on which the arrow appears was not necessarily the right side of the sample on the printing bed but could have been the left side as well.

Ultimaker Cura allows a user to preview a print layer by layer with a user interface. It essentially makes a video that details how the infill and walls will be printed and in which order. From these previews, it was found that the printer starts printing the walls for each layer at the end of the narrow section, albeit randomly ordered between the four available points due to the selection of slicer settings showed in the Cura settings table (Table 8). This causes a weakness in the specimen at the two ends due to the filament

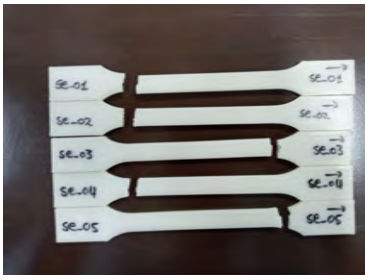

(a) First centre runs.

(b) Middle centre runs.

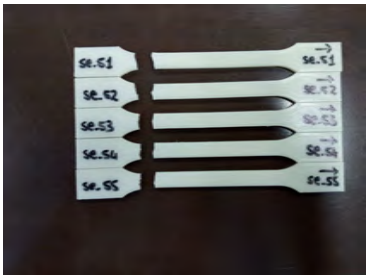

(c) Last centre runs.

(d) First experiment runs.

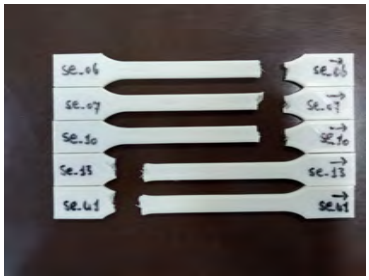

(e) Second experiment runs.

(f) Third experiment runs.

(g) Fourth experiment runs.

(h) Fifth experiment runs.

(i) Sixth experiment runs.

(j) Seventh experiment runs.

(k) Eighth experiment runs.

Figure 13: Images of all the broken tensile samples of the screening experiment grouped by experimental run showing the various fracture locations. The images before testing can be seen in Figure A.4.

cooling off too fast to allow complete fusion between the start and end points. It is believed that this is a large contributing factor to the break locations, rather than some material, processing or testing defect. If this is in fact the case, tensile stress and the tensile force will yield similar results. A few screen shots of such a preview is available in the appendix (Figure A.6).

4.2.3 Tensile stress

The stress strain graphs of all the specimens are shown in Figure 14. The graphs also show that specimens fractured in a brittle manner. There is no maximum before the fracture, and therefore properties at break are the same as ultimate tensile properties. All experiments show good repeatability, especially considering that they were conducted in random order. Figure 14d also shows all the centre runs together on one graph, and no clear deviation can be observed, thus suggesting no serious drift in the experimental procedure. The tensile samples that broke at a different place than most of the others (se_21, se_34 and se_46) did not deviate seriously from the other runs in the same experiment, except for se_46. That being said, se_46 did not deviate that much, and can be ascribed to experimental variance, since se_16 and se_36 in Figures 14k and 14h also deviated to the same extent.

The tensile stresses grouped according to experiment number are shown in Figure 15a. Using Tuckey's outlier whiskers, Equation 8, the six outliers present (se_15, se_16, se_19, se_36, se_46 and se_49) were removed. The box and whisker plot without the outliers is shown in Figure 15b. Two of the outliers are no surprise, as they could be visually identified in Figure 14. There is no clear correlation between the outliers and the location at which the sample broke.

The analysis of the response with respect to the experimental factors was completed on the data without outliers. Figure 16 shows how the tensile stress varies with the four factors selected. Although the centre points were included for determining the lack of fit (LoF) and not for fitting a model to the responses, they are included in the violin plots to provide a point of reference. The summary of the ANOVA of the half factorial screening experiment is shown in Table 18. Due to the LoF which is statistically significant, no statistical conclusions can be made from the results. This is because the LoF indicates that the linear model does not fit the data points sufficiently. Note that the number of distinct design points only allow the estimation of main effects. The variations in the replicated points provided by the pure error in the ANOVA table are within reasonable limits, thus the LoF does not indicate that an unaccounted factor influences the response. An optimum exists within the experimental region, and response surface modelling can be

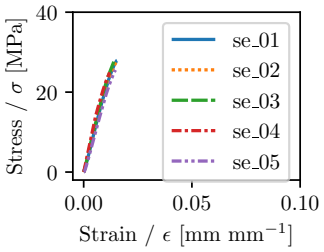

(a) First centre runs.

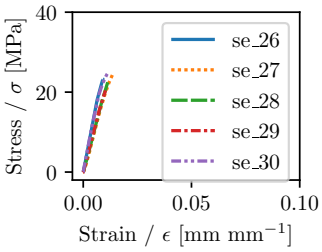

(b) Middle centre runs.

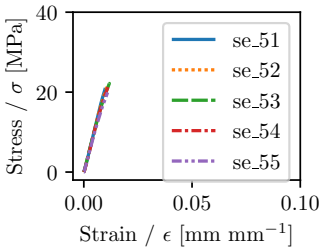

(c) Last centre runs.

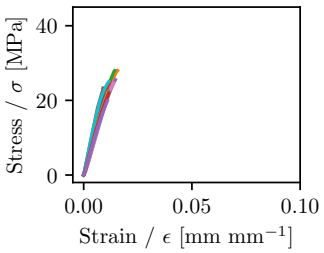

(d) All centre runs.

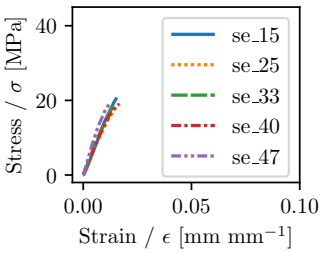

(e) First experiment runs.

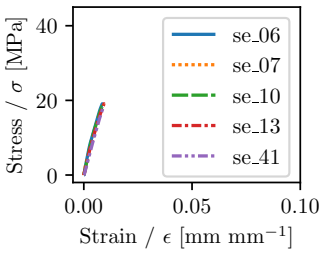

(f) Second experiment runs.

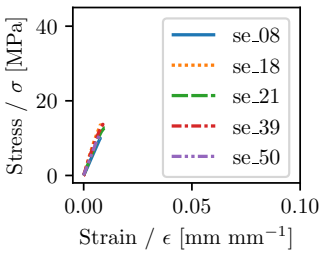

(g) Third experiment runs.

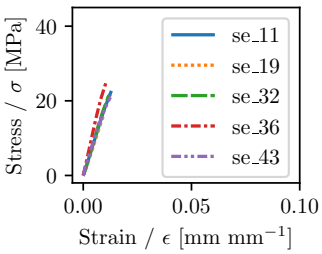

(h) Fourth experiment runs.

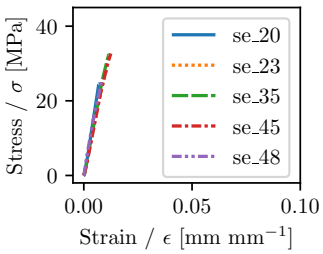

(i) Fifth experiment runs.

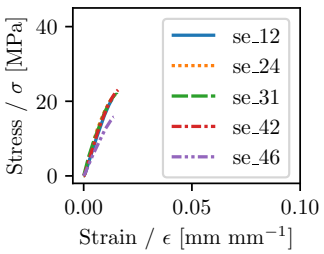

(j) Sixth experiment runs.

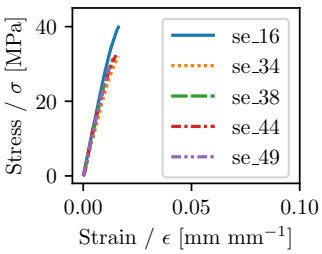

(k) Seventh experiment runs.

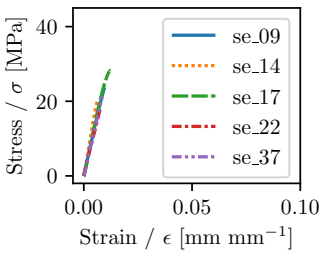

(l) Eighth experiment runs.

Figure 14: The stress strain graphs of all the tensile samples in the screening experiment.

applied to identify the optimum. Accordingly, the experiment was augmented by adding a second block to allow the estimation of more effects. This will allow the derivation of a second order model which can be used to determine the optimum levels of the factors. Many of the other properties considered also showed a statistically significant LoF. In these cases the ANOVA tables and box and whisker plots are only shown in Appendix A.

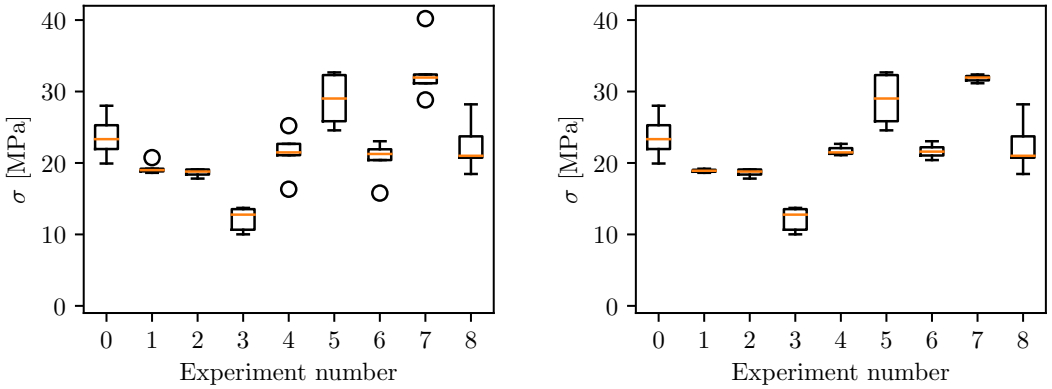

(a) With outliers (circles).

(b) Without outliers.

Figure 15: The box and whisker plots of the tensile stress results of the screening experiment ordered by the experiment conducted with and without outliers.

Table 18: The ANOVA table of the results of the screening experiment with tensile stress as response factor.

Source of variation	Sum of squares	Degrees of freedom	F ratio	p value
Model	705.8527	4	11.3714	< 0.0001
A	22.3573	1	1.4407	0.2364
B	10.2865	1	0.6629	0.4199
C	620.8267	1	40.0065	< 0.0001
D	60.3940	1	3.8918	0.0548
Lack of fit	450.2384	4	19.3601	< 0.0001
Pure error	232.5598	40		
Total error	682.7983	44		

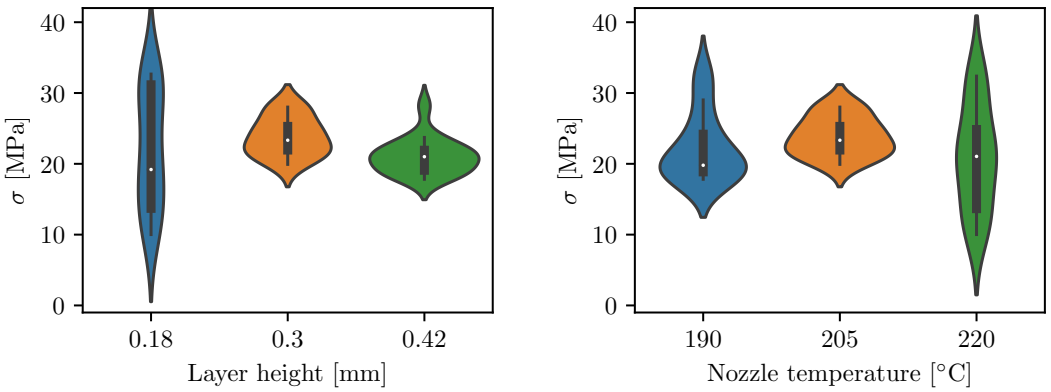

(a) Factor A.

(b) Factor B.

(c) Factor C.

(d) Factor D.

Figure 16: The violin plots of the tensile stress results of the screening experiment ordered by factor with the centre runs included.

4.2.4 Normalised tensile stress

Figure 16c shows that the tensile stress increases with infill density. Intuitively there is a direct correlation between the strength of a specimen and the amount of material in said specimen. This means results cannot be directly compared to results from other manufacturing processes in literature. Often, tensile test specimens are not made with FDM but rather with more traditional processing techniques. Most of these *e.g.* injection moulding, electrospinning, solution casting *etc.* results in a solid product, and do not have an infill density like the parts under consideration here. The strength of such a product will be more than the equivalent FDM artefact, simply because it contains more material. Theoretically, an injection moulded artefact has a 100 % infill density in FDM terms. Even if an artefact is printed with 100 % infill, the FDM sample will still not be a perfect solid because each layer printed consists of a melted round strand that deposits next to or on top of the other. This may be neglected as an inherent processing characteristic, the same way core and shell properties differ in injection moulding. Regardless, it is impractical to compare a tensile specimen that is not a solid, *i.e.* with an infill density less than 100 %, with a solid specimen manufactured with say injection moulding, due to the unequal amounts of material. In order to compare FDM tensile stresses with those manufactured in a different manner, it may be plausible to normalise the tensile stress with respect to mass, since it does not only vary with material properties but also with infill density.

Five outliers were identified with Tuckey's outlier whiskers on the normalised tensile stress ($\hat{\sigma}$) data, namely se_16, se_19, se_33, se_36 and se_46. There is one less outlier observed compared to those in the tensile stresses; thus normalising σ does not affect the outliers drastically. There is still no clear correlation between the outliers and the location at which the sample broke.

The analysis of $\hat{\sigma}$ was completed on the data without the outliers. Figure 17 shows how the normalised tensile stress varies with the four experimental factors. The ANOVA showed a statistically significant LoF and no statistical conclusions can be drawn from the results. As such, the same comments made about σ apply, and the optimum may be determined from a second order model once the experiment has been augmented and enough degrees of freedom are available.

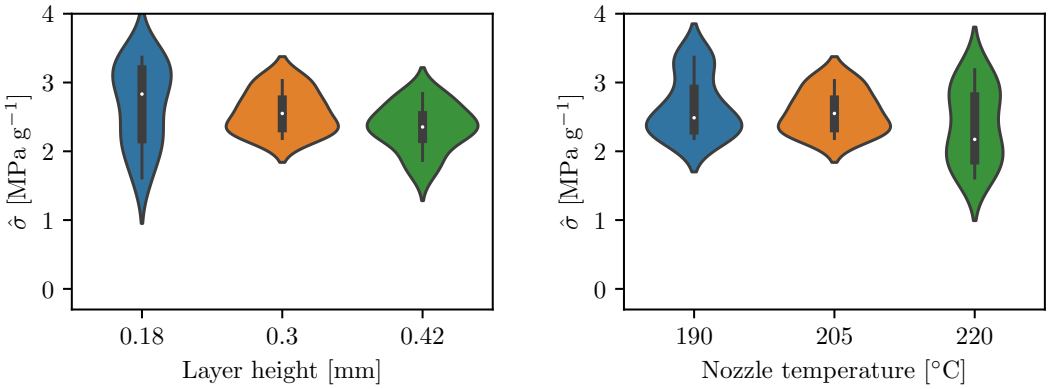

(a) Factor A.

(b) Factor B.

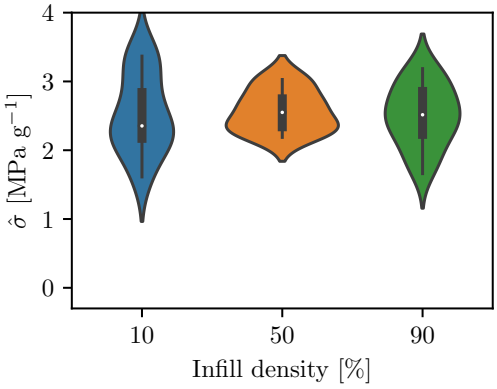

(c) Factor C.

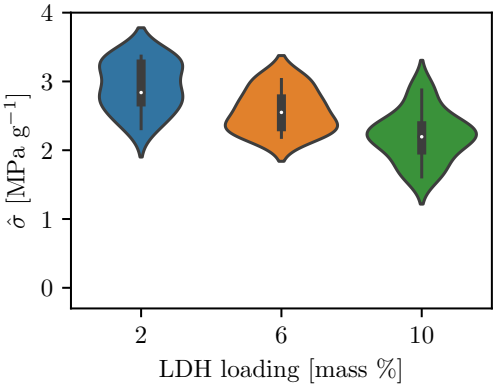

(d) Factor D.

Figure 17: The violin plots of the normalised tensile stress results of the screening experiment ordered by factor with the centre runs included.

4.2.5 Tensile force

Strictly speaking, some of the stresses recorded are inaccurate because of their fracture locations. Accordingly, the same process used for the tensile stress was also repeated for the tensile force, *i.e.* the ultimate tensile load (F) was considered separately. The standard tensile graphs with load on the y-axis is available in the appendix (Figure A.7). No significant differences can be observed between the graphs. Those samples that diverge slightly from the rest are still the same as with the stress strain graphs, namely se_36, se_46 and se_16.

Five tensile force outliers were identified, namely se_15, se_16, se_17, se_41 and se_46. The response as a function of the experimental factors are shown in Figure 18. There are too few degrees of freedom to fit a model to the experimental points, as indicated by the statistical significant LoF. In addition to not being able to conclude whether the experimental factors affect the response, no conclusion can be made about the differences or the lack thereof between the tensile stress and load, and more data is needed for useful interpretation of the data.

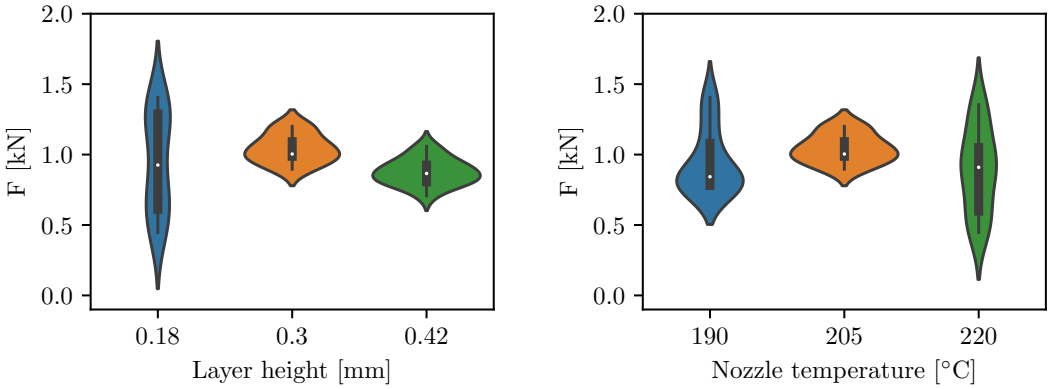

(a) Factor A.

(b) Factor B.

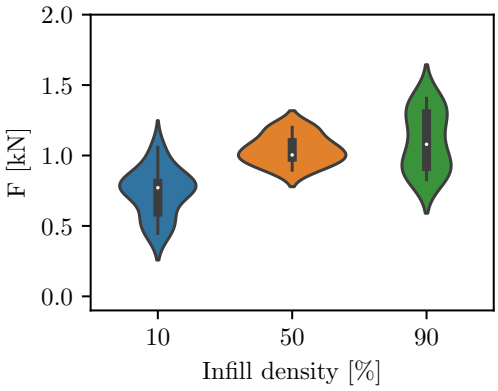

(c) Factor C.

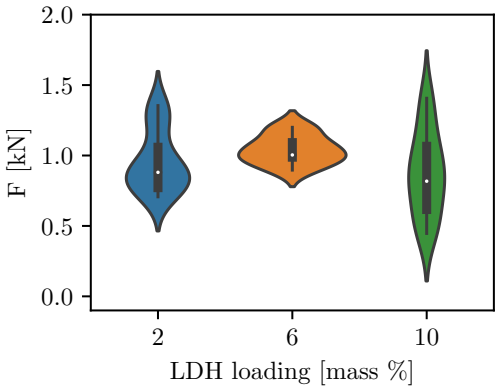

(d) Factor D.

Figure 18: The violin plots of the tensile force results of the screening experiment ordered by factor with the centre runs included.

4.2.6 Normalised tensile force

The tensile force was also normalised. The normalised ultimate tensile force ($\hat{F}$) data had five outliers, namely se_15, se_16, se_17, se_41 and se_46. These are exactly the same as for F. The response as a function of the experimental factors are shown in Figure 19. As before there is a statistical significant LoF indicating that a model cannot be fitted to the data.

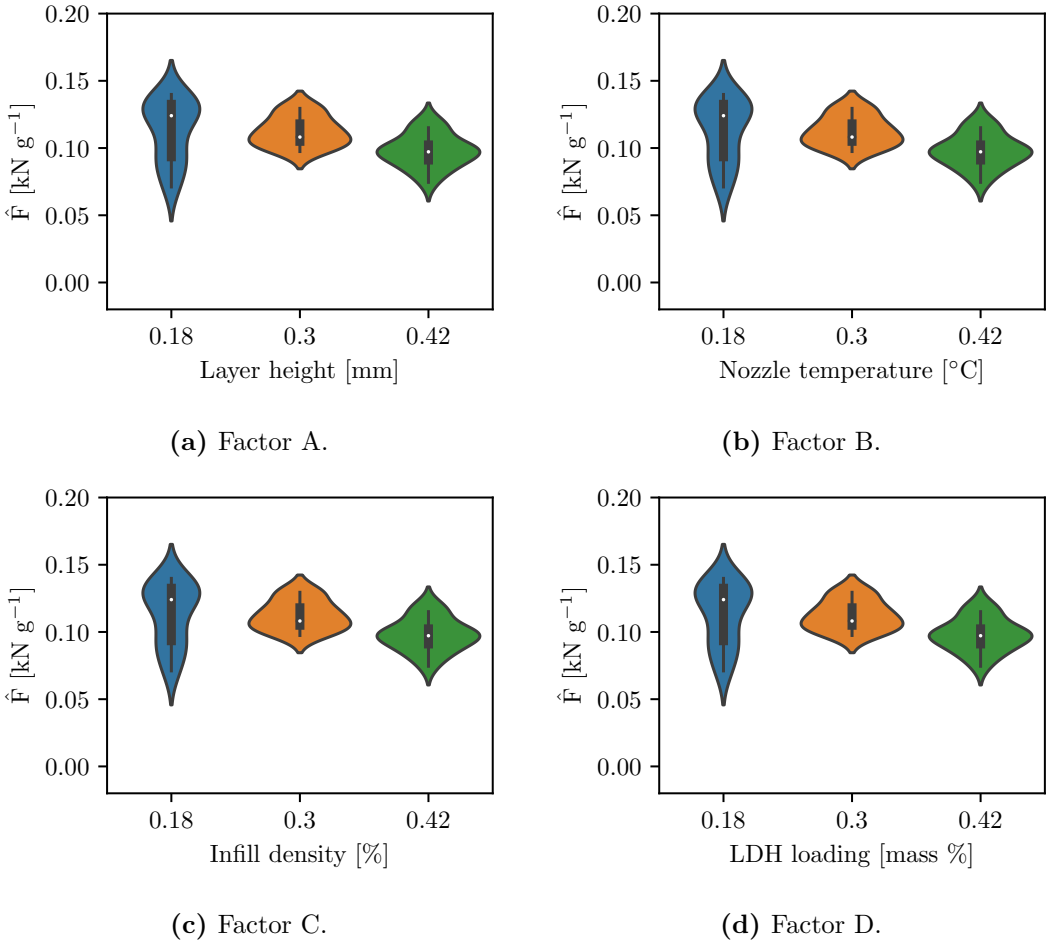

(a) Factor A. **(b)** Factor B.

(c) Factor C. **(d)** Factor D.

Figure 19: The violin plots of the normalised tensile force results of the screening experiment ordered by factor with the centre runs included.

4.2.7 Strain at break

There are no outliers present in the data set for ϵ_b. Figure 20 shows ϵ_b as a function of the factors selected. Table 19 shows the ANOVA table for the response. It does not show a statistical significant LoF, so a linear model can be fitted to the data. All of the linear effects were statistically insignificant. Removing the least significant factor one at a time

resulted in a model with only LDH loading as a significant factor. The model fitted to the data is given in Equation 24

$$\epsilon_b = 0.015930 - 6.7773 \times 10^{-4}\ \mathrm{D} \tag{24}$$

with ϵ_b in mm mm^{-1} and D the LDH loading in %. The maximum is where the LDH loading is the lowest, *i.e.* a loading of 2 %, yielding a ϵ_b of 0.014 574 mm mm^{-1}. The introduction of LDH reduced the mobility of the PLA chains by impeding their ability to realign under load. Its effect is not too drastic because PLA is already a brittle polymer.

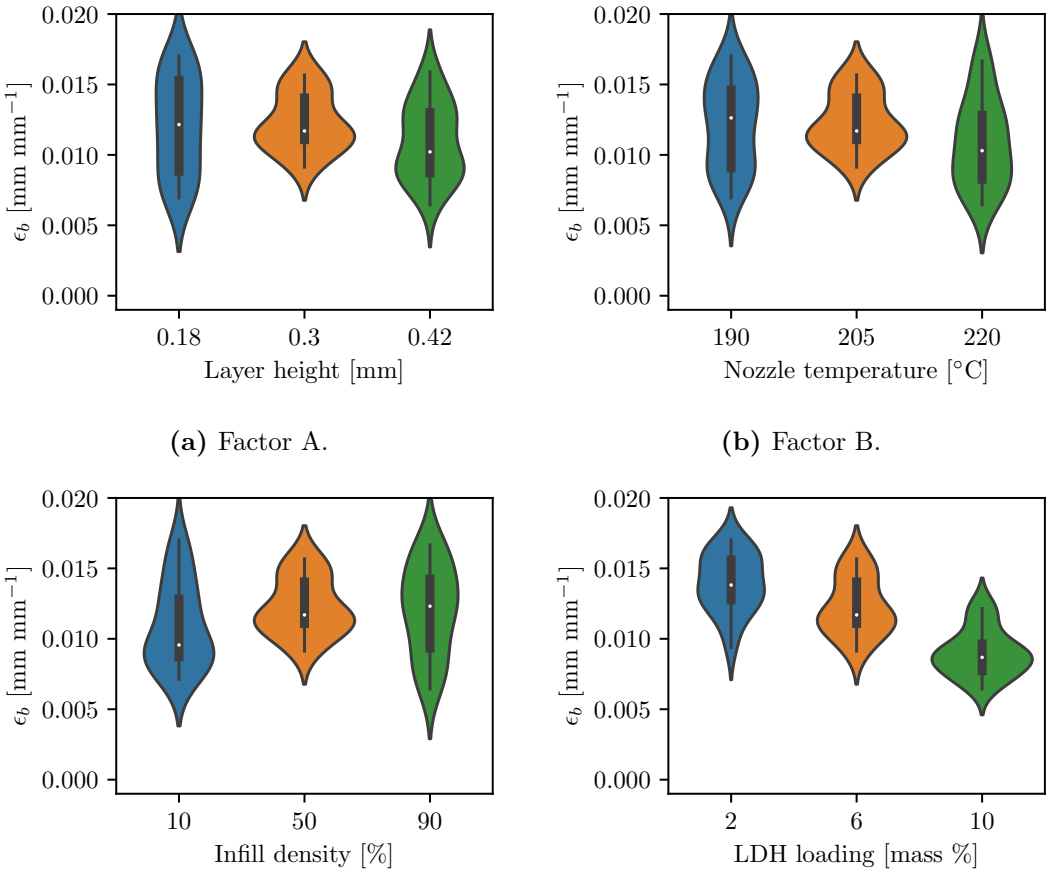

(a) Factor A.

(b) Factor B.

(c) Factor C.

(d) Factor D.

Figure 20: The violin plots of the strain at break results of the screening experiment ordered by factor with the centre runs included.

Table 19: The ANOVA table of the results of the screening experiment with strain at break as response factor.

Source of variation	Sum of squares	Degrees of freedom	F ratio	p value
Model	0.000 244 47	1	77.538	< 0.0001
D	0.000 244 47	1	77.538	< 0.0001
Lack of fit	0.000 003 34	1	1.060	0.3087
Pure error	0.000 144 85	46		
Total error	0.000 148 19	47		

4.2.8 Young's modulus

Since σ and F corresponded so well in their trends with respect to experiment number, E was investigated despite the fact that the accuracy of σ is questionable. Nine outliers was identified, *i.e.* se_14, se_15, se_19, se_30, se_31, se_36, se_46, se_47 and se_48. Although comparable to outliers from other analyses, the most outliers are seen for this response. This is because E takes into account two properties, stress and strain. Additionally, it is not calculated at the position where the ultimate tensile stress or the strain at break was recorded, but rather in the initial linear section of the graph. At most two outliers have been identified within an experimental set. The difference in the amount of outliers for E compared to the previous responses is not too concerning. Figure 21 shows the variation of E with the experimental factors. As before, the LoF is statistically significant, and therefore no statistical conclusions can be made yet.

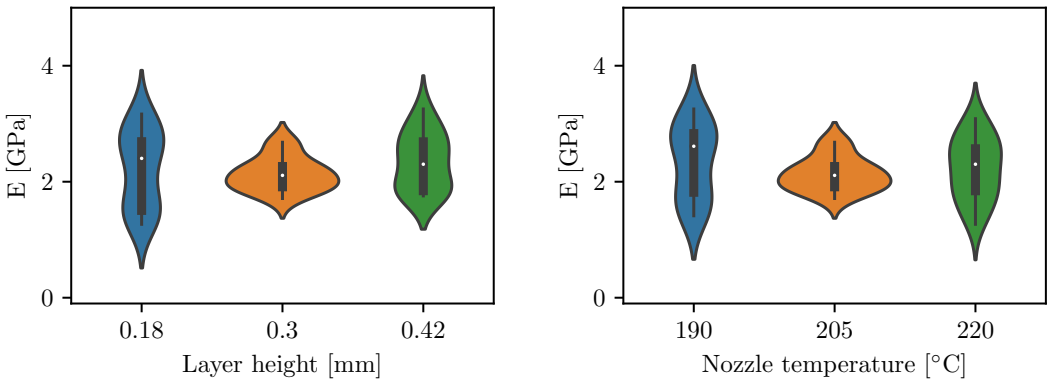

(a) Factor A.

(b) Factor B.

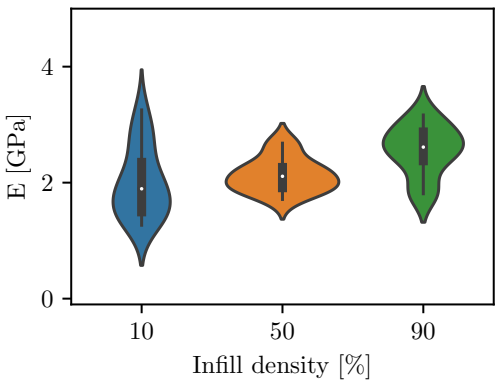

(c) Factor C.

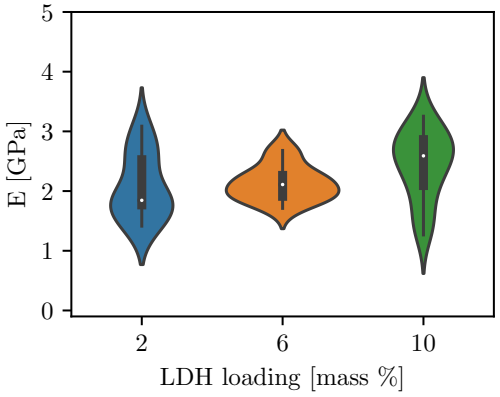

(d) Factor D.

Figure 21: The violin plots of the Young's modulus results of the screening experiment ordered by factor with the centre runs included.

4.2.9 Normalised Young's modulus

If $\hat{\sigma}$ instead of σ is used to calculate E, different results are observed. For the purposes of this work, this is called the normalised Young's modulus ($\hat{\mathrm{E}}$). The eight outliers identified were se_15, se_30, se_31, se_36, se_44, se_46, se_47 and se_48. These differ only slightly from the E outliers. New outliers can be identified with Tuckey's whisker fences from the data set after the above outliers have been removed. These appear because the interquartile ranges without the outliers become smaller, making two data points outliers that have not been considered outliers before. These are not removed again, since they fall within the Tuckey fences of the first interquartile ranges. $\hat{\mathrm{E}}$ sorted by factor are shown in Figure 22. The statistically significant LoF indicated by the ANOVA table shows that no conclusions can be drawn from the results.

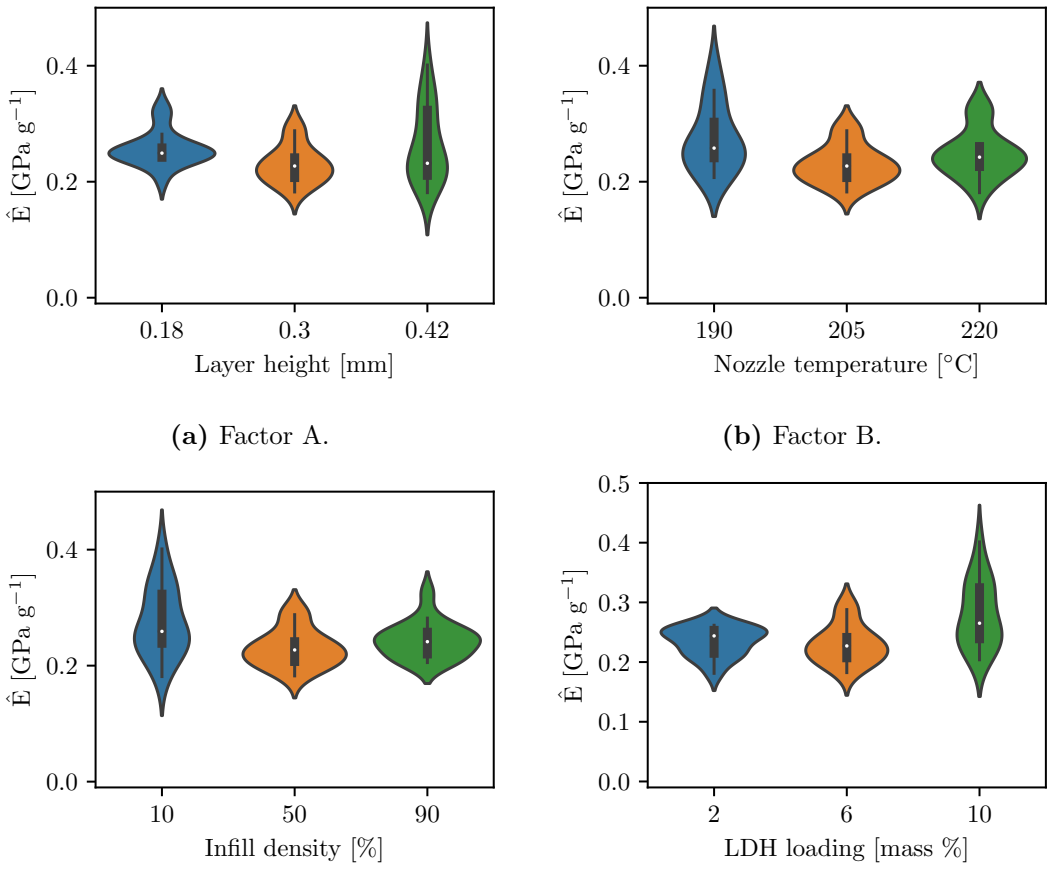

(a) Factor A. **(b)** Factor B.

(c) Factor C. **(d)** Factor D.

Figure 22: The violin plots of the normalised Young's modulus results of the screening experiment ordered by factor with the centre runs included.

4.2.10 Impact test samples

The same visual observations made of the tensile specimens were also seen for the printed impact samples. It is however more difficult to see the differences since the impact specimens are so much smaller than the tensile ones. Once again, the effect of high clay loading and high printing temperature on the print quality as well as the opacifying effect of the clay loading was distinguishable. Images of all the samples are in the appendix (Figure A.15).

4.2.11 Impact energy

All samples broke as expected. The accuracy of the impact tester is only 0.02 J, where the minimum, maximum and mode across all samples were 0.04 J, 0.14 J and 0.06 J respectively. Due to the lack of more accurate equipment, more precise results could not be achieved. Yet, it was believed that useful information was still gleaned from the results. Five impact energy (ξ) outliers were identified, namely se_08, se_09, se_16, se_39 and se_53. The response as a function of the experimental factors are shown in Figure 23. The available degrees of freedom are too little to fit a model to the experimental points, as indicated by the statistical significant LoF.

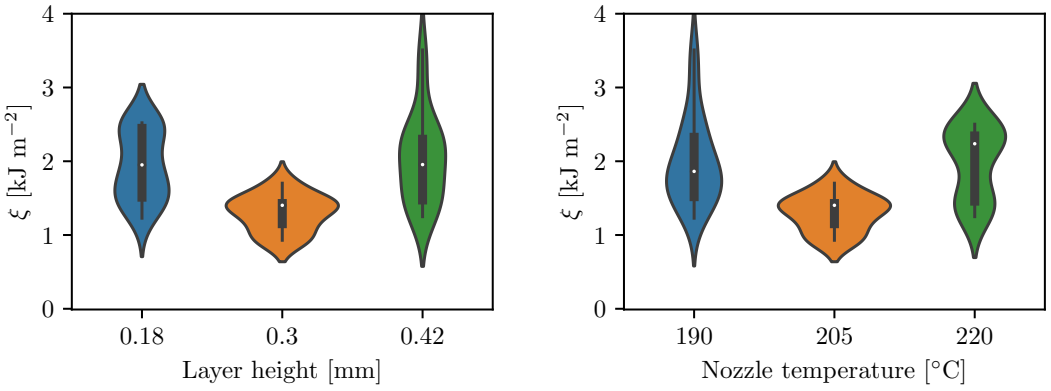

(a) Factor A.

(b) Factor B.

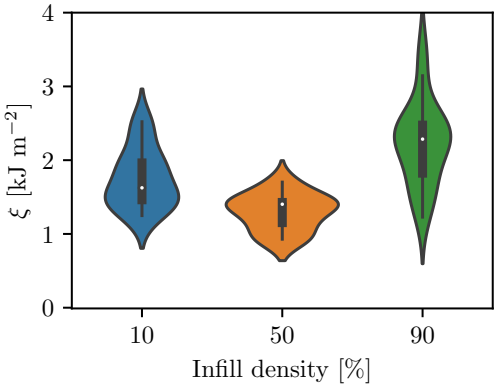

(c) Factor C.

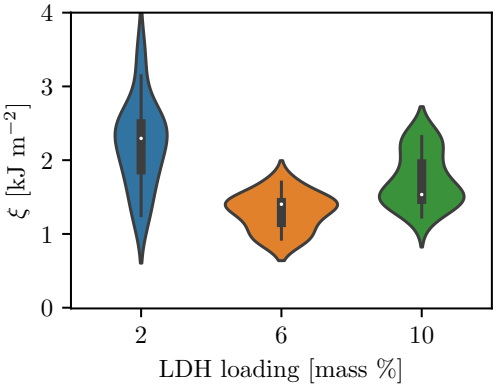

(d) Factor D.

Figure 23: The violin plots of the impact energy results of the screening experiment ordered by factor with the centre runs included.

4.2.12 Normalised impact energy

The impact energy was also normalised with respect to mass. Three outliers were identified with Equation 8, *i.e.* se_09, se_16 and se_53. All of them were also outliers for ξ. The normalised impact energy ($\hat{\xi}$) as a function of the experimental factors are shown in Figure 24. The ANOVA yields a statistical significant LoF, and no model can be fitted.

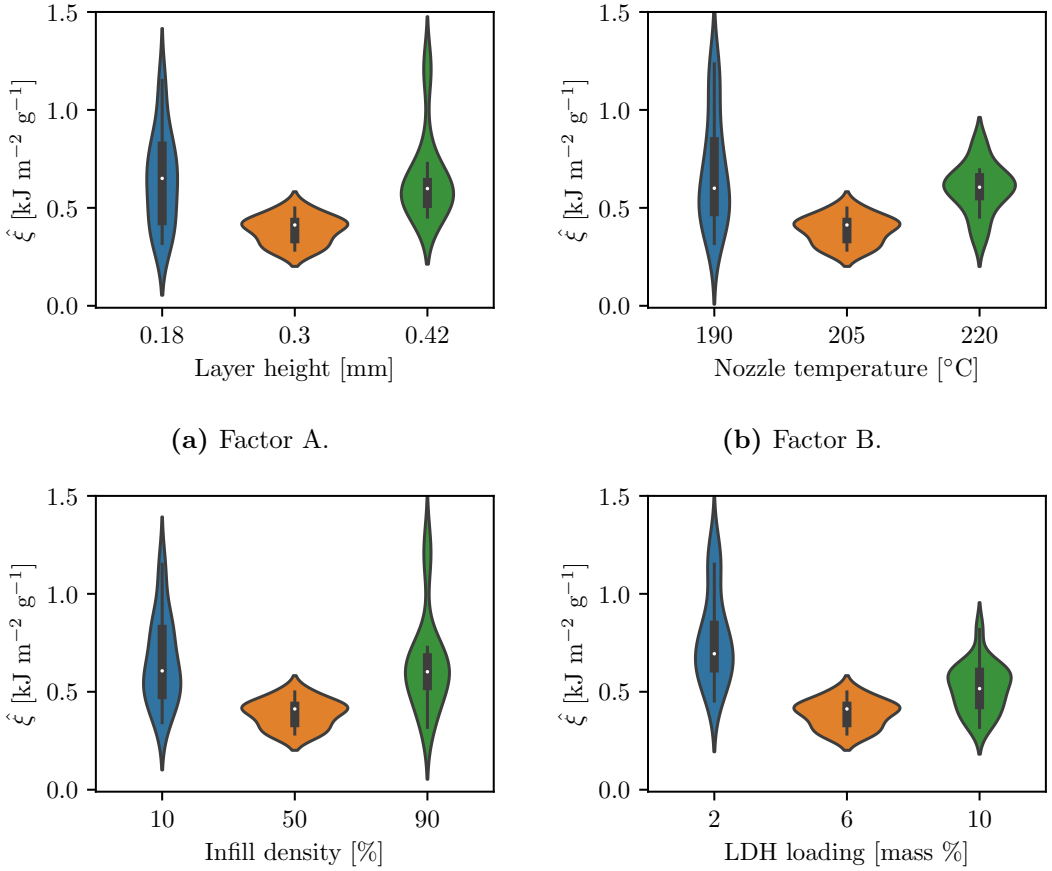

(a) Factor A. **(b)** Factor B.

(c) Factor C. **(d)** Factor D.

Figure 24: The violin plots of the normalised impact energy results of the screening experiment ordered by factor with the centre runs included.

4.2.13 Characterisation

Characterisation was completed on the tensile specimens after printing as well. Initially, DSC, XRD, FTIR, SEM and DMA would have been completed on both the tensile and the impact samples after printing. Some challenges arose. The filaments were granulated by hand for XRD analysis. This method was not feasible for the printed parts because the granules could not be cut small enough, and it took too long to prepare. Instead, small square sheets with sides 20 mm long consisting of only two layers, a top and bottom one,

were printed. The total thickness of said sheet is *ca.* 3 mm. These are further referred to as XRD sheets. The SEM of the fractured surfaces of the tensile and impact specimens also proved futile. This is mostly because the samples do not have a solid interior due to the infill densities being lower than 100 %. It is therefore very difficult to get well focused SEM images. Lastly, DMA also did not realise because all samples came loose from the clamps as soon as the temperature started to rise. Even after printing smaller specimens specifically for DMA, the problem persisted. As such, only DSC, XRD and FTIR were completed. To reduce the amount of tests to be run, only the tensile specimens were used. In § 4.3 a comparison between the different print geometries and their characterisation results have been made which shows that the print geometry does not affect results.

Whilst conducting the statistical analyses on the various responses of the screening experiment, it was realised that a lot of resources and time are being wasted by doing five repeats of each experimental point. This is especially true for DSC and XRD, and to a lesser extent for FTIR. In the discussion on the proper use of statistics, § 4.8, it is illustrated that it is unnecessary to have so many repeats when a statistical analysis will be completed on a statistically designed experiment.

The second heating runs of the DSCs completed on the printed tensile specimens are shown in Figure 25. This was compiled from DSC data with five replications of the centre point and two replications of all the experimental points. This is not all the replications of each point, but is still more than enough data points to observe any important differences between samples from a statistical point of view. Refer to the experimental setup of the screening experiment in Tables 9 and 10 for information on the different factors at each experimental point. The LDH loading clearly has an effect on the composite and its thermal properties. In all cases where a single melting peak was observed, *i.e.* Experiments 1, 4, 6 and 7, the LDH loading was at its low value (2 %). This corresponds well to the DSCs on the filaments used in the screening experiment, where the 2 % filament also had a single melting peak, but the higher loadings had double peaks. It is not clear if the other factors, *i.e.* layer height, nozzle temperature and infill density, have any effect on the melting behaviour from the DSC curves.

Figure 26 shows the violin plots of the properties determined from the second heating cycles plotted against the LDH loading. The full scale graphs are complimented by enlarged ones. Compared to the filaments' properties, similar trends are observed. A pure PLA reference is not applicable here, since it did not form part of the screening experiment. Transition temperatures still decrease with LDH loading, and the second melting peak temperature are not observed for 2 % LDH. The enthalpies of fusion and crystallisation show slightly different trends than before, but the differences are not of any practical value, which becomes clear when the full scale graphs are observed. Considering

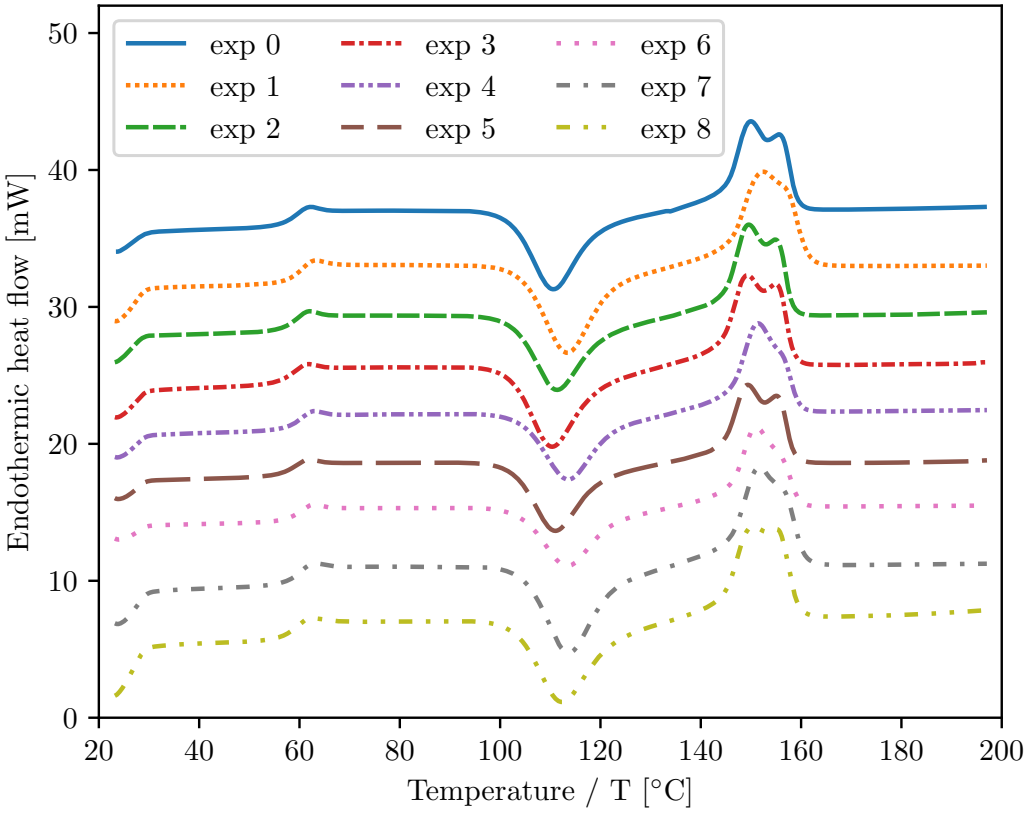

Figure 25: Representative DSC results of the second heating cycle of the tensile specimens printed in the screening experiments compiled from Figure A.18.

that no statistical conclusion could be drawn on the main response of interest, σ, it was not deemed worthwhile to complete statistical analyses on all the DSC results as well. Still, the properties as a function of the other printing factors are available in the appendix (Figures A.19, A.20 and A.21). None of these properties are expected to have a direct effect on the thermal properties determined from DSC, but differences between factor levels exist. The degree of crystallinity calculated with these enthalpies are still negative.

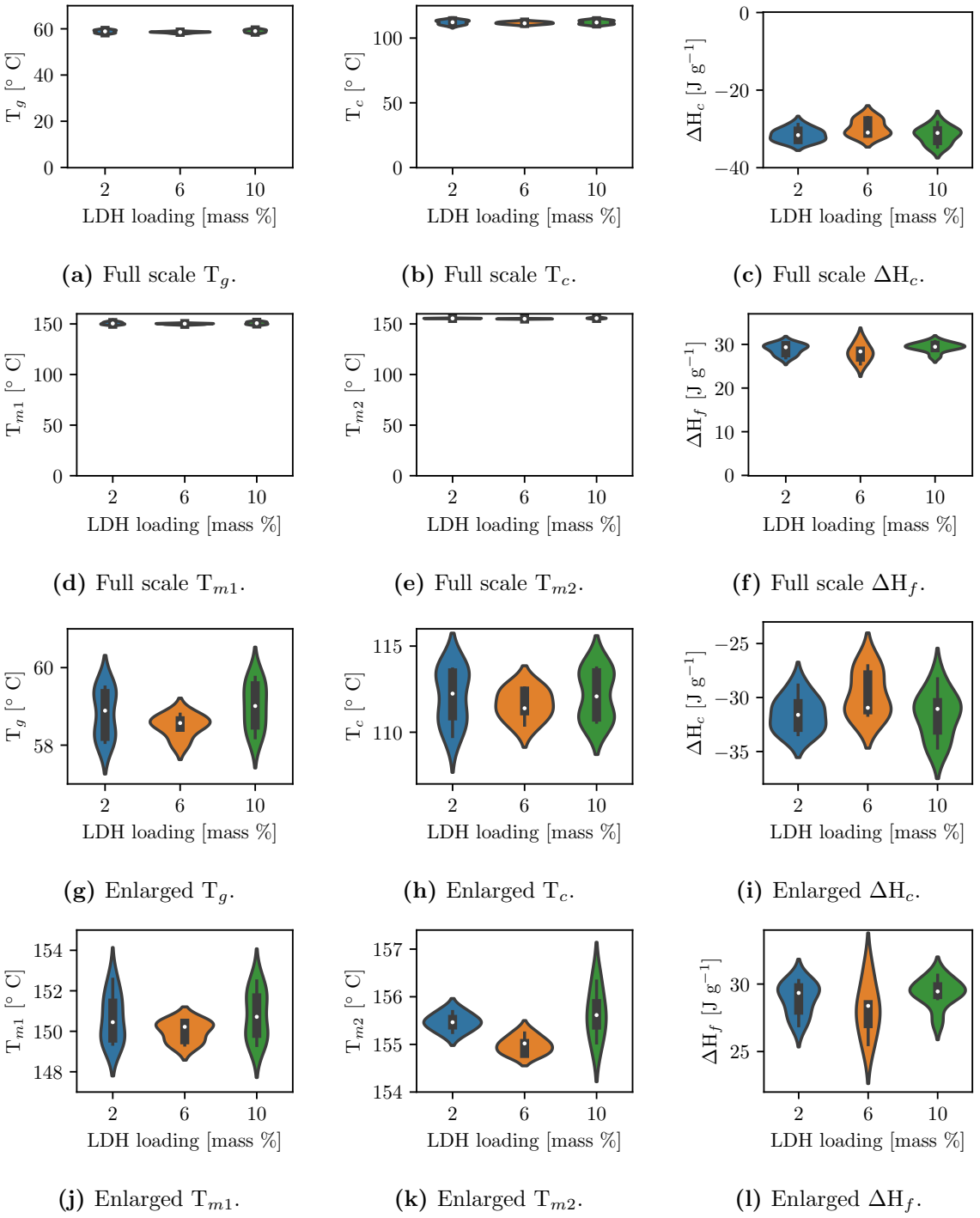

(a) Full scale T_g. **(b)** Full scale T_c. **(c)** Full scale ΔH_c.

(d) Full scale T_{m1}. **(e)** Full scale T_{m2}. **(f)** Full scale ΔH_f.

(g) Enlarged T_g. **(h)** Enlarged T_c. **(i)** Enlarged ΔH_c.

(j) Enlarged T_{m1}. **(k)** Enlarged T_{m2}. **(l)** Enlarged ΔH_f.

Figure 26: The average properties of the respective tensile samples printed for the screening experiment as determined from DSC as a function of LDH loading.

The results from the XRD sheets are given in Figure 27. Since the sheets had to be printed to be as thin as possible to allow characterisation, they do not have varying infill densities. Because the XRD spectra are used for tracking the presence of LDH in the PLA composite and no quantitative results are calculated from them, the effect of layer height and nozzle temperature does not affect results either. As such, only the spectra as a function of the LDH loading is shown. The printed sheets showed better resolution compared to the granules. Therefore, when comparing the spectra from the sheets to that of the filament, all the peaks from the PLA and the LDH had a higher intensities. That being said, the peak positions remain fixed at the locations already identified, and the incorporation of the LDH at different levels can clearly be distinguished and followed. No additional peaks are observed, and the broad spectra of the PLA can still be seen throughout. This indicates that from a structural point of view no changes occurred during the printing process, and that the dispersion, spacing and arrangement of different atoms, molecules and particles stayed constant.

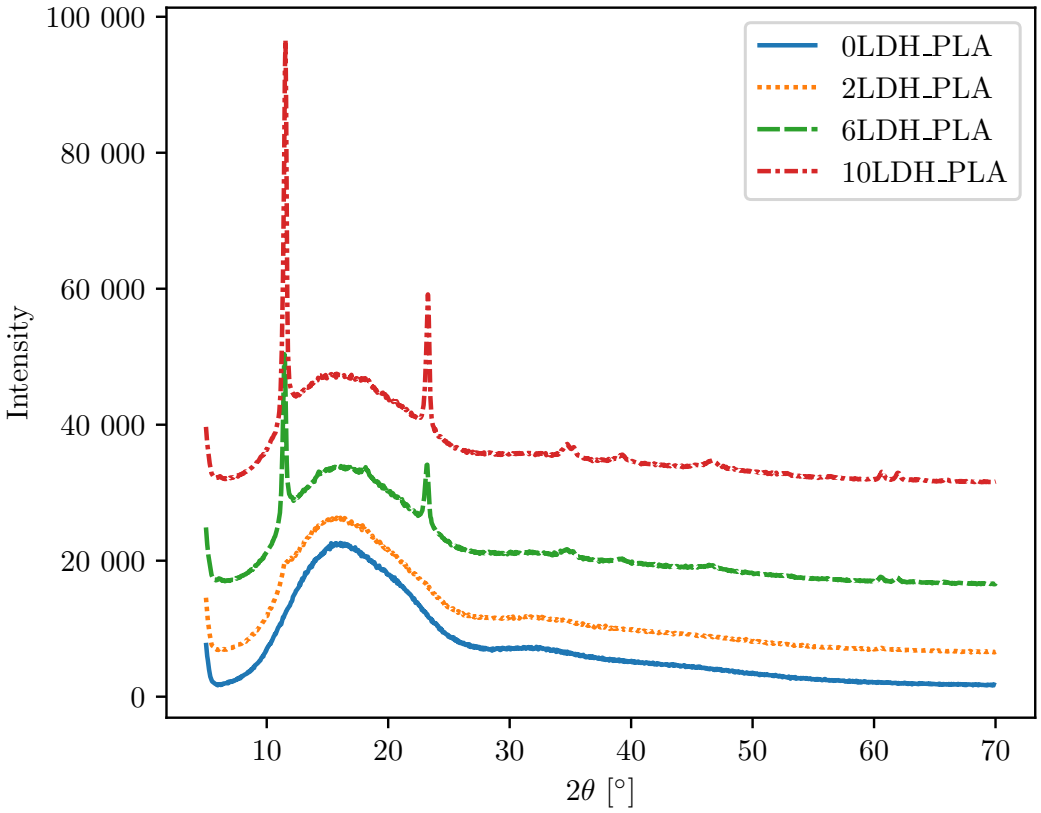

Figure 27: The XRD results of the XRD sheets printed in the screening experiment.

The FTIR spectra of the printed tensile specimens are given in Figure 28. This was compiled from data of all the printed specimens. The characteristic peaks observed for the filament are still present, although some more variances are observed in the lower wavenumber region. The spectra shown in Figure 28 is not truly representative of all the

repeats completed, because a lot of variation in peak heights have been observed within a set of five replications. Upon closer inspection some spectra appear flat because they are plotted together and the relative scales reduce the resolution of peaks. Even though their peaks are evidently smaller, they are still at the same locations. As such, exactly the same groups observed for the filament are still seen here. It is believed that the lower peaks in selected runs are due to interference during the testing procedure when a test surface is not as smooth as most of the others. This was also observed in the comparison already mentioned, and will be discussed in more depth in the following section.

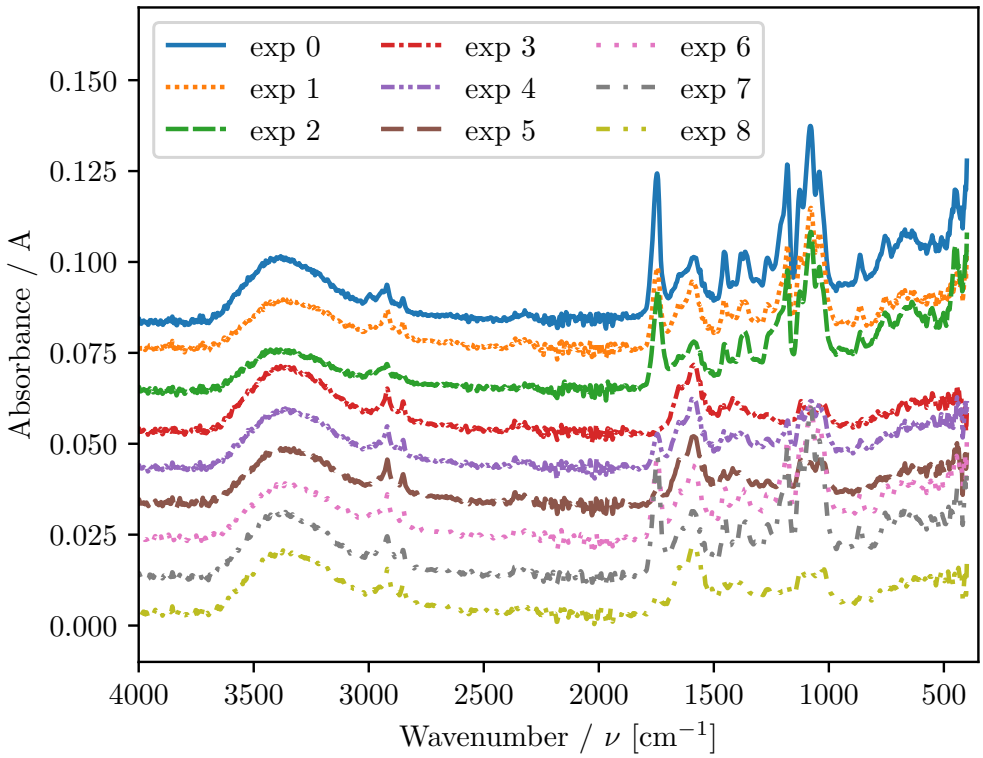

Figure 28: FTIR results of the tensile specimens printed in the screening experiments compiled from Figure A.22.

4.3 Comparison

Due to the limitations presented by the analytical instruments used, it is difficult to analyse each and every sample by XRD, FTIR, DSC and DMA. Moreover, the amount of repeats done in experiments result in a lot of time being spent on analysing each sample by all the different methods.

In order to determine whether it is necessary to fully characterise all samples, a comparison experiment was conducted. Five XRD samples were printed with the 10LDH_PLA

filament at the Experiment 8 material extrusion settings, and subjected to XRD, FTIR, DSC and DMA analysis. One DMA, one impact and one tensile sample was also printed. All of these were then analysed by XRD, FTIR and DSC analyses to compare whether the different sample geometries affect the results obtained. The XRD and DMA samples were tested using DMA analysis.

The XRD results are shown in Figure 29. Five of these sheets where printed. Good repeatability was achieved. The peaks for the top and bottom spectra are almost on top of one another, but the peak heights are lower for the top spectra and the PLA peak centred around 18.5° is only visible in the bottom spectra. Figures 29a and 29b refers. This might be because the first layer of the sheet is pressed against the bed during printing, thus causing a dense and compact layer, whereas the second layer is less dense because the layer height is not influenced by an external factor. The reason why the first layer is more dense is because during bed levelling, the bed is levelled so that the nozzle is very close to the bed to ensure proper bed adhesion. Thus, due to the printing procedure, the bottom is dense and has a smooth surface, whereas the top layer is less dense and has a rougher surface.

The DMA, impact and tensile samples were granulated by hand. This results in a very porous *i.e.* low density volume. The spectra of the DMA, impact and tensile granules are shown in Figure 29c. Their peak positions also compare well, but larger differences are observable in the peak and continuum heights. This is believed to be due the density of the granules and their orientations, since the density of the volume does have an effect on the XRD peak heights. Figure 29d emphasises these differences. There is a slight shift to the left in the XRD sheet peaks compared to the other samples' spectra. The amount of peaks and their general position remain fixed. This suggests that more information may be gleaned from the more dense sheets, more specifically from their bottom spectra. These yield the highest resolution and even identifies the PLA peak at around 18°. This is the reason why the sheets are used for all XRD spectra of printed specimens instead of granules.

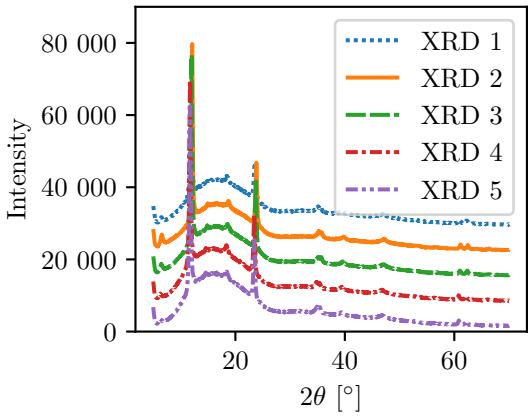

(a) Five XRD samples (bottom spectra).

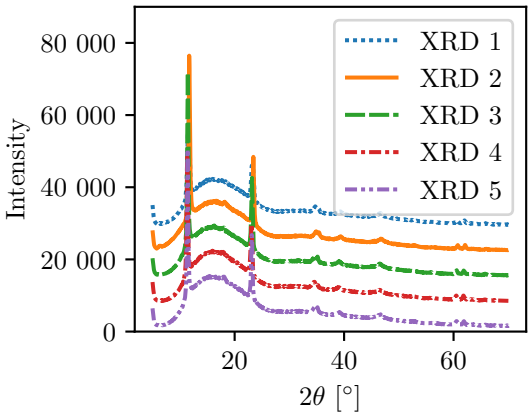

(b) Five XRD samples (top spectra).

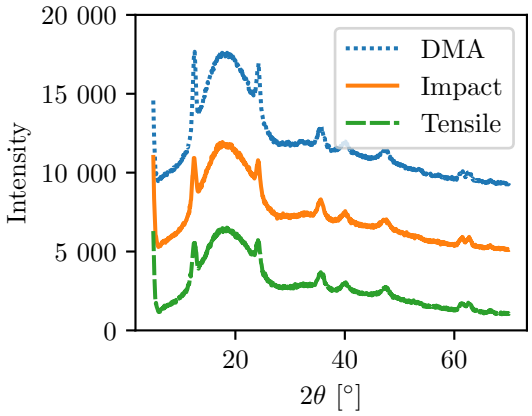

(c) Tensile, impact and DMA samples.

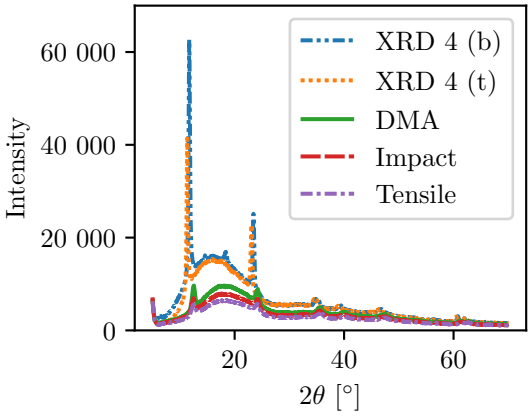

(d) Comparison of all samples.

Figure 29: The XRD results of the five XRD samples (top spectra), one DMA sample, one impact sample and one tensile sample for the comparison experiment as well as a comparison between them all. In Figure 29d b and t refers to bottom and top respectively.

The FTIR results of five XRD sheets, as well as one impact, tensile and DMA specimen are given in Figure 30. The respective peaks have already been identified. No drastic changes can be observed between the spectra of the 10LDH_PLA filament spectra (Figure 11) and the spectra of the printed samples shown here. Looking at the fourth and fifth spectra from the top in Figure 30a, there is however a variation in the peak height compared to the other spectra of the XRD sheets, although peak positions remain fixed. Two additional FTIR spectra were taken for these two samples but at different locations, which is shown in Figures 30b and 30d. It is clear that the positions of the peaks stay fixed, but that there is variability in the peak heights. Therefore, the height of peaks are dependent on the position where the FTIR spectra was taken on the sample. This is ascribed to the rough surface of samples, which causes the scattering of the infra red radiation. Accordingly, no quantitative conclusions can be drawn from the spectra peak heights and the spectra can only used for peak locations. In a similar fashion, three FTIR analyses where completed at different locations on a tensile sample as shown in Figure 30f. The same observations and conclusions apply. Figure 30c shows the respective spectra of a tensile, impact and DMA sample. No obvious differences are visible, except for some variability in peak heights. This is further confirmed by plotting the spectra of all the different samples together on one graph without any offset as shown in Figure 30e. Clearly, there is no reason to believe that the sample geometry affects the FTIR results. Instead, all variation is due to the surface roughness of a sample, and the location on the sample where the spectra was taken.

The DSC results are shown in Figure 31. Five repeats were done on the XRD sheets, and excellent repeatability was achieved. In fact, the ANOVA on the various peaks and enthalpies show no statistical significant difference. Figure 31a refers. The DSC results of the DMA, impact and tensile samples are given in Figure 31b and once again there is no observable differences. This was confirmed by ANOVA. Figure 31c illustrates this well, with all the DSCs plotted together without any offset. From this graph it seems as if T_c varies between the XRD and the other samples, as well as the areas under the peaks. Of course the latter can be ascribed to the different sample masses. That being said, the degree of crystallinity calculated from the enthalpies are negative, which is not possible in reality. As already mentioned, this unexpected observation will be discussed later. The ANOVA analysis of all the properties show that only the melting temperatures differ statistically significantly between the XRD and the other samples on a 95 % confidence interval. The p-values for the first and second melting peaks are 0.022 and 0.012 respectively. Even though statistically significant, these melting temperatures do not vary that much, as can be seen from the box and whisker plot. This plot shows the two melting temperature peaks for the XRD samples, the DMA, impact and tensile samples as well as all the samples together. The plots have to be zoomed in in order

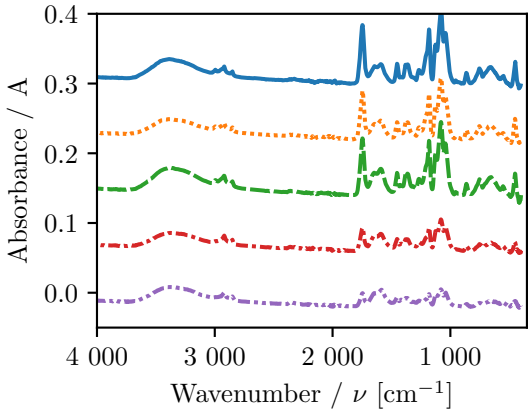

(a) Five XRD samples.

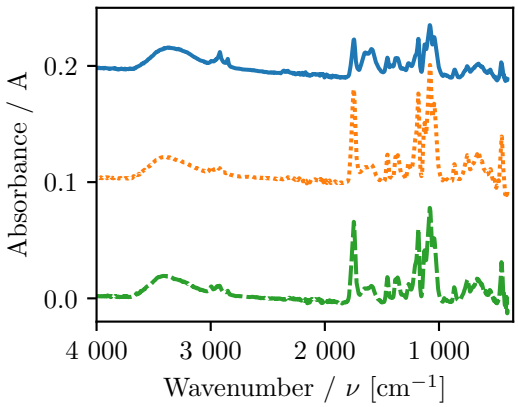

(b) Repeats on fourth XRD sample.

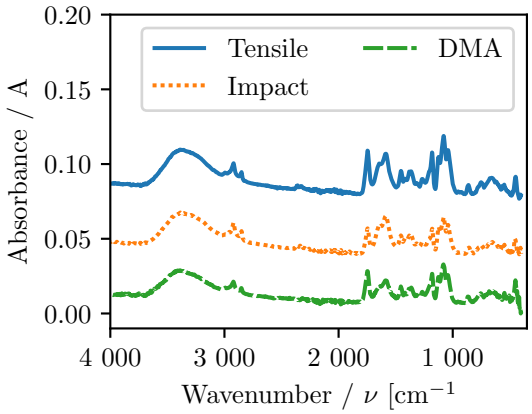

(c) Tensile, impact and DMA samples.

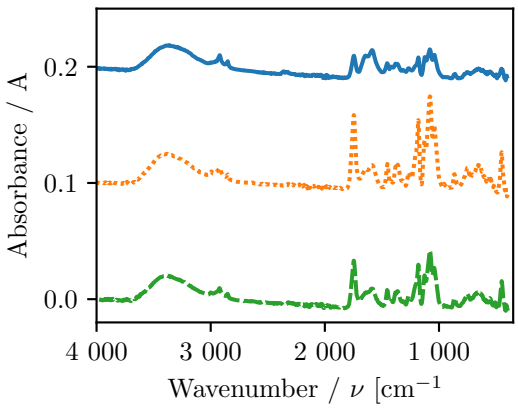

(d) Repeats on fifth XRD sample.

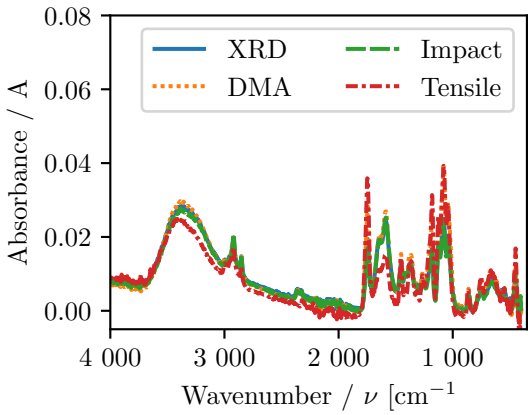

(e) Comparison of all samples.

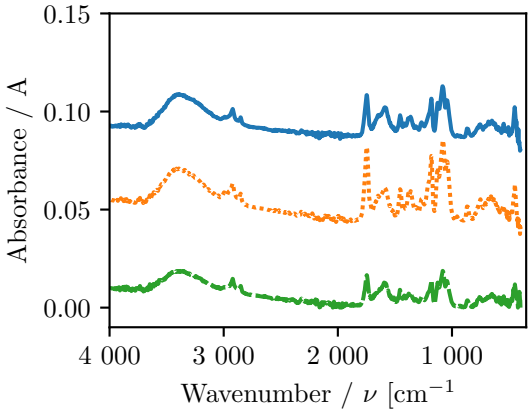

(f) Repeats on tensile sample.

Figure 30: The FTIR results of the five XRD samples, one DMA sample, one impact sample and one tensile sample for the comparison experiment.

to observe any differences, as can be seen in Figure 32. Clearly, DSC results do not differ enough between the different printed geometries to conclude that they cannot be compared. As such, a DSC can be done on any of the printed parts and can be regarded as representative of the set.

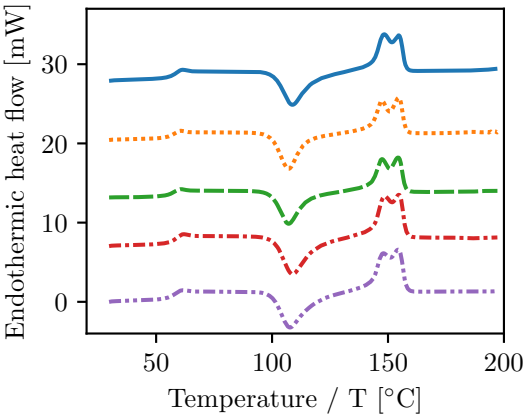

(a) Five XRD samples.

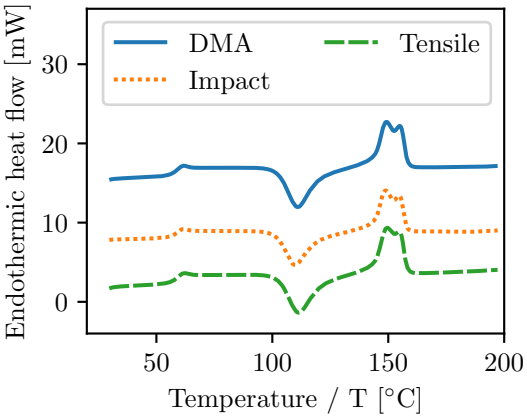

(b) Tensile, impact and DMA samples.

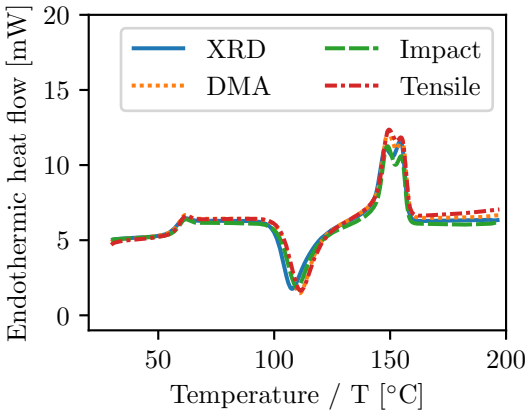

(c) Comparison of all samples.

Figure 31: The DSC results of the five XRD samples, one DMA sample, one impact sample and one tensile sample for the comparison experiment.

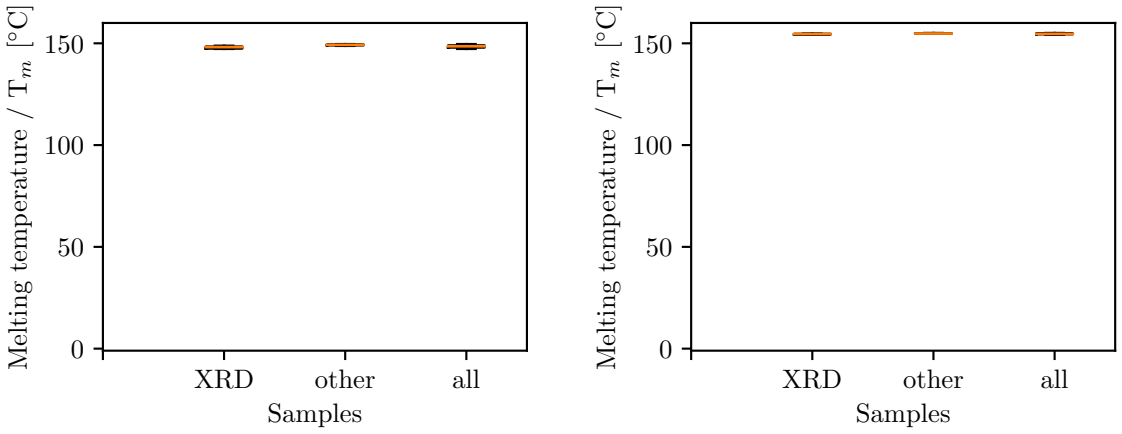

(a) First melting peak.

(b) Second melting peak.

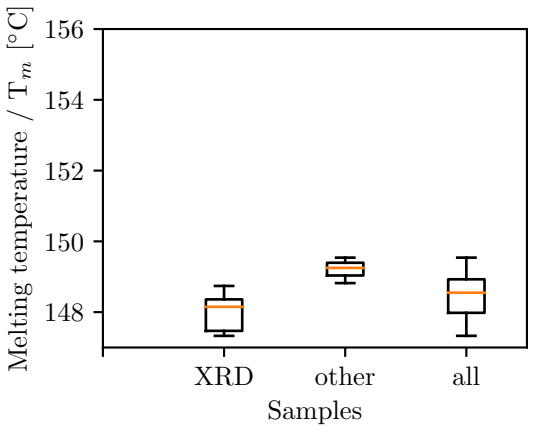

(c) First melting peak enlarged.

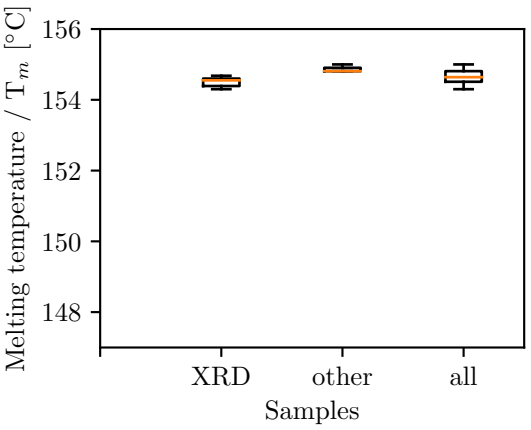

(d) Second melting peak enlarged.

Figure 32: The box and whisker plots of the two melting peaks for the samples shown in Figure 31 on full scale and enlarged.

The DMA results were inconclusive. Three samples were tested but results where not repeatable, because the samples came loose from the machine clamps at temperatures close to their T_g. Despite many attempts to test printed samples as well as the filament with different sample clamps and analysis methods, samples still came loose. The clamps were modified with sanding paper to provide more grip, and spring washers were added to the clamp assemblies to keep them locked, but to no avail. To ensure that this problem was not only occurring for the high clay loading of 10LDH_PLA, different clay loadings and printer settings were tested as well. The problem persisted. The samples cannot maintain their shape and form under the pressure exerted by the clamps when it approaches the T_g. It is proposed that as the sample approaches its glass transition, the rigid amorphous fraction in the composite has absorbed enough energy to re-orientate between the amorphous and crystalline fractions, and that this causes the deformation of the samples under the pressure exerted by the clamps. This would explain why the samples come loose from the clamps. Figure 33a shows how the filament still came loose from the clamps despite the modification with sanding paper, forming shavings. Figure! 33b shows how the sample gave way under pressure from the clamps.

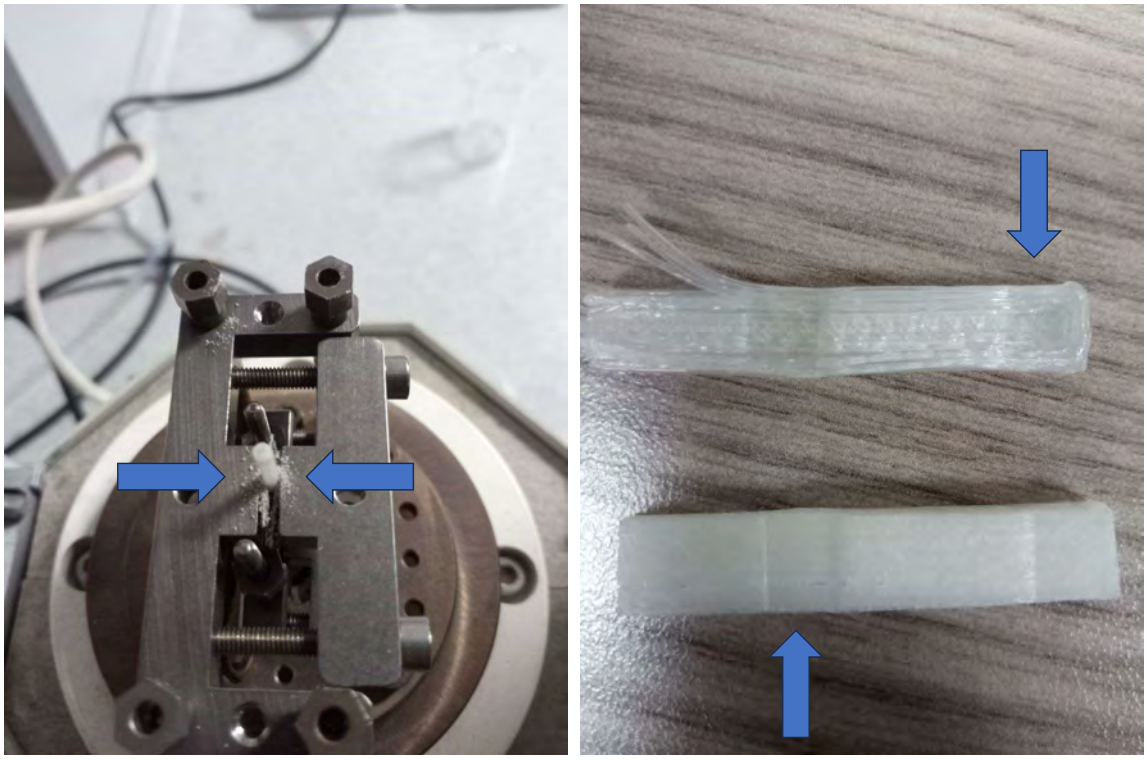

(a) Shavings despite clamps with sanding paper. **(b)** DMA samples after giving way to clamps.

Figure 33: Images showing one of the modifications tried to complete DMA and how the RAF gives way under pressure from the clamps.

4.4 Augmented screening experiment

The screening experiment was augmented to obtain more degrees of freedom so that a model can be fitted. Only single replications were used for this second block of the screening experiment, because it is ineffective and inefficient to use five replications per experimental point for a screening experiment. This will be illustrated and justified in the discussion on the proper use of statistics in § 4.8. Five centre point replications and two replications on one experimental point was used in order to properly calculate the LoF as well as pure and experimental errors. The observations of the tensile specimens after printing but before testing were as follows. The five centre runs were very similar to one another, save for se_61, which had a rougher surface than the others. The repeats of experiment 10, se_58 and se_71, had no visual differences. The rest of the runs had visual differences depending on the LDH loading, the infill density used and the other parameters or combinations thereof. The same comments made about the fracture locations of the specimens in the screening experiment applies. No visual differences between runs in the same experiment were observed for the printed impact samples, although differences between experiments could easily be distinguished.

Appendix B contains images of all the test specimens, an ANOVA table for a statistical analysis conducted on data with outliers and summaries of some DSC properties. These are not necessary to follow the results within this section, but might be of interest to the reader.

4.4.1 Tensile stress

The ANOVA results of the augmented experiment allowed the estimation of all two way interactions and quadratic effects. The least significant quadratic and interaction effects were removed from the model one by one until all of those that remained were statistically significant on a confidence interval of 95 %, *i.e.* $\alpha = 0.05$. The summary of the σ ANOVA is given in Table 20. Note the extra factor added to detect any differences between the two blocks, and that it did not have any statistical significant effect. The LoF is also statistically insignificant. All the other inscriptions are statistically significant, except for factors A and B. These are not removed from the table due to both factors being present in the significant interactions. As a matter of interest, the outliers were included in the same procedure described above. The ANOVA results of the data set including the outliers can be found in the appendix (Table B.9). The conclusions are almost exactly the same as without the outliers, with the p-values changing slightly. The only considerable difference between the two ANOVA tables is that the C^2 term is barely insignificant with

a p-value of 0.068. Outliers do not have a large effect on responses, especially when factors over a wide range have been selected as is the case here (Montgomery, 2013: 267 - 268). This fact is frequently used in unreplicated experiments.

Table 20: The ANOVA table of the results of the augmented screening experiment with tensile stress as response factor.

Source of variation	Sum of squares	Degrees of freedom	F ratio	p value
Model	1 313.4441	9	25.7743	<0.0001
Block	7.4991	1	1.3244	0.2548
A	5.9133	1	1.0444	0.3113
B	0.0374	1	0.0066	0.9355
C	682.8909	1	120.6059	<0.0001
D	97.9375	1	17.2968	0.0001
AB	41.0533	1	7.2504	0.0094
AC	372.6945	1	65.8219	<0.0001
BC	32.5811	1	5.7542	0.0199
C^2	23.0557	1	4.0719	0.0485
Lack of fit	59.2092	9	1.1999	0.3182
Pure error	252.2010	46		
Total error	311.4192	55		

A regression model given in Equation 25 was fitted to the statistically significant effects A, B, C, D, AB, AC, BC and C^2 on the data without outliers with σ in MPa, A in mm, B in °C, C in % and D in %. The coefficients of the effects cannot be used to judge the contribution of each factor to the response, since the model is based on the actual values of the factors. For example, the coefficient of layer height is larger than that of nozzle temperature because the former varies between 0.18 and 0.42, whereas the latter varies between 190 and 220. Rather, Table 20 should be used, because the ANOVA analysis yields comparable results.

$$\begin{aligned}\sigma = 21.670 &- 2.7893\ \mathrm{A} + 6.3712 \times 10^{-4}\ \mathrm{B} + 0.10344\ \mathrm{C} - 0.39071\ \mathrm{D} \\ &+ (\mathrm{A} - 0.30600)(0.57201\ \mathrm{B} - 117.14) \\ &+ (\mathrm{A} - 0.30600)(-0.66160\ \mathrm{C} + 31.808) \\ &+ (\mathrm{B} - 204.79)(0.0015243\ \mathrm{C} - 0.073\ 285) \\ &+ (0.044545 - 9.2654 \times 10^{-4}\ \mathrm{C})(\mathrm{C} - 48.077)\end{aligned} \tag{25}$$

Using JMP, the optimum point for σ was determined by using a maximising desirability function in the simulator, whilst adding random variation for the four factors based on the variation already present in the system. The optimum point was determined as 31.804 MPa. The factor values converged to one of the alternate factorial points with

the factors A to D at 0.18 mm layer height, 190 °C nozzle temperature, 90 % infill density and 2 % LDH loading. JMP does not allow the extrapolation of the model outside the limits of the factors of the experiment. It is therefore plausible that the optimum lies outside the experimental region. Since the optimum was predicted at the low levels of layer height, nozzle temperature and LDH loading, but the high level of infill density, this could be at even lower levels of the three former factors and a higher level of the latter. However, the practicality of decreasing or increasing factors have to be considered. It is not really possible to decrease layer height or nozzle temperature any further due to printing constraints. A lower layer height is theoretically possible with the 0.6 mm nozzle installed, but would be outside the recommended limits. Similarly, a lower nozzle temperature would cause problems during printing, because the melt would be too viscous, causing blockages in the nozzle and affecting print quality. This was attempted and confirmed at 180 °C for the filled filaments. The other two factors can however still be varied without violating physical constraints. Accordingly, a rotational CCD in the region of the optimum was designed, with layer height and nozzle temperature fixed at the optimum levels and varying the other two factors in the region of the predicted optimum.

4.4.2 Normalised tensile stress

The $\hat{\sigma}$ ANOVA table for the augmented design is shown in Table 21. The outliers on the new response were identified, and differed from those in the σ data. The data without the outliers was used. The statistically significant factors are exactly the same as for the tensile stress, save for the exclusion of the quadratic effect of the infill density, *i.e.* C^2. Therefore, a model with only main and interaction effects results. Dramatic changes in the significance of the main effects are observed, with the layer height and nozzle temperature increasing their effects by a large margin, and the infill density decreasing its effect considerably. It seems as if normalising σ removes a mask on the effect that factors have on the response, and thus gives a better representation of how the other factors influence it. This is compared to the σ analysis where the infill density dominated the other factors and their effects so that it may be concluded that they have a minimal effect. The LDH loading remained significant regardless the response, indicating that it does indeed have a large effect on the strength of parts, regardless how this strength is defined.

The model fitted on the significant effects A, B, C, D, AB, AC and BC are given in Equation 26.

Table 21: The ANOVA table of the results of the augmented screening experiment with normalised tensile stress as response factor.

Source of variation	Sum of squares	Degrees of freedom	F ratio	p value
Model	7.5849	8	17.3234	<0.0001
Block	0.1868	1	3.4126	0.0699
A	0.7455	1	13.6209	0.0005
B	0.5023	1	9.1784	0.0037
C	0.0522	1	0.9540	0.3328
D	4.7869	1	87.4632	<0.0001
AB	0.6104	1	11.1538	0.0015
AC	0.6076	1	11.1014	0.0015
BC	0.4372	1	7.9892	0.0065
Lack of fit	0.4997	10	0.8965	0.5436
Pure error	2.6199	47		
Total error	3.1196	57		

$$\begin{aligned}\hat{\sigma} = 4.9038 &- 1.0520\ \mathrm{A} - 0.0069796\ \mathrm{B} - 0.0010873\ \mathrm{C} - 0.085034\ \mathrm{D} \\ &+ (\mathrm{A} - 0.30409)(0.068224\ \mathrm{B} - 13.987) \\ &+ (\mathrm{A} - 0.30409)(-0.026628\ \mathrm{C} + 1.2971) \\ &+ (\mathrm{B} - 205.02)(1.734\ 0 \times 10^{-4}\ \mathrm{C} - 0.0084468)\end{aligned} \tag{26}$$

with $\hat{\sigma}$ in MPa g^{-1}, A in mm, B in °C, C in % and D in %. The maximising desirability function converged to the same combination of factors as for the tensile stress, namely 0.18 mm layer height, 190 °C nozzle temperature, 90 % infill density and 2 % LDH loading. The predicted value for $\hat{\sigma}$ was 3.3074 MPa g^{-1}. This is the same combination of factors at the optimum as predicted for σ, *i.e.* the statistics yielded the same answer despite the normalisation and the different contributions of the respective factors. This is especially noteworthy for infill density because not only did the quadratic term disappear, but the main effect's contribution is also substantially less significant than before.

4.4.3 Tensile force

The ANOVA table applied to the tensile force is given in Table 22. The same factors as those in the σ ANOVA are still statistically significant and the infill density is still the only factor with a quadratic effect. This indicates that despite the few specimens that did not break inside of the narrow parallel section as they should have, the statistical conclusion remains unchanged. This result supports the claim made that the location of the fractures are not a result of the material strength, processing or testing techniques, but rather of

the slicer settings. If the fracture location depended only on the material properties, then it would have fractured in the thin parallel section where the cross sectional area was the smallest. However, due to the slicer software starting the print of each layer at the same point more often than not, a weak point in the specimen results, and it fractures at that point. This is an error in the slicer software, since both the point where the walls and the infill starts to print were randomised. The model fitted to the significant effects A, B, C, D, AB, AC, BC and C^2 is given in Equation 27 with F in kN, A in mm, B in °C, C in % and D in %.

Table 22: The ANOVA table of the results of the augmented screening experiment with tensile force as response factor.

Source of variation	Sum of squares	Degrees of freedom	F ratio	p value
Model	2.5768	9	31.5647	<0.0001
Block	0.0050	1	0.5483	0.4621
A	0.0105	1	1.1617	0.2857
B	0.0005	1	0.0598	0.8077
C	1.4271	1	157.3399	<0.0001
D	0.0930	1	10.2478	0.0023
AB	0.0995	1	10.9710	0.0016
AC	0.7387	1	81.4427	<0.0001
BC	0.0447	1	4.9250	0.0305
C^2	0.1353	1	14.9141	0.0003
Lack of fit	0.1050	9	1.3613	0.2327
Pure error	0.5080	56		
Total error	3.0848	65		

$$\begin{aligned} \mathrm{F} = {} & 0.94330 - 0.12250\ \mathrm{A} - 1.9672 \times 10^{-4}\ \mathrm{B} + 0.0047172\ \mathrm{C} - 0.011693\ \mathrm{D} \\ & + (\mathrm{A} - 0.30409)(0.027\,538\ \mathrm{B} - 5.6581) \\ & + (\mathrm{A} - 0.30409)(-0.028589\ \mathrm{C} + 1.3580) \\ & + (\mathrm{B} - 205.47)(5.7008 \times 10^{-6}\ \mathrm{C} - 0.0027079) \\ & + (\mathrm{C} - 47.500)(-6.5576 \times 10^{-6}\ \mathrm{C} + 0.0031149) \end{aligned} \tag{27}$$

The maximising desirability function converged to the same combination of factors for the optimum point as before, namely 0.18 mm layer height, 190 °C nozzle temperature, 90 % infill density and 2 % LDH loading. The predicted value for F was 1.3327 kN. The implication of the F model converging to the same set factor levels as the σ model is significant. Statistically speaking, there is no difference between the two. This justifies the use of σ, which allows the calculation of E.

4.4.4 Normalised tensile force

Similar to $\hat{\sigma}$, normalising F to mass makes the C^2 interaction insignificant, and increases the significance of the other factors, as shown in Table 23. Equation 28 shows the fitted model to the significant effects A, B, C, D, AB, AC and BC with $\hat{F}$ in kN g^{-1}, A in mm, B in °C, C in % and D in %.

Table 23: The ANOVA table of the results of the augmented screening experiment with normalised tensile force as response factor.

Source of variation	Sum of squares	Degrees of freedom	F ratio	p value
Model	0.012198	8	19.7276	<0.0001
Block	0.000273	1	3.5288	0.0654
A	0.001569	1	20.2986	<0.0001
B	0.000710	1	9.1841	0.0037
C	0.000047	1	0.6072	0.4391
D	0.006123	1	79.2226	<0.0001
AB	0.001259	1	16.2942	0.0002
AC	0.001808	1	23.3911	<0.0001
BC	0.000749	1	9.6883	0.0029
Lack of fit	0.000891	10	1.1913	0.7883
Pure error	0.003515	47		
Total error	0.004405	57		

$$\begin{aligned}\hat{F} = {} & 0.19703 - 0.048223\ A - 0.00026017\ B - 0.000034703\ C - 0.0030268\ D \\ & + (A - 0.30045)(0.0030850\ B - 0.63108) \\ & + (A - 0.30045)(-0.0014521\ C + 0.070735) \\ & + (B - 204.56)(7.3168 \times 10^{-6}\ C - 0.00035641)\end{aligned} \tag{28}$$

The maximising desirability function yielded the same combination of factors for the optimum response as before, *i.e.* 0.18 mm layer height, 190°C, 90 % infill and 2 % LDH. The response was predicted as 0.13797 kN g^{-1}.

The fact that all the tensile strength properties, σ, $\hat{\sigma}$, F and $\hat{F}$, all converged to the same levels of the four experimental factors emphasise the power of statistics. Even though statistics are blind to what the response and factors are, and how they influence one another, the conclusion remains exactly the same. This highlights the impartiality and indifference of statistics.

Furthermore, the results have essentially been proven four times over. It is thus highly unlikely that any mistakes was made during processing, experimentation or testing. Sim-

ilarly, it is also unlikely that the conclusion about the fracture location being a function of the slicer software is wrong. If the fracture location made the stress results unreliable, it would definitely be observed in the results of the models and the convergence to the optimum point. Additionally, normalising with respect to mass increased the contribution of other printing parameters in both $\hat{\sigma}$ and $\hat{\mathrm{F}}$. Especially in FDM where infill density is a property often varied, it is important to consider the implications, which are that a lower layer height and nozzle temperature do indeed have an effect on the part strength, and that it would be wiser to operate in this region when stronger parts are required. As shown in the literature investigation these conclusions cannot necessarily be extrapolated to other materials, and are applicable specifically to PLA and LDH in this case. It should be confirmed for other polymers with LDH, or PLA with other fillers.

Two important and unbiased conclusions can be drawn. Firstly, the fracture location on tensile specimens are not a material property, and therefore tensile stress can be used as a response. Secondly, normalising with respect to mass yields more information on the effect of factors other than infill density without changing the final conclusion.

4.4.5 Strain at break

Even though a model was already proposed from the screening experiment data in § 4.2.7, it was considered worthwhile to analyse ϵ_b for the augmented experiment as well to confirm if the model still holds with the added experimental points. More factors seem to influence ϵ_b when the larger data set is used, but a much simpler model still results compared to the other responses. The ANOVA table is shown in Table 24. There are still no quadratic effects and the LDH loading still remains the most significant factor. A significant interaction between layer height and LDH loading is also observed, along with a significant effect from nozzle temperature. The resulting model to the significant factors A, B, D and AD is given in Equation 29 with ϵ_b in mm mm^{-1}, A in mm, B in °C and D in %.

$$\begin{aligned}\epsilon_b = 0.02522 - 0.0033603\ \mathrm{A} - 4.3555 \times 10^{-5}\ \mathrm{B} - 5.9027 \times 10^{-4}\ \mathrm{D} \\ + (\mathrm{A} - 0.30549)(0.0010765\ \mathrm{D} - 0.0066410)\end{aligned} \tag{29}$$

The optimising desirability function converges to the set of factor levels of 0.18 mm layer height, 190 °C and 2 % LDH loading. Note that infill density does not affect ϵ_b in this case. An optimum value for ϵ_b of 0.015723 mm mm^{-1} is predicted, which deviates only 0.001149 mm mm^{-1} from the optimum determined from the much simpler model

Table 24: The ANOVA table of the results of the augmented screening experiment with strain at break as response factor.

Source of variation	Sum of squares	Degrees of freedom	F ratio	p value
Model	0.00029830	5	20.1443	<0.0001
Block	0.00000062	1	0.2098	0.6485
A	0.00000806	1	2.7230	0.1037
B	0.00002085	1	7.0416	0.0100
D	0.00026061	1	87.9980	<0.0001
AD	0.00001240	1	4.1856	0.0448
Lack of fit	0.00003627	13	0.9285	0.5312
Pure error	0.00015624	52		
Total error	0.00019250	65		

in Equation 24; this indicates that the latter model is sufficient and can be used to a satisfactory accuracy.

4.4.6 Young's modulus

The E ANOVA table is given in Table 25. The statistically significant factors differ from the pattern observed before, with both layer height and infill density having quadratic effects. Moreover, AB is not significant any more, but the AC interaction becomes significant. The model fitted to the statistical significant factors A, B, C, D, AC, AD, BC, A^2 and C^2 is shown in Equation 27 with E in GPa, A in mm, B in °C, C in % and D in %.

Table 25: The ANOVA table of the results of the augmented screening experiment with Young's Modulus as response.

Source of variation	Sum of squares	Degrees of freedom	F ratio	p value
Model	11.196755	10	13.3338	<0.0001
Block	0.123327	1	1.4687	0.2311
A	0.054586	1	0.6500	0.4238
B	0.045873	1	0.5463	0.4632
C	2.639952	1	31.4383	<0.0001
D	1.739152	1	20.7110	<0.0001
AC	3.396923	1	40.4528	<0.0001
AD	0.499230	1	5.9452	0.0183
BC	1.792273	1	21.3436	<0.0001
A^2	0.339142	1	4.0387	0.0498
C^2	0.438248	1	5.2189	0.0265
Lack of fit	0.452070	8	0.6343	0.7444
Pure error	3.830529	43		
Total error	0.089082	51		

$$\begin{aligned} \mathrm{E} = {} & 1.9305 + 0.256793\ \mathrm{A} - 0.0027015\ \mathrm{B} + 0.0068437\ \mathrm{C} + 0.053851\ \mathrm{D} \\ & + (\mathrm{A} - 0.30242)(3.0866 - 0.064325\ \mathrm{C}) \\ & + (\mathrm{A} - 0.30242)(2.3030 - 0.35696\ \mathrm{D}) \\ & + (\mathrm{B} - 205.74)(5.7533 \times 10^{-4}\ \mathrm{C} - 0.027606) \\ & + (\mathrm{A} - 0.30242)(6.27890 - 20.762\ \mathrm{A}) \\ & + (\mathrm{C} - 47.9839)(2.3242 \times 10^{-4}\ \mathrm{C} - 0.011153) \end{aligned} \tag{30}$$

The maximising desirability function converged to a different combination of factor levels for the optimum point, namely 0.22 mm layer height, 220 °C nozzle temperature, 90 % infill density and 10 % LDH loading. A E of 3.4892 GPa was predicted. It is interesting that response has a different optimum compared to the tensile strength parameters. This is probably due to the modulus being calculated in the elastic region instead of the region

around the fracture point. The fact that it is a ratio of both the tensile strength and the strain is not necessarily the reason, since these properties at break all converged to the same combination of factor levels. Rather, the elastic region behaves differently from the fracture region, causing the alternative optimum point.This would suggest that depending on the material property of interest, different factor levels have to be selected. If ultimate tensile strength or ϵ_b is most important, the low levels of nozzle temperature and LDH loading would be most favourable, whereas the high levels for these factors will be beneficial if a high E is preferred. Layer height would also have to be slightly altered, but its optimum level is still located very near the lower bound of 0.18 mm. The infill density is the only factor whose level remain unchanged, but since it is an indication of the amount of material present, this is no surprise.

4.4.7 Normalised Young's modulus

The $\hat{E}$ ANOVA has one less statistically significant interaction compared to that of E, as shown in Table 26. The quadratic effect of both the layer height and the infill density remains. This is different from the observations after the normalisation of the tensile strengths, which reinforces the notion that the elastic region behaves differently than the ultimate tensile properties. The model fitted to the factors A, B, C, D, AD, BC, A^2 and C^2 is given as Equation 31 with $\hat{E}$ in GPa g^{-1}, A in mm, B in °C, C in % and D in %.

Table 26: The ANOVA table of the results of the augmented screening experiment with normalised Young's Modulus as response.

Source of variation	Sum of squares	Degrees of freedom	F ratio	p value
Model	0.058888	9	5.1052	<0.0001
Block	0.000872	1	0.6802	0.4132
A	0.002267	1	1.7691	0.1892
B	0.007171	1	5.5954	0.0217
C	0.016690	1	13.0221	0.0007
D	0.011301	1	8.8177	0.0045
AD	0.005322	1	4.1523	0.0466
BC	0.020394	1	15.9122	0.0002
A^2	0.006116	1	4.7723	0.0334
C^2	0.014106	1	11.0062	0.0334
Lack of fit	0.012053	9	1.0546	0.4142
Pure error	0.055875	44		
Total error	0.067928	53		

$$\begin{aligned}\hat{\mathrm{E}} = 0.44649 &- 0.06960\ \mathrm{A} - 9.4893 \times 10^{-4}\ \mathrm{B} - 5.2759 \times 10^{-4}\ \mathrm{C} + 0.0042428\ \mathrm{D} \\ &+ (\mathrm{A} - 0.30810)(0.24459 - 0.03758\ \mathrm{D}) \\ &+ (\mathrm{B} - 205.67)(6.1638 \times 10^{-5}\ \mathrm{C} - 0.0029204) \\ &+ (\mathrm{A} - 0.30810)(0.861452 - 2.79629\ \mathrm{A}) \\ &+ (\mathrm{C} - 47.381)(4.0444 \times 10^{-5}\ \mathrm{C} - 0.0019163)\end{aligned} \tag{31}$$

The maximising desirability function converged to an optimum at the factor levels of 0.27 mm layer height, 190 °C nozzle temperature, 10 % infill density and 10 % LDH loading. A $\hat{\mathrm{E}}$ of 378.81 MPa g^{-1} was predicted. Compared to the results from the Young's modulus, the low levels of nozzle temperature and infill density is most beneficial for $\hat{\mathrm{E}}$ whereas their high levels favour E. Even the layer height moves slightly higher so that it is exactly between the low level and the centre point. Only the LDH loading stays constant at 10 %.

4.4.8 Impact energy

The ANOVA table for the impact energy is shown in Table 27. Like with the tensile strengths, the infill density is the only factor with a quadratic effect and all the same interactions are statistically significant, save for AB. It is interesting that a model can be derived for impact energy despite the low precision of the impact machine. Even more interesting is that the resulting model compares so well with tensile results in terms of significant factors. The insignificant interaction might be ascribed to the size of the impact specimens, which are significantly smaller than the tensile samples. This could be due to several reasons, including the cooling time for each strand. The model fitted to the significant effects A, B, C, D, AC, BC and C^2 is given in Equation 32 with ξ in kJ m^{-2}, A in mm, B in °C, C in % and D in %.

$$\begin{aligned}\xi = 2.7184 &+ 0.50479\ \mathrm{A} - 0.0066539\ \mathrm{B} + 0.0043709\ \mathrm{C} - 0.057306\ \mathrm{D} \\ &+ (\mathrm{A} - 0.30955)(0.030263\ \mathrm{C} - 1.4559) \\ &+ (\mathrm{B} - 204.33)(0.00022812\ \mathrm{C} - 0.010974) \\ &+ (\mathrm{C} - 48.106)(0.00034834\ \mathrm{C} + -0.016757)\end{aligned} \tag{32}$$

The maximising desirability function converged an optimum at the combination of factor levels of 0.42 mm layer height, 220 °C nozzle temperature, 90 % infill density and 2 % LDH loading. The predicted value was an impact energy of 2.6464 kJ m^{-2}. The model

Table 27: The ANOVA table of the results of the augmented screening experiment with impact energy as response factor.

Source of variation	Sum of squares	Degrees of freedom	F ratio	p value
Model	11 215 790	8	11.1757	<0.0001
Block	2 707	1	0.0216	0.8837
A	151 400	1	1.2069	0.2766
B	436 275	1	3.4777	0.0674
C	1 284 329	1	10.2379	0.0022
D	2 185 730	1	17.4234	0.0001
AC	825 720	1	6.5822	0.0130
BC	767 820	1	6.1206	0.0164
C^2	4 163 304	1	33.1875	<0.0001
Lack of fit	1 884 923	10	1.6824	0.1133
Pure error	5 265 619	47		
Total error	7 150 542	57		

for ξ converged to a different set of factors for the optimum point compared to the other models considered thus far. It is the first property where the highest layer height are preferred. Moreover the highest level of the nozzle temperature is also most beneficial, similar to what was seen for E. That being said, the infill density and the LDH loading remain the same as for the tensile strength optima. Even though the same factors and interactions where significant, the influence of layer height and nozzle temperature seem to have opposite effects on impact energy and tensile strength.

4.4.9 Normalised impact energy

The $\hat{\xi}$ ANOVA table is shown in Table 28. The quadratic effect of the infill density is still very significant. Instead of this term becoming insignificant as expected, the interaction term between nozzle temperature and infill density became insignificant. Equation 33 shows the fitted model to the significant effects A, B, C, D, AC and C^2 with $\hat{\xi}$ in kJ m^{-2} g^{-1}, A in mm, B in °C, C in % and D in %.

$$\begin{aligned}\hat{\hat{\xi}} = 1.5900 &- 0.097590\ \mathrm{A} - 0.0044607\ \mathrm{B} - 0.0012306\ \mathrm{C} - 0.027820\ \mathrm{D} \\ &+ (\mathrm{A} - 0.30573)(0.018834\ \mathrm{C} - 0.88494) \\ &+ (\mathrm{C} - 46.985)(0.00013666\ \mathrm{C} - 0.0064214)\end{aligned} \tag{33}$$

The maximising desirability function converged to an optimum at the combination of factor levels of 0.18 mm layer height, 190°C, 10 % infill and 2 % LDH loading. The

Table 28: The ANOVA table of the results of the augmented screening experiment with normalised impact energy as response factor.

Source of variation	Sum of squares	Degrees of freedom	F ratio	p value
Model	1 838 945	7	13.5825	<0.0001
Block	8 074	1	0.4174	0.5207
A	7 730	1	0.3997	0.5297
B	209 942	1	10.8545	0.0017
C	102 023	1	5.2748	0.0251
D	555 253	1	28.7077	<0.0001
AC	346 102	1	17.8942	<0.0001
C^2	674 946	1	34.8961	<0.0001
Lack of fit	242 650	11	1.1776	0.3267
Pure error		49		
Total error		60		

response was predicted as 0.93150 kJ m^{-2} g^{-1}. As was the case with E, the normalisation of the impact energy yielded unexpected factor levels at which the optimum occurs. All the factors except LDH loading changed from its high levels to its low levels. It is not clear why this is the case. It might be possible that the normalisation yields different results because the infill density dominates the model when not normalised, because more voids would definitely assist with energy dissipation during impact. Since the tensile strengths al converged to the lower factor levels of layer height, nozzle temperature and LDH loading, it is no surprise that they yield better impact strengths as well.

4.4.10 Characterisation

The second heating curves of the DSCs completed on the printed parts are shown in Figure 34. Excellent repeatability was achieved in the centre runs, although repeatability for the tenth experiment was not outstanding. Even though the variation in the values of the first and second melting temperatures and the melting enthalpy are not as drastic, the double melting peak is not as clear as it should have been. As before, double melting peaks are only observed for LDH loadings larger than 2 %, and there is visible variance in the values of T_g and T_c between different experiments. The violin plots showing how each property varies with each factor individually can be found in the appendix (Figures B.26, B.27, B.28 and B.29). Although differences clearly exist between factor levels, they are not significant enough from a holistic perspective to warrant an in depth discussion, and are therefore only included for interest sake.

Since the same filaments were used in the augmented screening experiment as in the

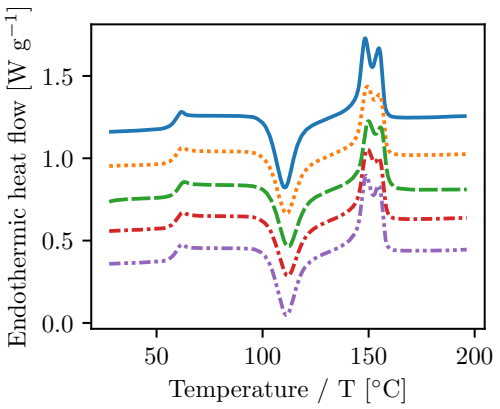

(a) Centre runs.

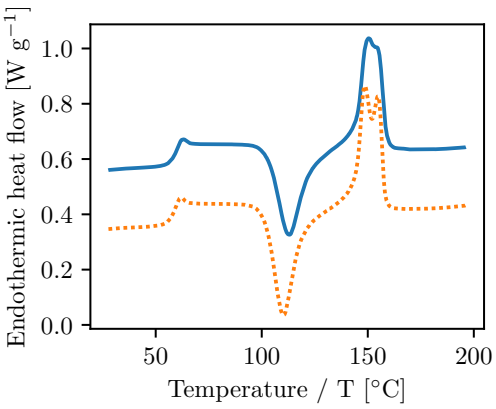

(b) Tenth experiment runs (two repeats).

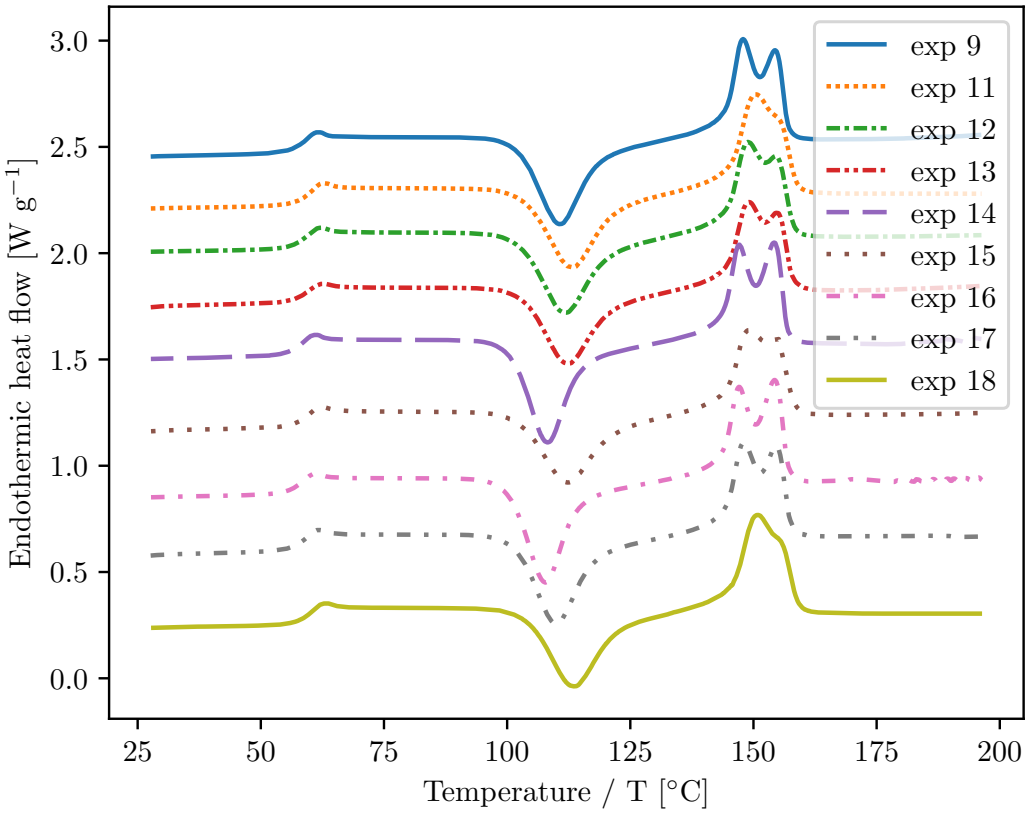

(c) Other experiments (1 repeat each).

Figure 34: The DSC curves of the second heating runs of the tensile specimens printed in the augmented screening experiment.

screening experiment, and only the LDH loading was of interest in the XRD spectra, there are no new observations from XRD analysis.

The FTIR spectra of the tensile specimens printed for the augmented screening experiment are shown in Figure 35. All the peaks that are expected are present with good resolution. Recall that single replications for most experiments where used, with five replications of the centre point and two replications of the tenth experiment. Both the centre runs and the replications of the tenth experiment show very good repeatability. This merely proves that the material did not undergo any changes during printing, and confirms the ANOVA results that there are no changes due to unmeasured factors between the screening and augmented screening experiment.

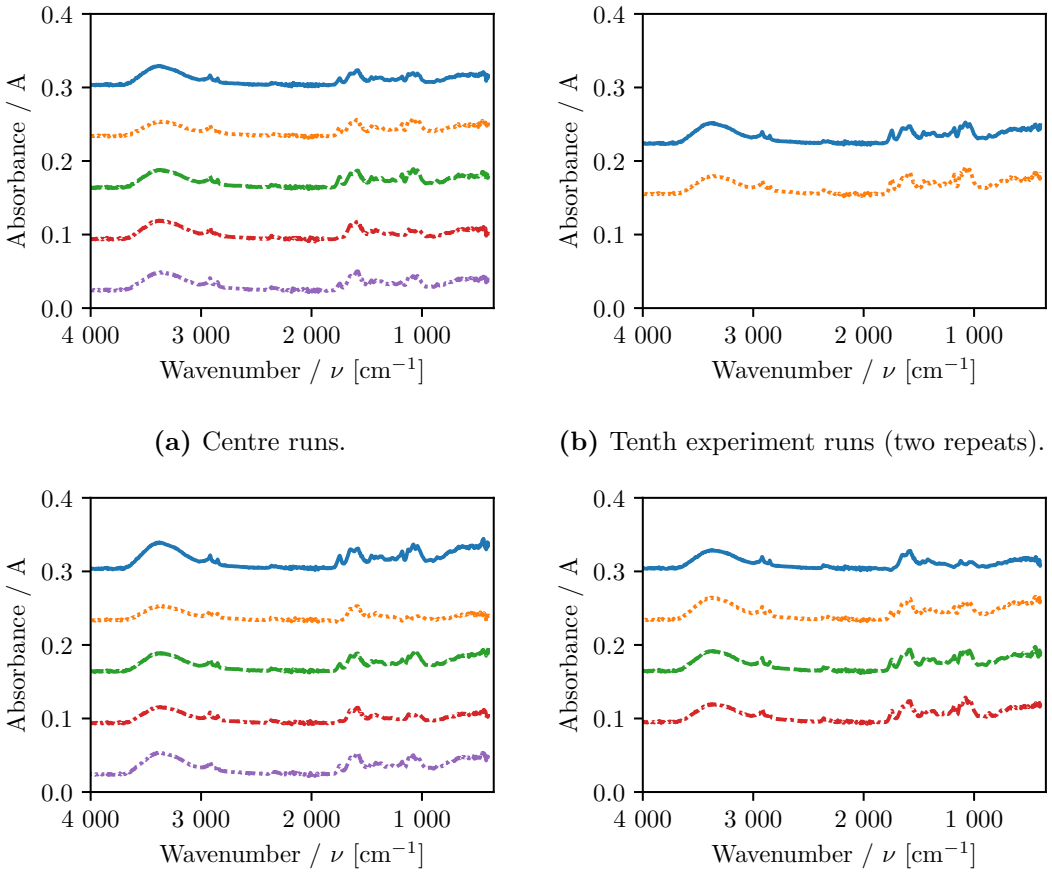

(a) Centre runs.

(b) Tenth experiment runs (two repeats).

(c) Experiments 9, 11, 12, 13 and 14 (1 repeat each).

(d) Experiments 15, 16, 17 and 18 (1 repeat each).

Figure 35: The FTIR results of the tensile specimens printed in the augmented screening experiment.

4.5 Central composite design experiment

A CCD was conducted in the region of the optimum. Since new filament was made for this experiment, it was characterised extensively, after which the analyses on the material properties of printed parts were completed. Because the optimum was expected within this region, and only two factors were tested, it was decided to increase the amount of replications to three per experimental point. Fifteen centre replications were spread throughout the experimental programme, with five at the start, in the middle and at the end respectively. All auxiliary information including images of test specimens as well as the repeat runs for all characterisations are available in Appendix C.

4.5.1 Filament

Recall that the same processing temperatures could not be used in the manufacturing of the filaments for the screening experiment. Although the experimental variation — which included the effect of these processing temperatures — was small enough compared to the variation of the centre points, allowing statistical conclusions to be drawn, it is better to keep as many variables as possible constant. As such, the additional filament made for the CCD was processed at 180 °C. The 2LDH_PLA filament used in the screening experiment was used again in the CCD, but its processing temperatures were the same as those for the CCD. A new 0LDH_PLA filament was made, which was first processed in the compounder before being filament extruded at 180 °C. This was done to give the same temperature and shear history as the other filaments. This is in contrast to the filament produced before, which was merely filament extruded.

A representative summary of the DSC results of the CCD filaments is shown in Figure 36. The DSC analysis was repeated for 2LDH_PLA. It is clear that the formation of the double melting peak only results from LDH loadings larger than 2 %, which compares well to the observations made about the screening experiment filaments. In both cases the formation of a shoulder can be observed on closer inspection. The DSC properties are summarised in Figure 37. Using ANOVA, it was found that within each experiment none of the properties differ in a statistically significant way. Moreover, all the properties differ in a statistically significant manner when compared to LDH loading, indicating that the LDH does have an effect on each response. A general reduction in T_c is observed with a maximum at 0.6 %. A general increase in the absolute value of ΔH_c is also observed, although the enthalpy at 0.6 % LDH loading also deviates significantly from the trend. This suggests that the LDH acts as a nucleating agent, but that at low loadings *i.e.* 0.6 %, it actually prevents cold crystallisation. Moreover, a reduction in both the T_g and T_{m1}

is observed whilst T_{m2} stays relatively constant and ΔH_f increases. The observation on T_{m2} is based on fewer LDH loadings since the formation of the second melting peak only becomes visible at loadings higher than 2 %. The increase in ΔH_f seems to correlate to this second melting peak, which strengthens the proposal that a second $\alpha\prime$ phase forms with higher LDH loadings which has to melt and conform to the stable α phase before the whole compound melts. That being said, observations based on the enthalpies are not put forward with confidence, since they result in negative degrees of crystallinities, which are impossible. This is further discussed in the next section.

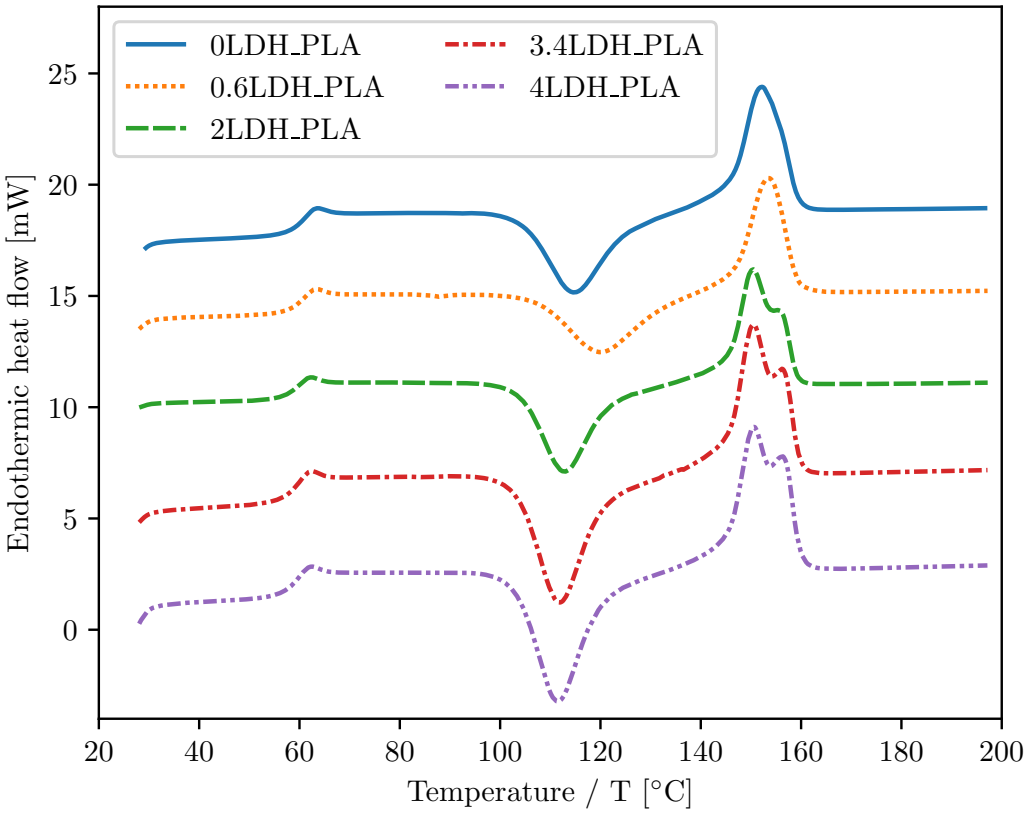

Figure 36: Representative DSC results of the second heating cycle of the filament made for use in the CCD experiment compiled from Figure C.31.

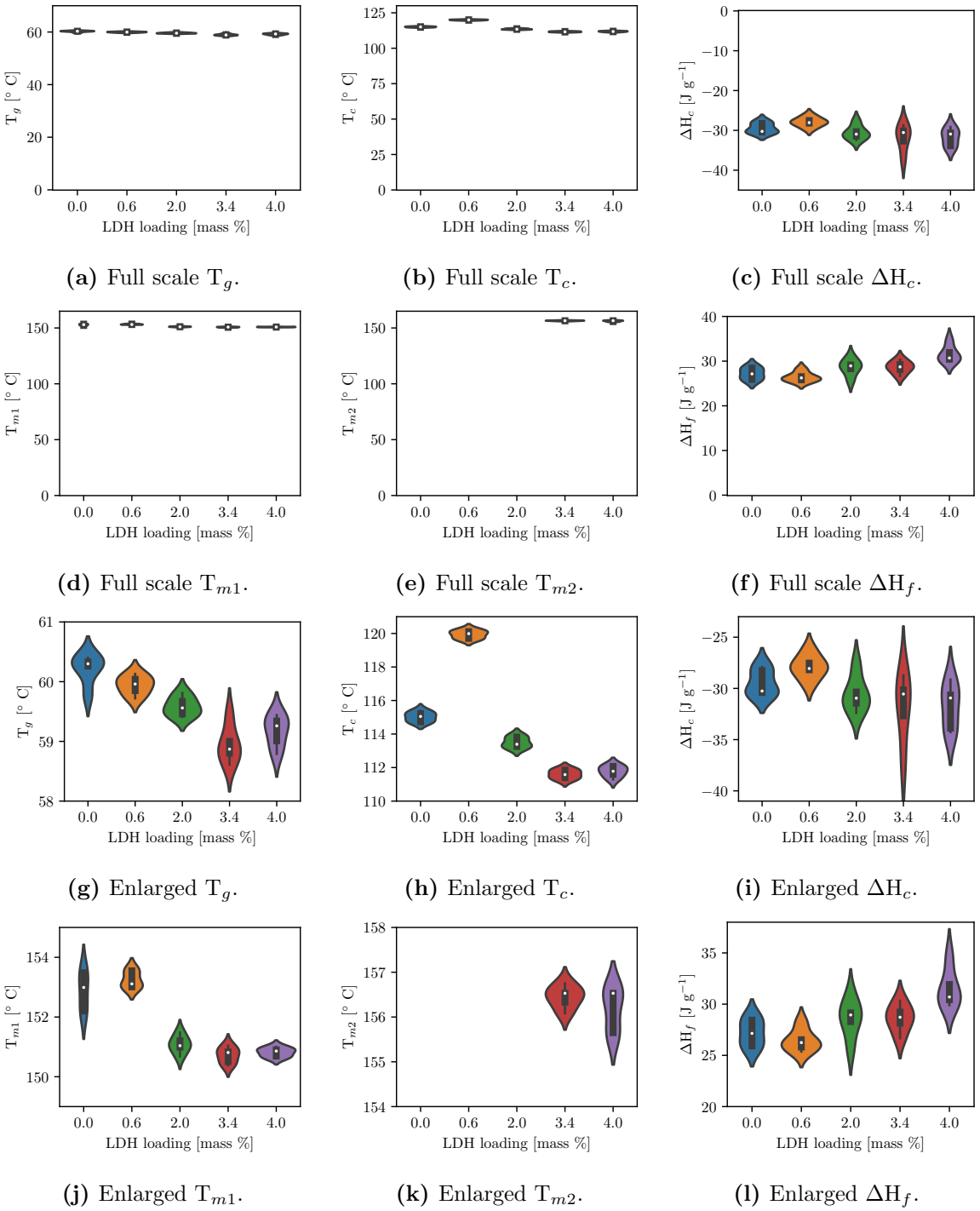

(a) Full scale T_g. **(b)** Full scale T_c. **(c)** Full scale ΔH_c.

(d) Full scale T_{m1}. **(e)** Full scale T_{m2}. **(f)** Full scale ΔH_f.

(g) Enlarged T_g. **(h)** Enlarged T_c. **(i)** Enlarged ΔH_c.

(j) Enlarged T_{m1}. **(k)** Enlarged T_{m2}. **(l)** Enlarged ΔH_f.

Figure 37: The average properties of the respective filaments made for the CCD experiment as determined from DSC.

The XRD spectra is given in Figure 38. In this smaller region of LDH loading, the incorporation of the LDH is not as distinct as was the case with the screening experiment filament. Yet, the characteristic peaks of the LDH can be identified from the 3.4LDH_PLA and 4LDH_PLA spectra, indicating that the LDH is indeed present and that its loading increased in each filament. Considering the general trend from the screening experiment filaments the results here fit quite well. Recall that clear LDH peaks were only being observed from 6LDH_PLA and higher on in the screening experiment. It seems as if the LDH presence only starts to dominate from this region, and that it is still suppressed at 4 % loading.

Contrary to the PLA peaks in the screening experiment, these spectra showed a sharper PLA peak centred at *ca.* 20°. Several repeats have been run to ensure that this is not some anomaly, and the sharper peak persisted. Since the DSC results did not show a significant change in the degree of crystallinities calculated, as already discussed, the sharper peaks cannot be attributed to a more crystalline PLA. The only explanation for this observation is that the granules do not yield a suitable control volume for XRD, and that lower resolution spectra are obtained from such samples. This can also be seen by the different heights of the main PLA peak for each sample measured. Since the XRD was only used to track the LDH peaks in the PLA, this does not affect any conclusions.

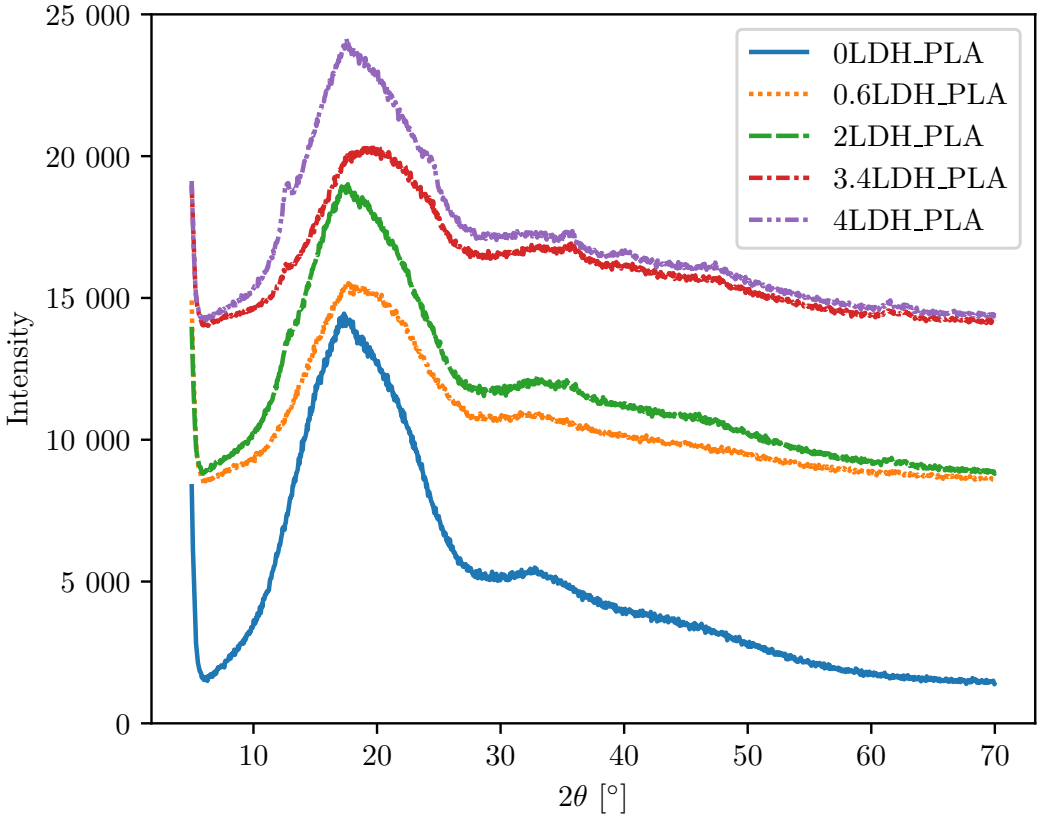

Figure 38: The XRD results of the filament made for use in the CCD experiments.

The representative FTIR spectra of the CCD filament is given in Figure 39. The repeats can be seen in Appendix C. Good repeatability was achieved, except in the first set of centre runs. In these, the broad O−H peak in the LDH centred around 3 412 cm^{-1} are much smaller than normally observed. It is not clear why, since this is not the case for the other ten centre runs. As with the screening experiment's filament, the incorporation of the LDH into the PLA can clearly be followed.

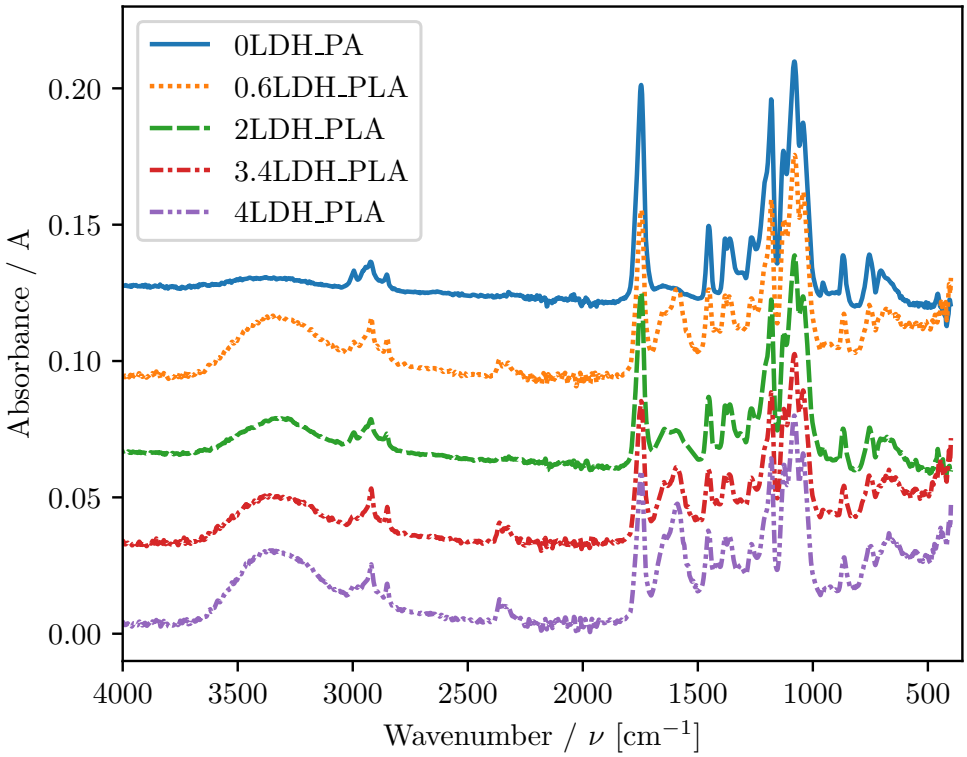

Figure 39: Representative FTIR results of the filament made for use in the screening experiments and the pure LDH compiled from Figure C.32.

Figure 40 shows the SEM images of the CCD filament. The good dispersion of the LDH dispersed in the PLA matrix is again observed. LDH particles are properly wetted. Particles are once again in the micro range, but now the largest ones are smaller than 200 nm. A few agglomerates formed, especially in the 4LDH_PLA, as can be seen in Figure 40o. These are about 400 nm in size. The 3.4LDH_PLA shows much less agglomerates, although particles are getting close together.

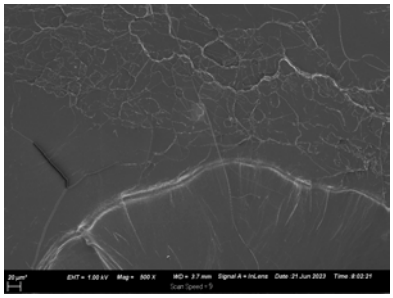

(a) 0LDH_PLA 500×

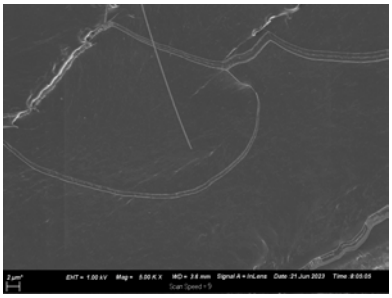

(b) 0LDH_PLA $5\times10^3\times$

(c) 0LDH_PLA $8\times10^4\times$

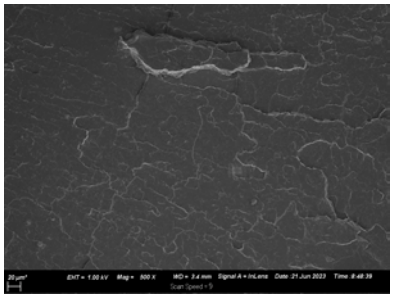

(d) 0.6LDH_PLA 500×

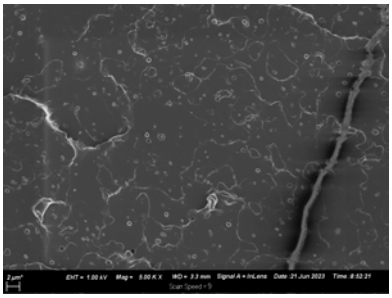

(e) 0.6LDH_PLA $5\times10^3\times$

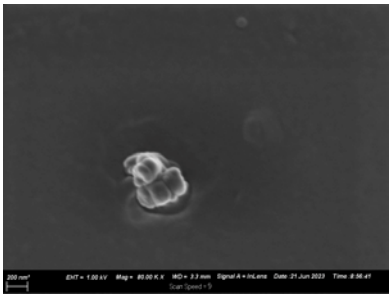

(f) 0.6LDH_PLA $8\times10^4\times$

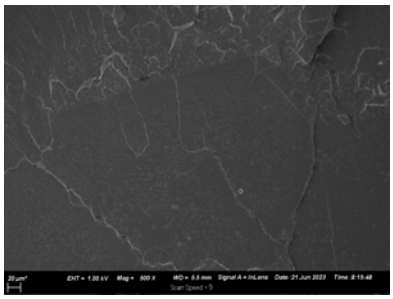

(g) 2LDH_PLA 500×

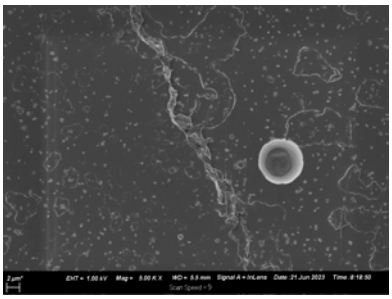

(h) 2LDH_PLA $5\times10^3\times$

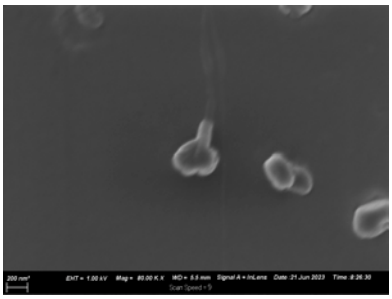

(i) 2LDH_PLA $8\times10^4\times$

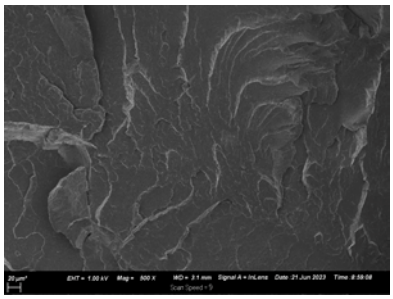

(j) 3.4LDH_PLA 500×

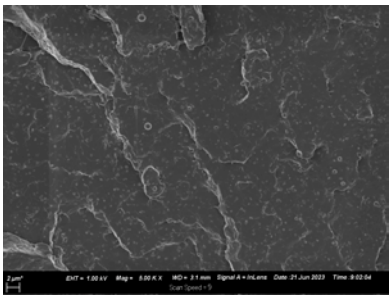

(k) 3.4LDH_PLA $5\times10^3\times$

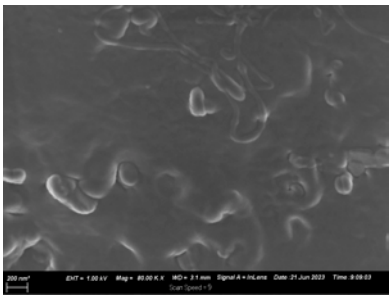

(l) 3.4LDH_PLA $8\times10^4\times$

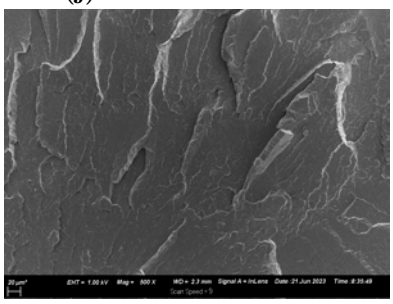

(m) 4LDH_PLA 500×

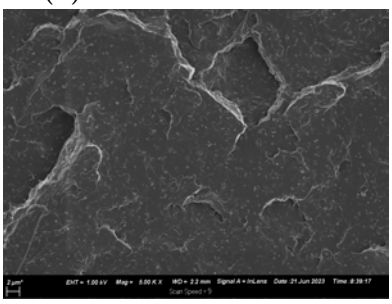

(n) 4LDH_PLA $5\times10^3\times$

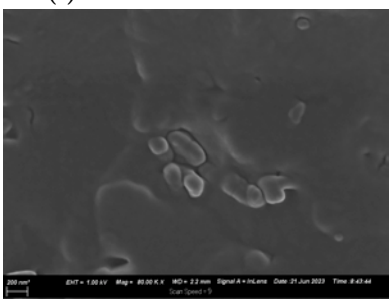

(o) 4LDH_PLA $8\times10^4\times$

Figure 40: The SEM results of the filament made for use in the CCD experiments.

4.5.2 Tensile test samples

The specimens for the CCD after printing but before testing are not shown again for the sake of brevity. The samples after testing can however be found in the appendix (Figure C.30). All samples had a decent surface finish, indicating good printing quality throughout the factors varied. All samples within a certain experiment also showed good uniformity. Regarding fracture locations the same comments as before apply. The only visual difference that could be observed was the different opacities of samples, which increased with LDH loading.

4.5.3 Tensile stress

The stress strain graphs of the CCD specimens are shown in Figure 41. The accompanying box and whisker plot and violin plots are given in Figure 42. The ANOVA of the results indicate that none of the linear, interaction or quadratic effects are statistically significant. Even after removing the least significant effect one at a time, none of the remaining factors become significant. All of the iterations are not shown, but for completeness sake the initial ANOVA table is given in Table 29. It shows that any of the LDH loadings and infill densities within the bounds of the CCD can be used without any impact on the final specimens tensile stress. This includes pure PLA. In terms of applications, this means that up to 4 % LDH can be compounded into PLA, and specimens can be printed with as low as 80 % infill density without affecting the strength of the final specimen. This is beneficial because typically a substance of importance — *e.g.* medicine or a flame retardant — is intercalated into LDH when it is used in a compound. If more LDH can be compounded into PLA then more of the intercalated substance can be added for the final product. Additionally, 80 % infill density will result in less material required for the final product, as well as faster production times compared to higher infill densities.

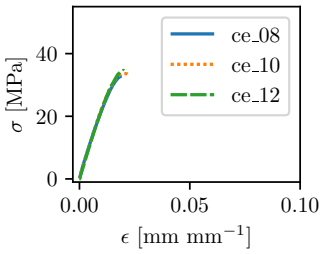

(a) First set of centre runs.

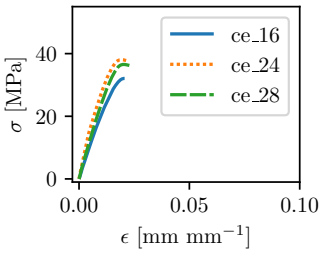

(b) Second set of centre runs.

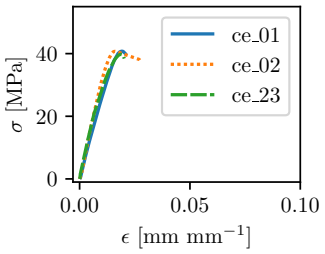

(c) Experiment 2.

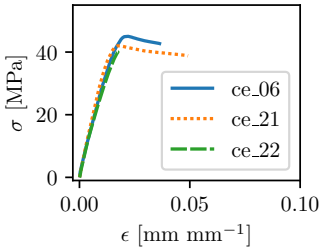

(d) Experiment 3.

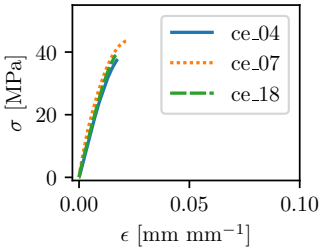

(e) Experiment 4.

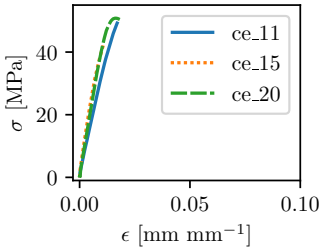

(f) Experiment 5.

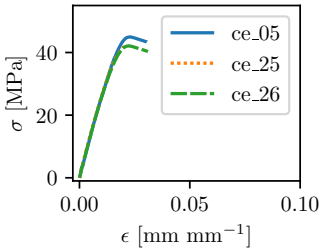

(g) Experiment 6.

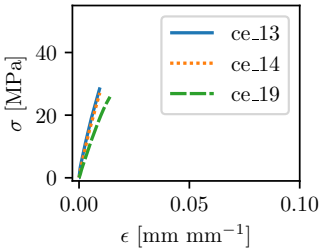

(h) Experiment 7.

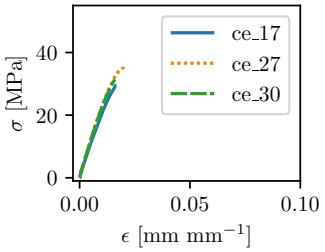

(i) Experiment 8.

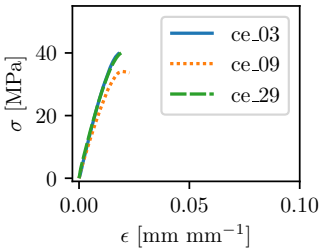

(j) Experiment 9.

Figure 41: The stress strain graphs of all the tensile samples in the CCD experiment.

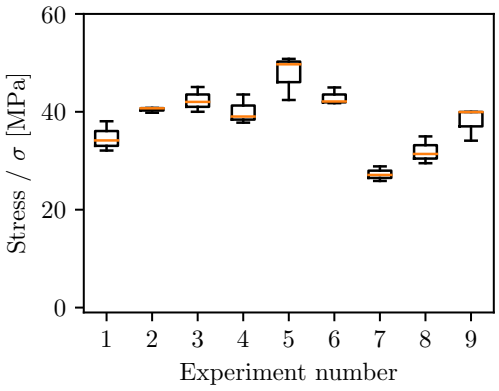

(a) Sorted by experiment.

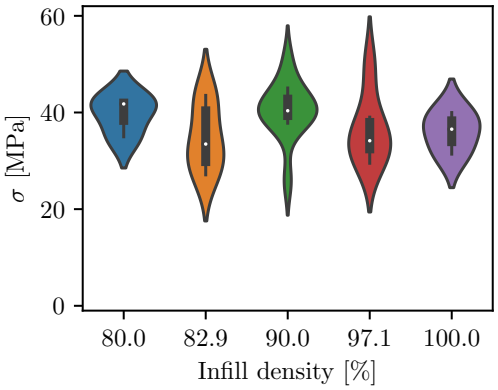

(b) Sorted by infill density.

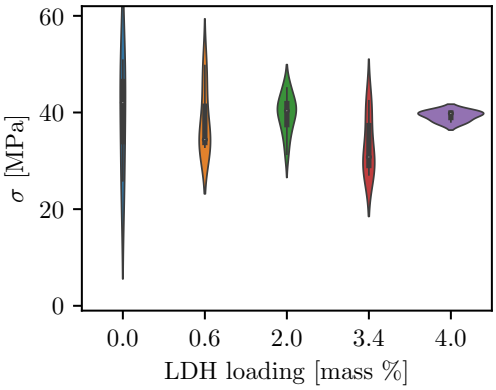

(c) Sorted by LDH loading.

Figure 42: The box and whisker and the violin plots of the stresses recorded in the CCD experiment as a function of experiment number, infill density and LDH loading.

Table 29: The ANOVA table of the results of the CCD experiment with stress as response factor.

Source of variation	Sum of squares	Degrees of freedom	F ratio	p value
Model	144.0662	5	0.7143	0.7143
C	1.3167	1	0.0326	0.8581
D	38.8323	1	0.9627	0.3363
CD	2.3300	1	0.0578	0.8121
C^2	94.5372	1	2.3436	0.1389
D^2	43.3840	1	1.0755	0.3100
Lack of fit	114.6525	3	0.9404	0.4388
Pure error	853.4593	21		
Total error	968.1118	24		

4.5.4 Normalised tensile stress

The $\hat{\sigma}$ results are represented in Figure 43 and the initial ANOVA table is shown in Table 30. Once again, no statistically significant differences are present in the region of the CCD, which means that the mean of the whole region can be regarded as an optimum.

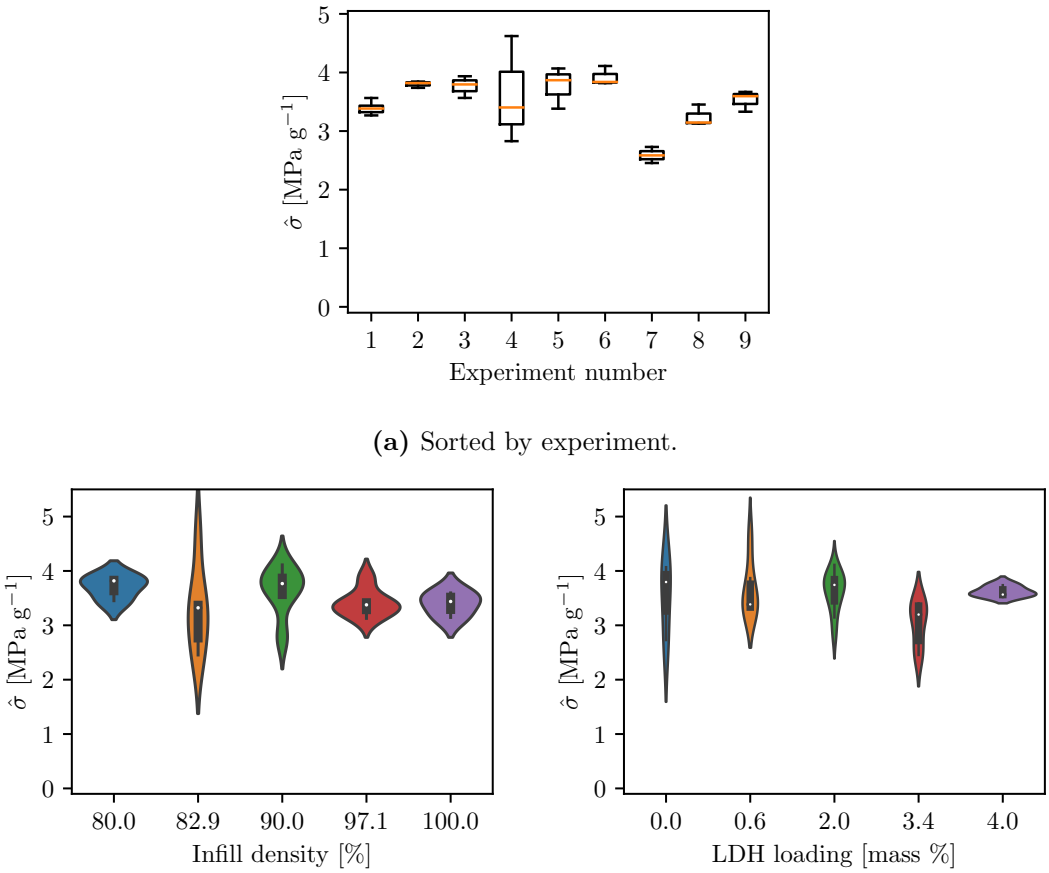

(a) Sorted by experiment.

(b) Sorted by infill density.

(c) Sorted by LDH loading.

Figure 43: The box and whisker and the violin plots of the normalised stresses recorded in the CCD experiment as a function of experiment number, infill density and LDH loading.

Table 30: The ANOVA table of the results of the CCD experiment with normalised stress as response factor.

Source of variation	Sum of squares	Degrees of freedom	F ratio	p value
Model	1.0889080	5	0.9989	0.4395
C	0.0131991	1	0.0605	0.8077
D	0.4465109	1	2.0480	0.1653
CD	0.3346636	1	1.5350	0.2273
C^2	0.2372203	1	1.0881	0.3073
D^2	0.1814345	1	0.8322	0.3707
Lack of fit	1.1644837	3	2.0038	0.1443
Pure error	4.0680255	21		
Total error	5.2325092	24		

4.5.5 Tensile force

The ultimate tensile force instead of the stress was also considered. There are no visible differences between the force strain and stress strain graphs in Figures 44 and 41. This confirms that the fracture locations are not due to material or printing properties but rather due to the slicer software. There is no practical difference between the force and the stress in this situation. The procedure is however repeated to confirm that this is the case for the CCD as well. The tensile force results are shown in Figure 45. Not a single effect of the factors are statistically significant. The initial ANOVA table is given in Table 31. The significance and application of this result remain the same as for σ.

Table 31: The ANOVA table of the results of the CCD experiment with force as response factor.

Source of variation	Sum of squares	Degrees of freedom	F ratio	p value
Model	0.2864455	5	0.6117	0.6919
C	0.0000859	1	0.0009	0.9761
D	0.0617978	1	0.6598	0.4246
CD	0.0279078	1	0.2980	0.5902
C^2	0.1893103	1	2.0212	0.1680
D^2	0.0701510	1	0.7490	0.3954
Lack of fit	0.2028520	3	0.6943	0.5658
Pure error	2.0450574	21		
Total error	2.2479094	24		

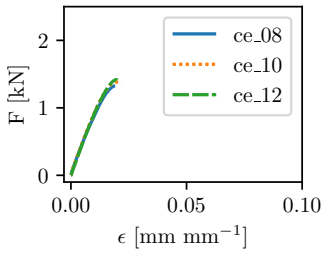

(a) First set of centre runs.

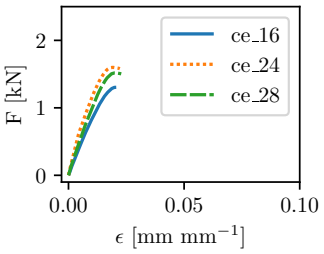

(b) Second set of centre runs.

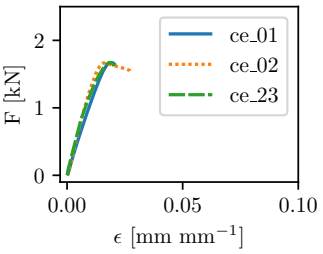

(c) Experiment 2.

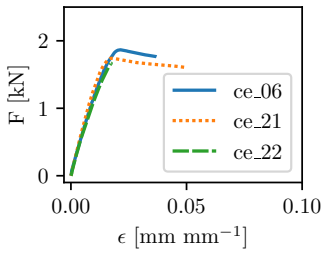

(d) Experiment 3.

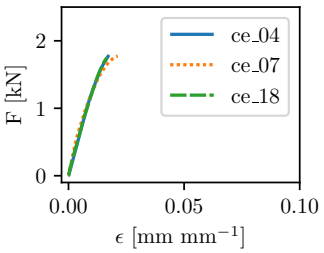

(e) Experiment 4.

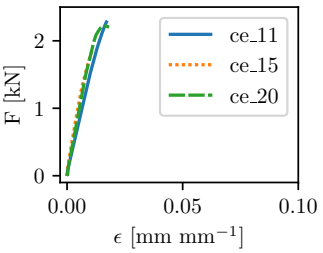

(f) Experiment 5.

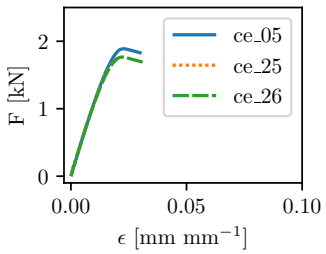

(g) Experiment 6.

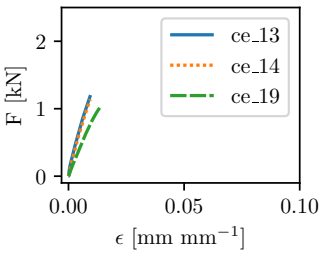

(h) Experiment 7.

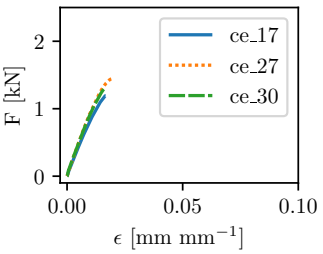

(i) Experiment 8.

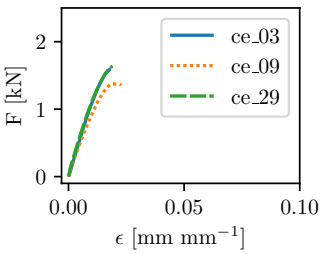

(j) Experiment 9.

Figure 44: The force strain graphs of all the tensile samples in the CCD experiment.

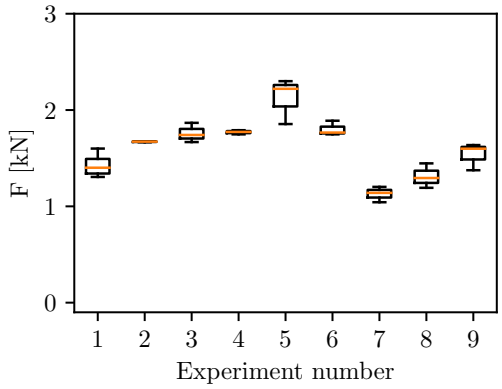

(a) Sorted by experiment.

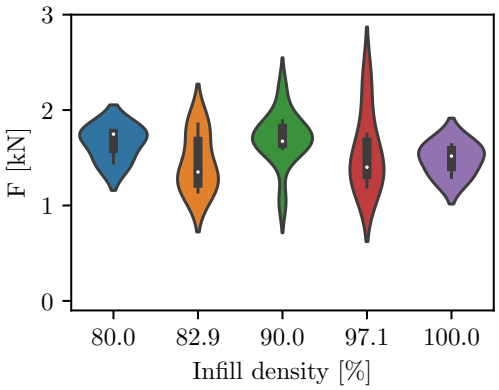

(b) Sorted by infill density.

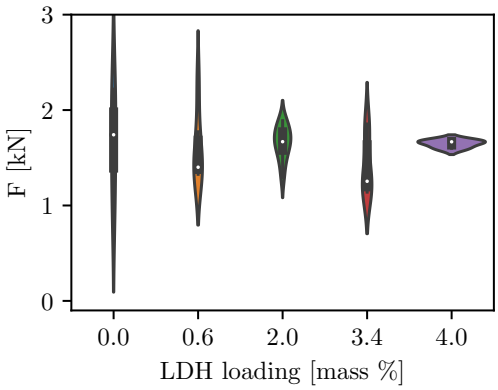

(c) Sorted by LDH loading.

Figure 45: The box and whisker and the violin plots of the forces recorded in the CCD experiment as a function of experiment number, infill density and LDH loading.

4.5.6 Normalised tensile force

The $\hat{F}$ results are shown in Figure 46 and the initial ANOVA table are given in Table 32. Once again, no statistical significant difference could be found between the different experimental points.

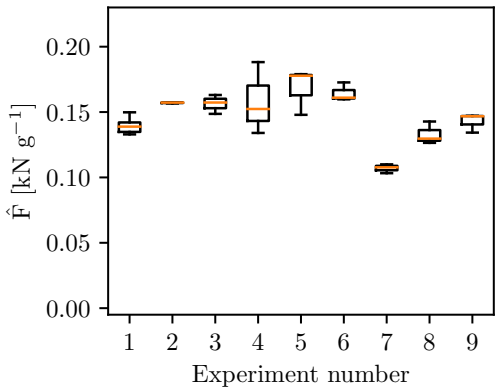

(a) Sorted by experiment.

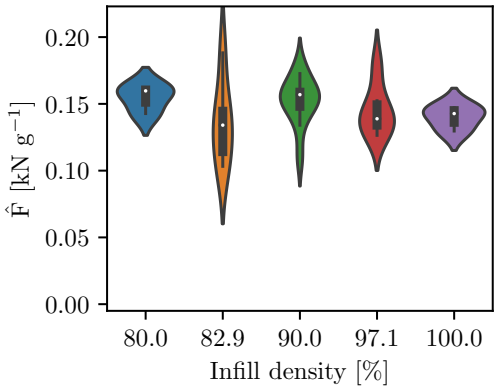

(b) Sorted by infill density.

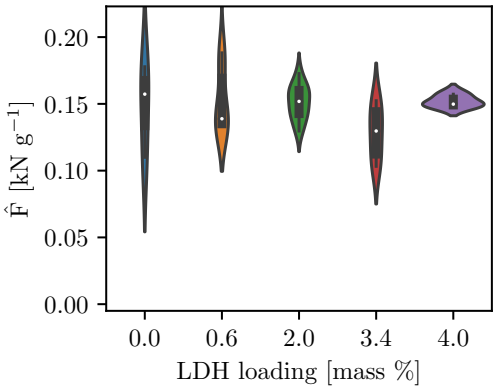

(c) Sorted by LDH loading.

Figure 46: The box and whisker and the violin plots of the normalised forces recorded in the CCD experiment as a function of experiment number, infill density and LDH loading.

Table 32: The ANOVA table of the results of the CCD experiment with normalised tensile force as response factor.

Source of variation	Sum of squares	Degrees of freedom	F ratio	p value
Model	0.00146146	5	0.6781	0.6442
C	0.00000317	1	0.0073	0.9324
D	0.00066864	1	1.5513	0.2250
CD	0.00023008	1	0.5338	0.4721
C^2	0.00049970	1	1.1593	0.2923
D^2	0.00027613	1	0.6406	0.4313
Lack of fit	0.00201779	3	1.6963	0.1984
Pure error	0.00832684	21		
Total error	0.01034463	24		

4.5.7 Strain at break

The ϵ_b results are shown in Figure 47. More variance is visible for the third experiment than in the other experiments. It is also higher than any variance observed for the tensile responses. Despite this, there are still no statistically significant effects when the ANOVA is completed, although the LDH loading would be the only statistically significant effect with a p-value of 0.075 if a 90 % confidence interval was acceptable. Since a 95 % confidence interval is used in this work, a model is not fitted. It is noteworthy that a similar correlation was applicable in the screening experiment. The initial ANOVA table is given in Table 33. Clearly the same conclusions and comments made for the other tensile properties in the CCD still apply, despite the different response. ϵ_b might be important for some applications, and if this is a material property important for a designer, they can achieve a LDH loading of 4 % and an infill density as low as 80 % without affecting ϵ_b.

Table 33: The ANOVA table of the results of the CCD experiment with strain at break as response factor.

Source of variation	Sum of squares	Degrees of freedom	F ratio	p value
Model	0.00041797	5	1.4156	0.2544
C	0.00000009	1	0.0015	0.9696
D	0.00020017	1	3.3897	0.0780
CD	0.00006635	1	1.1236	0.2997
C^2	0.00014125	1	2.3920	0.1350
D^2	0.00006387	1	1.0816	0.3087
Lack of fit	0.00024003	3	1.4273	0.2629
Pure error	0.00117722	21		
Total error	0.00141725	24		

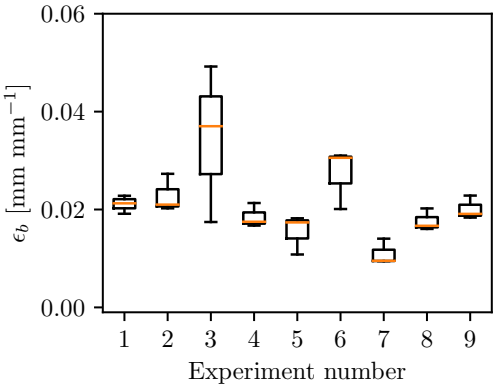

(a) Sorted by experiment.

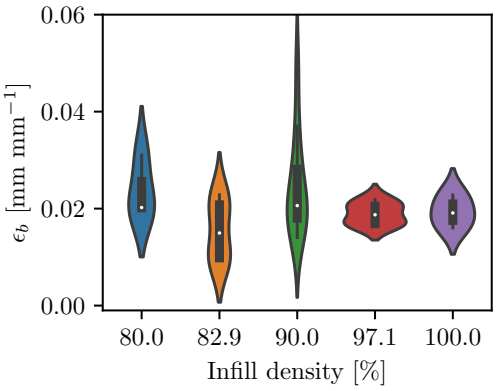

(b) Sorted by infill density.

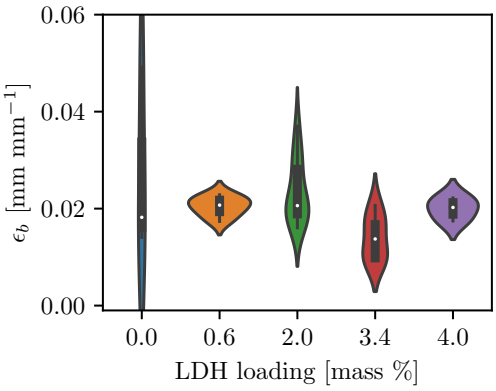

(c) Sorted by LDH loading.

Figure 47: The box and whisker and the violin plots of the strain at break recorded in the CCD experiment as a function of experiment number, infill density and LDH loading.

4.5.8 Young's modulus

The augmented screening experiment predicted a maximum in E in a different region than that tested for with the CCD. Since this property was not the main one considered in this work, E was simply added to give a holistic picture of the mechanical properties in the region considered in the CCD.

The results of E are represented in Figure 48. Contrary to the other responses considered thus far the ANOVA analysis shows a significant LoF for the response when only the significant factors are considered, as detailed in Table 34. This indicates one of two things: either the model is too simple to be fitted or there is an experimental factor that was not considered as part of the model which affects the response. Since a quadratic model is not rudimentary, the latter explanation is probably the case. Since E is not the response that is focused on in this work, further work is not done to find such a factor or factors.

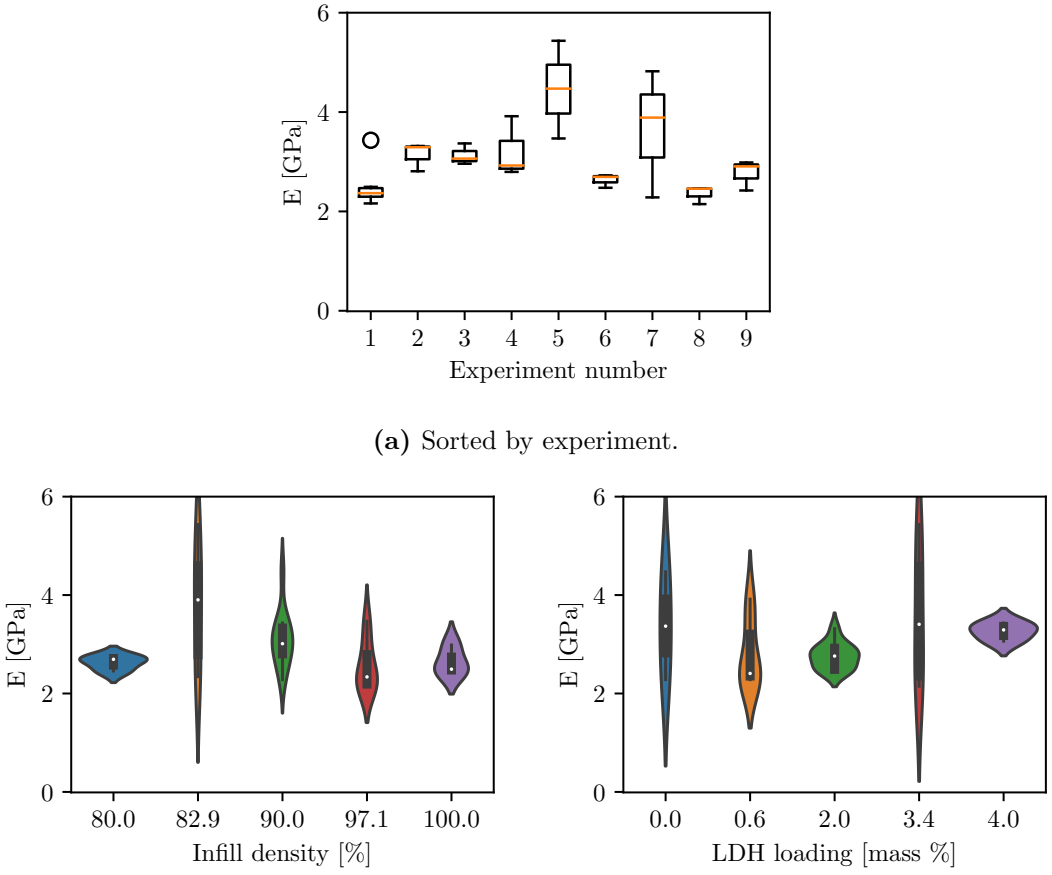

(a) Sorted by experiment.

(b) Sorted by infill density.

(c) Sorted by LDH loading.

Figure 48: The box and whisker and the violin plots of the Young's moduli recorded in the CCD experiment as a function of experiment number, infill density and LDH loading.

Table 34: The ANOVA table of the results of the CCD experiment with Young's modulus as response factor.

Source of variation	Sum of squares	Degrees of freedom	F ratio	p value
Model	6.338816	3	4.4436	0.0120
C	2.267817	1	4.7693	0.0382
D	0.685157	1	1.4409	0.2408
CD	3.385842	1	7.1205	0.0129
Lack of fit	6.338816	5	4.4436	0.0120
Pure error	12.363135	26		
Total error	18.701950	29		

4.5.9 Normalised Young's modulus

Figure 49 summarises the $\hat{E}$ recorded from the CCD. The ANOVA analysis on these results have a statistically significant LoF regardless the combination of effects considered. The initial ANOVA table is shown in Table 35. Although not ideal, this scenario is expected from the discussion on the CCD E, since the variation of the masses recorded is added to the already large variation in experimental points. That being said, it confirms that the material mass does not mask this observation. This shows that a quadratic model with interaction effects cannot be accurately fitted to the response. It might be possible that the large variations in Experiments 4, 5 and 7 are also partly responsible for this large LoF, since clearly the variation in these are larger than that of the centre points (Experiment 1 in Figure 49a). It is not clear what the cause of this might be, since these experiments do not have anything specifically in common. Moreover, runs were randomly ordered, so it cannot be a drift in results. This variation is carried over to the 82.9 °C and 3.4 % data shown in Figures 49b and 49c respectively. Since a similar pattern in variation by experiment is evident from Figure 48a, it is believed that the normalisation simply magnifies the variation and is not the direct cause of it. Therefore it is safe to conclude that some other factor influences $\hat{E}$. The determination of this factor or factors are not part of the scope of this work.

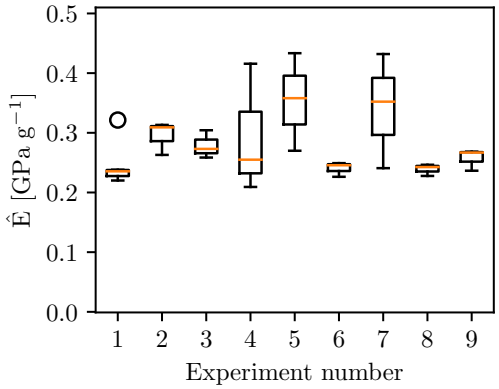

(a) Sorted by experiment.

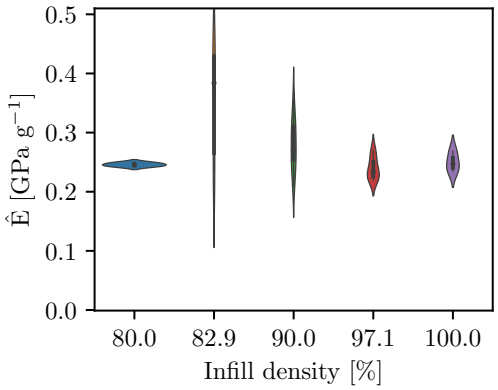

(b) Sorted by infill density.

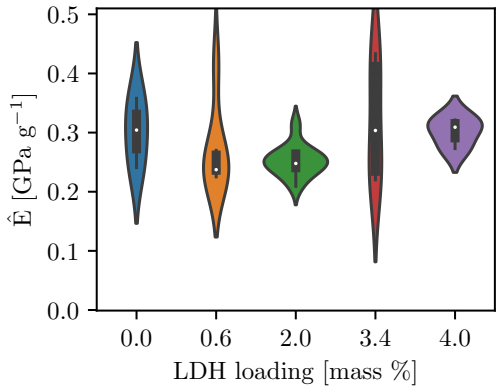

(c) Sorted by LDH loading.

Figure 49: The box and whisker and the violin plots of the normalised Young's moduli recorded in the CCD experiment as a function of experiment number, infill density and LDH loading.

Table 35: The ANOVA table of the results of the CCD experiment with normalised Young's modulus as response factor.

Source of variation	Sum of squares	Degrees of freedom	F ratio	p value
Model	0.04461919	5	3.1118	0.0264
C	0.01784293	1	6.2219	0.0199
D	0.00369154	1	1.2873	0.2678
CD	0.01077149	1	3.7561	0.0645
C^2	0.00001735	1	0.0060	0.9386
D^2	0.01037412	1	3.6175	0.0692
Lack of fit	0.02604872	3	4.2626	0.0169
Pure error	0.04277729	21		
Total error	0.06882601	24		

4.5.10 Impact test samples

The impact specimens showed decent uniformity within each experiment. Despite the slight differences in opacity between samples with different LDH loadings, no other visual changes were observed. All samples broke as they should have, and there are no other observations during the printing or testing processes worth mentioning.

4.5.11 Impact energy

The impact energy model derived in the augmented screening experiment predicted an optimum in a different experimental region than that considered in the CCD. Yet, impact energy was still determined in order to provide a holistic set of mechanical properties in the experimental region. Interestingly, the impact energy shows the same behaviour as the tensile stress in the region of the CCD. This was not the case before in the screening and augmented screening experiments. The results are summarised in Figure 50, and the initial ANOVA table is given in Table 36. Even though the C^2 factor seems statistically significant, it becomes insignificant as soon as the D^2 term is removed, without affecting the LoF. Continuing the process of removing the least significant effect one by one leaves only C with a large p-value, which shows it is also statistically insignificant. This means that regardless of which point in the region of the CCD is selected, the impact strength will stay the same for all statistical purposes. Therefore, impact strength will not be compromised if 4LDH_PLA is used to print a part with 80 % infill.

Table 36: The ANOVA table of the results of the CCD experiment with impact energy as response factor.

Source of variation	Sum of squares	Degrees of freedom	F ratio	p value
Model	2.6008256	5	1.7032	0.1722
C	0.5023285	1	1.6448	0.2119
D	0.1307671	1	0.4282	0.5191
CD	0.0355660	1	0.1165	0.7359
C^2	1.7568482	1	5.7526	0.0246
D^2	0.9008122	1	2.9496	0.0988
Lack of fit	0.5681602	3	0.5882	0.6295
Pure error	6.7614267	21		
Total error	7.3295868	24		

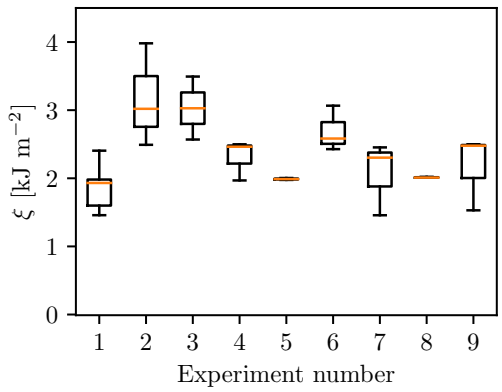

(a) Sorted by experiment.

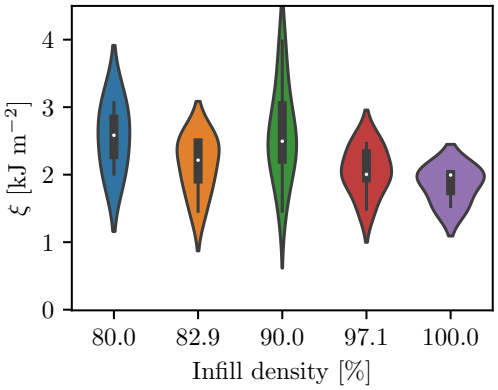

(b) Sorted by infill density.

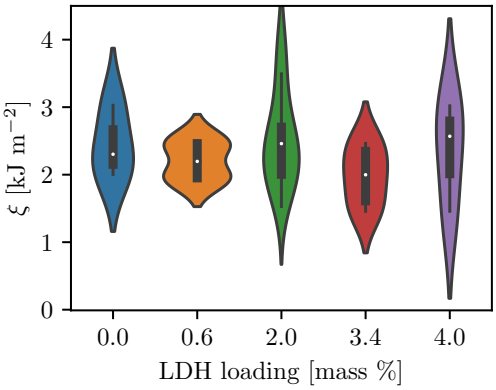

(c) Sorted by LDH loading.

Figure 50: The box and whisker and the violin plots of the impact energies recorded in the CCD experiment as a function of experiment number, infill density and LDH loading.

4.5.12 Normalised impact energy

The normalised impact energies also do not show a statistically significant difference within the CCD. Figure 51 summarises the response and Table 37 gives the initial ANOVA table. As with the impact energy, the C^2 term seems significant, but becomes insignificant as soon as the insignificant D^2 is removed. This means that the conclusions made for the impact energy above remain the same.

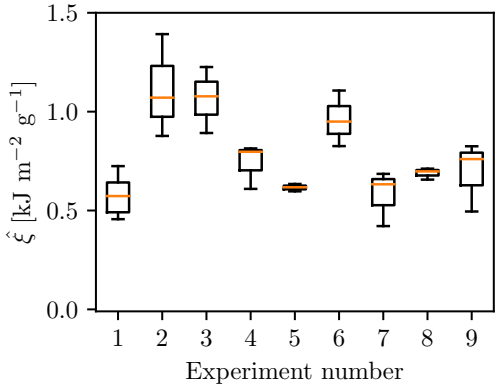

(a) Sorted by experiment.

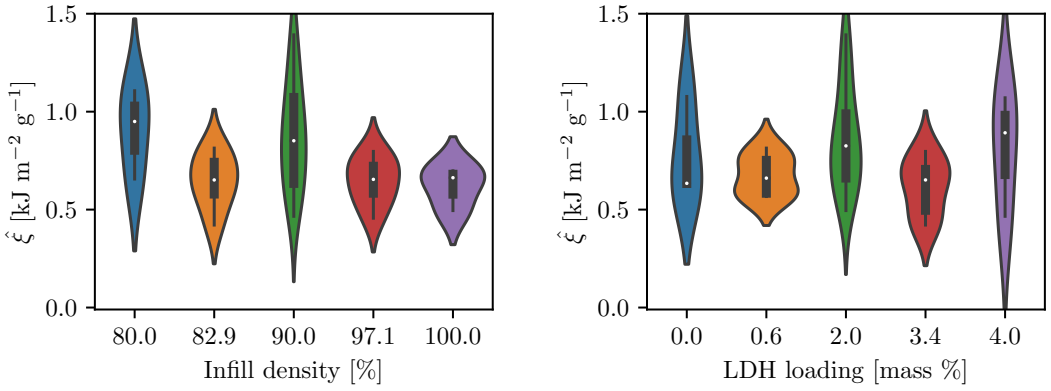

(b) Sorted by infill density.

(c) Sorted by LDH loading.

Figure 51: The box and whisker and the violin plots of the normalised impact energies recorded in the CCD experiment as a function of experiment number, infill density and LDH loading.

Table 37: The ANOVA table of the results of the CCD experiment with normalised impact energy as response factor.

Source of variation	Sum of squares	Degrees of freedom	F ratio	p value
Model	0.3787327	5	1.5100	0.2239
C	0.0608853	1	1.2138	0.2815
D	0.0022227	1	0.0443	0.8351
CD	0.0192783	1	0.3843	0.5411
C^2	0.2415196	1	4.8148	0.0381
D^2	0.1790185	1	3.5688	0.0710
Lack of fit	0.1809493	3	1.2383	0.3209
Pure error	1.0229297	21		
Total error	1.2038791	24		

4.5.13 Characterisation

The second heating runs from the DSC results are given in Figure 52. The repeats are in the Appendix C. Relatively good repeatability was observed for most experiments, with the exception of Experiments 2 and 3 where the endothermic melting peak of one run was much smaller than the other two in the set. In some of the other sets the same behaviour is observed to a lesser extent. Once again, the double melting peaks were only observed for parts printed from filaments exceeding a 2 % LDH loading, although a shoulder starts developing in Experiment 9. This is the only experiment with 100 % infill density, which would impede the rate at which the material cools. This gives the material more time to conform between the different crystal forms, which results in the formation of the shoulder. It also seems that the T_c shifts to lower temperatures with increasing LDH loading, even though the general T_m region stays constant.

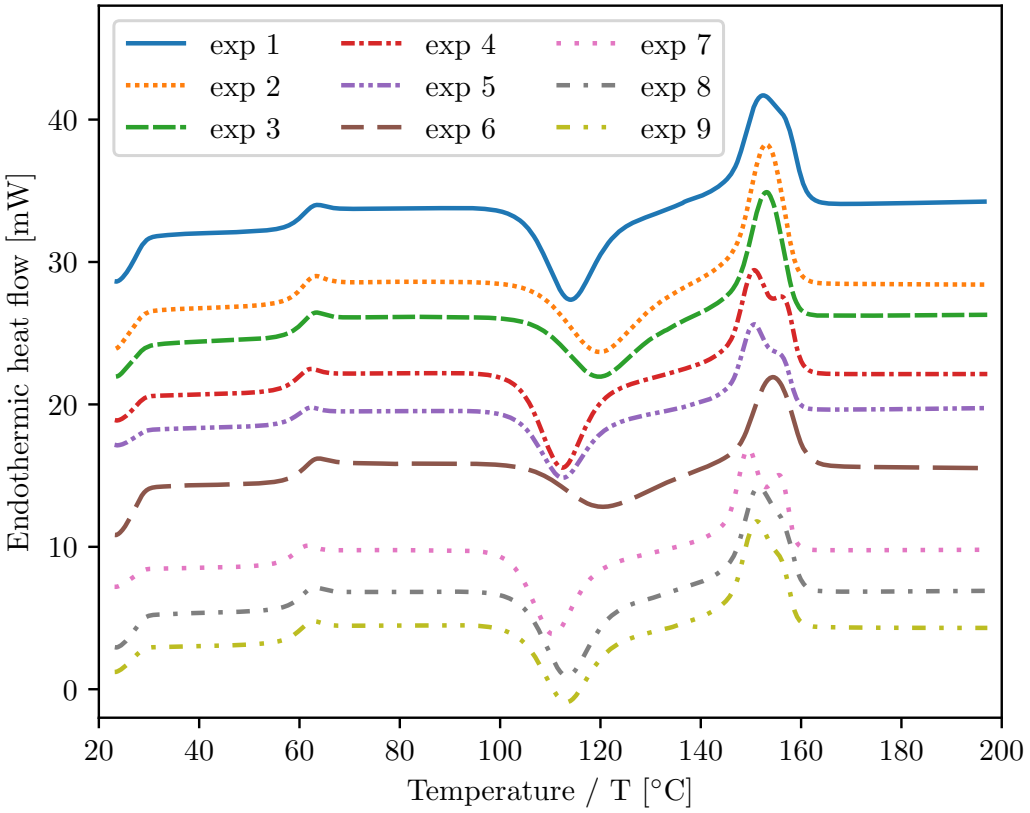

Figure 52: Representative DSC results of the second heating cycle of the tensile specimens printed in the CCD experiments compiled from Figure C.33.

The properties determined from the second heating cycles as a function of LDH loading are illustrated in Figure 53. Enlarged graphs are included to show differences, or in this case the lack thereof. No clear trend can be deduced. This reinforces the statistical observations on almost all of the mechanical properties from the CCD: that there are no statistical differences between properties in this region. It is however interesting that compared to the properties determined from the filaments used in the CCD (Figure 37), the printed specimens' properties differ substantially. It seems as if the printing affected the properties in some way. This was not the case in the screening and augmented screening experiments. It is postulated that this difference is due to the region in which the CCD was conducted. It was already shown that only two properties do not stay unchanged in this region — E and $\hat{E}$. As such, the interaction between the PLA matrix and the LDH additive does not cause any drastic changes in the compound's properties overall. Since the changes observed in the transition temperatures did not vary by much for the filaments it is likely that they were merely present due to the processing history from the two extrusion processes, and that it is then erased by the printing process. The enthalpies also stay relatively constant, but they still yield negative degrees of crystallinity, which is of course impossible. This has consistently been the case with all the DSCs completed for the screening, augmented screening, comparison and CCD experiments on both the filaments and printed tensile specimens. This warranted further investigation into the DSC analysis and the material, which is further discussed in in the next section.

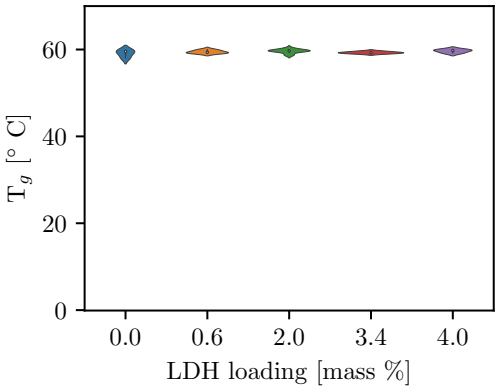

(a) Full scale T_g.

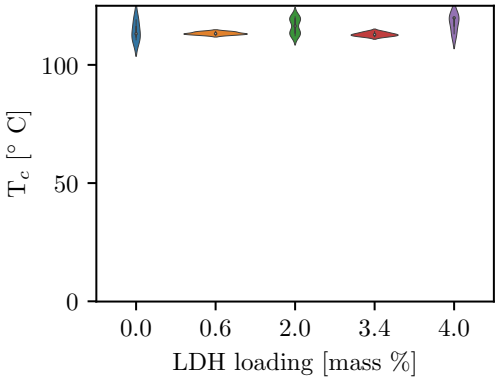

(b) Full scale T_c.

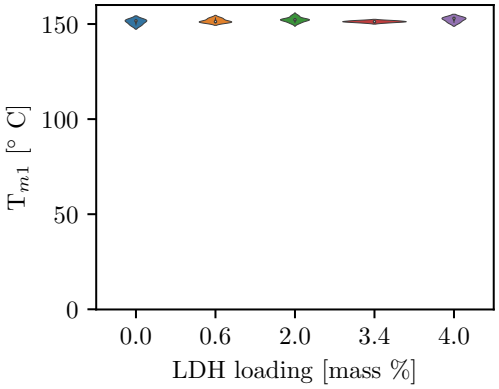

(c) Full scale T_{m1}.

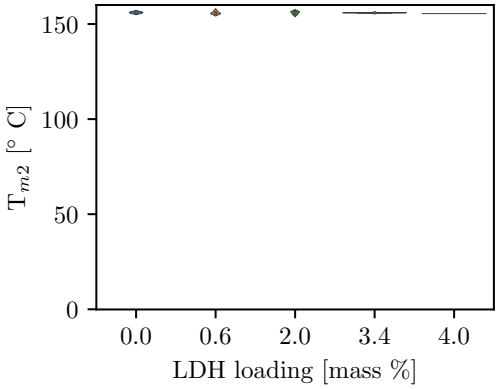

(d) Full scale T_{m2}.

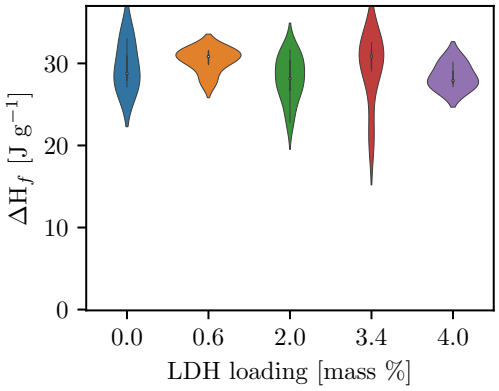

(e) Full scale ΔH_f.

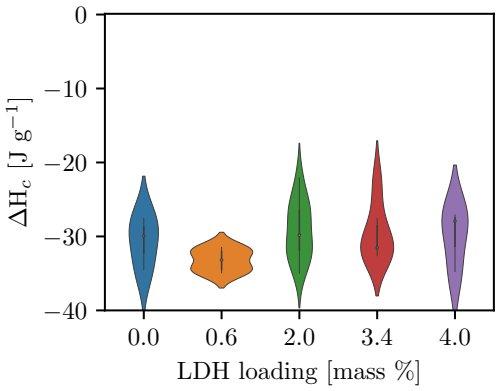

(f) Full scale ΔH_c.

Figure 53: The average properties of the printed tensile specimens made for the CCD experiment as determined from DSC. Continued on the next page...

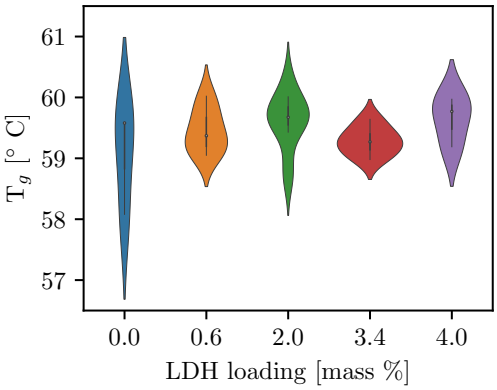

(g) Enlarged T_g.

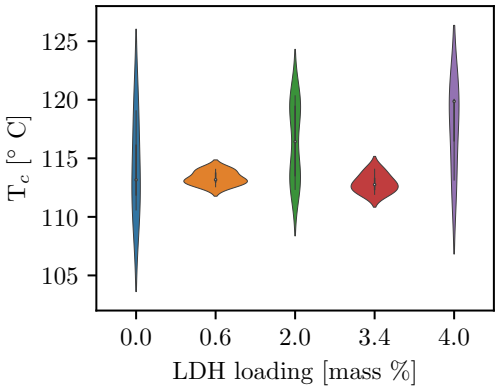

(h) Enlarged T_c.

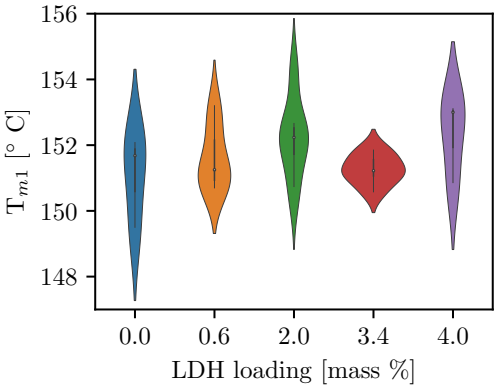

(i) Enlarged T_{m1}.

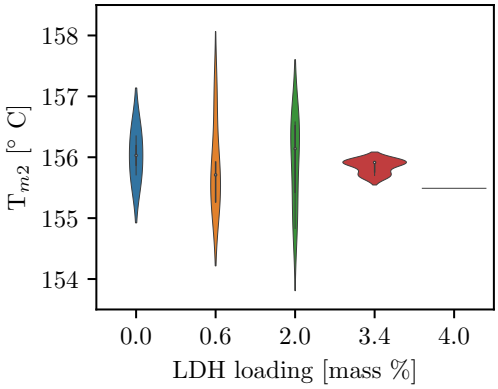

(j) Enlarged T_{m2}.

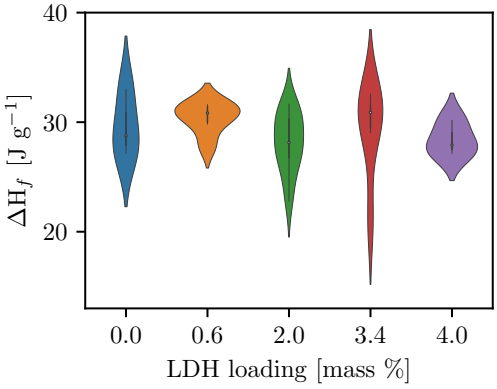

(k) Enlarged ΔH_f.

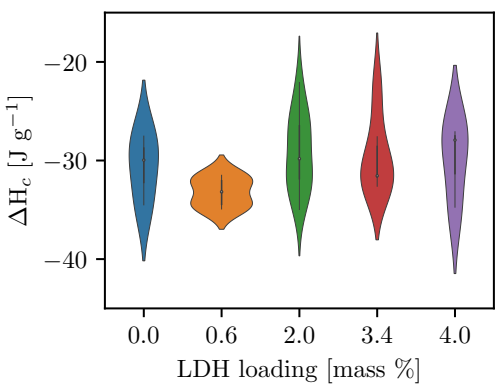

(l) Enlarged ΔH_c.

Figure 53: Continued from the previous page... The average properties of the printed tensile specimens made for the CCD experiment as determined from DSC.

Figure 54 shows the XRD spectra of the printed sheets form the CCD experiment. As was observed in all previous cases, better resolution spectra resulted. Although the conclusions remain the same as for the CCD filament, the respective peaks can be distinguished with more ease. Compared to the spectra of the sheets from the screening experiment, it is clear the LDH does not have a significant effect on the structural arrangement of the compound as was the case with 6LDH_PLA and 10LDH_PLA. This corresponds well with the statistical analyses that indicated that no statistically significant changes exist for most mechanical properties in the region of the CCD. That being said, the inconsistent resolutions observed for the filament is visible for the printed sheets as well, albeit to a lesser extent. This does not affect any conclusions made from the results.

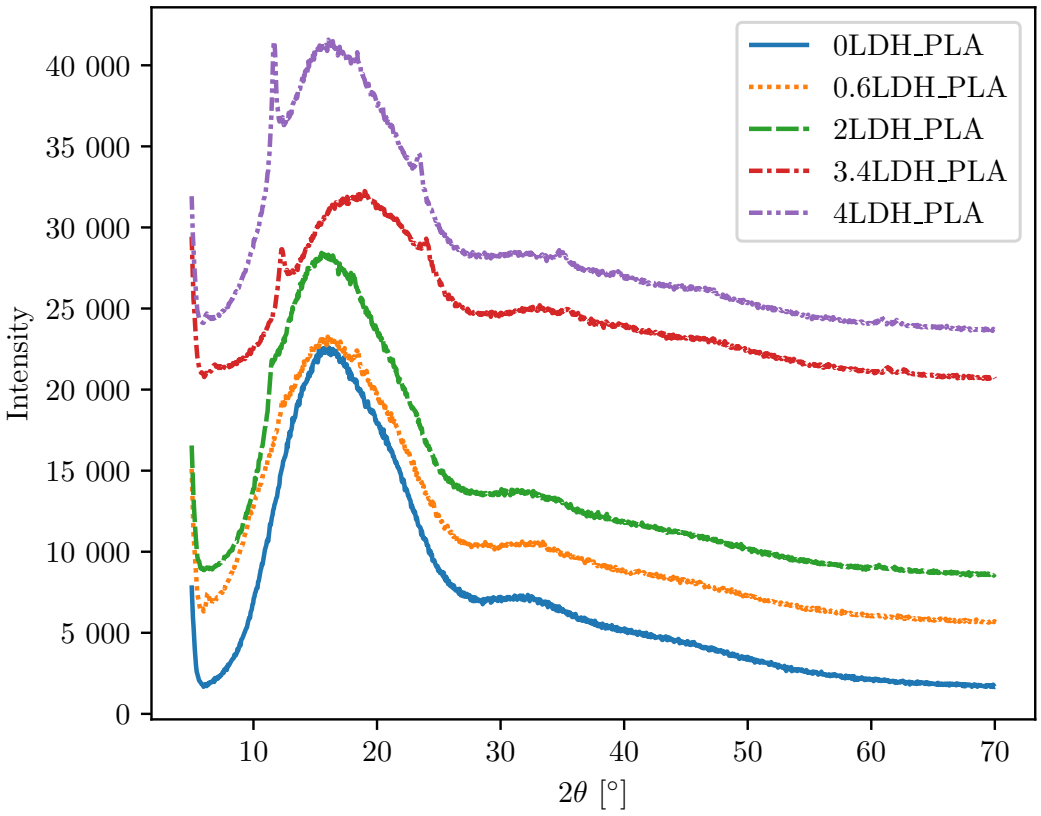

Figure 54: The XRD results of the XRD sheets printed in the CCD experiments.

A representative summary of the FTIR spectra are shown in Figure 55. As before, all the peaks remained at the same locations as for other samples. Good repeatability has been achieved within all experiments. That being said, as with the tensile specimens from the augmented screening experiment, some of the spectra were not as clear as others. It is believed that this is due to interference because of reflectance due to the rough surface.

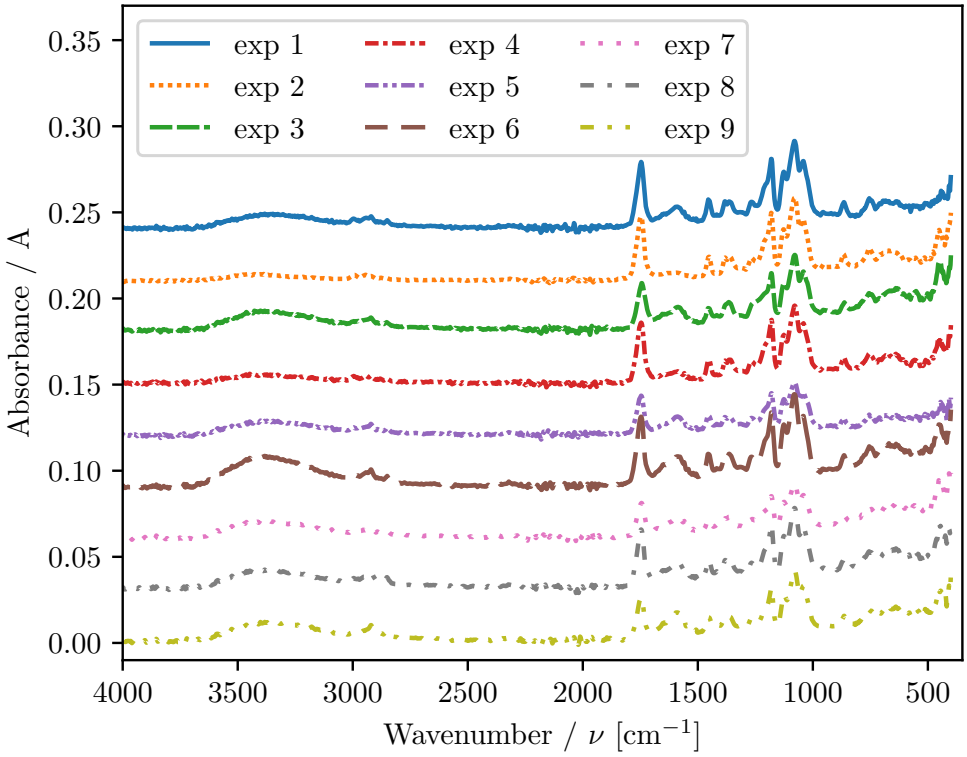

Figure 55: Representative FTIR results of the second heating cycle of the tensile specimens printed in the CCD experiments compiled from Figure C.34.

4.6 DSC investigation

Negative crystallinities were recorded whenever DSC results have been obtained. This is impossible, and as such, more DSCs were completed on samples but with different DSC parameters. The materials considered were the 0LDH_PLA and 10LDH_PLA filaments, because these are on the extreme limits considered in this work. Auxiliary DSC graphs are available in Appendix D.

First, 5 min isothermal equilibrating times where used between steps instead of the 2 min used for all the other DSCs to see if more time is required to erase the thermal history. No changes were observed for the resulting DSCs compared to those conducted before. The isothermal equilibrating time was increased to 10 min, but negative degrees of crystallinity were still observed. This indicated that the equilibrating time is not the cause of the negative degrees of crystallinity.

As such, more DSCs were conducted up to 220 °C instead of 200 °C to see if the initial melt temperature was too low to delete the thermal history of the sample. This was done with equilibrating times of 2 min and 5 min respectively. Results did not show positive degrees of crystallinity for either material. This shows that the the temperature and isothermal equilibrating times used before were sufficient in deleting the thermal history, and that this is not the cause of negative degrees of crystallinity.

Next, different heating rates (2 K min^{-1} and 5 K min^{-1}) where considered to see if the materials need more time to show the respective transitions more clearly and to record more accurate enthalpies. No drastic changes could be observed.

Lastly, a method similar to that used by Righetti *et al* (2015) was used to see if the different crystal phases can be identified under isothermal conditions. Samples were heated form 20 °C to 200 °C at 10 K min^{-1}, after which it was cooled at 30 K min^{-1} to the isothermal temperature. Isothermal temperatures of 90 °C and 130 °C were used for 480 min. After this time, cooling was continued at the same rate to 20 °C, after which a second heating run followed. The DSCs were repeated once for each material at each isothermal temperature.

The isothermal results from the DSC at 90 °C and 130 °C are given in Figures 56 and 57. Isothermal crystallisation only occurred at 90 °C, which may be attributed to crystallisation of the metastable $\alpha\prime$ phase. However, no isothermal crystallisation can be seen at 130 °C, which suggests that none of the stable α crystals formed. Looking at Figure 56, repeatability for 0LDH_PLA is sufficient, but some differences can be observed for the 10LDH_PLA. The recorded enthalpies for 0LDH_PLA and 10LDH_PLA and their repeats

were 28.38 J g^{-1} and 26.72 J g^{-1} as well as 31.09 J g^{-1} and 31.13 J g^{-1} respectively. In terms of these, better repeatability was observed for the filled filament. Regardless, it is clear that the LDH acts as a nucleating agent, as already concluded.

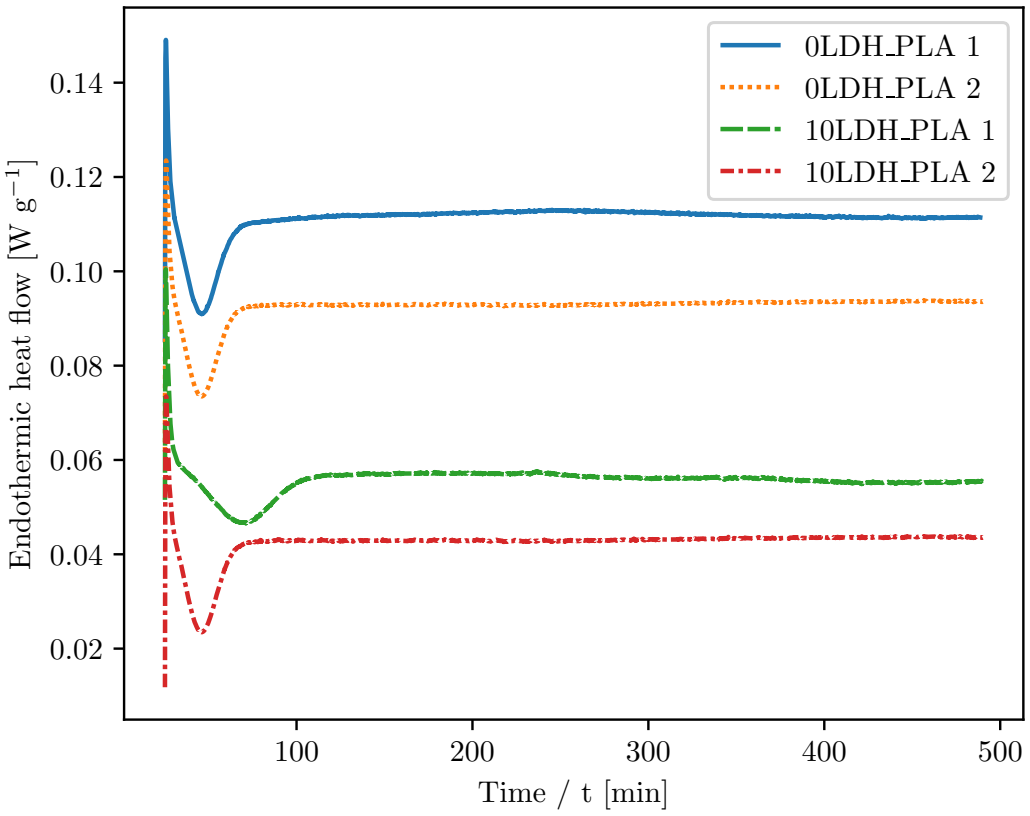

Figure 56: The DSC results for the isothermal runs at 90 °C for both the 0LDH_PLA and 10LDH_PLA filaments. The repeat of each is shown as well.

The second heating of the samples after the isothermal periods also yield some information. For those after the 90 °C isothermal period, the cold crystallisation trough disappears. As before, the double melting peak is still observed for both the pure and filled PLA filaments. This is the first time that the pure PLA filament shows a double melting peak. As already discussed before, this is due to the metastable $\alpha\prime$ phase conforming to the α phase in between the melting of the two phases. This confirms the observation. For the second heating after the 130 °C isothermal period, a cold crystallisation peak is still visible, but it is much smaller than before, suggesting that crystallisation did indeed occur during the isothermal period, although it cannot be identified. This also yields positive degrees of crystallinity since the melting enthalpies are visibly larger than the cold crystallisation enthalpies. Since the 0LDH_PLA also shows a double melting peak here, it is possible that some $\alpha\prime$ crystals formed during the cooling period after the isothermal period at 130 °C. The second heating DSC results can be seen in the appendix (Figures D.35 and D.36).

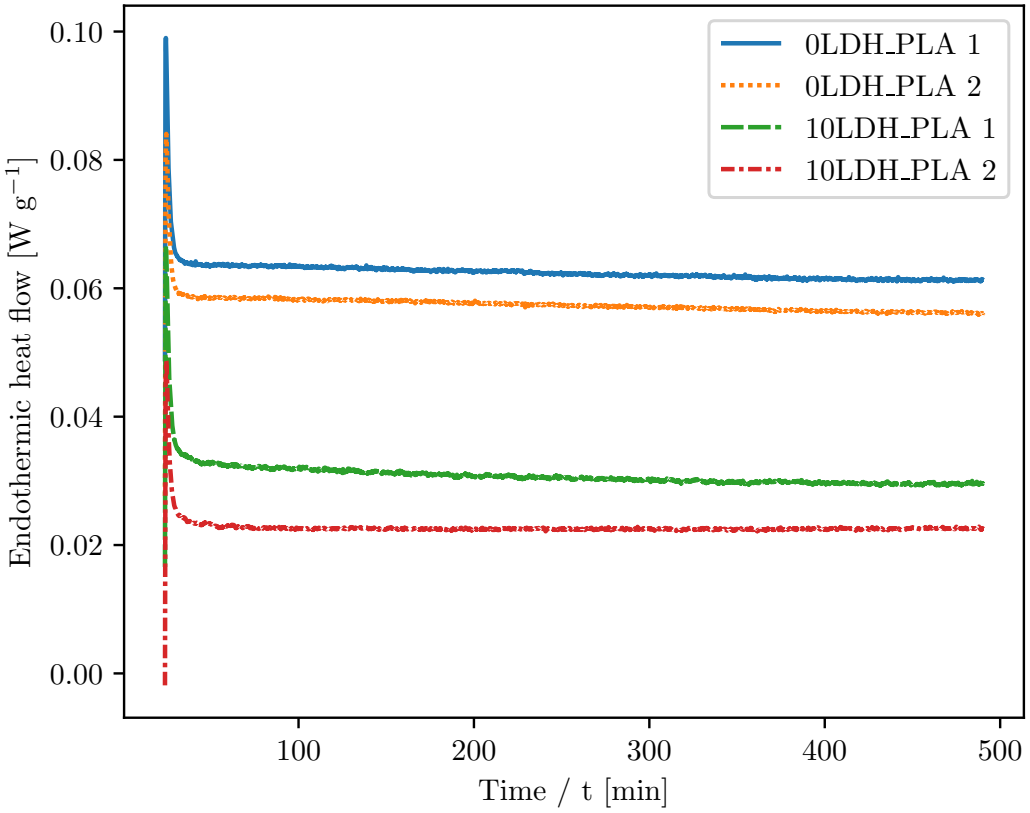

Figure 57: The DSC results for the isothermal runs at 130 °C for both the 0LDH_PLA and 10LDH_PLA filaments. The repeat of each is shown as well.

Recall that a DSC was completed on the pure PLA as received. The cold crystallisation and melting enthalpies recorded for the second heating was 24.57 J g^{-1} and 22.91 J g^{-1} respectively, which also yields a negative degree of crystallinity.

It is clear that much more can be investigated by DSC on these materials. However, this is outside the scope of this work. The negative degrees of crystallinity cannot be explained with the available information. Thus, it has to be assumed that the materials are mostly amorphous under the processing and printing conditions used in this work. That being said, LDH is clearly a nucleating agent for the metastable $\alpha\prime$ crystals. It is believed that all the DSCs conducted are still of value, and that relative to one another, all the results can be compared since they were all conducted with the same procedure.

4.7 Injection moulding

Injection moulding is not the main focus of this work, and is only included to provide a comparison of mechanical properties between FDM and injection moulding. As such the injection moulding parameters were not optimised like the FDM properties, and only the effect of LDH loading was observed. Images of the tensile specimens and the stress strain graphs are available in Appendix E.

In preparation for injection moulding, the rheology of 0LDH_PLA, 2LDH_PLA and 10LDH_PLA granules was considered. The 2LDH_PLA granules was considered because it is centre to the range determined as an optimum in the CCD experiment. 0LDH_PLA was included to give a reference to the unfilled material, and 10LDH_PLA was considered to see how the most filled material behaves in the new process. Using Fischer-Tropsch titration, it was shown that samples had a moisture content of 0.014 %, 0.127 % and 0.441 % for the 0LDH_PLA, 2LDH_PLA and 10LDH_PLA respectively after drying overnight at 50 °C. Drying the 10LDH_PLA at 80 °C for six hours increased the moisture content to 0.616 %. MFR tests were only completed on 0LDH_PLA since it was the only material with a moisture content below 0.05 %. The results are summarised in Table 38. The increase in moisture with higher drying temperature in the filled materials could be due to some reaction, perhaps degradation, because 80 °C is well above the T_g of the compounds, and therefore any free or crystallised water should have been removed. Moreover, the presence of water cannot be observed from FTIR or DSC analyses. It is also possible that the Fischer-Tropsch titration is sensitive to another compound other than water.

TGA was completed on the dried and undried 0LDH_PLA and 10LDH_PLA granules to see if the moisture can be identified and whether anything noteworthy happens during

drying. Firstly, the dried and undried samples yielded the same TGA curves, as shown in Figure 58. There is a shift to lower temperatures from the OLDH_PLA to the 10LDH_PLA due to the catalytic effect of LDH on the degradation of PLA. Mass loss only starts at *ca.* 210 °C and 280 °C for 10LDH_PLA and 0LDH_PLA respectively. No other steps before this point can be observed, as confirmed by the derivative mass loss. Therefore, the source of moisture cannot be identified by the TGA analyses either.

Table 38: The MFR results of the 0LDH_PLA granules at various melt temperatures using a 2.16 kg mass.

Temperature °C	MFR g 10min^{-1}	MVR cm^3 10min^{-1}
170	1.84	1.62
190	4.54	4.06
210	10.8	9.79

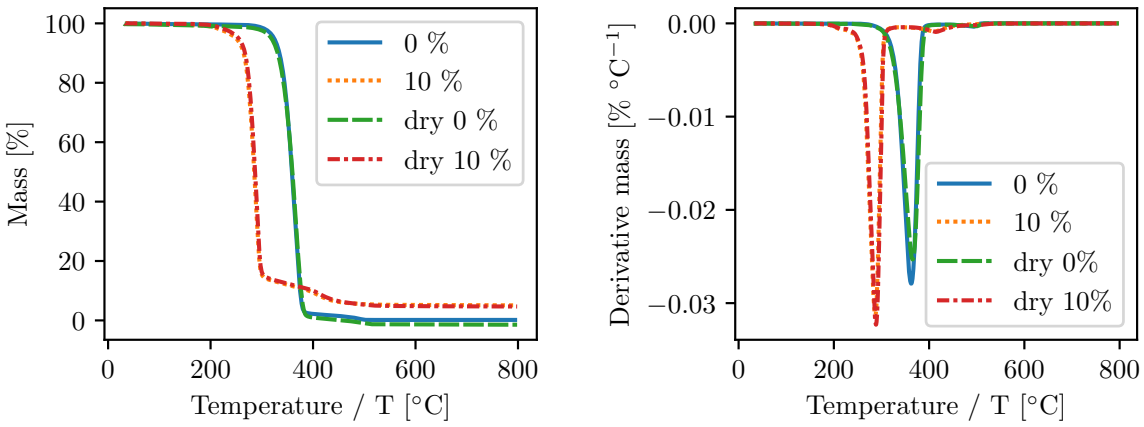

(a) Mass loss. **(b)** Derivative mass loss.

Figure 58: The TGA curves for the 0LDH_PLA and 10LDH_PLA granules before and after drying.

Oscillatory rheology was used as an alternative to MFR. First, a time sweep was run to see if the materials remain stable long enough to conduct a frequency sweep. Figure 59 refers. It was interesting to observe that there are significant differences between the complex viscosities of the various materials, and even between the pure PLA (pPLA) and the processed PLA granules (0LDH_PLA). This suggests that decomposition occurred during the compounding process regardless of the LDH loading used, and that LDH merely catalysed the decomposition. The latter observation was discussed by many of the authors in the systematic review. Moreover, it is also believed that the shear in the melt increases with LDH loading as discussed in the screening experiment, which will also have an influence on the decomposition. The 10LDH_PLA sample had such a low viscosity that it could not be measured for the whole time span.

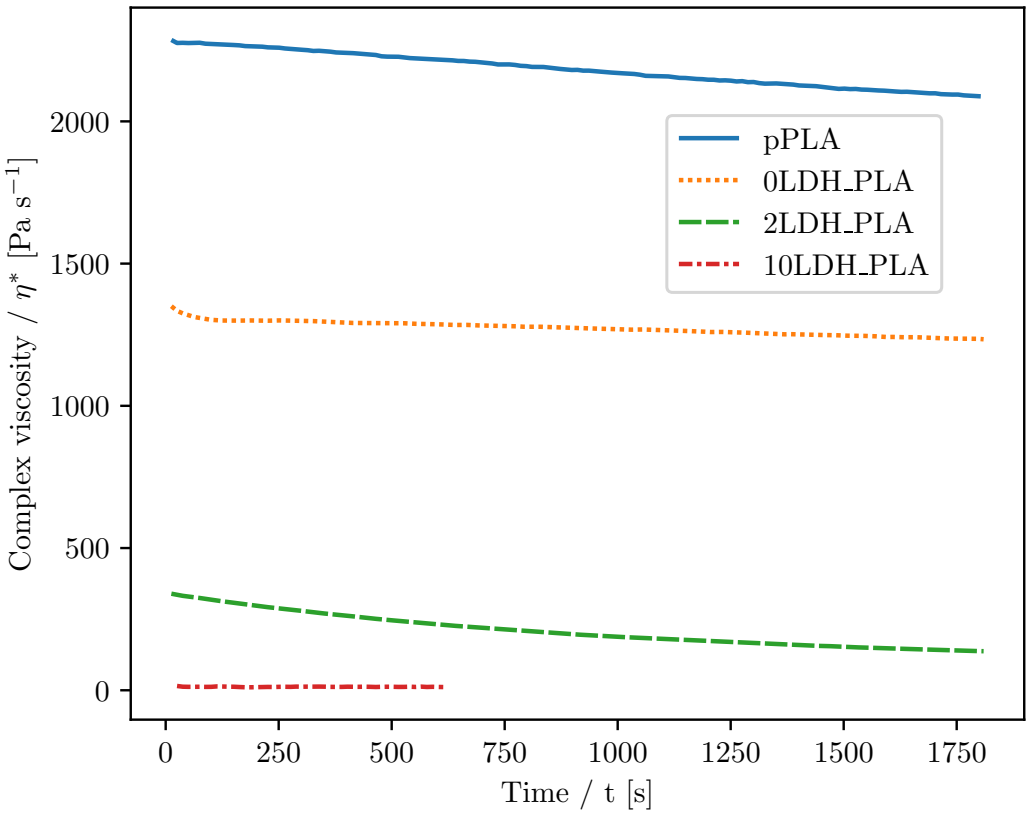

Figure 59: The time sweeps as determined from oscillatory rheology.

Another interesting observation was that the decrease in viscosity over time did not really vary between pPLA, 0LDH_PLA and 2LDH_PLA, but that the shape did. The pPLA sample merely decreased linearly, while the 0LDH_PLA had a faster initial decrease before decreasing linearly and the 2LDH_PLA had a more quadratic decrease over the region considered. Accordingly, frequency sweeps will not be accurate, and will loose accuracy as time proceeds. Nevertheless, frequency sweeps were conducted from high to low angular frequencies. The high frequency region will be more accurate. These can be seen in Figure 60. The crossover point between the storage and loss moduli shift to higher frequencies with increased processing or LDH loading, suggesting that the molecular mass of the polymer chains have decreased.

Despite the evident degradation that occurred during processing, it was possible to print all samples. Based on this, it was decided to continue with injection moulding. Images of the tensile specimens before and after testing can be found in Appendix E. Similar to before, the differences in opacity were clearly distinguishable. Samples did not show any other visual defects, and compared well to one another in all other regards like shrinkage (or the lack thereof), surface roughness and appearance. Contrary to printed samples, injection moulded samples where placed into the testing clamps in exactly the same orientation, with the end farthest from the flow gate in the top clamp. The break

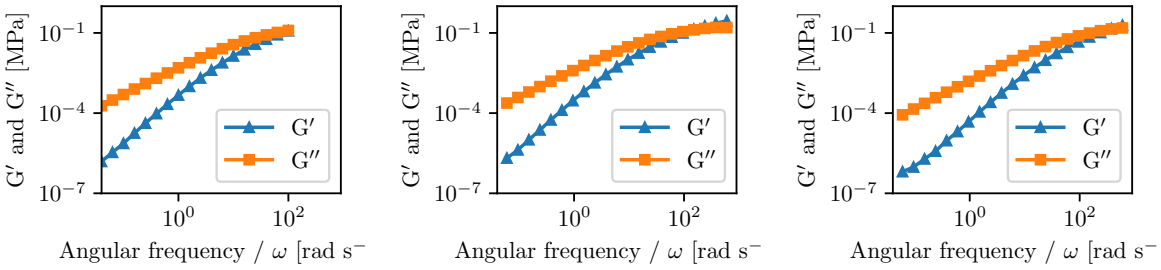

(a) pPLA. **(b)** 0LDH_PLA. **(c)** 2LDH_PLA.

Figure 60: The frequency sweeps as determined from oscillatory rheology.

location was more randomised in these parts, although four of the five 2LDH_PLA samples broke in the same general location. All break locations were within the narrow parallel section. The stress strain graphs are in Appendix E. A summary of the respective tensile properties considered for the printed samples are shown in Figure 61. Properties are shown only as a function of LDH loading, since this was the only factor varied. Note that tensile force was not considered here because samples broke where they should have.

The 10LDH_PLA samples had inferior σ and ϵ_b compared to the other two materials tested. The same is however not so obvious for E. This might give some insight into why the Young's moduli considered during printing optimised to unexpected factor levels, and confirm that optimisation should rather target σ or ϵ_b rather than E. The ANOVA analyses of σ, $\hat{\sigma}$ and ϵ_b have a significant LoF for linear models, but no LoF can be reported for quadratic models because the models are saturated. Moreover, although optimisation is definitely possible, it was outside the scope of this work. As such, an in depth statistical analysis was not completed as for the printed specimens. Even though an acceptable LoF results from linear models on E and $\hat{\text{E}}$, LDH loading is not a statistically significant factor. This can be attributed to the large variation in especially the 0LDH_PLA and LDH_PLA samples, but also suggests that other factors not considered in the model play a role. A decrease in viscosity for samples were observed in the rheology results, which can be one such a factor.

Consider only σ, $\hat{\sigma}$ and ϵ_b. Contrary to the CCD experiment, there is a decrease in each property between the 0LDH_PLA and 2LDH_PLA. Still, the tensile stress is substantially larger than for the printed samples. This difference gets smaller when the normalised stress is compared instead, but remain nevertheless, especially for the 0LDH_PLA samples. That being said, the printed specimens do have a comparable strength to the injection moulded ones, especially between those of the CCD and the 2LDH_PLA injection moulded samples. The same observations apply to ϵ_b. On the other hand, the 10LDH_PLA samples compare quite well between the printed and injection moulded specimens, with the former even showing superior ϵ_b results.

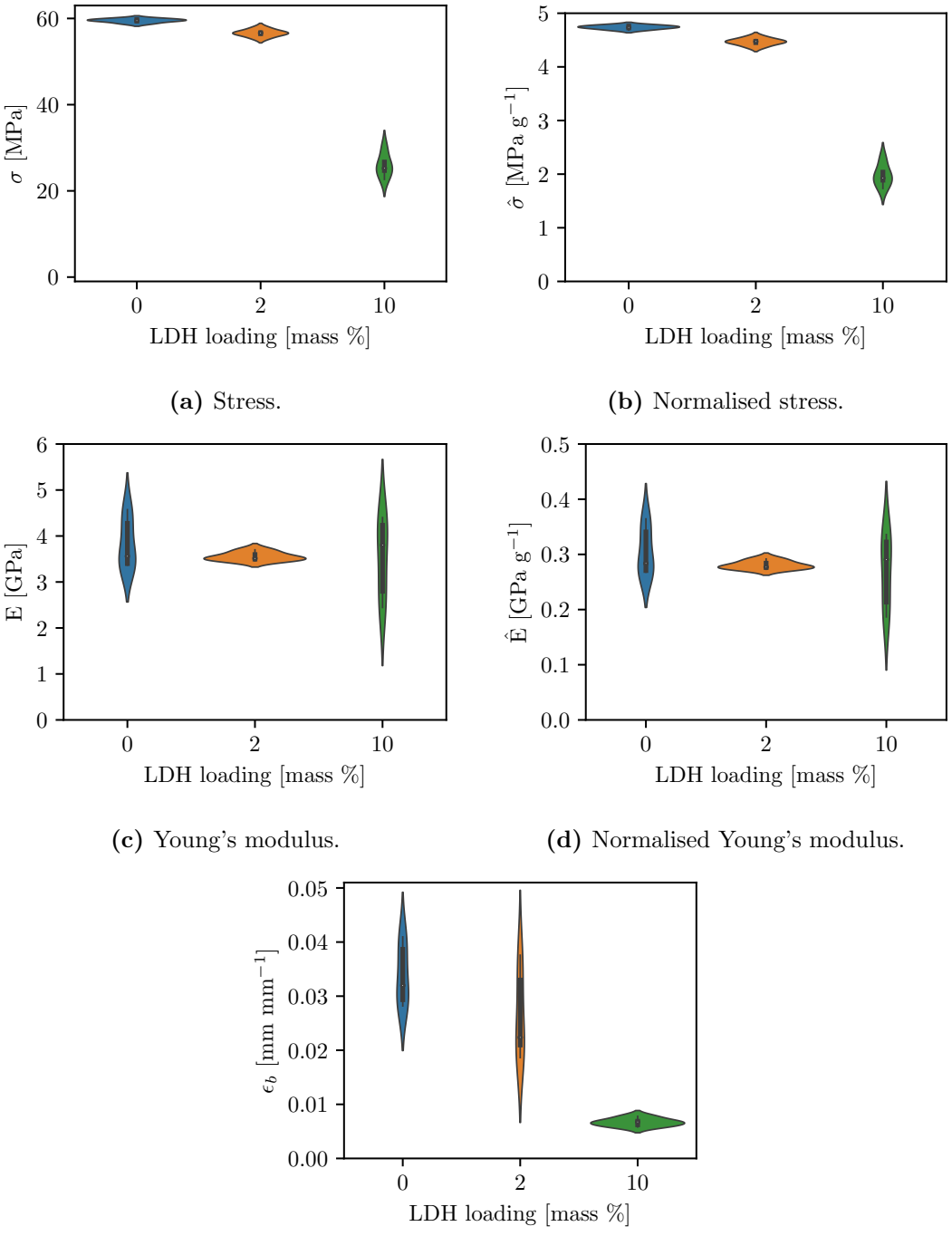

(a) Stress.

(b) Normalised stress.

(c) Young's modulus.

(d) Normalised Young's modulus.

(e) Strain at break.

Figure 61: A summary of all the tensile properties as a function of LDH loading for the samples prepared with injection moulding.

Clearly there are differences in mechanical properties when different processing techniques are employed, even if they are normalised with respect to mass. Considering that the injection moulding can also be optimised for properties, it is highly unlikely that FDM will produce parts that are stronger than those made from injection moulding. That being said, FDM seems to be able to accommodate higher LDH loadings, whereas injection moulding immediately shows a decrease in properties. The decrease in viscosity observed indicated that a too aggressive screw was used in the compounder. It will therefore be worthwhile to find the optimum processing conditions for compounding LDH into PLA without degrading the material so much. An increase in mechanical properties are sure to follow.

4.8 The proper use of statistics

Statistics is a vast subject, and definitely a field in its own right. However, it is unfortunate that only some realises its full potential. Typically, engineers have an introductory background to statistics, but not enough for them to fully exploit it. This is paradoxial because engineers always have to optimise and save resources. Standards, *e.g.* the ISO 527 tensile testing standard, shows that only rudimentary statistics form part of the *status quo*. It is unlikely that the experts who set up standards are unaware of the statistical possibilities, but standards are supposed to lead anyone, even someone without any knowledge on the specific topic, to produce reliable data. If statistics allow it, the authors of standards do not necessarily object to deviating from the amount of replications suggested. Yet, it is often frowned upon when someone deviates from a standard, especially within the engineering and natural sciences establishments. Herewith, it is proposed that a lot of resources can be saved if statistics are properly employed.

Whilst conducting the screening experiment in this work, it was realised that a lot of resources are being wasted to comply to the expectation by the standard of five replications for each experimental condition. Each replication requires time and resources to make filament, characterise it, print specimens and characterise them as well. Each replication also requires extra resources, *e.g.* all the materials and chemicals used for characterisation. Even though this was mitigated to some extent by conducting a half fractional factorial experiment, 55 specimens were printed to test only four factors at two levels. This does not include the experiments following from the result of the screening experiment. If there was no other way to achieve the same results, this would be the only approach to research and development. However, statistical thinking offers the ability to significantly reduce the amount of replications and therefore exponentially reduce the amount of resources required to reach the same conclusions, and often with additional

insight.

Statistics does this in a elegant yet simple manner. In a statistically designed experimental programme a few replications are performed on a single set of conditions, called centre points. The centre point is the experimental condition where all the variables are at their centre values, *i.e.* the middle of the experimental region or design space. Given a homogeneous environment during the execution of the experimental programme, the responses observed from the centre point experiments are expected to be relatively similar, *i.e.* having small variance. The reason is that the variability observed at the centre point should only be due to random variation. Therefore, the variation at the centre point is used to specify the experimental error. Now, the variation in the response observed from the experiments where the levels of the variables under investigation have been varied is compared to the variation at the centre point. Consider a one variable experiment where the factor is investigated at two levels along with a centre point. A simple statistical analysis can be done to compare the difference in the response between the two levels to the standard error observed at the centre point. Logically, if the difference between the two levels in the response is greater than the standard error it cannot be by chance, and it can safely be concluded that the variable affects the response. A significance level can also be added to this effect.

The standard procedure used by engineers, and other scientists for that matter, are to run five or more replications for each level of a factor and to consider the five responses at each factor level as a set. This is evident in most standards. Some simple statistical parameter, *e.g.* the mean or median, is then compared throughout the different sets. Standard deviations are sometimes included. Clearly, this is a rigorous approach, but it is also a bloated one. Essentially, the procedure used by statistics on the centre points is conducted for every set of factor levels, but because the statistics are not applied correctly the information available are not exploited to its full potential. For one or two factors with a small amount of levels this might still be acceptable, but it rapidly becomes a waste of resources as the amount of experimental points increase. Consider the following analogy. An engineer wants to do a mass balance of a compound consisting of five elements. He has to run an expensive test to determine each element's mass. Instead of recalling that all the masses have to sum to the total mass of the compound and determining four masses before calculating the fifth, he conducts five tests to determine the elemental masses. This might be excusable if only a few compounds have to be analysed, but what if he has to analyse 55 compounds, or perhaps 100?

To illustrate this point consider the data from the screening experiment. This was a 2^{4-1} fractional factorial experiment with 15 centre point replications and five replications per experimental point (Tables 10 and 11). It is impossible to visualise the response

as a function of four factors, so consider the effect of only two factors on the response. There are two ways to do this: (1) assume two of the factors did not affect the response, which will collapse the half factorial experiment into a full factorial experiment with 10 replications per level for the remaining factors, or (2) assume one of the factors did not affect the response and select one experimental condition for another factor so that only the two remaining factors vary. The first will not be useful for illustrating the point, since the variance of the two factors will be included in experimental error, yielding heterogeneous experimental conditions. It can be shown that the statistics will indicate that results are inconclusive in such a scenario, but for the sake of brevity this is not done. Instead, the second procedure is used since it will yield a more homogenous hypothetical experiment.

Suppose tensile strength is the response. Considering the ANOVA table from the screening experiment with all the data, Table 18, the least significant factors were A and B. Since B was the least significant of the two, this was selected as the factor that did not affect the response, whilst A was kept constant at its low level. This yields a full factorial data set with the data from Experiments 0, 1, 3, 5, and 7 of the screening experiment. This is the best representation of homogenous experimental conditions in factors C and D with the available data. The data is represented as scatter and surface plots in Figures 62a and 62d respectively. In order to illustrate the power of statistics, the experimental and centre point replications have to be reduced. First consider a reduction in experimental replications. This was achieved by averaging the five replications of Experiments 1, 3, 5, and 7 respectively, thus yielding only one response for each experiment instead of five. This was done instead of selecting one out of the five points, because it is more representative. The new data set can be seen in Figures 62b and 62e. Lastly, consider a further reduction in the centre point replications from fifteen to five. This was done by averaging three centre points into one. This last scenario is shown in Figures 62c and 62f.

Visually, a similar surface results from all three experiments. The variance in the centre points are smaller than the difference between the low and high levels of each factor. As such, both factors are expected to be significant. The ANOVA results of the three models are summarised in Table 39. First off, the LoF for all three models are statistically insignificant, indicating that a linear model was successfully fitted. Secondly, each model is statistically significant on a 5 % confidence interval. C remains statistically significant, while the interaction term CD remains insignificant for all three models. Only D is slightly insignificant in the second and third models compared to the first one. If however a 10 % confidence interval is used, all models yield identical conclusions. More importantly, each model predicts the optimum at the same combination of factor levels, namely 90 % infill density and 2 % LDH loading. Only the value for the response predicted by the model

differs between the three hypothetical experiments.

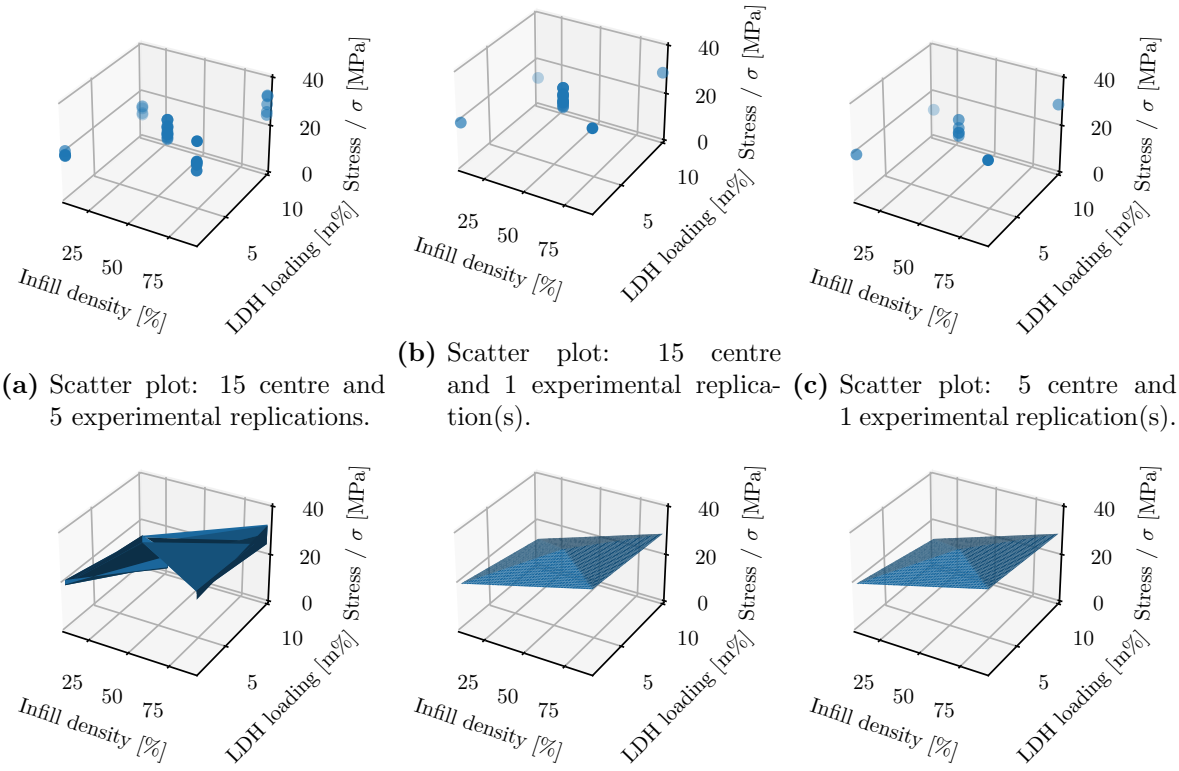

(a) Scatter plot: 15 centre and 5 experimental replications.

(b) Scatter plot: 15 centre and 1 experimental replication(s).

(c) Scatter plot: 5 centre and 1 experimental replication(s).

(d) Surface plot: 15 centre and 5 experimental replications.

(e) Surface plot: 15 centre and 1 experimental replication(s).

(f) Surface plot: 5 centre and 1 experimental replication(s).

Figure 62: The 3D scatter and surface plots of stress as a function of infill density and LDH loading for the three different theoretical experiments selected from the screening experiment data.

Table 39: A summary of the p-values from the ANOVA for the effects of infill density and LDH loading for the three hypothetical experiments from the screening experiment.

Replications	Lack of fit	Model	C	D	CD
15 centre 5 experimental	0.598	<0.0001	<0.0001	0.0001	0.229
15 centre 1 experimental	0.739	0.0002	<0.0001	0.052	0.565
5 centre 1 experimental	0.780	0.005	0.001	0.064	0.537

The changes in the p-values between the different models can be explained by the degrees of freedom available for calculating the pure and experimental errors, and the LoF. Consider again the first model with all replications in Figure 62a. There is variance in the experimental points, especially for the experimental point at 90 % infill density and 2 % LDH loading where the one point is clearly an outlier. Despite this, there are enough replications so that the majority of degrees of freedom are used to calculate the experimental errors. The p-values increase slightly because there are fewer degrees of freedom available for calculating the pure and experimental errors.

The above example clearly illustrates the benefit of using statistics and a statistical design of experiments. Specifically, the same information that would be gleaned from a bloated experiment with 35 replications over nine experimental points was determined from only one replication per experimental point in an elegant manner. This is a 74 % reduction in experimental effort. Even though the significance of the model reduces slightly with fewer replications in this case, the final conclusion from the experiment remains the same. The factor levels at which an optimum will occur are accurately and identically predicted by bloated and elegant models alike. More replications may improve the accuracy of the response predicted, and as such more replications are fully justified for experiments where very accurate models are essential. This does not necessarily mean that five replications of each point is required, but rather two or three replications, or merely more replications of the centre point. Montgomery (2013) also have a plethora of real life examples where statistics are applied to engineering problems which illustrate the same. Of course, the experimenter has to decide on the amount of replications based on the problem of interest. In this work for example, five replications on each experimental point for the screening experiment was unnecessary, and thus a waste of resources.

The critical reader might note that situations may arise where the variation at the experimental points are larger than that recorded at the centre points. Firstly, it is most important to understand the variables that have an effect on the response, and to include these variables in the statistical model. Secondly, the example shows that the experimental error must be minimised in order to quantify the effect of the variables of interest on the response. Therefore, in situations where the variation in experimental conditions are larger than at the centre points, it is usually due to extraneous variables not accounted for in the experimental design, and thus also not in the model. A significant LoF, although not exclusively, is an indicator of such a situation. Therefore understanding the problem, its variables of interest and the selection of the correct statistical experimental design are critical components for a successful experiment, and can prevent unnecessary effort.

4.9 Discussion

Three successive statistical experiments were conducted. The first was a half fraction factorial experiment with four factors at two levels, with five replications each, and fifteen replications of the centre point. This experiment showed a significant LoF for all properties considered, except for ϵ_b. By augmenting the screening experiment, a second block of runs were added, which allowed the fit of a quadratic model. This model was used to predict an optimum response. Depending on the property investigated, the optimum was observed at different factor levels. A CCD was conducted in the region of the optimum

predicted for σ, which was the main property of interest in this work. Instead of finding a better optimum in this region, it was determined that the response does not vary with a statistical significance. This means that the CCD essentially became a rigorous model verification.

A few observations worth mentioning have been made during the course of the experiments. Firstly, it has been shown that the slicer software used, Ultimaker Cura, caused weak points in the printed parts. This happens because the software selects the same points for starting the print of each individual layer, despite randomising the z seam alignment, infill start and printing the infill before the walls. Although all these settings prevent each layer to start printing from the exact same point, the software still does not completely randomise the starting point of each layer. Instead, it starts printing from one point which it randomly selects from a set of fixed points. These points have been observed from the preview user interface in Ultimaker Cura, and are generally located at the intersection where two geometries meet. For the impact specimen this is only at the four corners. However, for the tensile specimen this also includes the locations where the arc connects to the narrow parallel section in the middle of the specimen and where the arc connects to the broader parallel sections on the ends. Statistically, it was proved with the screening experiment that the fracture locations are dependent on the slicer software; this was confirmed in the other experiments. No way of addressing this problem in Ultimaker Cura could be found. It is therefore important to realise this defect in the software and to keep this in mind when designing parts and during the selection of slicer parameters *e.g.* number of walls, infill density used and so forth.

The outliers identified differed depending on the response investigated, as summarised in Table 40. Outliers were only observed in the screening experiment. Identical runs that were outliers for more than one response were put on the same row by using matrix notation, *i.e.* the vertical dots represent runs not shown between outliers. The fracture outliers are specimens that actually broke in the middle of the narrow section instead of the edges as most of the others, and the visual outliers are those identified from the stress strain graphs. All other outliers have been determined using Tuckey's outlier fences. Only one of the fracture outliers, se_46, was also identified as an outlier in all the other tensile properties. This sample was definitely an outlier although the reason is unclear. It was not identified for ϵ_b, but this might be because the variation for this property was generally larger for each experimental point compared to other properties. It was aslo not an outlier for the impact samples, because these were different samples than the tensile specimens. Considering the tensile stress and force as well as their normalised versions, only se_16 and se_46 were present in all of the properties. The latter is no surprise, but it seems as if something went wrong during the tensile test with se_16. The same might be said for se_15, although it was not an outlier for $\hat{\sigma}$. This might be because of the combined

effect of this sample's mass and cross sectional area. Moreover, se_19 was an outlier for both σ and $\hat{\sigma}$, but not for the force properties. It broke within the narrow parallel section, thus it is probably due to some printing flaw affecting its mass or cross sectional area. The other outliers for the tensile and normalised tensile stress appear to be random in nature. The outliers identified for F and $\hat{\text{F}}$ were always the same, and F had to be the cause of this. These were presumably not observed for the stresses because of the division by each sample's cross sectional area. Generally, outliers present in E or $\hat{\text{E}}$ were also outliers in σ or $\hat{\sigma}$, indicating these as the source of variation. There are some additional outliers, presumably present because of the different region in which E is calculated, the elastic region. The outliers se_9, se_16 and se_53 are present in both ξ and $\hat{\xi}$, indicating that something went wrong during printing or testing. The two outliers only observed for the ξ, se_8 and se_39, is probably not present in $\hat{\xi}$ due to the larger allowed variance caused by the normalisation. All in all, few outliers have been observed compared to the total of 55 samples, and there are no major concerns about the experimental procedure based on these. This is reinforced by the fact that outliers were not from the same experimental point. Since the statistical procedures were completed on the data with outliers, they did not affect conclusions, and this discussion merely serves to show that the experiment as a whole was successful and raised no major concerns.

Table 41 summarises each optimum property along with its associated factor levels predicted from the augmented screening experiment models. Most of the properties converged to the same point in the experimental region located at 0.18 mm layer height, 190 °C nozzle temperature, 90 % infill density and 2 % LDH loading. Only E, $\hat{\text{E}}$, ξ and $\hat{\xi}$ converged to different points. It seems as if E and ξ have some correlation in their deviation because they both converged to the high temperature and infill density levels of 220 °C and 90 %, whereas their normalised versions converged to the low temperature and infill density levels of 190 °C and 10 % respectively. On the other hand, both E and $\hat{\text{E}}$ converged to the high LDH loading level of 10 % contrary to ξ and $\hat{\xi}$, which converged to the low level of 2 %. None of these four properties had the same layer height. There are no clear reasons for the deviations, except for the different mechanisms occurring during the testing of the various properties. For example, E is determined in the elastic region which will naturally have a different mechanism than the ultimate tensile properties or the properties at break. The impact energies have a completely different test and mechanism.

Table 42 shows the mean of the response over the whole of the CCD for each property along with the percentage increase compared with the predicted optimum from Table 41. In the case of E, the mean is not shown because another optimum was found in the region, which was located at the factor levels of 80 % infill density and 4 % LDH loading. The model had a low p-value for the LoF, and could barely be classified as statistically

Table 40: A comparison of all the outliers identified from the different responses considered in the screening experiment.

Fractures [a]	Visual [b]	σ	$\hat{\sigma}$	F	$\hat{\text{F}}$	ϵ_b	E	$\hat{E}$	ξ	$\hat{\xi}$
⋮	⋮	⋮	⋮	⋮	⋮	⋮	⋮	⋮	⋮	⋮
									8	
									9	9
							14		⋮	⋮
		15		15	15		15	15		
	16	16	16	16	16		⋮	⋮	16	16
	⋮	⋮	⋮	17	17				⋮	⋮
		19	19	⋮	⋮		19			
21		⋮	⋮				⋮			
⋮							30	30		
							31	31		
			33				⋮	⋮		
34			⋮							
⋮	36	36	36				36	36		
	⋮	⋮	⋮				⋮	⋮	39	
				41	41				⋮	
								44		
								⋮		
46	46	46	46	46	46		46	46		
⋮	⋮	⋮	⋮	⋮	⋮		47	47	⋮	
							48	48		
		49					⋮	⋮		
		⋮							53	53
⋮	⋮	⋮	⋮	⋮	⋮	⋮	⋮	⋮	⋮	⋮

[a] tensile samples broken in the middle
[b] tensile samples deviating from others on the stress strain graph

insignificant. $\hat{\text{E}}$ showed a statistical significant LoF. This has to be because of some factor that influences $\hat{\text{E}}$ that was not included in the experimental design, because it is highly unlikely that a quadratic model with main effects and interactions cannot be fitted. In fact, if this is the case it would explain the odd behaviour of E as well. Moreover, the optimum determined for E in the CCD is higher by a large margin (32 %) compared to the E optimum from the augmented screening experiment. Therefore the model derived for E

in the augmented screening experiment is violated by the model resulting from the CCD, because the E optimum was predicted in a different experimental region. The opposite can be seen for all the other properties, including ξ and $\hat{\xi}$. Although these two properties also did not vary within the region of the CCD, the mean value of each response was lower than that predicted by the models derived in the augmented screening experiment. The models are thus validated, since they predicted optima at different locations than where the CCD was conducted. Along the same reasoning, the models for σ, $\hat{\sigma}$, F, $\hat{\text{F}}$ an ϵ_b are also validated, because the optima was observed at the location predicted by the models.

Table 41: Summary of the augmented screening experiment optima for the various mechanical properties considered.

Predicted optimum response			Layer height [mm]	Nozzle temperature [°C]	Infill density [%]	LDH loading [%]
σ	31.804	MPa	0.18	190	90	2
$\hat{\sigma}$	3.307 4	MPa g^{-1}	0.18	190	90	2
F	1.332 7	kN	0.18	190	90	2
$\hat{\text{F}}$	0.137 97	kN g^{-1}	0.18	190	90	2
ϵ_b	0.015 723	mm mm^{-1}	0.18	190	90	2
E	3.489 2	GPa	0.22	220	90	10
$\hat{E}$	0.378 81	GPa g^{-1}	0.27	190	10	10
ξ	2.646 4	kJ m^{-2}	0.42	220	90	2
$\hat{\xi}$	0.931 50	kJ m^{-2} g^{-1}	0.18	190	10	2

Table 42: Summary of the CCD means compared with the optima determined from the augmented screening experiment for the various mechanical properties considered.

Mean response			Infill density [%]	LDH loading [%]	Percentage increase [%]
σ	38.005	MPa	80 - 100	0 - 4	16.3
$\hat{\sigma}$	3.5028	MPa g^{-1}	80 - 100	0 - 4	5.6
F	1.5951	kN	80 - 100	0 - 4	16.4
$\hat{\text{F}}$	0.146 59	kN g^{-1}	80 - 100	0 - 4	6.9
ϵ_b	0.020 960	mm mm^{-1}	80 - 100	0 - 4	28.4
E	5.1464[a]	GPa	80	4	32.2
$\hat{E}$	statistical significant lack of fit				
ξ	2.3177	kJ m^{-2}	80 - 100	0 - 4	- 14.2
$\hat{\xi}$	0.760 92	kJ m^{-2} g^{-1}	80 - 100	0 - 4	- 22.4

[a] optimum, not mean (refer to § 4.5.8)

On that note, the elegance and efficiency of using statistics also became evident during experimentation. The screening experiment was only a 2^{4-1} fractional factorial experiment, and was augmented with a few random points within the region in order to fit quadratic models. Save for E and $\hat{\text{E}}$, all the models were validated by the CCD conducted later. This is because the predictions from the models were accurate. When they predicted an increase, it was observed, and the same for a predicted decrease. Considering that the experimental point where the optimum was predicted was part of the alternate half fraction, and the wide range of the respective factor levels, the models' validity are impressive. The models accurately predicted increases or decreases, even though the location of the optimum was not one of the points tested. The CCD showed that the precision of said models were not immaculate, since the increases observed for σ, $\hat{\sigma}$, F, $\hat{\text{F}}$ an ϵ_b were larger than predicted. This is not as concerning, because the augmented screening experiment spanned a large experimental region, and the CCD acted as a comprehensive validation experiment. The statistics also indicated that another factor influences E and $\hat{\text{E}}$, and that more research and experimentation is required for these properties. The statistics was not used to its full potential, and the screening experiment could have been conducted with 74 % less effort if this was realised earlier. This could have saved a lot of resources and time.

A comparison between tensile specimens manufactured by injection moulding and FDM showed that the former processing technique is superior to FDM in terms of mechanical properties. Even when properties are normalised with respect to mass, FDM tensile specimens were still inferior. The deterioration of properties with increasing LDH loading in injection moulded parts were not seen for printed parts in the CCD. Rheology tests on the feedstock material to the injection moulder and the filament extruder suggested degradation occurred during processing which was catalysed by the LDH. The latter has been well documented in literature, as shown in the systematic literature review, but more work can be done on optimising compounding conditions for LDH into PLA. It seems as if the decrease in viscosity had a more detrimental effect on injection moulded parts than on printed specimens. This might be because less viscous melts fuse together well and have more contact surface in the FDM process, thus combatting the expected decrease in polymer properties. Clearly both processing techniques have their respective advantages and disadvantages, and the right one should be selected for the right application.

Despite the degradation that occurred, the LDH_PLA printed parts compare well to other filled PLA printed parts, such as those manufactured by Prashantha & Roger (2017) and Vinyas *et al* (2019). Although this might be due to different grades of PLA used, it shows that if the degradation of PLA due to LDH can be limited, the filled filament has great potential in the FDM and AM industry.

The value of LDH can only be as a functional filler. It is clear that an increase in properties compared to pure PLA will not be achieved, and cheaper options for straight forward fillers are available. However, the multiplicity of applications of intercalated LDH are apparent. A variety of medical applications have been researched for intercalated LDH in PLA specifically as discussed in in the systematic literature review. Most of these required customised products. Moreover, since LDH acts as a carrier for some medicine or drug in each case, it would be beneficial to be able to customise the materials as well with different LDH loadings and as a result different amounts of medicine. The other applications that came up in the systematic literature review also showed potential for various other applications, although the value of the additive was always the intercalated substance instead of the LDH itself. For the first time it was shown that PLA filaments with up to 10 % LDH can be produced and successfully printed using FDM. This can be revolutionary to various industries, especially so for the medical and prosthetic industries where customisation is required. In fact, any product that can be derived from all the studies in the systematic literature review can benefit from these results.

5 Conclusions and Recommendations

For the first time, LDH filled PLA filament was used to print tensile and impact specimens with FDM. Mechanical properties for LDH loadings between 0.6 % and 10 % were reported, including ultimate tensile stress, ultimate tensile force, Young's modulus, impact energy, and all their normalised versions. The elongation at break was also reported.

From a thorough statistical experimental design and procedure it was determined that optimum σ, $\hat{\sigma}$, F, $\hat{\text{F}}$ and $\hat{\xi}$ properties occur at lower layer height and nozzle temperatures (0.18 mm and 190 °C). Infill density and LDH loading can be varied between 80 % and 100 % as well as 0 % and 4 %, respectively, without affecting said properties. Although ξ also do not change within this region, it had an optimum at the high levels of layer height and nozzle temperature (0.42 mm and 220 °C). The latter optimum was not statistically confirmed. Inconclusive results were found for E and $\hat{\text{E}}$, and it is expected that another factor affects the response that was not considered. The factor was not identified.

The results are significant for a variety of applications, of which medical applications show the most potential, as shown in a systematic literature review on LDH in PLA. This was the first review on this topic. Uses varied between medical, flame retardance and environmental applications, although LDH can be tailored for other uses as well. The ability of FDM to print customised parts at low cost and effort, combined with the medicinal benefits of LDH in PLA, creates the possibility of tremendous advancement in the field. Further work is required to determine if FDM printed parts are suitable for the production of specific artefacts, especially in terms of strength and the efficacy of intercalated substances. The same applies to other LDH uses.

For injection moulding, 0LDH_PLA, 2LDH_PLA and 10LDH_PLA granules were used. The FDM parts were still inferior. If normalised strengths are considered, FDM parts did have comparable strength, but it is expected that the injection moulding parameters can be further optimised. Contrary to injection moulding, FDM was able to retain more strength at high clay loadings. This might be of importance where LDH loadings in the region of 10 % are required, because it was shown that the PLA degraded during compounding, and that degradation increased with increasing LDH loading.

FDM tensile printed parts had fracture locations at the boundaries of the narrow section. These should rather be in the middle of said section. It was found that this is caused by the slicer settings, and does not affect the conclusions about tensile properties. It is recommended that other slicer software be investigated to see if this problem can be avoided. An improvement in mechanical properties is not expected, but might be possible.

One of the most impactful recommendations that can be made is that statistics should be fully exploited by future researchers, especially in natural sciences and engineering. In this work, the conclusion of screening experiment could have been made with 74 % less work if the statistics were applied correctly. It is a waste of resources and time to conduct experiments with a vast amount of replications, especially during the screening phase. The efficiency and output from research can be enhanced by a large margin, if statistical design of experiments and the analysis thereof are properly conducted.

It is recommended that more work be done on the printing of PLA filaments filled with LDH. Except for this work, no other research on the topic exists. With PLA dominating the FDM landscape, and projected to continue doing so, possibilities and applications are legion. It was also found that only one work exists with LDH filled ABS filament. Therefore, any polymer filled with LDH for FDM purposes can be researched to develop the field. The compounding process can be optimised to minimise degradation occurring because of processing. This will improve mechanical properties. The effect of different grades of LDH and PLA also still have to be investigated within this context. It is suggested that LDH_PLA filaments be tested for specific applications to see if FDM can be used to make strong enough parts, and if the intercalated substance remains functional. Moreover, other FDM parameters that influence part strength can also be investigated, because only three parameters were included in the scope of this work.

This work provided sufficient information on mechanical properties over a broad range of LDH loading, layer height, nozzle temperature and infill density levels. Characterisations, including DSC, FTIR, XRD and SEM, were completed at every step of the process. As such, useful information for any future research on this topic is now available. Moreover, because the systematic literature reviews were conducted using PRISMA guidelines, they can also be used by future researchers as a basis for a growing systematic literature review.

References

Adepu, S, Luo, H and Ramakrishna, S (2021) "Heparin-tagged PLA-PEG copolymer-encapsulated biochanin A-loaded (Mg/Al) LDH nanoparticles recommended for non-thrombogenic and anti-proliferative stent coating" *International Journal of Molecular Sciences*, *22*, (11) ISSN: 14220067 DOI: 10.3390/ijms22115433.

Amaro, LP, Cicogna, F, Passaglia, E, Morici, E, Oberhauser, W, Al-Malaika, S, Dintcheva, NT and Coiai, S (2016) "Thermo-oxidative stabilisation of poly(lactic acid) with antioxidant intercalated layered double hydroxides" *Polymer Degradation and Stability*, *133*, 92–100 ISSN: 01413910 DOI: 10.1016/j.polymdegradstab.2016.08.005.

Anton Paar GmbH (2023) *Basics of rheology* URL: https://wiki.anton-paar.com/us-en/basics-of-rheology/%5C#introduction-to-rheology (visited on 2023-10-17).

ASTM D1238 (2023) *ASTM D1238-23 Standard test method for melt flow rates of thermoplastics by extursion plastomer* American Society for Testing Materials International URL: https://www.astm.org/standards/d1238.

ASTM D6110 (2018) *ASTM D6110-18 Standard test method for determining the Charpy impact resistance of notched specimens of plastics* American Society for Testing Materials International URL: https://www.astm.org/standards/d6110.

ASTM D638 (2022) *ASTM D638-22 Standard test method for tensile properties of plastics* American Society for Testing Materials International URL: https://www.astm.org/d0638-22.html.

Baltazar-y-Jimenez, A and Sain, M (2012) "Effect of bismaleimide reactive extrusion on the crystallinity and mechanical performance of poly(lactic acid) green composites" *Journal of Applied Polymer Science*, *124*, (4) ISSN: 00218995 DOI: 10.1002/app.35331.

Bardot, M and Schulz, MD (2020) "Biodegradable poly(lactic acid) nanocomposites for fused deposition modelling 3D printing" *Nanomaterials*, *10*, (12) ISSN: 20794991 DOI: 10.3390/nano10122567.

Benvenutti, DF, Bresolin, TMB, Corrêa, R, Giovagnoli, S, Vivani, R and Ricci, M (2019) "A novel stabilising approach to improve the manufacturing of biodegradable microparticles entrapping plasticizing active molecules: the case of 4-methoxychalcone" *Journal*

of Pharmaceutical Innovation, *14*, (2): 159–175 ISSN: 19398042 DOI: 10.1007/s12247-018-9346-9.

Bugatti, V, Livi, S, Hayrapetyan, S, Wang, Y, Estevez, L, Vittoria, V and Giannelis, EP (2013) "Deposition of LDH on plasma treated polylactic acid to reduce water permeability" *Journal of Colloid and Interface Science*, *396*, 47–52 ISSN: 00219797 DOI: 10.1016/j.jcis.2013.01.006.

Carreau, P, De Kee, D and Chhabra, R (2021) *Understanding Polymer Processing*, 2nd Hanser, München ISBN: 9781569907238.

Chakraborti, M, Jackson, J, Plackett, D, Brunette, D and Burt, H (2011) "Drug intercalation in layered double hydroxide clay: Application in the development of a nanocomposite film for guided tissue regeneration" *International Journal of Pharmaceutics*, *416*, (1): 305–313 DOI: 10.1016/j.ijpharm.2011.06.016.

Chakraborti, M, Jackson, J, Plackett, D, Gilchrist, S and Burt, H (2012) "The application of layered double hydroxide clay (LDH)-poly(lactide-co- glycolic acid) (PLGA) film composites for the controlled release of antibiotics" *Journal of Materials Science: Materials in Medicine*, *23*, (7): 1705–1713 DOI: 10.1007/s10856-012-4638-y.

Chatterjee, A and Hansora, D (2016) "Green polymer nanocomposites: preparation, properties and biomedical applications", in: *Green Polymer Composite Technology: Preparation and Properties*, CRC Press ISBN: 9781315371184.

Chatterjee, A, Bharadiya, P and Hansora, D (2019) "Layered double hydroxide based bionanocomposites" *Applied Clay Science*, *177*, 19–36 ISSN: 01691317 DOI: 10.1016/j.clay.2019.04.022.

Cheng, XQ, Liu, W, Zhang, C, Chen, XC, Duan, SQ and Fu, H (2022) "Synthesis and electrospinning of multiscale-ordered PLA/LDH@AgGB composite nanofibrous membrane for antibacterial and oil–water separation" *Journal of Applied Polymer Science*, *139*, (28) ISSN: 10974628 DOI: 10.1002/app.52621.

Chiang, MF, Chu, MZ and Wu, TM (2011) "Effect of layered double hydroxides on the thermal degradation behaviour of biodegradable poly(l-lactide) nanocomposites" *Polymer Degradation and Stability*, *96*, (1): 60–66 ISSN: 01413910 DOI: 10.1016/j.polymdegradstab.2010.11.002.

Chiang, MF and Wu, TM (2008) "Thermal degradation of novel exfoliated PLLA/LDH nanocomposites" *Advanced Materials Research*, *47-50 PART 1*, 415–418 DOI: 10.4028/www.scientific.net/amr.47-50.415.

Chiang, MF and Wu, TM (2010) "Synthesis and characterisation of biodegradable poly(l-lactide)/layered double hydroxide nanocomposites" *Composites Science and Technology*, *70*, (1): 110–115 ISSN: 02663538 DOI: 10.1016/j.compscitech.2009.09.012.

Chouzouri, G and Xanthos, M (2003) "Modification of biodegradable polyesters with inorganic fillers", in: *Annual Technical Conference - ANTEC, Conference Proceedings*, *2*, pp. 2561–2565.

Coiai, S, Cicogna, F, De Santi, A, Amaro, LP, Spiniello, R, Signori, F, Fiori, S, Oberhauser, W and Passaglia, E (2017) "MMT and LDH organo-modification with surfactants tailored for PLA nanocomposites" *Express Polymer Letters*, *11*, (3): 163–175 ISSN: 1788618X DOI: 10.3144/expresspolymlett.2017.18.

Coiai, S, Javarone, S, Cicogna, F, Oberhauser, W, Onor, M, Pucci, A, Minei, P, Iasilli, G and Passaglia, E (2018) "Fluorescent LDPE and PLA nanocomposites containing fluorescein-modified layered double hydroxides and their ON/OFF responsive behaviour towards humidity" *European Polymer Journal*, *99*, 189–201 ISSN: 00143057 DOI: 10.1016/j.eurpolymj.2017.12.021.

Dagnon, KL, Ambadapadi, RS, Shaito, A, Ogbomo, SM, Deleon, V, Golden, TD, Rahimi, M, Nguyen, K, Braterman, PS and D'souza, NA (2009) "Poly(L-lactic acid) nanocomposites with layered double hydroxides functionalized with ibuprofen" *Journal of Applied Polymer Science*, *113*, (3): 1905–1915 ISSN: 00218995 DOI: 10.1002/app.30159.

Dai, Y, Cao, H, Yu, X, Han, D, Tian, H, Guo, L and Zhou, X (2022) "Ammonium polyphosphate intercalated yttrium-doped layered double hydroxides to enhance the thermal stability and flame retardancy of poly(lactic acid)" *Advances in Polymer Technology*, *2022*, ISSN: 10982329 DOI: 10.1155/2022/9205119.

De Roy, A, Forano, C, El Malki, K and Besse, J (1992) "Anionic Clays: Trends in Pillaring Chemistry", in: *Expanded Clays and Other Microporous Solids*, Occelli, ML and Robson, HE (Eds.), Springer ISBN: 9781468488685.

Delpouve, N, Saiter, A and Dargent, E (2011) "Cooperativity length evolution during crystallisation of poly(lactic acid)" *European Polymer Journal*, *47*, (12) ISSN: 00143057 DOI: 10.1016/j.eurpolymj.2011.09.027.

Delpouve, N, Saiter-Fourcin, A, Coiai, S, Cicogna, F, Spiniello, R, Oberhauser, W, Legnaioli, S, Ishak, R and Passaglia, E (2020) "Effects of organo-LDH dispersion on thermal stability, crystallinity and mechanical features of PLA" *Polymer*, *208*, ISSN: 00323861 DOI: 10.1016/j.polymer.2020.122952.

Demirkaya, ZD, Sengul, B, Eroglu, MS and Dilsiz, N (2015) "Comprehensive characterisation of polylactide-layered double hydroxides nanocomposites as packaging materials" *Journal of Polymer Research*, *22*, (7) ISSN: 10229760 DOI: 10.1007/s10965-015-0759-6.

Dilberoglu, UM, Gharehpapagh, B, Yaman, U and Dolen, M (2017) "The role of additive manufacturing in the era of Industry 4.0" *Procedia Manufacturing*, *11*, DOI: 10.1016/j.promfg.2017.07.148.

Ding, P, Kang, B, Zhang, J, Yang, J, Song, N, Tang, S and Shi, L (2015) "Phosphorus-containing flame retardant modified layered double hydroxides and their applications on polylactide film with good transparency" *Journal of Colloid and Interface Science*, *440*, 46–52 ISSN: 10957103 DOI: 10.1016/j.jcis.2014.10.048.

Du Plessis, J, Du Preez, S and Stefaniak, AB (2022) *Identification of effective control technologies for additive manufacturing* DOI: 10.1080/10937404.2022.2092569.

Eili, M, Shameli, K, Ibrahim, NA and Yunus, WMZW (2012) "Degradability enhancement of poly(lactic acid) by stearate-$Zn_3$3Al LDH nanolayers" *International Journal of Molecular Sciences*, *13*, (7): 7938–7951 ISSN: 14220067 DOI: 10.3390/ijms13077938.

Feng, LD, Sun, B, Bian, XC, Chen, ZM and Chen, XS (2010) "Determination of d-lactate content in poly(lactic acid) using polarimetry" *Polymer Testing*, *29*, (7) ISSN: 01429418 DOI: 10.1016/j.polymertesting.2010.06.005.

Figueiredo, MP, Layrac, G, Hébraud, A, Limousy, L, Brendle, J, Schlatter, G and Constantino, VR (2020) "Design of 3D multi-layered electrospun membranes embedding iron-based layered double hydroxide for drug storage and control of sustained release" *European Polymer Journal*, *131*, ISSN: 00143057 DOI: 10.1016/j.eurpolymj.2020.109675.

Forano, C, Hibino, T, Leroux, F and Taviot-Guého, C (2006) "Layered Double Hydroxides", in: *Handbook of Clay Science*, Bergaya, F, Theng, B and Lagaly, G (Eds.), Elsevier DOI: 10.1016/S1572-4352(05)01039-1.

Gardan, J (2016) "Additive manufacturing technologies: State of the art and trends" *International Journal of Production Research*, *54*, ISSN: 1366588X DOI: 10.1080/00207543.2015.1115909.

Geng, Z, Bian, S, Zhen, W, Song, Z and Wang, X (2019) "Preparation, structure-property relationships of zinc oxide pillared organic layered double hydroxides and its effect on the performance of poly (lactic acid)" *Polymer-Plastics Technology and Materials*, *58*, (6): 641–655 ISSN: 2574089X DOI: 10.1080/03602559.2018.1520246.

Geng, Z and Zhen, W (2019a) "Preparation, characterisation, structure-property relationships, and thermal degradation kinetics of poly (lactic acid)/amidated potassium hydrogen phthalate intercalated layered double hydroxides nanocomposites" *Polymers for Advanced Technologies*, *30*, (3): 504–518 ISSN: 10991581 DOI: 10.1002/pat.4486.

Geng, Z and Zhen, W (2019b) "Preparation, performance, and kinetics of poly(lactic-acid)/amidated benzoic acid intercalated layered double hydroxides nanocomposites by reactive extrusion process" *Polymer Composites*, *40*, (7): 2668–2680 ISSN: 15480569 DOI: 10.1002/pc.25064.

Geng, Z, Zhen, W, Song, Z and Wang, X (2018a) "Structure and performance of poly(lactic acid)/amide ethylenediamine tetraacetic acid disodium salt intercalation layered double hydroxides nanocomposites" *Journal of Polymer Research*, *25*, (5) ISSN: 15728935 DOI: 10.1007/s10965-018-1482-x.

Geng, Z, Zhen, W, Song, Z and Wang, X (2018b) "Synthesis, characterisation of layered double hydroxide-poly(methylmethacrylate) graft copolymers via activators regenerated by electron transfer for atom transfer radical polymerisation and its effect on the performance of poly(lactic acid)" *Polymers for Advanced Technologies*, *29*, (6): 1765–1778 ISSN: 10991581 DOI: 10.1002/pat.4283.

Gerds, N, Katiyar, V, Koch, CB, Hansen, HCB, Plackett, D, Larsen, EH and Risbo, J (2012) "Degradation of l-polylactide during melt processing with layered double hydroxides" *Polymer Degradation and Stability*, *97*, (10): 2002–2009 ISSN: 01413910 DOI: 10.1016/j.polymdegradstab.2012.04.014.

Gong, Y, Zhang, D, He, M, Song, W, Li, L and Yu, J (2018) "Progress in grassroots nanocomposites based on poly(lactic acid)" *Gaofenzi Cailiao Kexue Yu Gongcheng/Polymeric Materials Science and Engineering*, *34*, (6): 184–190 DOI: 10.16865/j.cnki.1000-7555.2018.06.032.

Ha, JU and Xanthos, M (2009) "Polylactic acid composites based on ionic liquid modified cationic and anionic clays", in: *Annual Technical Conference - ANTEC, Conference Proceedings*, *2*, pp. 1136–1141 ISBN: 9781615673278.

Ha, JU and Xanthos, M (2010) "Novel modifiers for layered double hydroxides and their effects on the properties of polylactic acid composites" *Applied Clay Science*, *47*, (3-4): 303–310 ISSN: 01691317 DOI: 10.1016/j.clay.2009.11.033.

He, S (2019) "Organic modification of inorganic ions (montmorillonite, hydrotalcite) and its application in polylactic acid-based nanocomposites", in: *IOP Conference Series: Earth and Environmental Science*, *300*, Institute of Physics Publishing DOI: 10.1088/1755-1315/300/2/022109.

Hennous, M, Derriche, Z, Privas, E, Navard, P, Verney, V and Leroux, F (2013) "Lignosulfonate interleaved layered double hydroxide: a novel green organoclay for bio-related polymer" *Applied Clay Science*, *71*, 42–48 ISSN: 01691317 DOI: 10.1016/j.clay.2012.10.011.

Hu, Z, Zhang, P, Xie, R, Li, M, Lu, Z, Xu, X, Song, L, Zhou, L, Wu, Y, Chen, M and Zhao, X (2018) "Controlled synthesis of train-structured montmorillonite/layered double hydroxide nanocomposites by regulating the hydrolysis of polylactic acid" *Journal of Materials Science*, *53*, (23): 15859–15870 ISSN: 15734803 DOI: 10.1007/s10853-018-2758-6.

Iancu, C (2018) "About 3D printing file formats" *Annals of the ,,Constantin Brancusi" University of Targu Jiu, Engineering Series*, (2).

ISO 1133 (2022) *ISO 1133-1:2022 Plastics — Determination of the melt mass-flow rate (MFR) and melt volume-flow rate (MVR) of thermoplastics* International Organisation for Standardisation URL: https://www.iso.org/standard/83905.html.

ISO 179 (2010) *ISO 179-1:2010 Plastics — Determination of Charpy impact properties* International Organisation for Standardisation URL: https://www.iso.org/standard/44852.html.

ISO 527 (2019) *ISO 527-1:2019 Plastics — Determination of tensile properties* International Organisation for Standardisation URL: https://www.iso.org/standard/75824.html.

Jilili, Y, Zhen, W, Li, H and Luo, D (2022) "Preparation of modified hydrotalcite based on click chemistry and its effect on the shear induced crystallisation, rheological behaviour and thermal degradability of poly(lactic acid) film" *Polymer-Plastics Technology and Materials*, *61*, (10): 1102–1117 DOI: 10.1080/25740881.2022.2033773.

Jin, X, Gu, X, Chen, C, Tang, W, Li, H, Liu, X, Bourbigot, S, Zhang, Z, Sun, J and Zhang, S (2017) "The fire performance of polylactic acid containing a novel intumescent flame retardant and intercalated layered double hydroxides" *Journal of Materials Science*, *52*, (20): 12235–12250 ISSN: 15734803 DOI: 10.1007/s10853-017-1354-5.

Katiyar, V, Gerds, N, Koch, CB, Risbo, J, Hansen, HCB and Plackett, D (2010) "Poly l-lactide-layered double hydroxide nanocomposites via in situ polymerisation of l-lactide" *Polymer Degradation and Stability*, *95*, (12): 2563–2573 ISSN: 01413910 DOI: 10.1016/j.polymdegradstab.2010.07.031.

Katiyar, V, Gerds, N, Koch, CB, Risbo, J, Hansen, HCB and Plackett, D (2011) "Melt processing of poly(L-lactic acid) in the presence of organomodified anionic or cationic clays" *Journal of Applied Polymer Science*, *122*, (1): 112–125 ISSN: 00218995 DOI: 10.1002/app.33984.

Kim, MH, Hur, W, Choi, G, Min, HS, Choi, TH, Choy, YB and Choy, JH (2016) "Theranostic bioabsorbable bone fixation plate with drug-layered double hydroxide nanohybrids" *Advanced Healthcare Materials*, *5*, (21): 2765–2775 ISSN: 21922659 DOI: 10.1002/adhm.201600761.

Krajangsawasdi, N, Blok, LG, Hamerton, I, Longana, ML, Woods, BK and Ivanov, DS (2021) "Fused deposition modelling of fibre reinforced polymer composites: A parametric review" *Journal of Composites Science*, *5*, (1) ISSN: 2504477X DOI: 10.3390/jcs5010029.

Krüss Optronic GmbH (2005) *Operating manual: automatic digital polarimeter P 3001/3002 RS*.

Lei, Y, Mao, L, Yao, J and Li, Z (2020) "Efficient gas barrier and antibacterial properties of poly(lactic acid) nanocomposites: functionalization with phytic acid-Cu(II) loaded layered clay" *Materials*, *13*, (9) ISSN: 19961944 DOI: 10.3390/MA13092033.

Leng, J, Kang, N, Wang, DY, Falkenhagen, J, Thünemann, AF and Schönhals, A (2017a) "Structure–property relationships of nanocomposites based on polylactide and layered double hydroxides – comparison of MgAl and NiAl LDH as nanofiller" *Macromolecular Chemistry and Physics*, *218*, (20) ISSN: 15213935 DOI: 10.1002/macp.201700232.

Leng, J, Kang, N, Wang, DY, Wurm, A, Schick, C and Schönhals, A (2017b) "Crystallisation behaviour of nanocomposites based on poly(L-lactide) and MgAl layered double hydroxides – unbiased determination of the rigid amorphous phases due to the crystals and the nanofiller" *Polymer*, *108*, 257–264 ISSN: 00323861 DOI: 10.1016/j.polymer.2016.11.065.

Leng, J, Purohit, PJ, Kang, N, Wang, DY, Falkenhagen, J, Emmerling, F, Thünemann, AF and Schönhals, A (2015) "Structure-property relationships of nanocomposites based on polylactide and MgAl layered double hydroxides" *European Polymer Journal*, *68*, 338–354 ISSN: 00143057 DOI: 10.1016/j.eurpolymj.2015.05.008.

Lim, LT, Auras, R and Rubino, M (2008) "Processing technologies for poly(lactic acid)" *Progress in Polymer Science*, *33*, ISSN: 00796700 DOI: 10.1016/j.progpolymsci.2008.05.004.

Liu, H, Huang, Z, Chen, X, Chen, Y, Lian, H and Li, C (2021a) "Preparation and performance study of hydrotalcites/PLA composites", in: *E3S Web of Conferences*, *257*, EDP Sciences DOI: 10.1051/e3sconf/202125701073.

Liu, H, Huang, Z, Chen, X, Zhong, J, Wang, Y, He, X and Liu, X (2021b) "Preparation and properties of hydrotalcite inorganic filler / polylactic acid composites", in: *Journal of Physics: Conference Series*, *2009*, IOP Publishing Ltd DOI: 10.1088/1742-6596/2009/1/012009.

Livi, S, Bugatti, V, Estevez, L, Duchet-Rumeau, J and Giannelis, EP (2012) "Synthesis and physical properties of new layered double hydroxides based on ionic liquids: application to a polylactide matrix" *Journal of Colloid and Interface Science*, *388*, (1): 123–129 ISSN: 00219797 DOI: 10.1016/j.jcis.2012.08.031.

Lütkemeyer, M (2023) *3D printing layer height vs nozzle size — table and guide* URL: https://the3dprinterbee.com/3d-printing-layer-height-vs-nozzle-size/ (visited on 2023-02-17).

Mahboobeh, E, Yunus, WMZW, Hussein, Z, Ahmad, M and Ibrahim, NA (2010) "Flexibility improvement of poly(lactic acid) by stearate-modified layered double hydroxide" *Journal of Applied Polymer Science*, *118*, (2): 1077–1083 ISSN: 00218995 DOI: 10.1002/app.32461.

Malafatti, JO, Bernardo, MP, Moreira, FK, Ciol, H, Inada, NM, Mattoso, LH and Paris, EC (2020) "Electrospun poly(lactic acid) nanofibres loaded with silver sulfadiazine/[Mg–Al]-layered double hydroxide as an antimicrobial wound dressing" *Polymers for Advanced Technologies*, *31*, (6): 1377–1387 ISSN: 10991581 DOI: 10.1002/pat.4867.

Mallakpour, S and Khadem, E (2018) "Applications of biodegradable polymer/layered double hydroxide nanocomposites: current status and recent prospects", in: *Biodegradable and Biocompatible Polymer Composites*, Woodhead Publishing: pp. 265–296 ISBN: 978-0-08-100970-3 DOI: https://doi.org/10.1016/B978-0-08-100970-3.00009-2.

Mallikarjuna, B, Bhargav, P, Hiremath, S, Jayachristiyan, KG and Jayanth, N (2023) *A review on the melt extrusion-based fused deposition modelling (FDM): background, materials, process parameters and military applications* DOI: 10.1007/s12008-023-01354-0.

Mao, L, Bai, Z, Yao, J and Liu, Y (2022) "Development of novel poly(lactic acid) active multilayer composite films by incorporating catechol-functionalized layered clay into chitosan/poly(vinyl alcohol) coatings" *Progress in Organic Coatings*, *170*, 107000 ISSN: 03009440 DOI: 10.1016/j.porgcoat.2022.107000.

McCarthy, ED, Zammarano, M, Fox, DM, Nieuwendaal, RC, Kim, YS, Maupin, PH, Trulove, PC and Gilman, JW (2013) "Formation of extended ionomeric network by bulk polymerisation of l,d-lactide with layered-double-hydroxide" *Polymer*, *54*, (1): 90–101 ISSN: 00323861 DOI: 10.1016/j.polymer.2012.11.037.

Medibew, TM (2022) "A comprehensive review on the optimisation of the fused deposition modelling process parameter for better tensile strength of PLA printed parts" *Advances in Materials Science and Engineering*, ISSN: 16878442 DOI: 10.1155/2022/5490831.

Menard, K (2008) *Dynamic Mechanical Analysis: A Practical Introduction*, 2nd ed. CRC Press ISBN: 9781420053128.

Mhlabeni, T, Pillai, SK and Ray, SS (2020) "Effect of organically modified layered double hydroxides on the properties of poly(lactic acid)/poly[(butylene succinate)-co-adipate]

immiscible blends" *Journal of Applied Polymer Science*, *137*, (19) ISSN: 10974628 DOI: 10.1002/app.48654.

Miao, YE, Zhu, H, Chen, D, Wang, R, Tjiu, WW and Liu, T (2012) "Electrospun fibres of layered double hydroxide/biopolymer nanocomposites as effective drug delivery systems" *Materials Chemistry and Physics*, *134*, (2-3): 623–630 ISSN: 02540584 DOI: 10.1016/j.matchemphys.2012.03.041.

Monshizadeh, M, Seifi, S, Hejazi, I, Seyfi, J and Khonakdar, HA (2021) "Enhanced properties of poly(lactic acid) by concurrent addition of organo-modified Mg-Al layered double hydroxide (LDH) and triethyl citrate" *Journal of Thermoplastic Composite Materials*, *34*, (10): 1334–1349 ISSN: 15307980 DOI: 10.1177/0892705719868272.

Montgomery, DC (2013) *Design and Analysis of Experiments*, 8th ed. John Wiley & Sons ISBN: 9781118097939.

Mwema, FM and Akinlabi, ET (2020) "Basics of fused deposition modelling (FDM)", in: *Briefs in Applied Sciences and Technology*, Springer DOI: 10.1007/978-3-030-48259-6_1.

Neppalli, R, Causin, V, Marega, C, Modesti, M, Adhikari, R, Scholtyssek, S, Ray, SS and Marigo, A (2014) "The effect of different clays on the structure, morphology and degradation behaviour of poly(lactic acid)" *Applied Clay Science*, *87*, 278–284 ISSN: 01691317 DOI: 10.1016/j.clay.2013.11.029.

Ngo, TD, Kashani, A, Imbalzano, G, Nguyen, KT and Hui, D (2018) "Additive manufacturing (3D printing): A review of materials, methods, applications and challenges" *Composites Part B: Engineering*, *143*, ISSN: 13598368 DOI: 10.1016/j.compositesb.2018.02.012.

Nguyen, DM, Vu, TN, Nguyen, TML, Nguyen, TD, Thuc, CNH, Bui, QB, Colin, J and Perré, P (2020) "Synergistic influences of stearic acid coating and recycled PET microfibres on the enhanced properties of composite materials" *Materials*, *13*, (6) ISSN: 19961944 DOI: 10.3390/ma13061461.

Osswald, TA (2017) *Understanding Polymer Processing*, 2nd Hanser, München ISBN: 9781569906477 DOI: 10.3139/9781569906484.fm.

Oyarzabal, A, Mugica, A, Müller, AJ and Zubitur, M (2016) "Hydrolytic degradation of nanocomposites based on poly(l -lactic acid) and layered double hydroxides modified with a model drug" *Journal of Applied Polymer Science*, *133*, (28) ISSN: 10974628 DOI: 10.1002/app.43648.

Ozturk, EA, Ege, ZR, Murat, S, Erdemir, G, Kuruca, S, Erkmen, ZE, Duygulu, O, Gunduz, O, Caykara, T and Eroglu, MS (2022) "Poly(L-lactic acid)/poly(ethylene oxide) based composite electrospun fibres loaded with magnesium-aluminium layered double hydroxide nanoparticles" *International Journal of Biological Macromolecules*, *217*, 562–571 ISSN: 01418130 DOI: 10.1016/j.ijbiomac.2022.07.055.

Page, MJ, McKenzie, JE, Bossuyt, PM, Boutron, I, Hoffmann, TC, Mulrow, CD, Shamseer, L, Tetzlaff, JM, Akl, EA, Brennan, SE, Chou, R, Glanville, J, Grimshaw, JM, Hróbjartsson, A, Lalu, MM, Li, T, Loder, EW, Mayo-Wilson, E, McDonald, S, McGuinness, LA, Stewart, LA, Thomas, J, Tricco, AC, Welch, VA, Whiting, P and Moher, D (2021) "The PRISMA 2020 statement: an updated guideline for reporting systematic reviews" *The BMJ*, *372*, ISSN: 17561833 DOI: 10.1136/bmj.n71.

Pan, P, Zhu, B, Dong, T and Inoue, Y (2008) "Poly(L-lactide)/layered double hydroxides nanocomposites: preparation and crystallisation behaviour" *Journal of Polymer Science, Part B: Polymer Physics*, *46*, (20): 2222–2233 ISSN: 08876266 DOI: 10.1002/polb.21554.

Plackett, D (2011) "Summary and Future Perspectives", in: *Biopolymers - New Materials for Sustainable Films and Coatings*, pp. 317–323 ISBN: 9780470683415 DOI: 10.1002/9781119994312.ch15.

Prashantha, K and Roger, F (2017) "Multifunctional properties of 3D printed poly(lactic acid)/graphene nanocomposites by fused deposition modelling" *Journal of Macromolecular Science, Part A: Pure and Applied Chemistry*, *54*, (1) ISSN: 15205738 DOI: 10.1080/10601325.2017.1250311.

Pu, L, Yu, H, Du, J, Zhang, Y and Chen, S (2020) "Hydrotalcite-PLGA composite nanoparticles for loading and delivery of danshensu" *RSC Advances*, *10*, (37): 22010–22018 ISSN: 20462069 DOI: 10.1039/d0ra01593h.

Quispe-Dominguez, R, Naseem, S, Leuteritz, A and Kuehnert, I (2019) "Synthesis and characterisation of MgAl-DBS LDH/PLA composite by sonication-assisted masterbatch (SAM) melt mixing method" *RSC Advances*, *9*, (2): 658–667 ISSN: 20462069 DOI: 10.1039/c8ra08780f.

Ray, S, Saha, S, Sa, B and Chakraborty, J (2017) "In vivo pharmacological evaluation and efficacy study of methotrexate-encapsulated polymer-coated layered double hydroxide nanoparticles for possible application in the treatment of osteosarcoma" *Drug Delivery and Translational Research*, *7*, (2): 259–275 ISSN: 21903948 DOI: 10.1007/s13346-016-0351-6.

Righetti, MC, Gazzano, M, Lorenzo, MLD and Androsch, R (2015) "Enthalpy of melting of α'- and α-crystals of poly(L-lactic acid)" *European Polymer Journal*, *70*, ISSN: 00143057 DOI: 10.1016/j.eurpolymj.2015.07.024.

Rives, V, Holgado, P, Holgado, M and Román, MS (2014) "Controlled drug delivery systems based on PLA", in: *New Developments in Polylactic Acid Research*, pp. 27–78 ISBN: 9781634630931.

Ruiz-Hitzky, E, Aranda, P, Darder, M and Rytwo, G (2010) "Hybrid materials based on clays for environmental and biomedical applications" *Journal of Materials Chemistry*, *20*, (42): 9306–9321 ISSN: 09599428 DOI: 10.1039/c0jm00432d.

Sahithya, K, Das, D and Das, N (2016) "Biopolymers fabricated Mg-Fe layered double hydroxide/montmorillonite nanobiocomposites for effective removal of dichlorvos from aqueous environment: equilibrium, kinetics, thermodynamics and Ex-situ studies" *International Journal of Pharmacy and Technology*, *8*, (4): 22062–22084.

San Román, MS, Holgado, MJ, Salinas, B and Rives, V (2013) "Drug release from layered double hydroxides and from their polylactic acid (PLA) nanocomposites" *Applied Clay Science*, *71*, 1–7 ISSN: 01691317 DOI: 10.1016/j.clay.2012.10.014.

Sandanamsamy, L, Harun, WS, Ishak, I, Romlay, FR, Kadirgama, K, Ramasamy, D, Idris, SR and Tsumori, F (2022) "A comprehensive review on fused deposition modelling of polylactic acid" *Progress in Additive Manufacturing*, ISSN: 23639520 DOI: 10.1007/s40964-022-00356-w.

Scaffaro, R, Botta, L, Passaglia, E, Oberhauser, W, Frediani, M and Landro, LD (2014) "Comparison of different processing methods to prepare poly(lactid acid)-hydrotalcite composites" *Polymer Engineering and Science*, *54*, (8): 1804–1810 ISSN: 15482634 DOI: 10.1002/pen.23724.

Scaffaro, R, Sutera, F, Mistretta, MC, Botta, L and Mantia, FPL (2017) "Structure-properties relationships in melt reprocessed PLA/hydrotalcites nanocomposites" *Express*

Polymer Letters, *11*, (7): 555–564 ISSN: 1788618X DOI: 10.3144/expresspolymlett.2017.53.

Schmidt, B, Katiyar, V, Plackett, D, Larsen, EH, Gerds, N, Koch, CB and Petersen, JH (2011) "Migration of nanosized layered double hydroxide platelets from polylactide nanocomposite films" *Food Additives and Contaminants - Part A Chemistry, Analysis, Control, Exposure and Risk Assessment*, *28*, (7): 956–966 ISSN: 19440049 DOI: 10.1080/19440049.2011.572927.

Seeliger, F, Bester, KM, Mentz, J and Labuschagné, FJWJ (2017) "Nano-additives for use in 3D printing polymers", in: *RAPDASA 18th Annual Conference*,

Shan, X, Jiang, K, Song, Y and Li, J (2018) "Flame resistance of polylactic acid with cyclophosphazene derivative and NiAl layered double hydroxide doped Zn" *Polymer Composites*, *39*, (11): 3994–3999 ISSN: 15480569 DOI: 10.1002/pc.24446.

Shan, X, Song, L, Xing, W, Hu, Y and Lo, S (2012) "Effect of nickel-containing layered double hydroxides and cyclophosphazene compound on the thermal stability and flame retardancy of poly(lactic acid)" *Industrial and Engineering Chemistry Research*, *51*, (40): 13037–13045 ISSN: 15205045 DOI: 10.1021/ie300589p.

Shi, X, Rosa, R and Lazzeri, A (2010) "On the coating of precipitated calcium carbonate with stearic acid in aqueous medium" *Langmuir*, *26*, (11) ISSN: 07437463 DOI: 10.1021/la904914h.

Skoog, DA, Holler, FJ and Crouch, SR (2018) *Principles of Instrumental Analysis*, 7th ed. Cengage ISBN: 9781305577213.

Syrlybayev, D, Zharylkassyn, B, Seisekulova, A, Akhmetov, M, Perveen, A and Talamona, D (2021) "Optimisation of strength properties of FDM printed parts — a critical review" *Polymers*, *13*, ISSN: 20734360 DOI: 10.3390/polym13101587.

Teh, S, Ahmad, M, Shameli, K, Ibrahim, N, Zainuddin, N and Then, Y (2014) "Mechanical and morphological properties of sterate modified layered double hydroxide blend with poly(hydroxybutyrate)/poly(lactic acid) nanocomposites" *Digest Journal of Nanomaterials and Biostructures*, *9*, (2): 831–840.

Tipachan, C, Gupta, RK, Agarwal, S and Kajorncheappunngam, S (2020) "Flame retardant properties and thermal stability of polylactic acid filled with layered double hydrox-

ide and rice husk ash silica" *Journal of Polymers and the Environment*, *28*, (3): 948–961 ISSN: 15728919 DOI: 10.1007/s10924-020-01658-2.

Tipachan, C, Gupta, RK and Kajorncheappunngam, S (2019) "Water vapour barrier property of PLA nanocomposites using rice husk ash and layered double hydroxides as fillers" *Engineering and Applied Science Research*, *46*, (4): 285–291 ISSN: 25396218 DOI: 10.14456/easr.2019.32.

Tipachan, C and Kajorncheappunngam, S (2017) "Biodegradable poly(lactic acid)/Perkalite clay nanocomposites: gas barrier properties" *Key Engineering Materials*, *718*, 10–14 DOI: 10.4028/www.scientific.net/KEM.718.10.

Tuckey, J (1977) *Exploratory Data Analysis*, Addison-Wesley, Reading, Massachusetts ISBN: 9780201076165.

Valentina, I, Haroutioun, A, Fabrice, L, Vincent, V and Roberto, P (2017) "Tuning the hydrolytic degradation rate of poly-lactic acid (PLA) to more durable applications", in: *AIP Conference Proceedings*, American Institute of Physics Inc. ISBN: 9780735416062 DOI: 10.1063/1.5016801.

Valentina, I, Haroutioun, A, Fabrice, L, Vincent, V and Roberto, P (2018) "Poly(lactic acid)-based nanobiocomposites with modulated degradation rates" *Materials*, *11*, (10) ISSN: 19961944 DOI: 10.3390/ma11101943.

Valino, AD, Dizon, JRC, Espera, AH, Chen, Q, Messman, J and Advincula, RC (2019) "Advances in 3D printing of thermoplastic polymer composites and nanocomposites" *Progress in Polymer Science*, *98*, ISSN: 0079-6700 DOI: https://doi.org/10.1016/j.progpolymsci.2019.101162.

Vinyas, M, Athul, SJ, Harursampath, D and Thoi, TN (2019) "Mechanical characterisation of the poly lactic acid (PLA) composites prepared through the fused deposition modelling process" *Materials Research Express*, *6*, (10) ISSN: 20531591 DOI: 10.1088/2053-1591/ab3ff3.

Vishal, K, Rajkumar, K, Sabarinathan, P and Dhinakaran, V (2022) "Mechanical and wear characteristics investigation on 3D printed silicon filled poly(lactic acid) biopolymer composite fabricated by fused deposition modelling" *Silicon*, *14*, (15) ISSN: 18769918 DOI: 10.1007/s12633-022-01712-9.

Wang, DY, Leuteritz, A, Wang, YZ, Wagenknecht, U and Heinrich, G (2010) "Preparation and burning behaviours of flame retarding biodegradable poly(lactic acid) nanocomposite based on zinc aluminium layered double hydroxide" *Polymer Degradation and Stability*, *95*, (12): 2474–2480 ISSN: 01413910 DOI: 10.1016/j.polymdegradstab.2010.08.007.

Wang, MM, Li, HL and Liu, MR (2019) "Preparation and properties of polylactic acid-based composite fluorescent membrane based on layer-by-layer assembly" *Express Polymer Letters*, *13*, (7): 673–684 ISSN: 1788618X DOI: 10.3144/expresspolymlett.2019.56.

Wei, Z, Cai, C, Huang, Y, Wang, P, Song, J, Deng, L and Fu, Y (2021) "Eco-friendly strategy to a dual-2D graphene-derived complex for poly(lactic acid) with exceptional smoke suppression and low CO2 production" *Journal of Cleaner Production*, *280*, ISSN: 09596526 DOI: 10.1016/j.jclepro.2020.124433.

Wong, KV and Hernandez, A (2012) "A review of additive manufacturing" *ISRN Mechanical Engineering*, ISSN: 20905130 DOI: 10.5402/2012/208760.

Xueying, S, Yuan, H, Haiqun, C and Xiongjun, Y (2015) "Study on thermal property, flame retardancy and mechanism of poly(lactic acid)/intumescent flame retardant/NiAl layer double hydroxide nanocomposites" *Science of Advanced Materials*, *7*, (9): 1848–1857 DOI: 10.1166/sam.2015.2418.

Yan, Y, Gu, X, Li, L, Li, H, Sun, J and Zhang, S (2017) "Preparation and characterisation of intumescent flame retardant biodegradable poly(lactic acid) nanocomposites based on sulfamic acid intercalated layered double hydroxides" *Fibres and Polymers*, *18*, (11): 2060–2069 ISSN: 12299197 DOI: 10.1007/s12221-017-1153-2.

Yang, Z, Shi, K, Jin, Z, Liu, Z, Li, Y, Huang, Y, Gao, F and Han, J (2022) "Biodegradable layered double hydroxide/polymer films for efficient oxygen and water vapour barriers" *Industrial and Engineering Chemistry Research*, *61*, (3): 1367–1374 ISSN: 15205045 DOI: 10.1021/acs.iecr.1c04069.

Yi, M (2023) *A complete guide to violin plots* Chartio data tutorials (Ed.), URL: https://chartio.com/learn/charts/violin-plot-complete-guide/ (visited on 2023-09-22).

Yu, J, Liu, J, Clearfield, A, Sims, JE, Speiegle, MT, Suib, SL and Sun, L (2016) "Synthesis of layered double hydroxide single-layer nanosheets in formamide" *Inorganic Chemistry*, *55*, (22): 12036–12041 ISSN: 1520510X DOI: 10.1021/acs.inorgchem.6b02203.

Zeng, RC, Li, XT, Liu, ZG, Zhang, F, Li, SQ and Cui, HZ (2015) "Corrosion resistance of Zn–Al layered double hydroxide/poly(lactic acid) composite coating on magnesium alloy AZ31" *Frontiers of Materials Science*, *9*, (4): 355–365 ISSN: 20950268 DOI: 10.1007/s11706-015-0307-7.

Zhang, J, Tashiro, K, Tsuji, H and Domb, AJ (2008) "Disorder-to-order phase transition and multiple melting behaviour of poly(L-lactide) investigated by simultaneous measurements of WAXD and DSC" *Macromolecules*, *41*, (4) ISSN: 00249297 DOI: 10.1021/ma0706071.

Zhang, M, Jin, X and Gou, G (2016) "Preparation and characterisation of magnetic thermosensitive fluorouracil micelles" *Journal of Biomaterials Science, Polymer Edition*, *27*, (8): 773–791 ISSN: 15685624 DOI: 10.1080/09205063.2016.1162626.

Zhang, P, Gan, S, Chen, L, Chen, H, Jia, C, Fu, Y and Xiong, Y (2022) "Effect of MMT on flame retardancy of PLA/IFR/LDH Composites" *Journal of Renewable Materials*, *10*, (6): 1–11 ISSN: 2164-6341 DOI: 10.32604/jrm.2022.019590.

Zhang, S, Yan, Y, Wang, W, Gu, X, Li, H, Li, J and Sun, J (2018) "Intercalation of phosphotungstic acid into layered double hydroxides by reconstruction method and its application in intumescent flame retardant poly (lactic acid) composites" *Polymer Degradation and Stability*, *147*, 142–150 ISSN: 01413910 DOI: 10.1016/j.polymdegradstab.2017.12.004.

Zhao, N, Shi, S, Lu, G and Wei, M (2008) "Polylactide (PLA)/layered double hydroxides composite fibres by electrospinning method" *Journal of Physics and Chemistry of Solids*, *69*, (5-6): 1564–1568 ISSN: 00223697 DOI: 10.1016/j.jpcs.2007.10.046.

Zhou, Q and Xanthos, M (2010) "Effects of cationic and anionic clays on the hydrolytic degradation of polylactides" *Polymer Engineering and Science*, *50*, (2): 320–330 ISSN: 00323888 DOI: 10.1002/pen.21520.

Zhou, T, McCarthy, ED, Soutis, C and Cartmell, SH (2020) "Novel lactone-layered double hydroxide ionomer powders for bone tissue repair" *Journal of Biomedical Materials Research - Part B Applied Biomaterials*, *108*, (7): 2835–2846 ISSN: 15524981 DOI: 10.1002/jbm.b.34614.

Zuza, M (2023) *Everything about nozzles with a different diameter* URL: https://blog.prusa3d.com/everything-about-nozzles-with-a-different-diameter_8344/

%5C#:~:text=Layer%5C%20height%5C%20should%5C%20not%5C%20exceed,are%5C%20independent%5C%20of%5C%20each%5C%20other (visited on 2023-02-17).

Appendix A Screening experiment

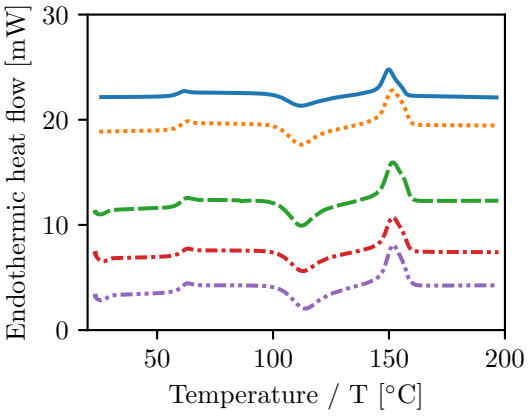

(a) 0LDH_PLA.

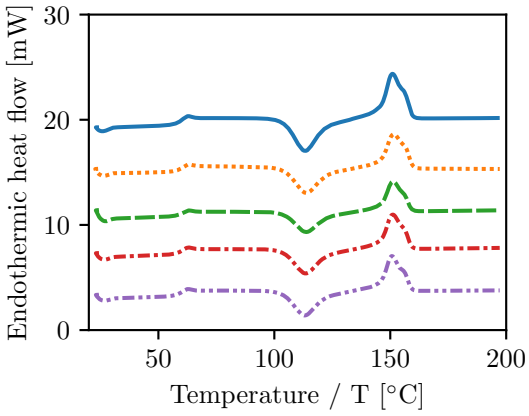

(b) 2LDH_PLA.

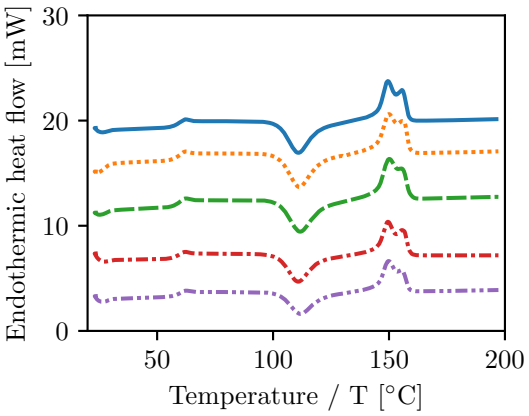

(c) 6LDH_PLA.

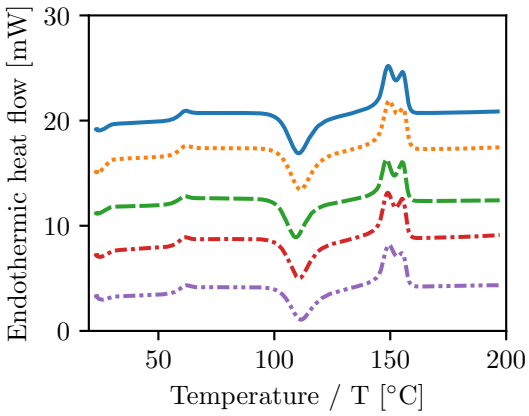

(d) 10LDH_PLA.

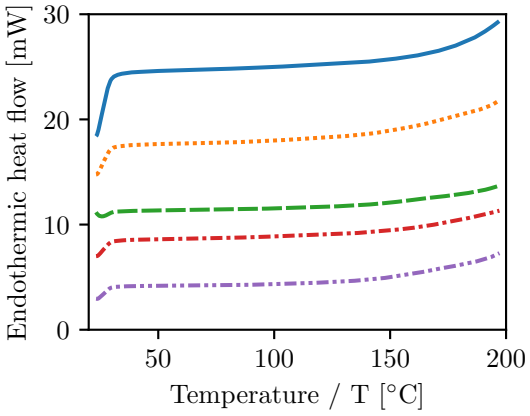

(e) LDH.

Figure A.1: The DSC results of the second heating cycle of the filament made for use in the screening experiments as well as the pure LDH and pure PLA filament. Five repeats for each LDH loading are shown.

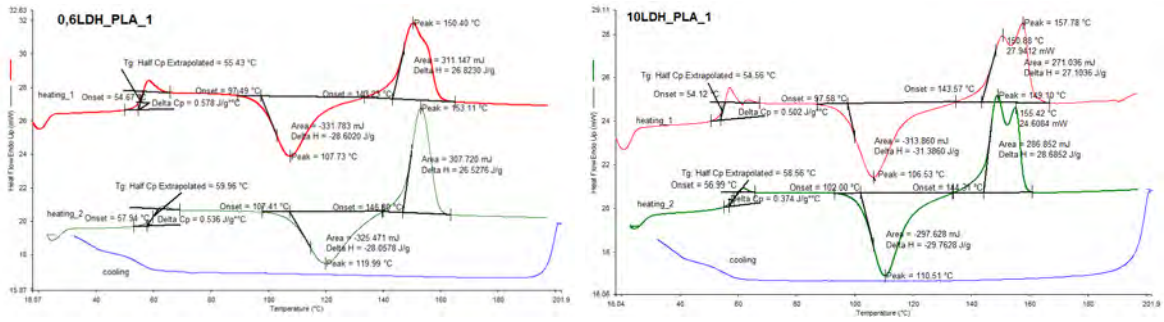

(a) 0.6LDH_PLA_1. **(b)** 10LDH_PLA_1.

Figure A.2: The raw output of results from the DSC programme used detailing how the various results have been obtained as reported in this work.

Table A.1: The ANOVA table of the results of the screening experiment with tensile stress as response factor.

Source of variation	Sum of squares	Degrees of freedom	F ratio	p value
Model	705.8527	4	11.3714	< 0.0001
A	22.3573	1	1.4407	0.2364
B	10.2865	1	0.6629	0.4199
C	620.8267	1	40.0065	< 0.0001
D	60.3940	1	3.8918	0.0548
Lack of fit	450.2384	4	19.3601	< 0.0001
Pure error	232.5598	40		
Total error	682.7983	44		

Table A.2: The ANOVA table of the results of the screening experiment with normalised tensile stress as response factor.

Source of variation	Sum of squares	Degrees of freedom	F ratio	p value
Model	5.8935	4	16.4949	< 0.0001
A	0.8676	1	9.7129	0.0032
B	0.6079	1	6.8061	0.0123
C	0.0065	1	0.0732	0.7879
D	4.2154	1	47.1928	< 0.0001
Lack of fit	1.4495	4	5.7808	0.0009
Pure error	2.5701	41		
Total error	4.0195	45		

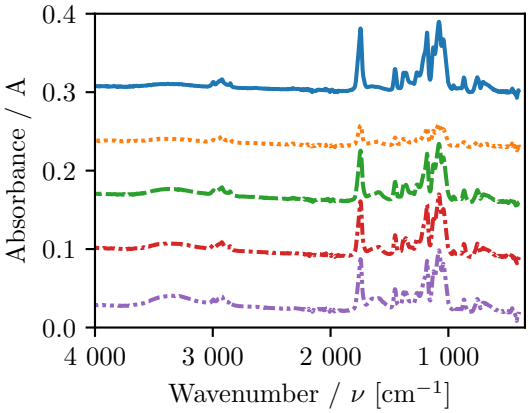

(a) 0LDH_PLA.

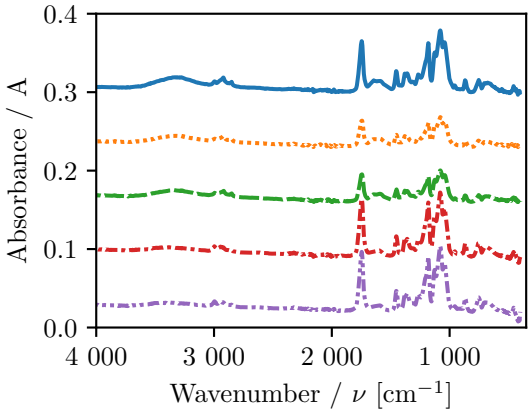

(b) 2LDH_PLA.

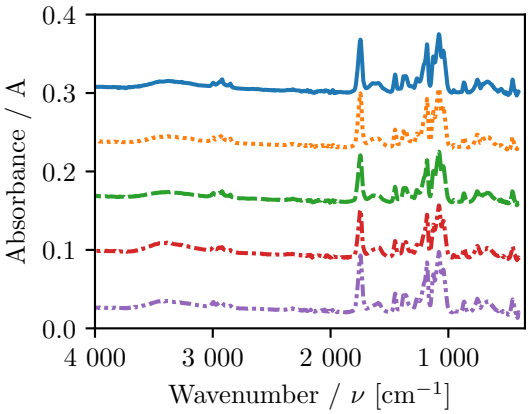

(c) 6LDH_PLA.

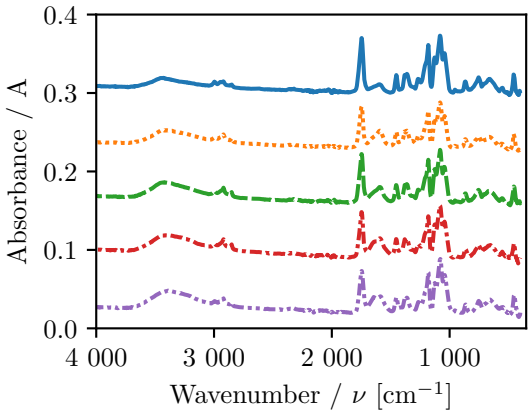

(d) 10LDH_PLA.

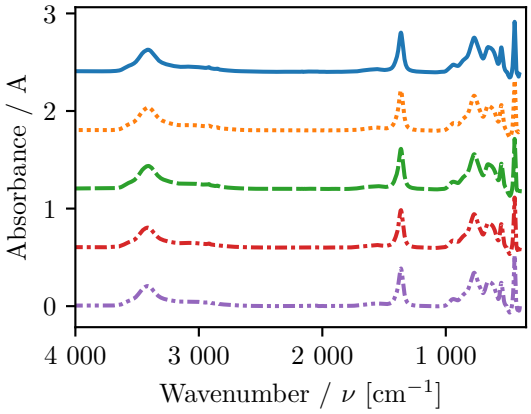

(e) LDH.

Figure A.3: The FTIR results of the filament made for use in the screening experiments as well as the pure LDH powder and the pure PLA filament. Five repeats for each filament and the clay is shown.

(a) First centre runs.

(b) Middle centre runs.

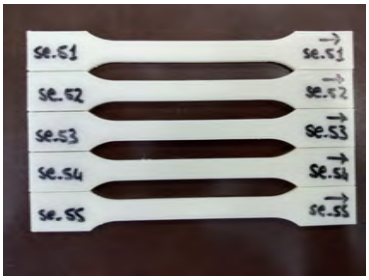

(c) Last centre runs.

(d) First experiment runs.

(e) Second experiment runs.

(f) Third experiment runs.

(g) Fourth experiment runs.

(h) Fifth experiment runs.

(i) Sixth experiment runs.

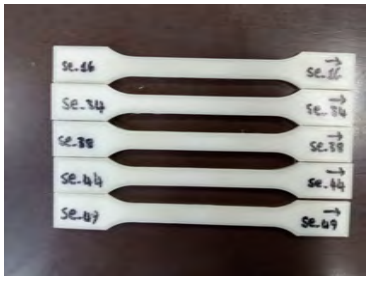

(j) Seventh experiment runs.

(k) Eighth experiment runs.

Figure A.4: Images of all the tensile samples of the screening experiment grouped by experimental run.

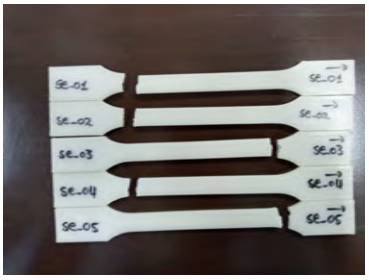

(a) First centre runs.

(b) Middle centre runs.

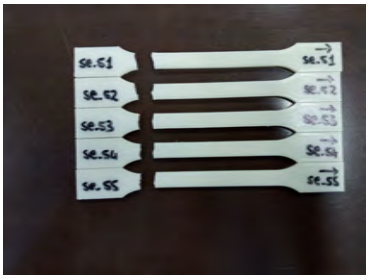

(c) Last centre runs.

(d) First experiment runs.

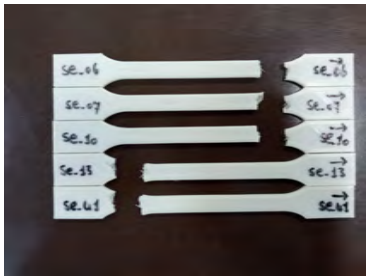

(e) Second experiment runs.

(f) Third experiment runs.

(g) Fourth experiment runs.

(h) Fifth experiment runs.

(i) Sixth experiment runs.

(j) Seventh experiment runs.

(k) Eighth experiment runs.

Figure A.5: Images of all the broken tensile samples of the screening experiment grouped by experimental run showing the various fracture locations. The images before testing can be seen in Figure A.4.

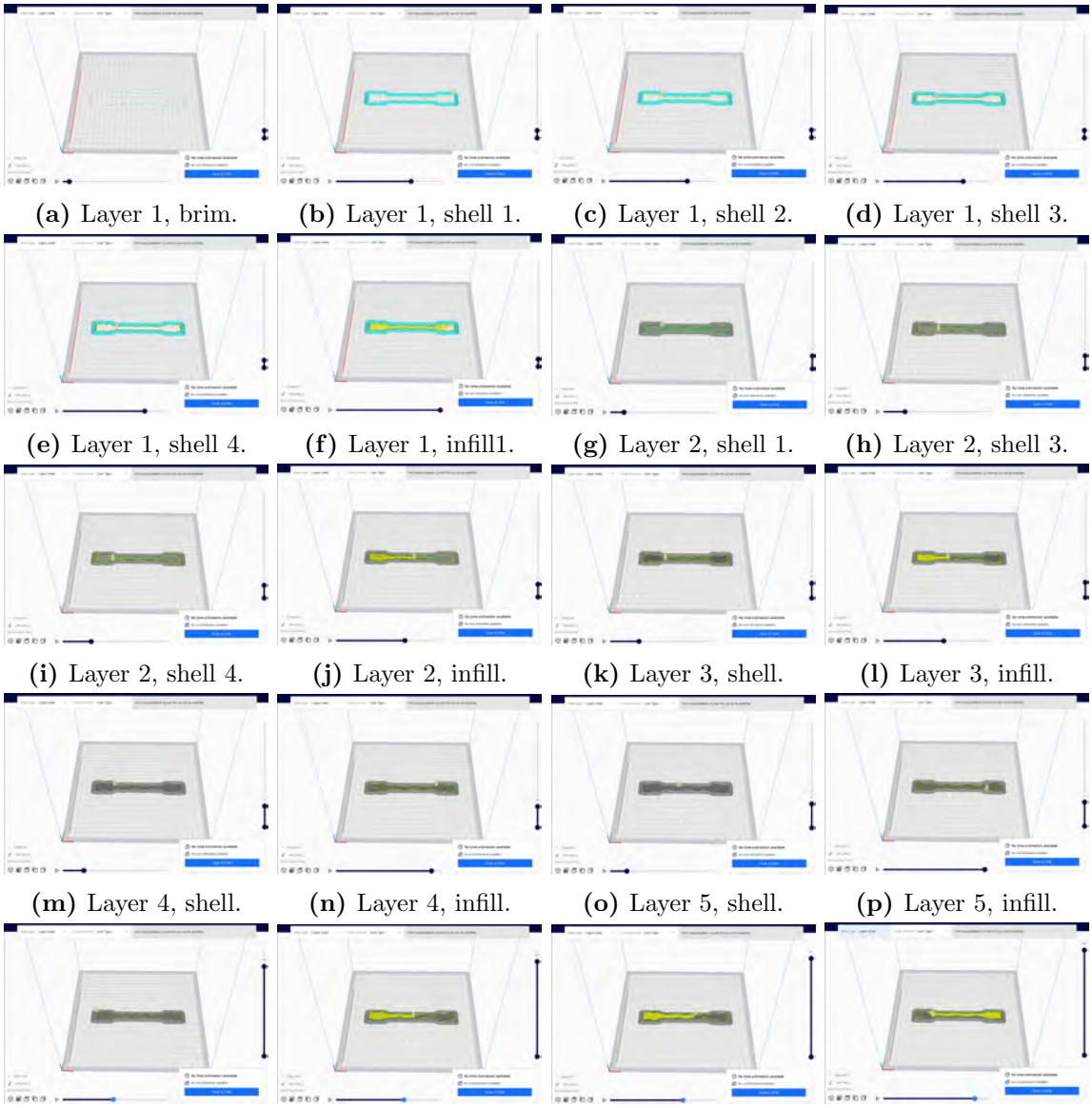

(a) Layer 1, brim. **(b)** Layer 1, shell 1. **(c)** Layer 1, shell 2. **(d)** Layer 1, shell 3.

(e) Layer 1, shell 4. **(f)** Layer 1, infill1. **(g)** Layer 2, shell 1. **(h)** Layer 2, shell 3.

(i) Layer 2, shell 4. **(j)** Layer 2, infill. **(k)** Layer 3, shell. **(l)** Layer 3, infill.

(m) Layer 4, shell. **(n)** Layer 4, infill. **(o)** Layer 5, shell. **(p)** Layer 5, infill.

(q) Layer 19. **(r)** Layer 20. **(s)** Layer 21. **(t)** Layer 22.

Figure A.6: The Ultimaker Cura preview user interface which allows an user to observe how the infill and walls will be printed layer by layer.

Table A.3: The ANOVA table of the results of the screening experiment with tensile force as response factor.

Source of variation	Sum of squares	Degrees of freedom	F ratio	p value
Model	1.284 9	4	10.588 1	< 0.0001
A	0.039 0	1	1.285 3	0.262 9
B	0.006 4	1	0.212 0	0.647 5
C	1.140 2	1	37.583 9	< 0.0001
D	0.090 7	1	2.990 5	0.0906
Lack of fit	1.009 1	4	29.044 9	< 0.0001
Pure error	0.356 1	41		
Total error	1.365 2	45		

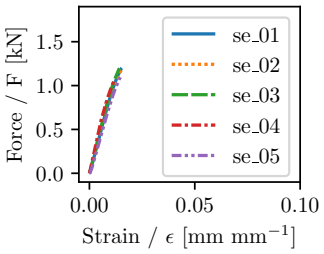

(a) First centre runs.

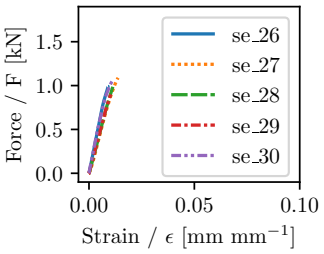

(b) Middle centre runs.

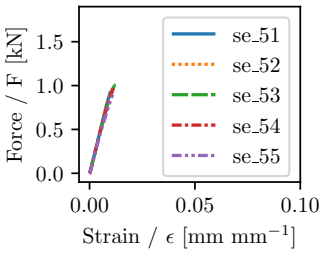

(c) Last centre runs.

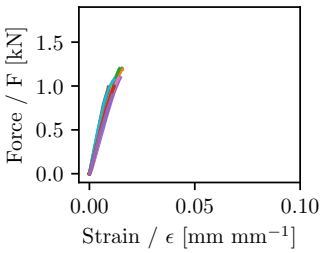

(d) All centre runs.

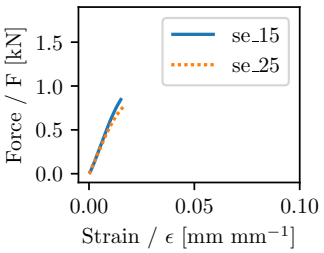

(e) First experiment runs.

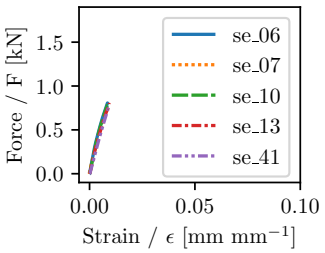

(f) Second experiment runs.

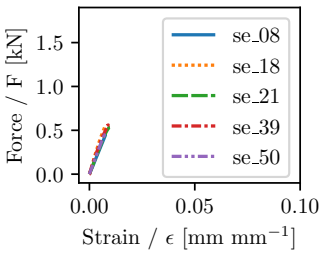

(g) Third experiment runs.

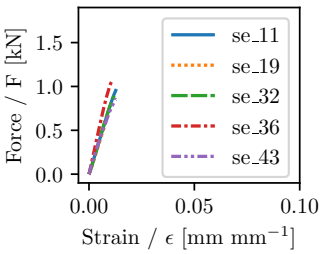

(h) Fourth experiment runs.

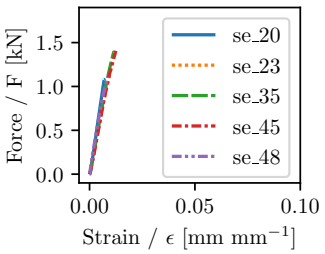

(i) Fifth experiment runs.

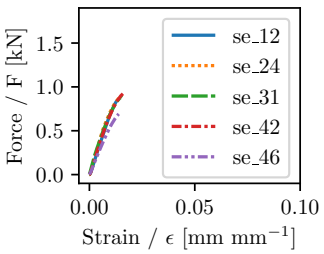

(j) Sixth experiment runs.

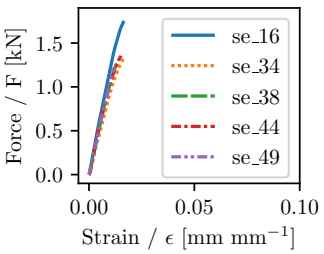

(k) Seventh experiment runs.

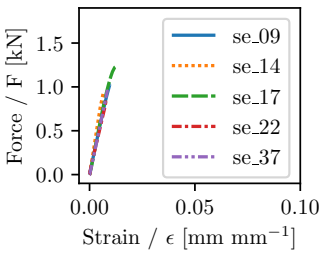

(l) Eighth experiment runs.

Figure A.7: The force strain graphs of all the tensile samples in the screening experiment.

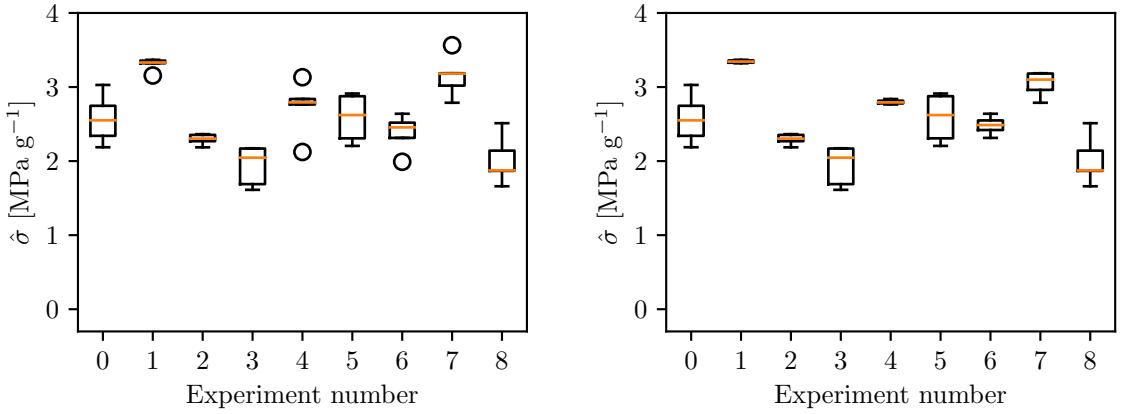

(a) With outliers (circles). **(b)** Without outliers.

Figure A.8: The box and whisker plots of the normalised tensile stresses of the screening experiment ordered by the experiment conducted with and without outliers.

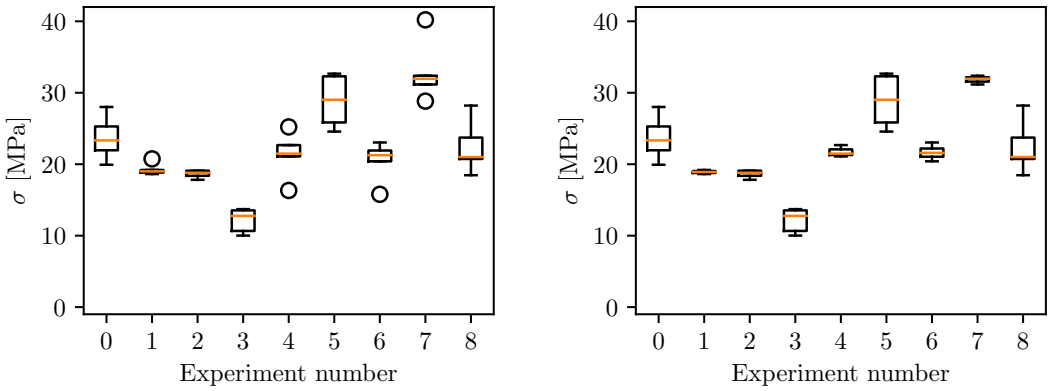

(a) With outliers (circles). **(b)** Without outliers.

Figure A.9: The box and whisker plots of the tensile stress results of the screening experiment ordered by the experiment conducted with and without outliers.

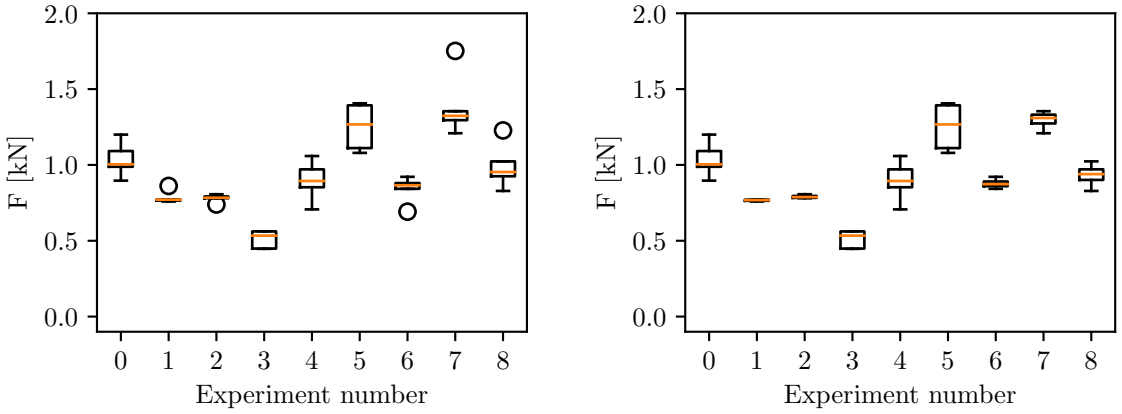

(a) With outliers (circles). **(b)** Without outliers.

Figure A.10: The box and whisker plots of the tensile force of the screening experiment ordered by the experiment conducted with and without outliers.

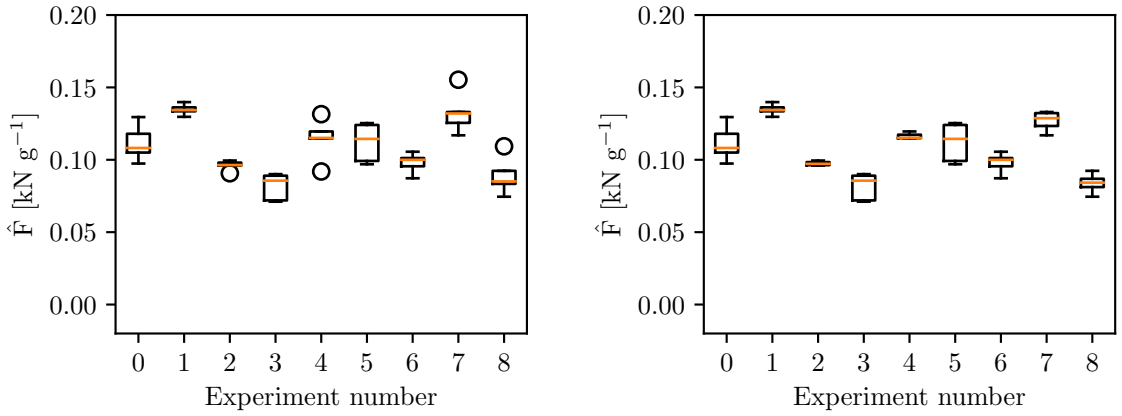

(a) With outliers (circles).

(b) Without outliers.

Figure A.11: The box and whisker plots of the normalised tensile force of the screening experiment ordered by the experiment conducted with and without outliers.

Table A.4: The ANOVA table of the results of the screening experiment with normalised tensile force as response factor.

Source of variation	Sum of squares	Degrees of freedom	F ratio	p value
Model	0.009 24	4	11.7931	< 0.0001
A	0.002 50	1	12.760 7	0.000 8
B	0.000 33	1	1.707 5	0.197 3
C	0.000 12	1	0.062 1	0.804 2
D	0.006 40	1	32.642 1	< 0.0001
Lack of fit	0.004 41	4	9.405 5	< 0.0001
Pure error	0.005 39	46		
Total error	0.009 80	50		

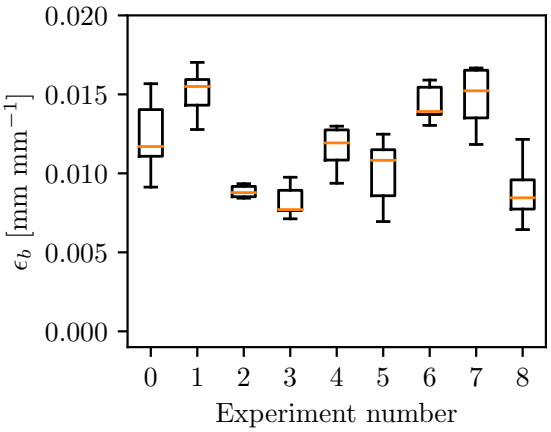

Figure A.12: The box and whisker plot of the strain at break of the screening experiment ordered by the experiment conducted.

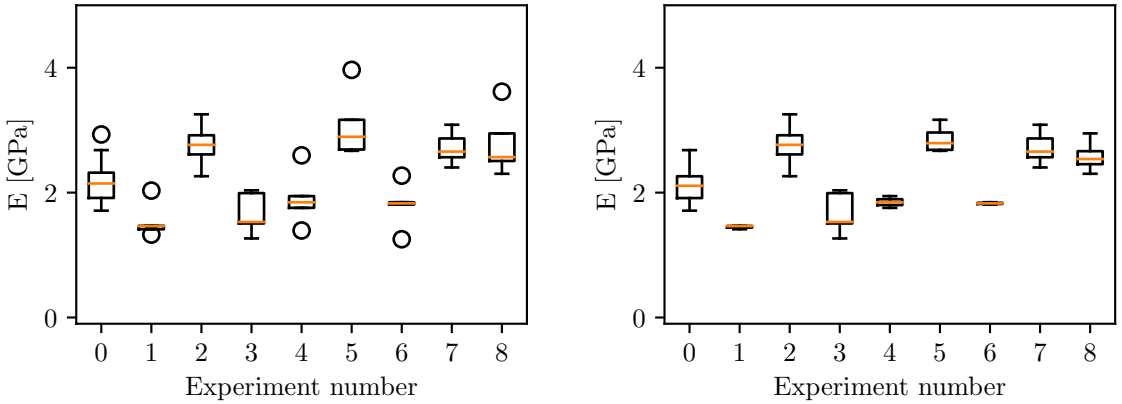

(a) With outliers (circles). **(b)** Without outliers.

Figure A.13: The box and whisker plots of the Young's modulus of the screening experiment ordered by the experiment conducted with and without outliers.

Table A.5: The ANOVA table of the results of the screening experiment with Young's modulus as response factor.

Source of variation	Sum of squares	Degrees of freedom	F ratio	p value
Model	4.245 167	4	5.685 7	0.0010
A	0.108 952	1	0.583 7	0.449 2
B	0.083 424	1	0.446 9	0.507 5
C	2.988 031	1	16.007 9	0.000 3
D	1.514 828	1	8.115 4	0.006 8
Lack of fit	4.897 801	4	16.443 0	< 0.0001
Pure error	2.755 260	37		
Total error	7.653 060	41		

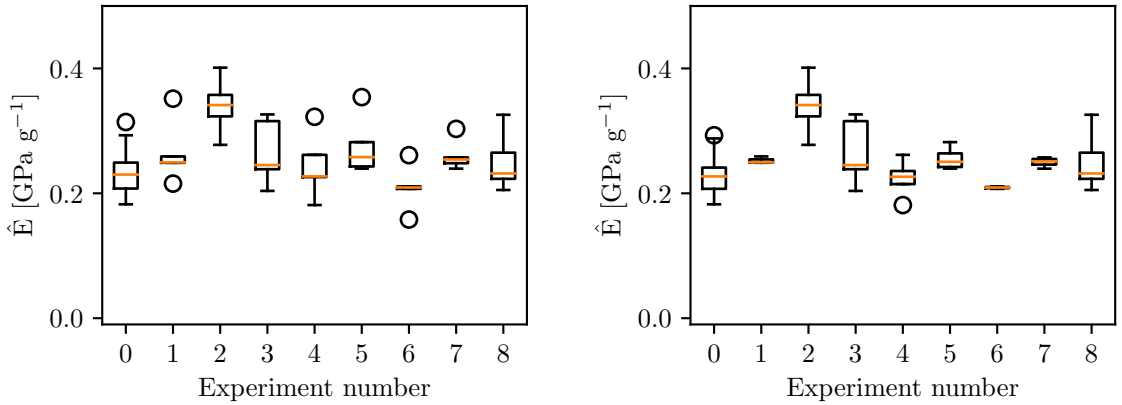

(a) With outliers (circles). **(b)** Without outliers.

Figure A.14: The box and whisker plots of the normalised Young's modulus of the screening experiment ordered by the experiment conducted with and without outliers.

Table A.6: The ANOVA table of the results of the screening experiment with normalised Young's modulus as response factor.

Source of variation	Sum of squares	Degrees of freedom	F ratio	p value
Model	0.029 784	4	4.3216	0.0051
A	0.000 145	1	0.0844	0.7728
B	0.003 455	1	2.0051	0.1641
C	0.007 535	1	4.3732	0.0426
D	0.016 809	1	9.7554	0.0032
Lack of fit	0.025 807	4	5.2656	0.0018
Pure error	0.046 560	38		
Total error	0.072 366	42		

Table A.7: The ANOVA table of the results of the screening experiment with impact energy as response factor.

Source of variation	Sum of squares	Degrees of freedom	F ratio	p value
Model	4 817 836	4	4.394 6	0.002 1
A	229 836	1	0.950 6	0.334 8
B	104 351	1	0.431 6	0.514 5
C	2 395 342	1	9.907 4	0.002 9
D	2 494 796	1	10.318 8	0.002 4
Lack of Fit	6 341 522	4	14. 322 8	<0.0001
Pure error	4 538 259	41		
Total error	10 879 781	45		

Table A.8: The ANOVA table of the results of the screening experiment with normalised impact energy as response factor.

Source of variation	Sum of squares	Degrees of freedom	F ratio	p value
Model	712 451.3	4	4.394 6	0.004 2
A	643.2	1	0.015 9	0.900 3
B	95 439.2	1	2.354 8	0.131 6
C	8 376. 6	1	0.206 7	0.651 5
D	611 179.7	1	15.079 7	0.000 3
Lack of Fit	1 058 7272.2	4	13.450 3	<0.000 1
Pure error	846 176.3	43		
Total error	1 904 903.5	47		

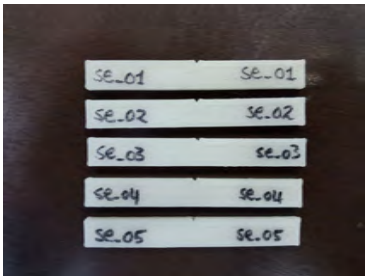

(a) First centre runs.

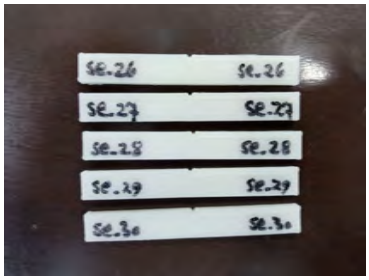

(b) Middle centre runs.

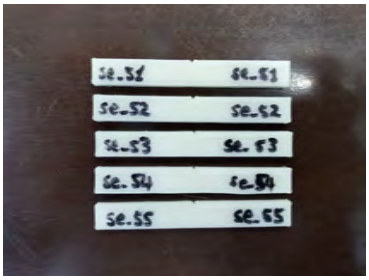

(c) Last centre runs.

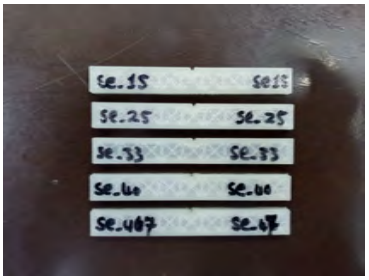

(d) First experiment runs.

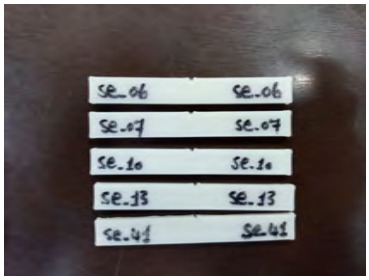

(e) Second experiment runs.

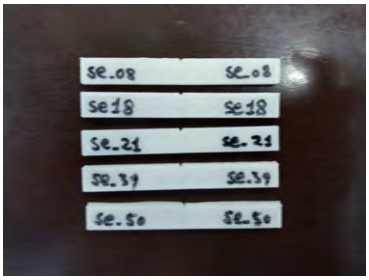

(f) Third experiment runs.

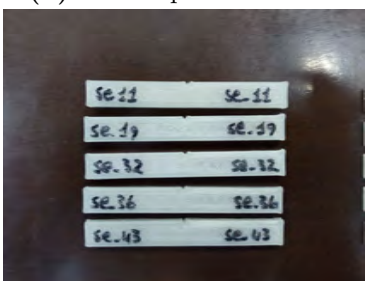

(g) Fourth experiment runs.

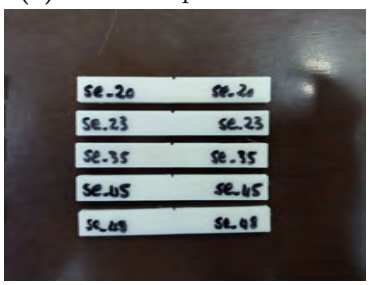

(h) Fifth experiment runs.

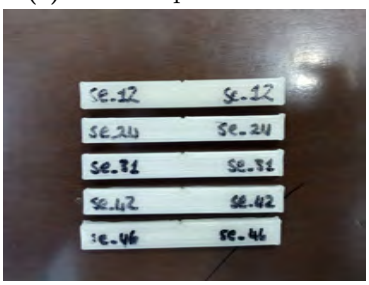

(i) Sixth experiment runs.

(j) Seventh experiment runs.

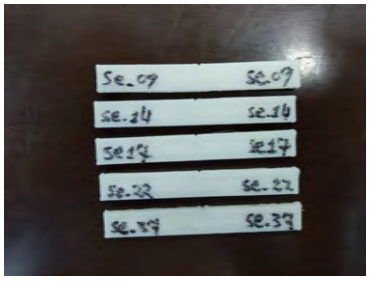

(k) Eighth experiment runs.

Figure A.15: Images of all the impact samples of the screening experiment grouped by experimental run.

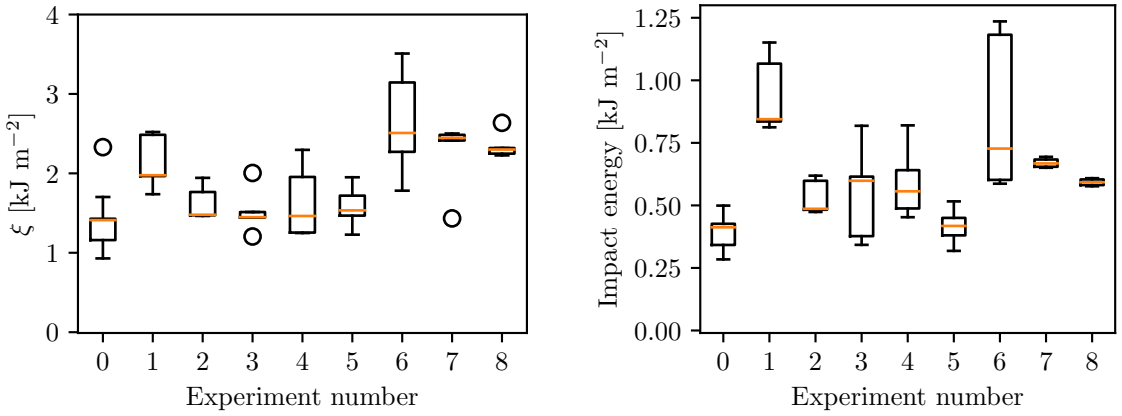

(a) With outliers (circles).

(b) Without outliers.

Figure A.16: The box and whisker plots of the impact energy of the screening experiment ordered by the experiment conducted with and without outliers.

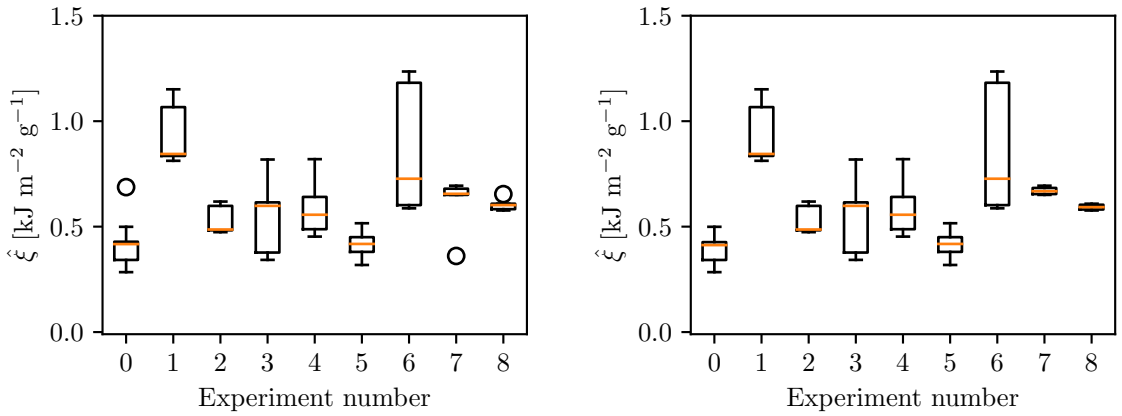

(a) With outliers (circles).

(b) Without outliers.

Figure A.17: The box and whisker plots of the normalised impact energy of the screening experiment ordered by the experiment conducted with and without outliers.

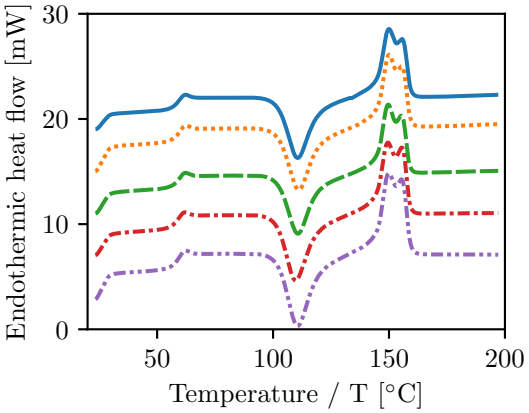

(a) Experiment 0.

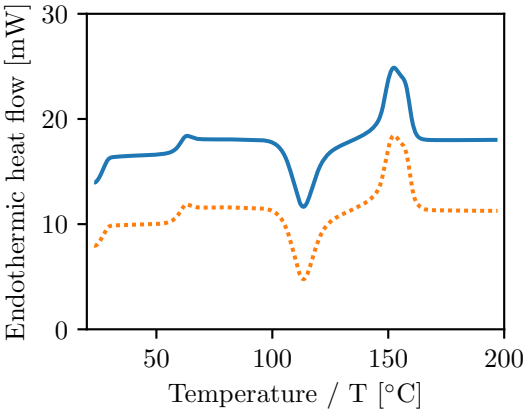

(b) Experiment 1.

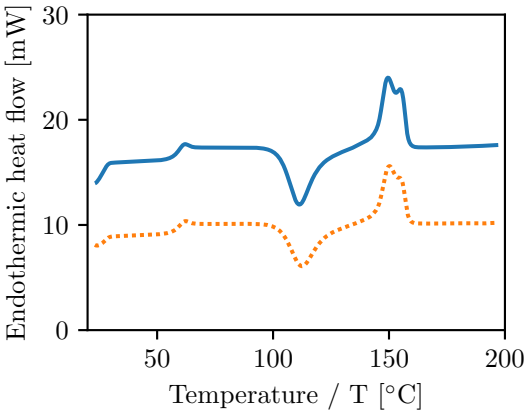

(c) Experiment 2.

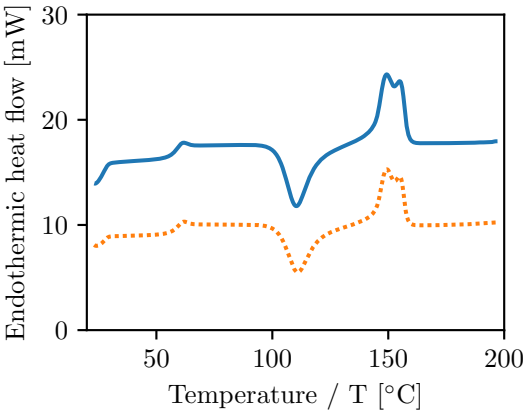

(d) Experiment 3.

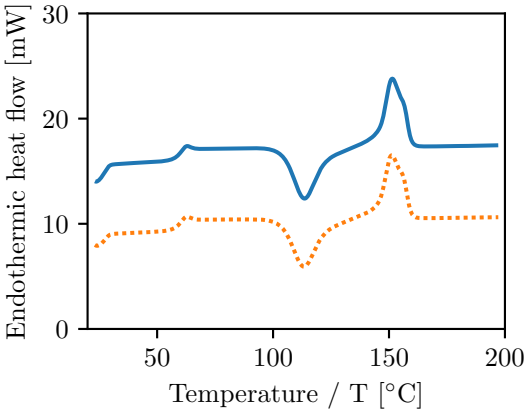

(e) Experiment 4.

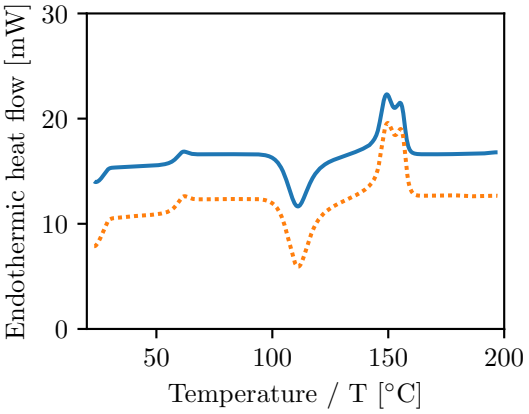

(f) Experiment 5.

Figure A.18: The DSC results of the second heating cycle of the tensile samples printed in the screening experiment. Continued on next page...

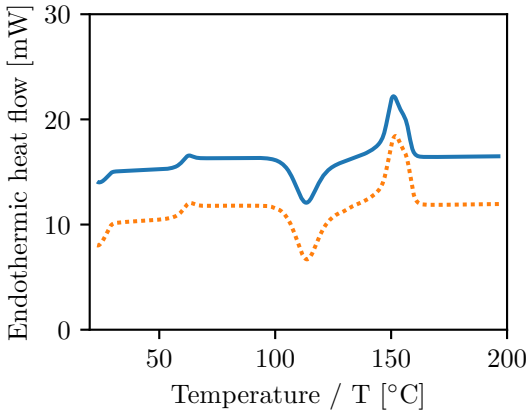

(g) Experiment 6.

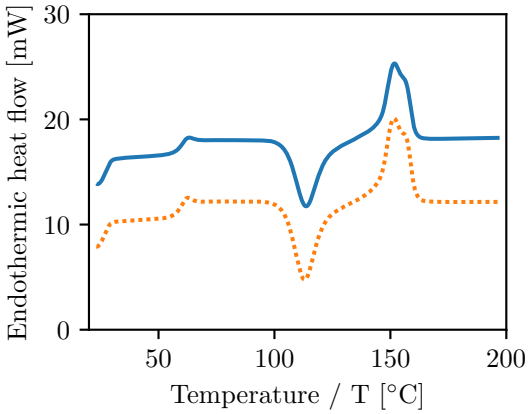

(h) Experiment 7.

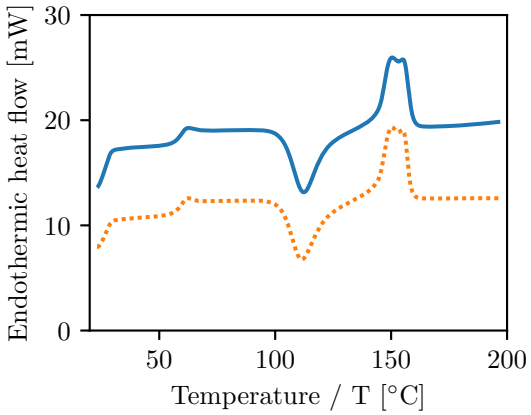

(i) Experiment 8.

Figure A.18: Continued from previous page... The DSC results of the second heating cycle of the tensile samples printed in the screening experiment.

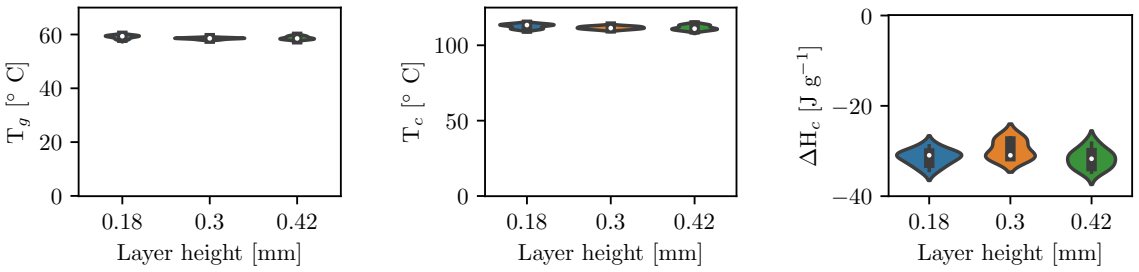

(a) Full scale T_g. **(b)** Full scale T_c. **(c)** Full scale ΔH_c.

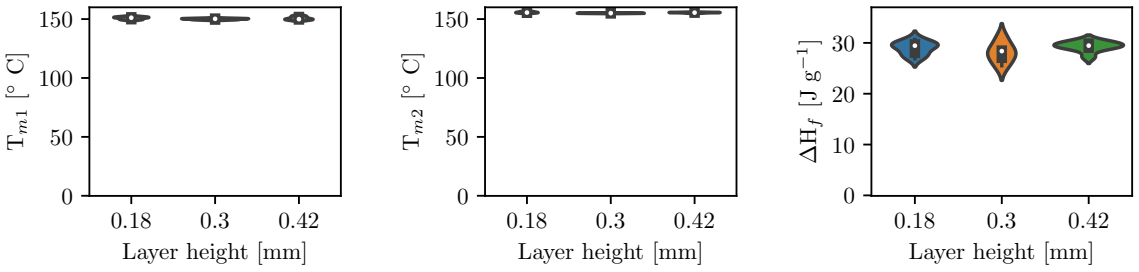

(d) Full scale T_{m1}. **(e)** Full scale T_{m2}. **(f)** Full scale ΔH_f.

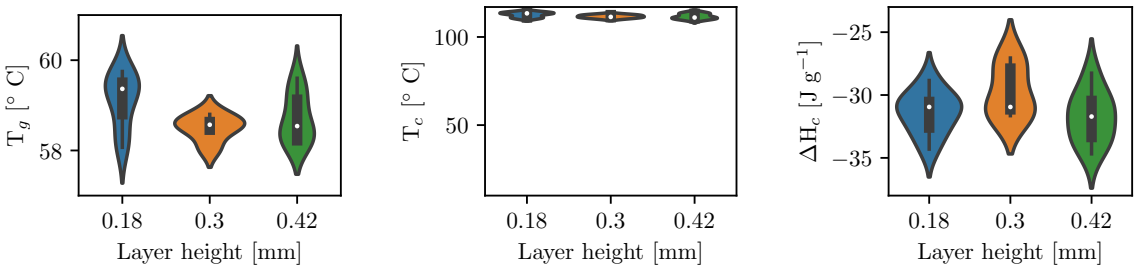

(g) Enlarged T_g. **(h)** Enlarged T_c. **(i)** Enlarged ΔH_c.

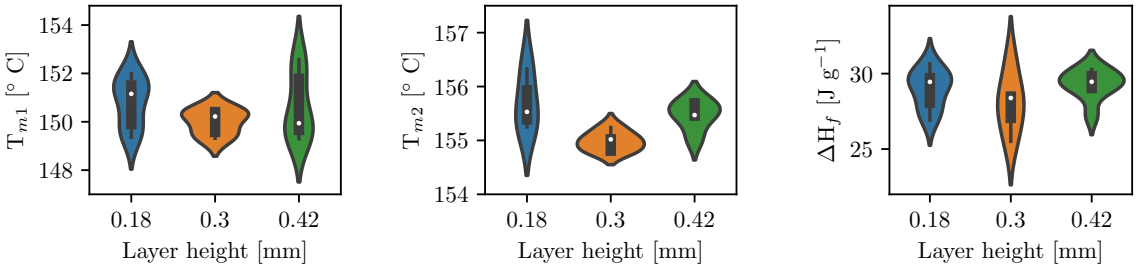

(j) Enlarged T_{m1}. **(k)** Enlarged T_{m2}. **(l)** Enlarged ΔH_f.

Figure A.19: The average properties of the respective tensile samples printed for the screening experiment as determined from DSC as a function of layer height.

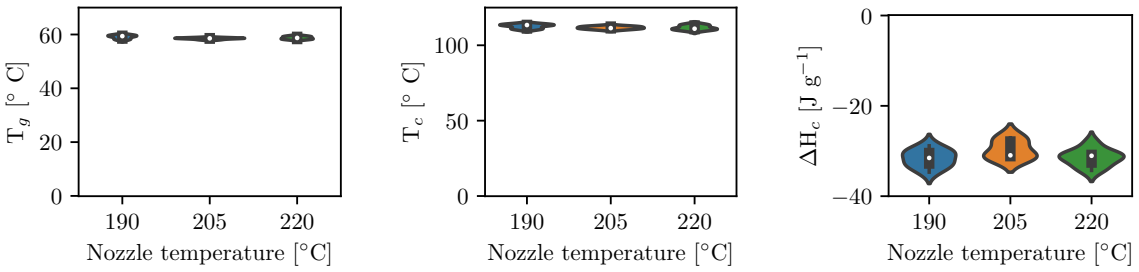

(a) Full scale T_g. **(b)** Full scale T_c. **(c)** Full scale ΔH_c.

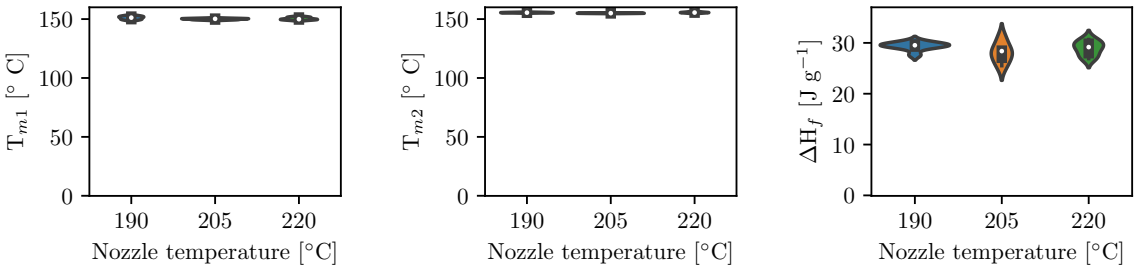

(d) Full scale T_{m1}. **(e)** Full scale T_{m2}. **(f)** Full scale ΔH_f.

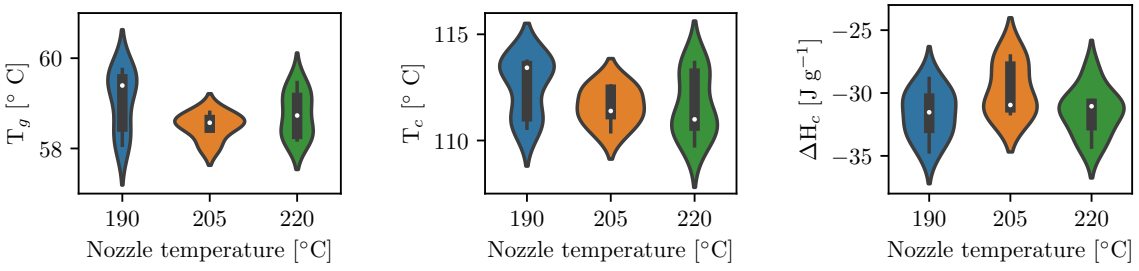

(g) Enlarged T_g. **(h)** Enlarged T_c. **(i)** Enlarged ΔH_c.

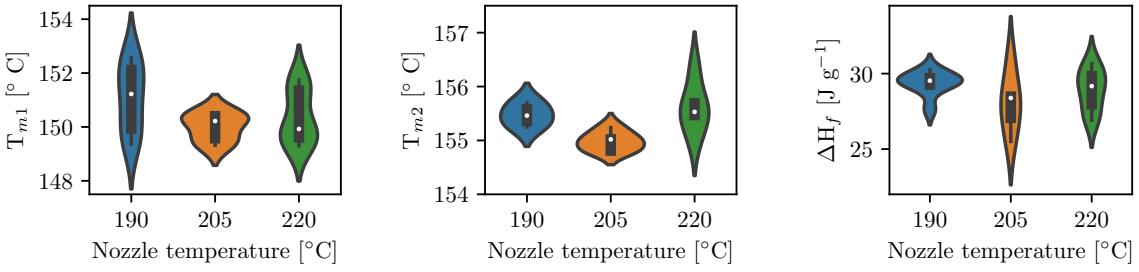

(j) Enlarged T_{m1}. **(k)** Enlarged T_{m2}. **(l)** Enlarged ΔH_f.

Figure A.20: The average properties of the respective tensile samples printed for the screening experiment as determined from DSC as a function of nozzle temperature.

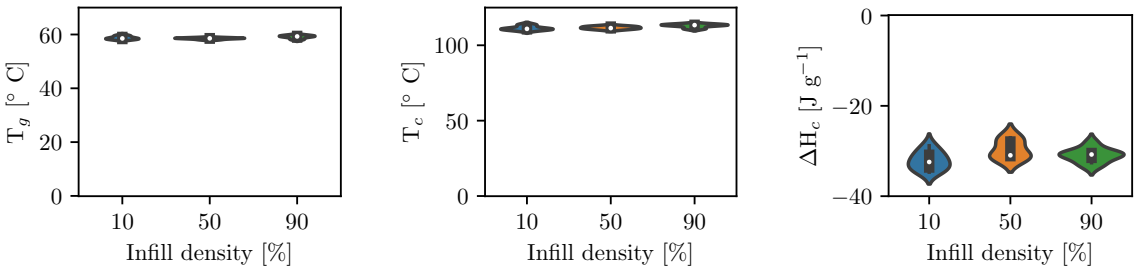

(a) Full scale T_g.

(b) Full scale T_c.

(c) Full scale ΔH_c.

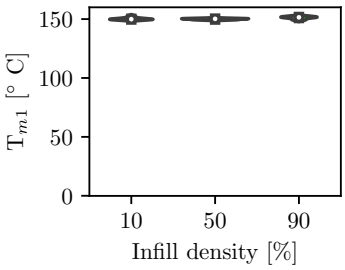

(d) Full scale T_{m1}.

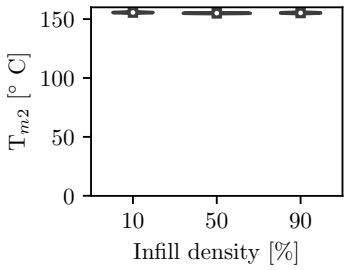

(e) Full scale T_{m2}.

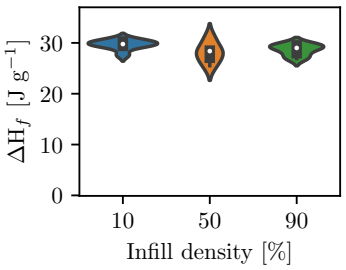

(f) Full scale ΔH_f.

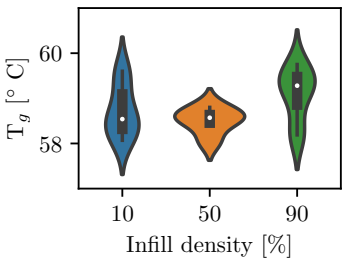

(g) Enlarged T_g.

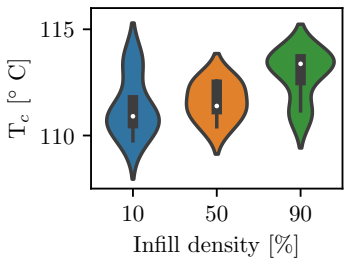

(h) Enlarged T_c.

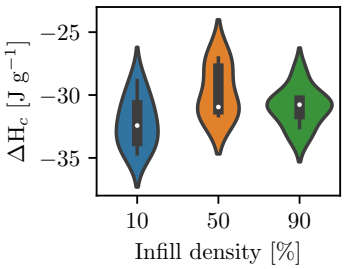

(i) Enlarged ΔH_c.

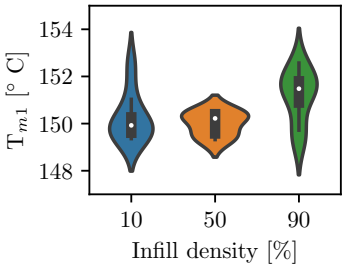

(j) Enlarged T_{m1}.

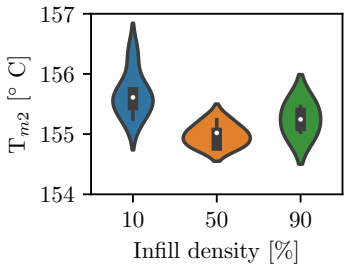

(k) Enlarged T_{m2}.

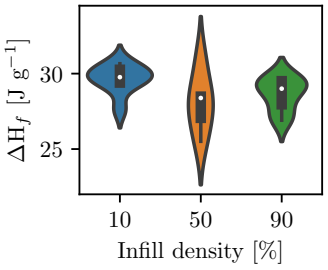

(l) Enlarged ΔH_f.

Figure A.21: The average properties of the respective tensile samples printed for the screening experiment as determined from DSC as a function of infill density.

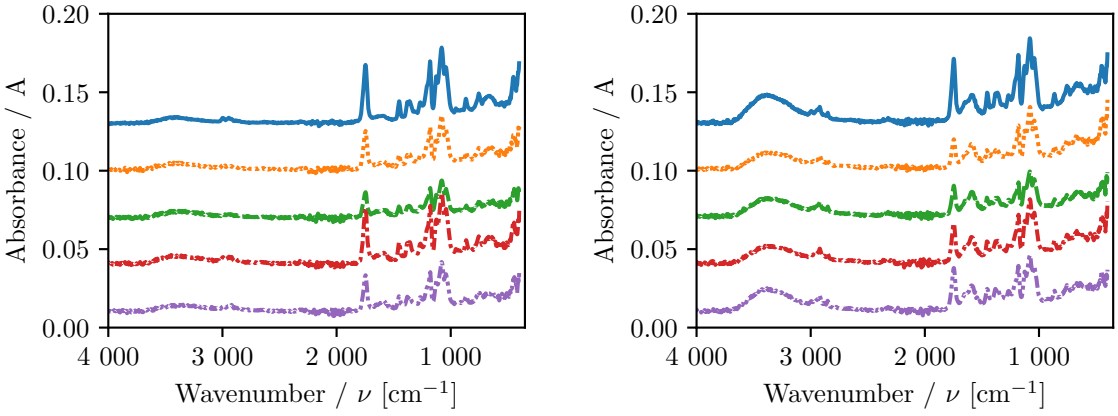

(a) First centre runs.

(b) Second centre runs.

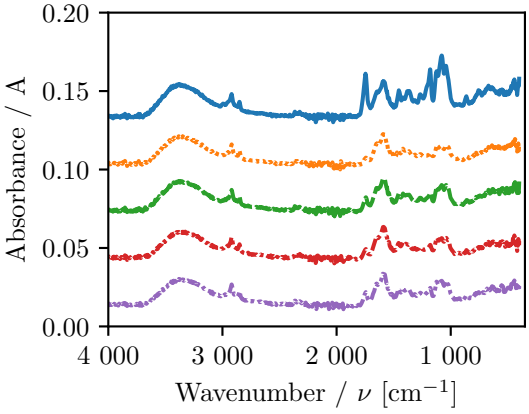

(c) Last centre runs.

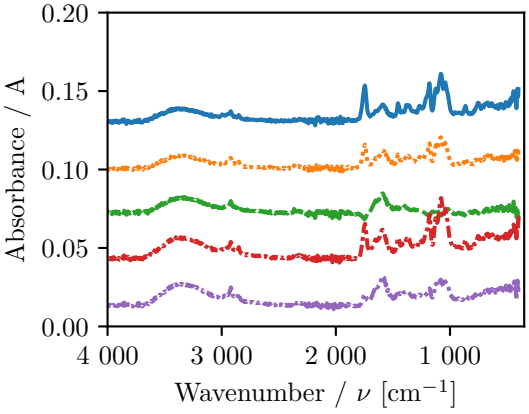

(d) First experiment runs.

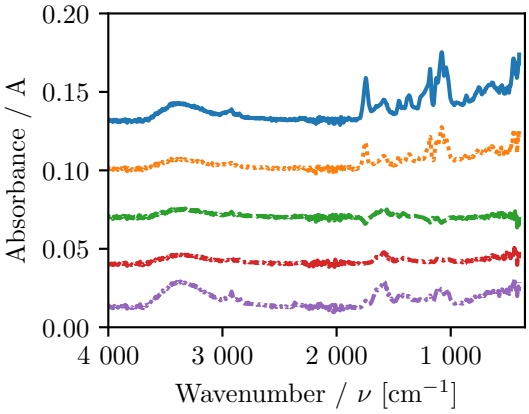

(e) Second experiment runs.

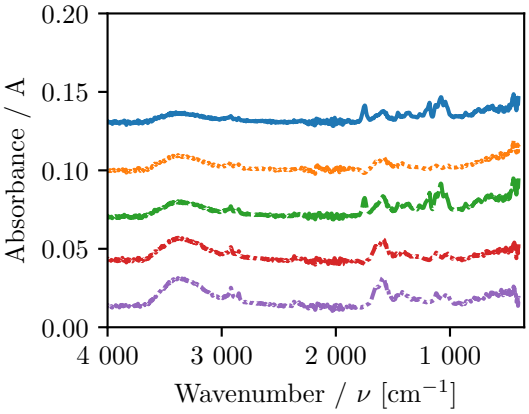

(f) Third experiment runs.

Figure A.22: The FTIR spectra of the tensile samples printed in the screening experiment. Continued on next page...

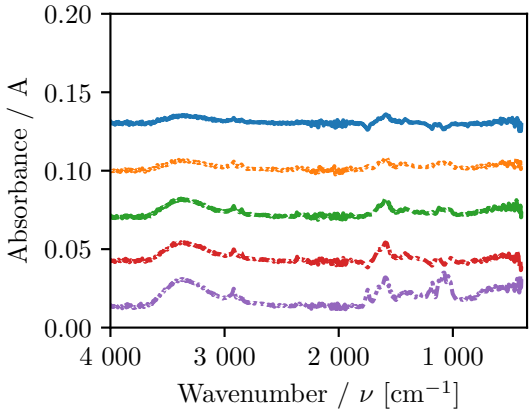

(g) Fourth experiment runs.

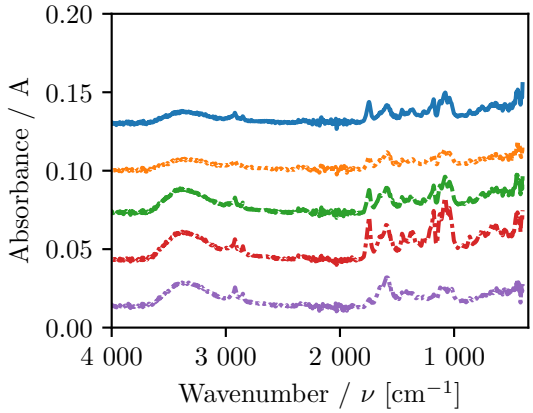

(h) Fifth experiment runs.

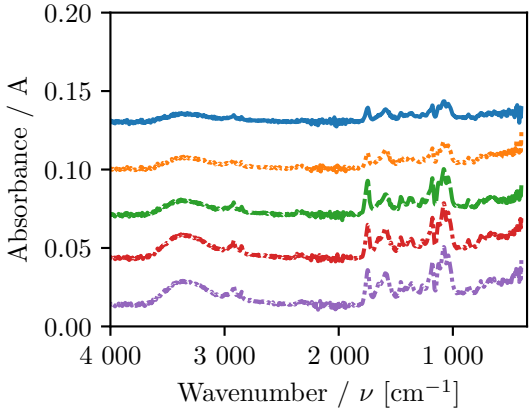

(i) Sixth experiment runs.

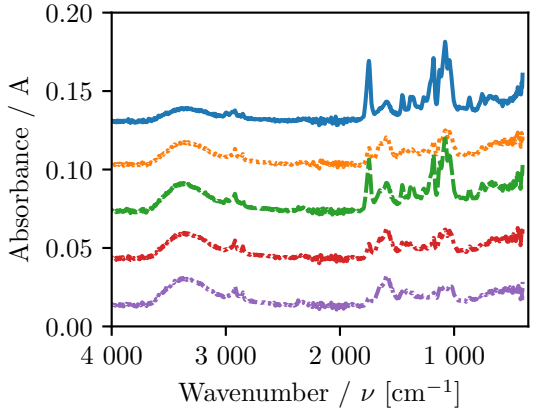

(j) Seventh experiment runs.

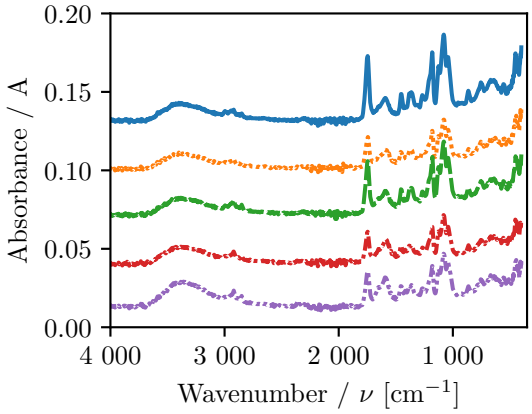

(k) Eighth experiment runs.

Figure A.22: Continued from previous page... The FTIR results of the tensile specimens printed in the screening experiment.

Appendix B Augmented screening experiment

(a) Centre runs. **(b)** Tenth experiment runs. **(c)** Other experiments.

Figure B.23: Images of all the tensile samples of the second block of the screening experiment grouped by experimental run.

(a) Centre runs. **(b)** Tenth experiment runs. **(c)** Other experiments.

Figure B.24: Images of all the tensile samples of the second block of the screening experiment grouped by experimental run after the tensile test was completed.

(a) Centre runs. **(b)** Tenth experiment runs. **(c)** Other experiments.

Figure B.25: Images of all the impact samples of the second block of the screening experiment grouped by experimental run.

Table B.9: The ANOVA table of the results of the augmented screening experiment with tensile stress as response factor including the outliers.

Source of variation	Sum of squares	Degrees of freedom	F ratio	p value
Model	1604.6826	9	23.1784	<0.0001
Block	8.7479	1	1.1372	0.2904
A	24.2060	1	3.1467	0.0811
B	0.6844	1	0.0890	0.7665
C	800.4735	1	104.0598	<0.0001
D	112.2371	1	14.5906	0.0003
AB	48.1457	1	6.2588	0.0151
AC	493.8283	1	64.1966	<0.0001
BC	76.8485	1	9.9901	0.0025
C^2	26.6461	1	3.4639	0.0675
Lack of fit	72.7531	9	1.0602	0.4072
Pure error	396.4857	52		
Total error	469.2388	61		

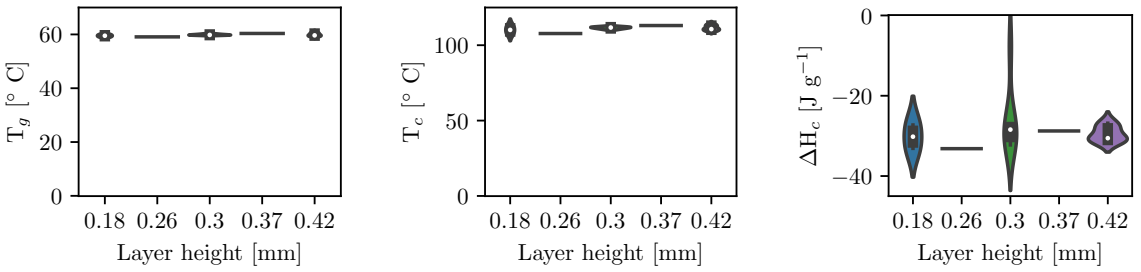

(a) Full scale T_g. **(b)** Full scale T_c. **(c)** Full scale ΔH_c.

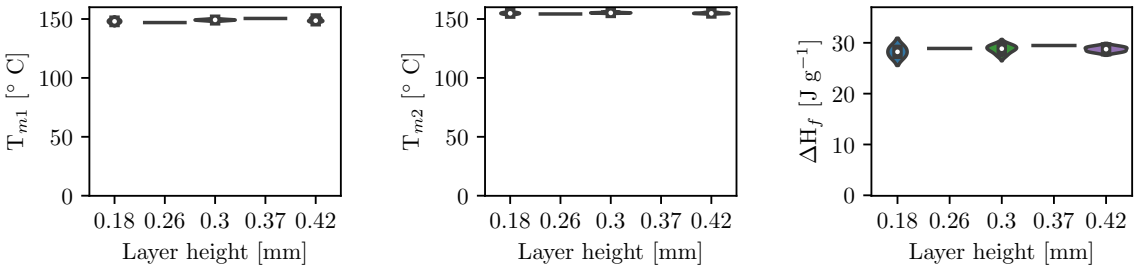

(d) Full scale T_{m1}. **(e)** Full scale T_{m2}. **(f)** Full scale ΔH_f.

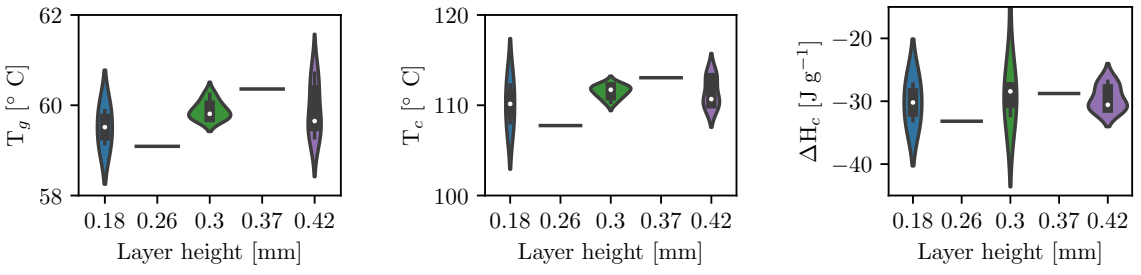

(g) Enlarged T_g. **(h)** Enlarged T_c. **(i)** Enlarged ΔH_c.

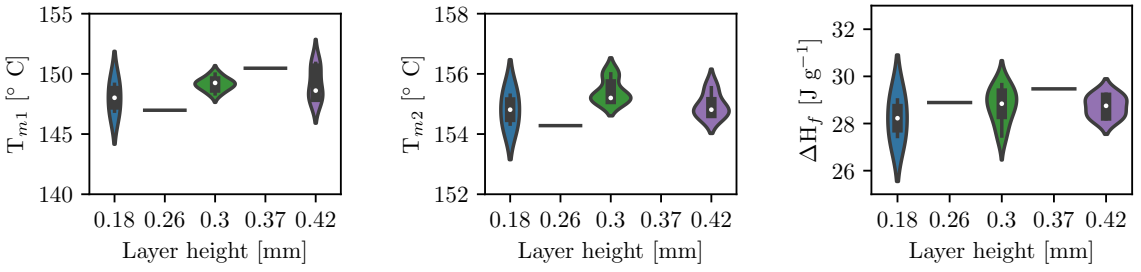

(j) Enlarged T_{m1}. **(k)** Enlarged T_{m2}. **(l)** Enlarged ΔH_f.

Figure B.26: The average properties of the respective tensile samples printed for the augmented screening experiment as determined from DSC as a function of layer height.

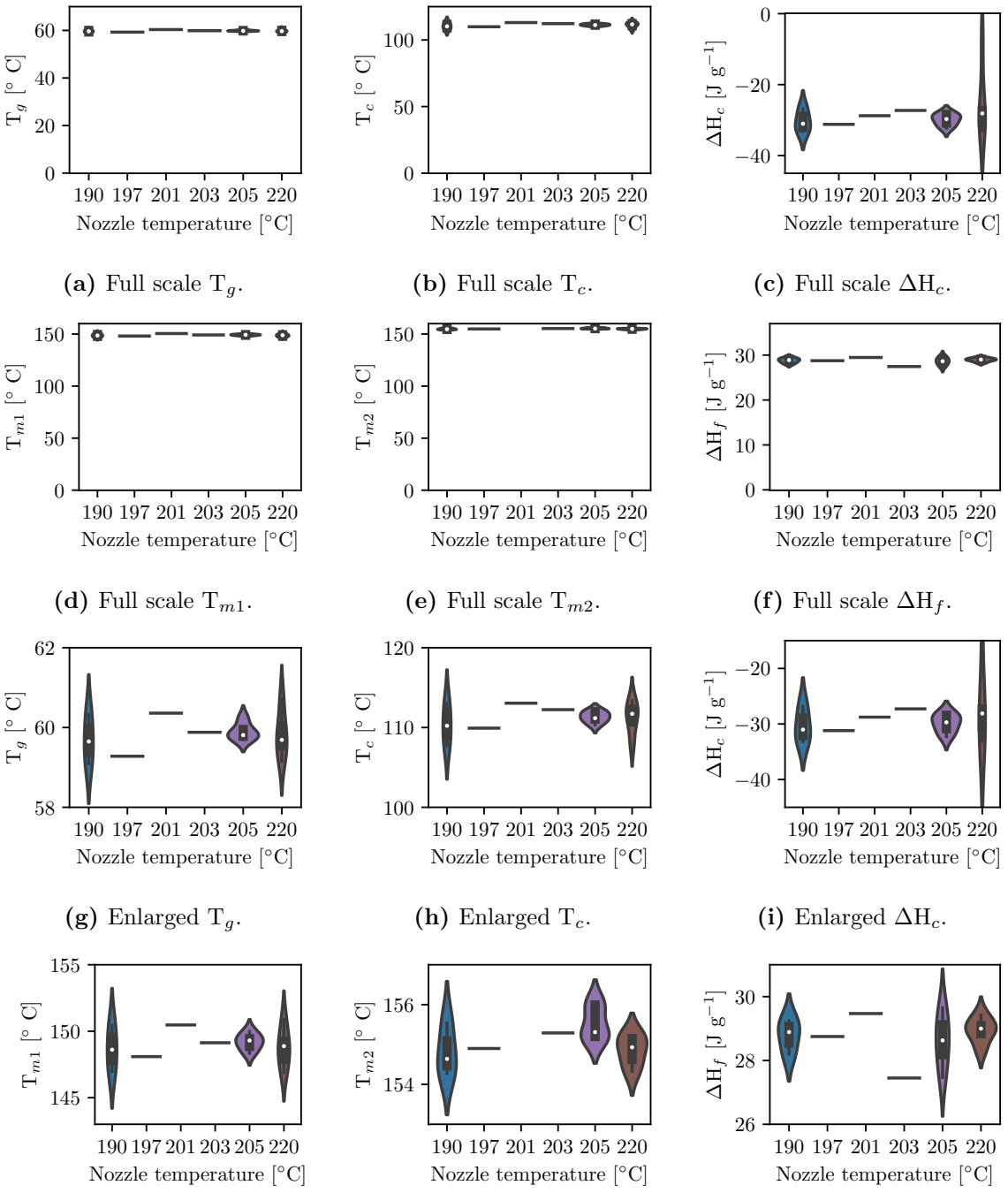

(a) Full scale T_g. **(b)** Full scale T_c. **(c)** Full scale ΔH_c.

(d) Full scale T_{m1}. **(e)** Full scale T_{m2}. **(f)** Full scale ΔH_f.

(g) Enlarged T_g. **(h)** Enlarged T_c. **(i)** Enlarged ΔH_c.

(j) Enlarged T_{m1}. **(k)** Enlarged T_{m2}. **(l)** Enlarged ΔH_f.

Figure B.27: The average properties of the respective tensile samples printed for the augmented screening experiment as determined from DSC as a function of nozzle temperature.

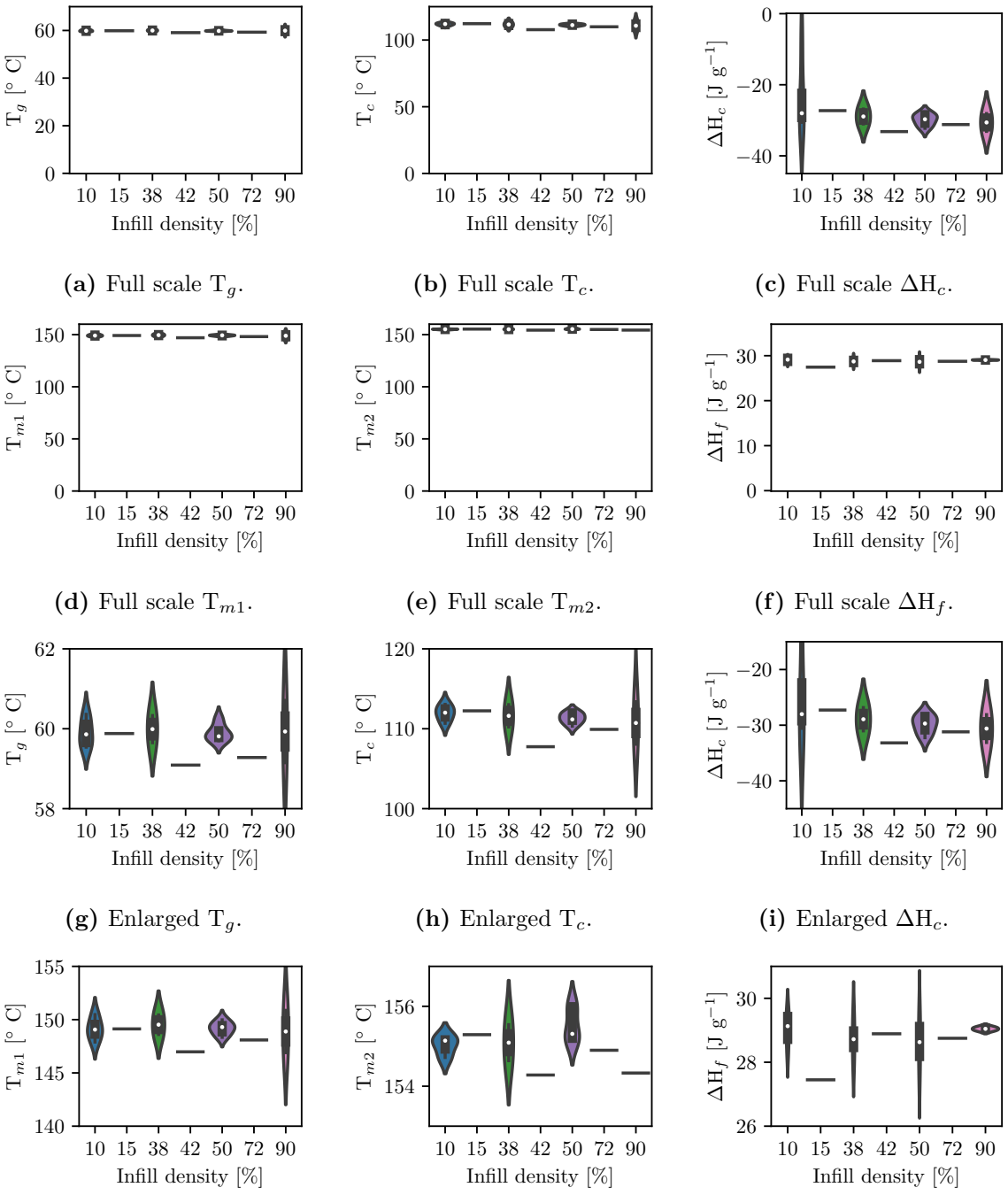

(a) Full scale T_g. **(b)** Full scale T_c. **(c)** Full scale ΔH_c.

(d) Full scale T_{m1}. **(e)** Full scale T_{m2}. **(f)** Full scale ΔH_f.

(g) Enlarged T_g. **(h)** Enlarged T_c. **(i)** Enlarged ΔH_c.

(j) Enlarged T_{m1}. **(k)** Enlarged T_{m2}. **(l)** Enlarged ΔH_f.

Figure B.28: The average properties of the respective tensile samples printed for the augmented screening experiment as determined from DSC as a function of infill density.

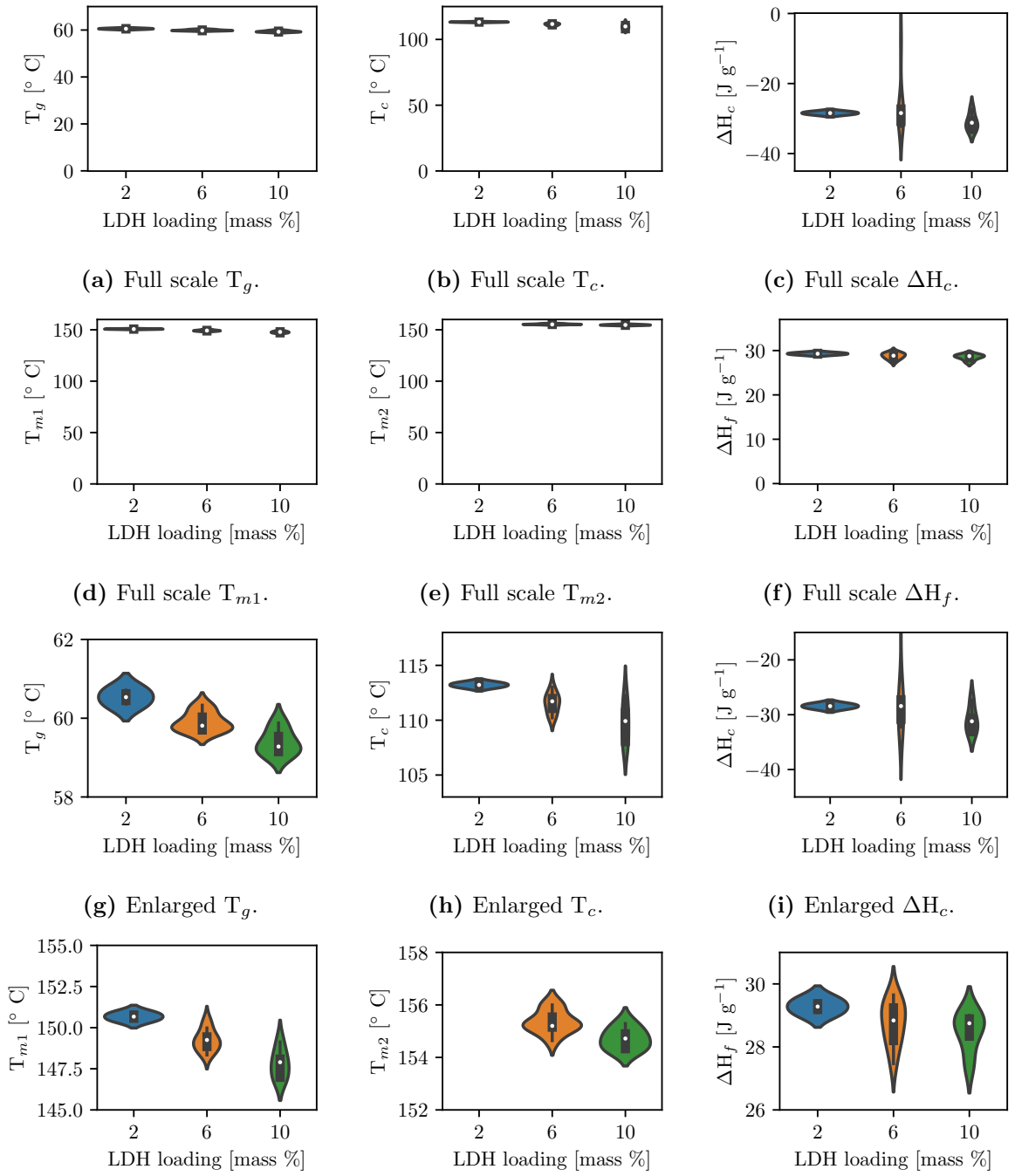

(a) Full scale T_g. **(b)** Full scale T_c. **(c)** Full scale ΔH_c.

(d) Full scale T_{m1}. **(e)** Full scale T_{m2}. **(f)** Full scale ΔH_f.

(g) Enlarged T_g. **(h)** Enlarged T_c. **(i)** Enlarged ΔH_c.

(j) Enlarged T_{m1}. **(k)** Enlarged T_{m2}. **(l)** Enlarged ΔH_f.

Figure B.29: The average properties of the respective tensile samples printed for the augmented screening experiment as determined from DSC as a function of LDH loading.

Appendix C CCD

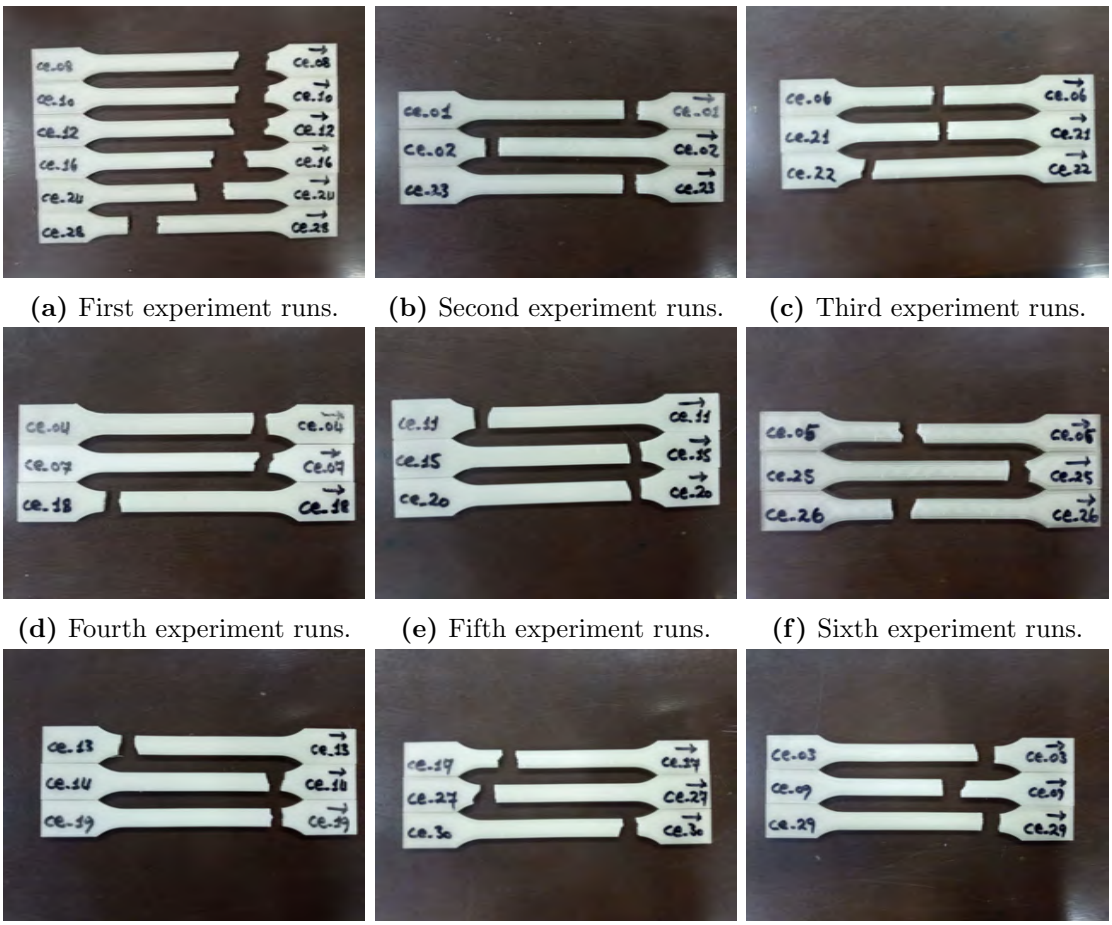

(a) First experiment runs. **(b)** Second experiment runs. **(c)** Third experiment runs.

(d) Fourth experiment runs. **(e)** Fifth experiment runs. **(f)** Sixth experiment runs.

(g) Seventh experiment runs. **(h)** Eighth experiment runs. **(i)** Ninth experiment runs.

Figure C.30: Images of all the broken tensile samples of the central composite design experiment grouped by experimental run.

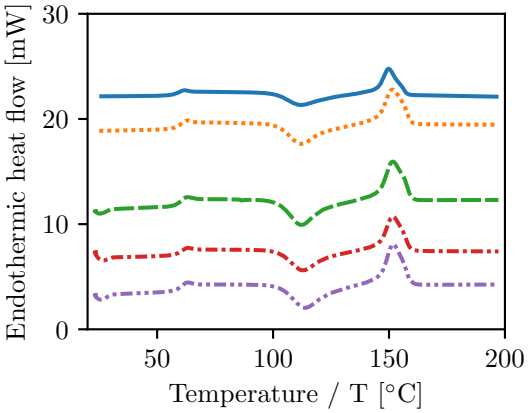

(a) 0LDH_PLA.

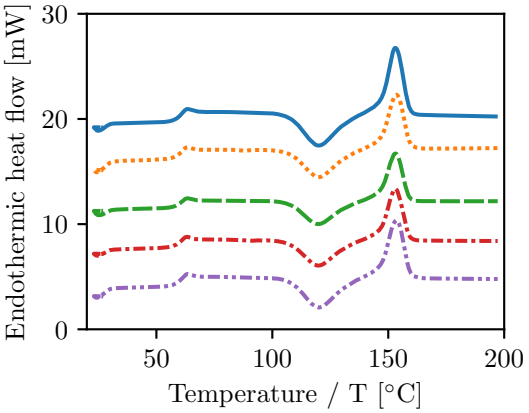

(b) 0.6LDH_PLA.

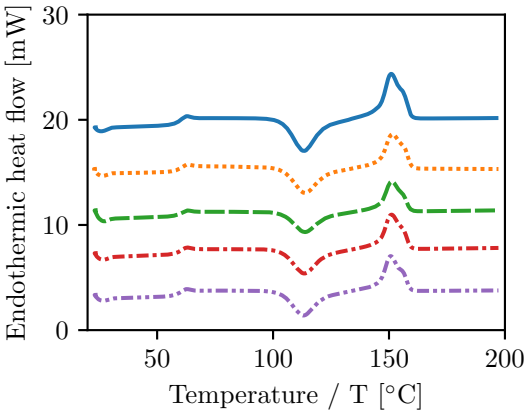

(c) 2LDH_PLA.

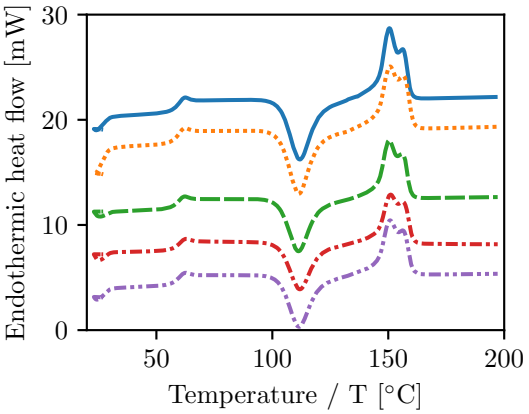

(d) 3.4LDH_PLA.

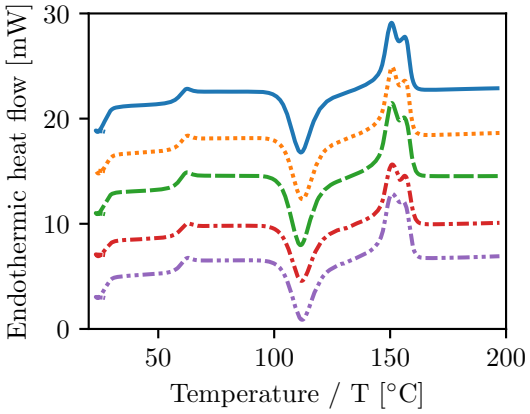

(e) 4LDH_PLA.

Figure C.31: The DSC results of second heating cycle of the filament made for use in the CCD. Five repeats for each LDH loading are shown.

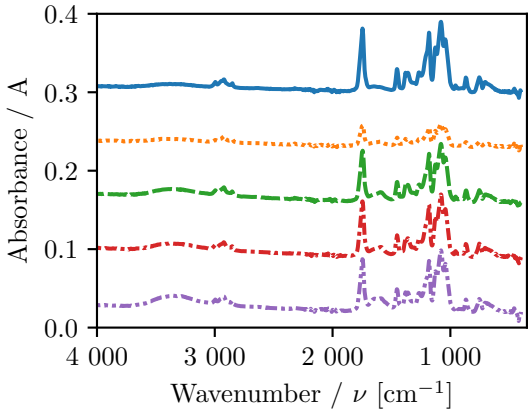

(a) 0LDH_PLA.

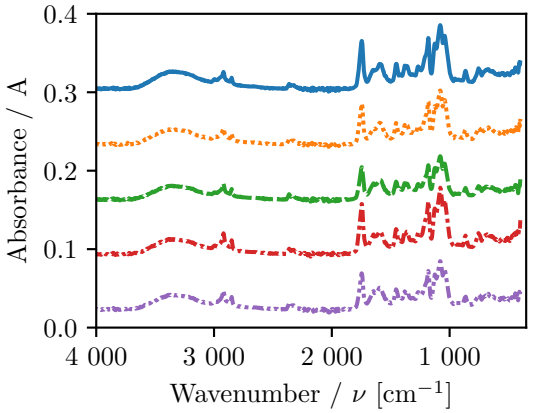

(b) 0.6LDH_PLA.

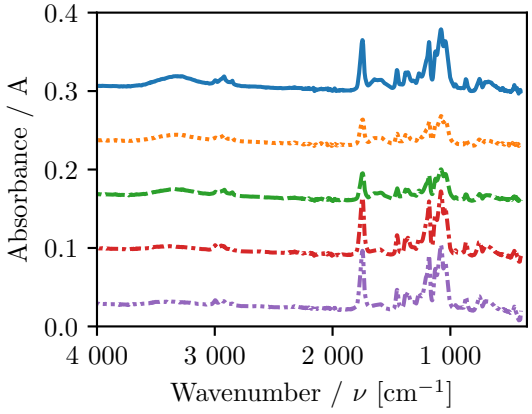

(c) 2LDH_PLA.

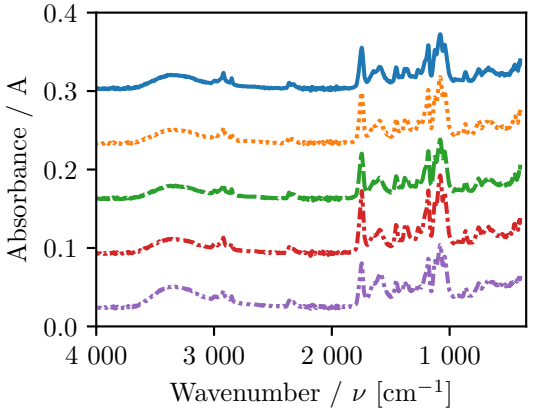

(d) 3.4PLA_LDH.

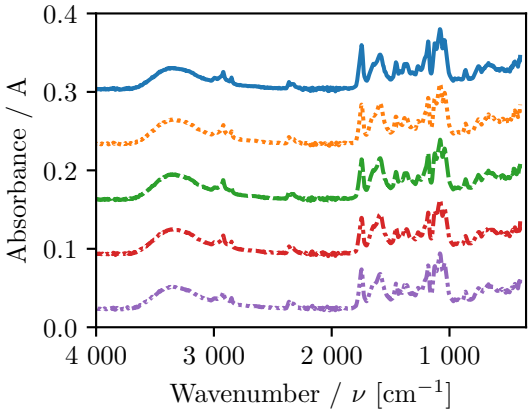

(e) 4LDH_PLA.

Figure C.32: The FTIR results of the filament made for use in the CCD. Five repeats for each filament is shown.

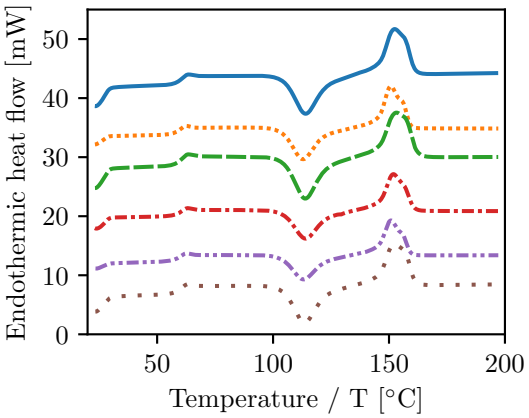

(a) Experiment 1.

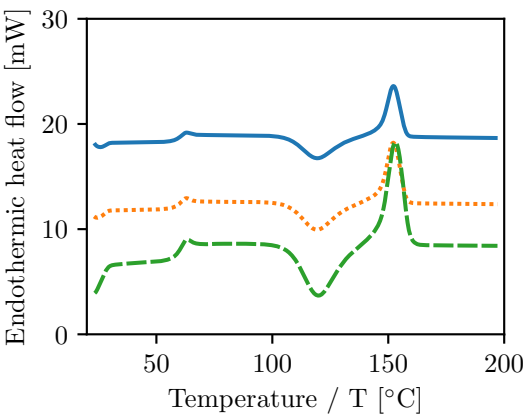

(b) Experiment 2.

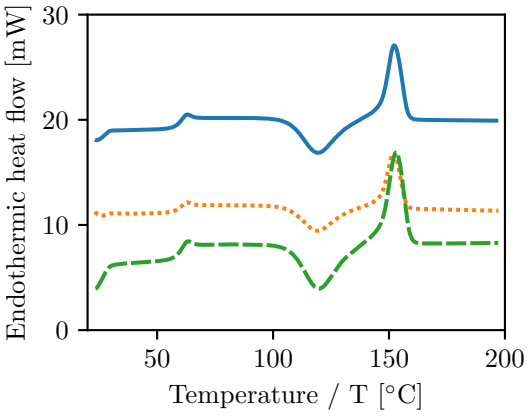

(c) Experiment 3.

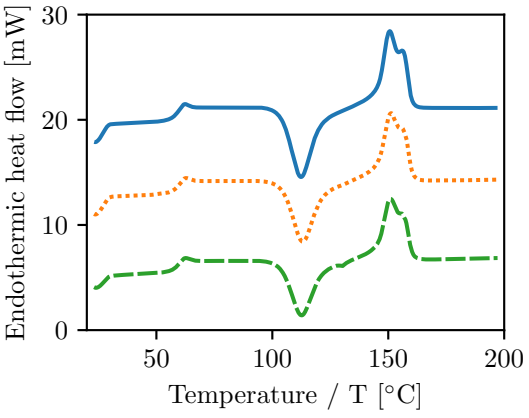

(d) Experiment 4.

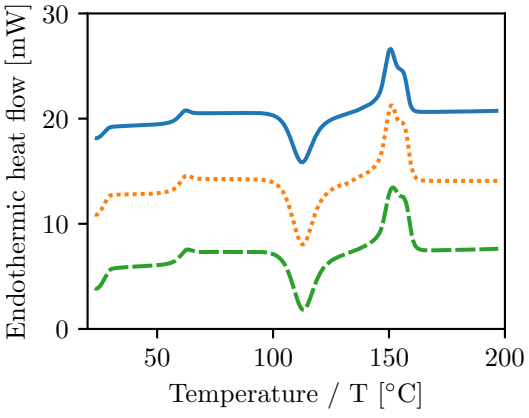

(e) Experiment 5.

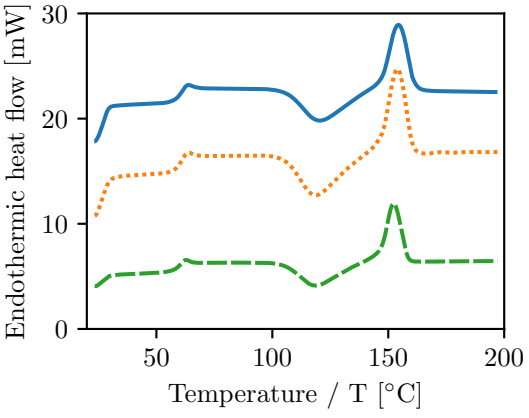

(f) Experiment 6.

Figure C.33: The DSC results of the second heating cycle of the tensile samples printed in the CCD. Continued on next page...

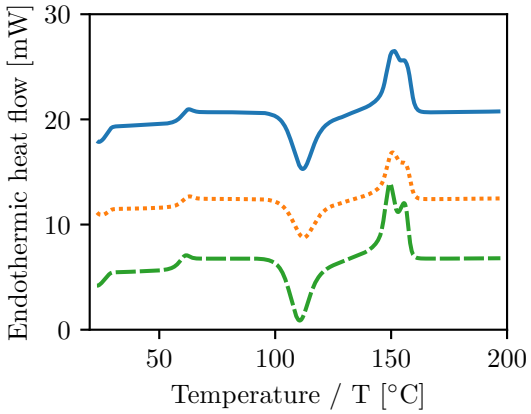

(g) Experiment 7.

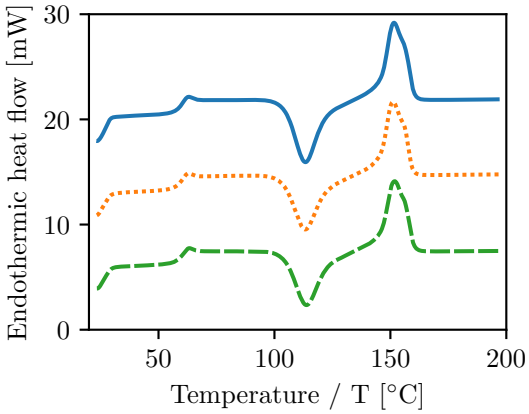

(h) Experiment 8.

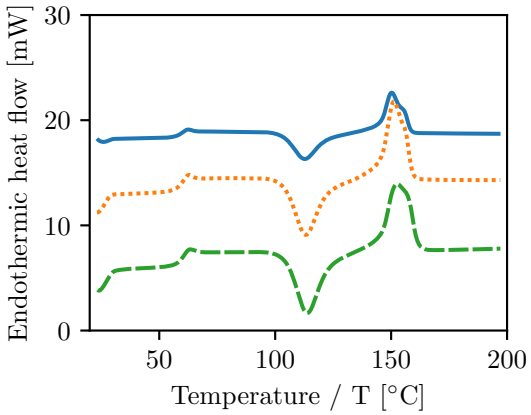

(i) Experiment 9.

Figure C.33: Continued from previous page... The DSC results of second heating cycle of the tensile samples printed in the CCD.

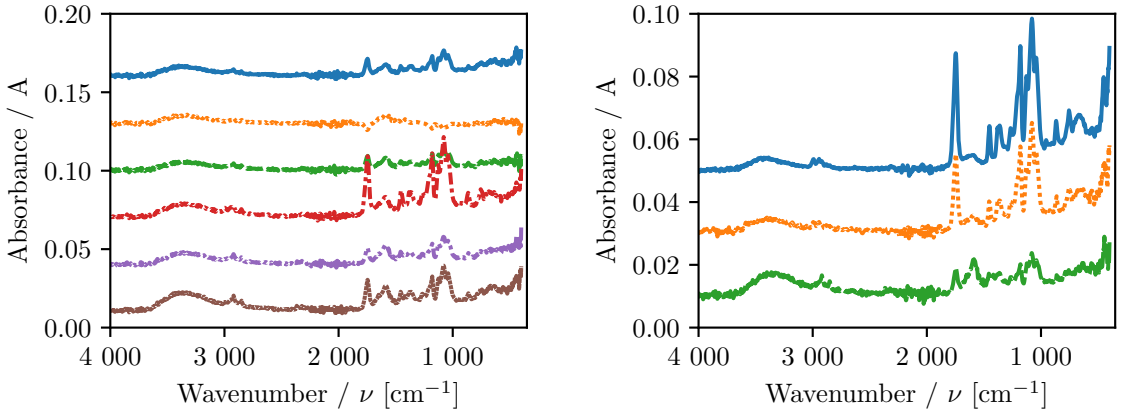

(a) Experiment 1.

(b) Experiment 2.

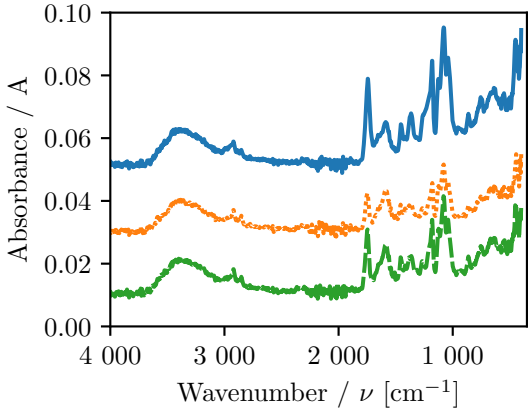

(c) Experiment 3.

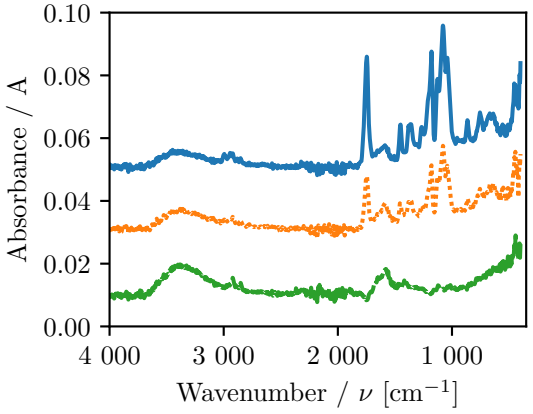

(d) Experiment 4.

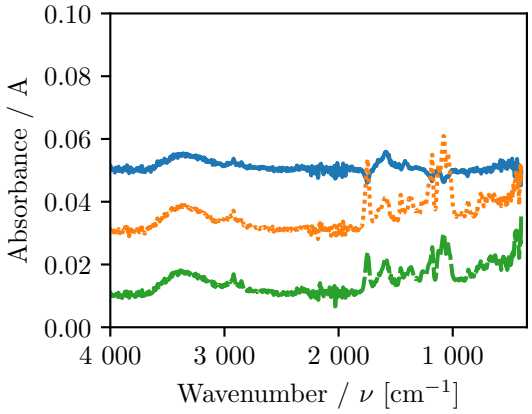

(e) Experiment 5.

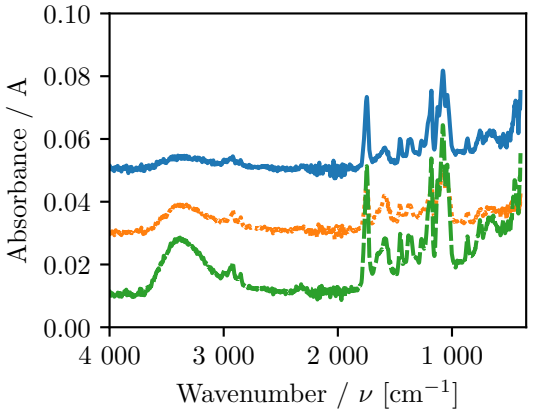

(f) Experiment 6.

Figure C.34: The FTIR spectra of the tensile samples printed in the CCD. Continued on next page...

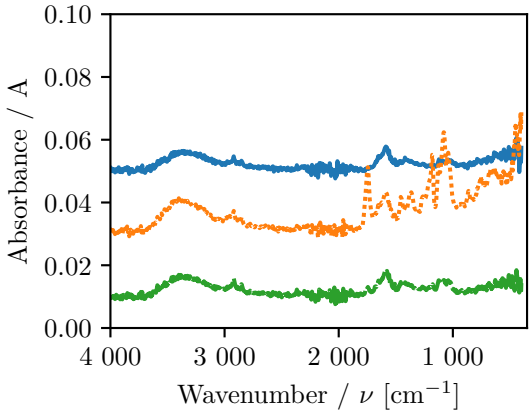

(g) Experiment 7.

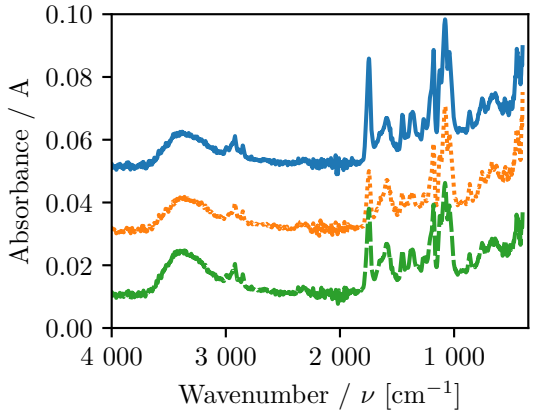

(h) Experiment 8.

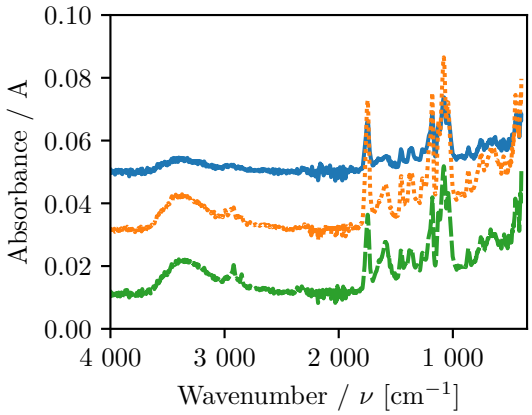

(i) Experiment 9.

Figure C.34: Continued from previous page... The FTIR spectra of the tensile samples printed in the CCD.

Appendix D DSC investigation

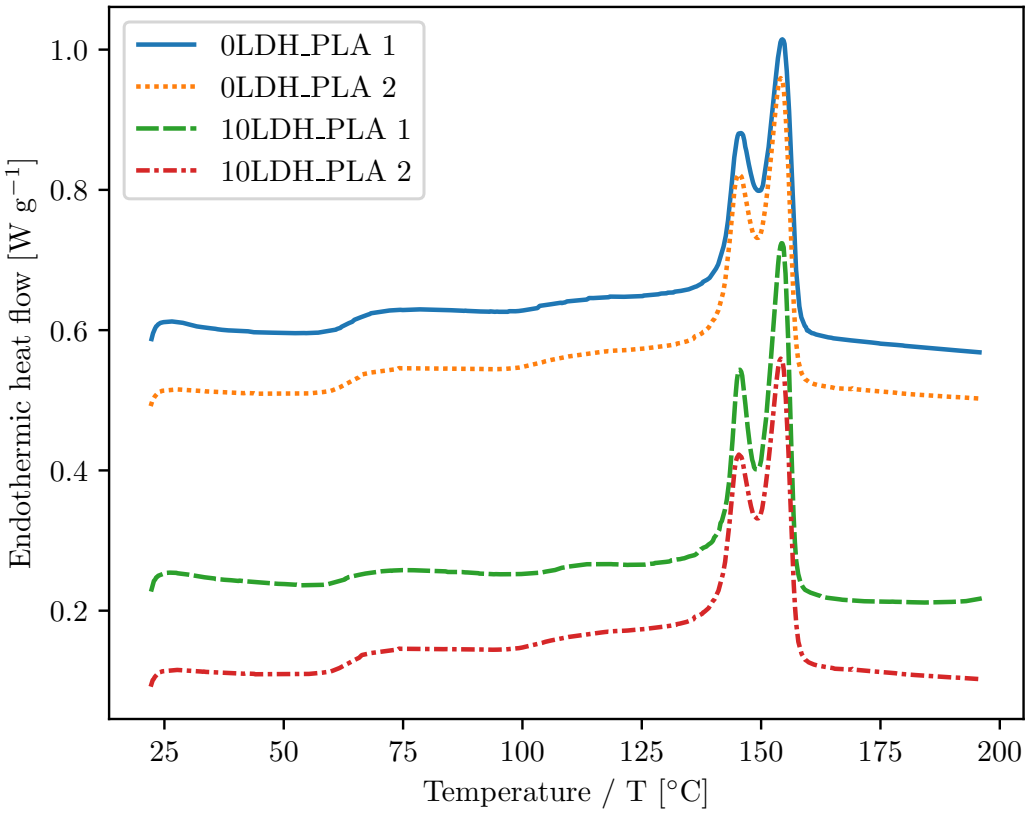

Figure D.35: The DSC results for the second heatings after the isothermal period at 90 °C for both the 0LDH_PLA and 10LDH_PLA filaments. The repeat of each is shown as well.

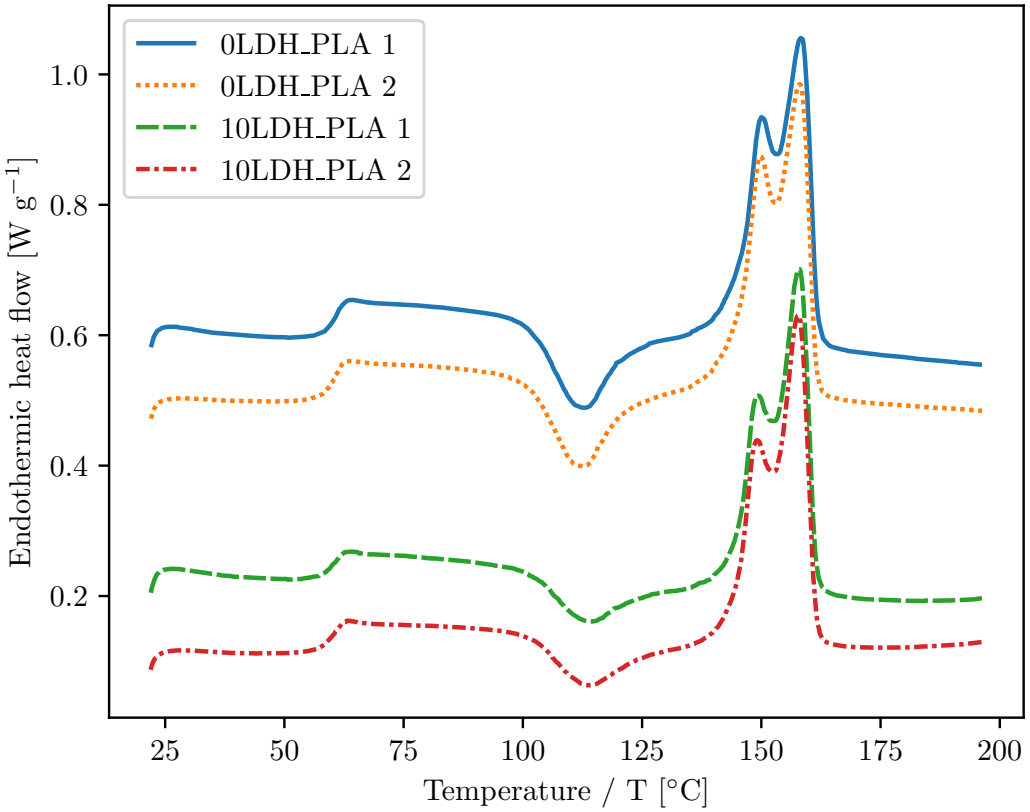

Figure D.36: The DSC results for the second heatings after the isothermal period at 130 °C for both the 0LDH_PLA and 10LDH_PLA filaments. The repeat of each is shown as well.

Appendix E Injection moulding

(a) 0LDH_PLA. **(b)** 2LDH_PLA. **(c)** 10LDH_PLA.

Figure E.37: Images of all the tensile samples made with injection moulding.

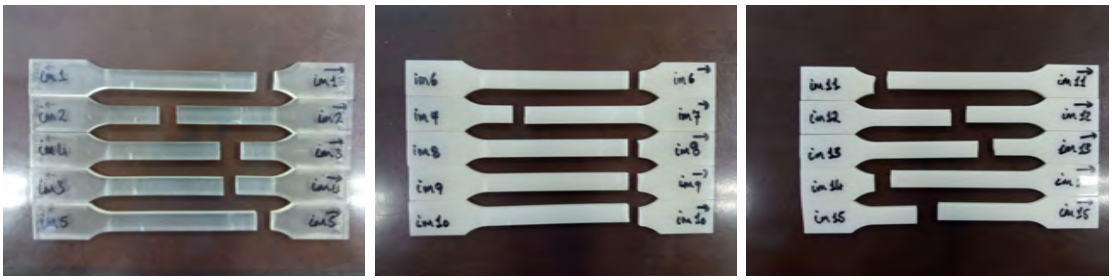

(a) 0LDH_PLA. **(b)** 2LDH_PLA. **(c)** 10LDH_PLA.

Figure E.38: Images of all the broken tensile samples after tensile testing made with injection moulding.

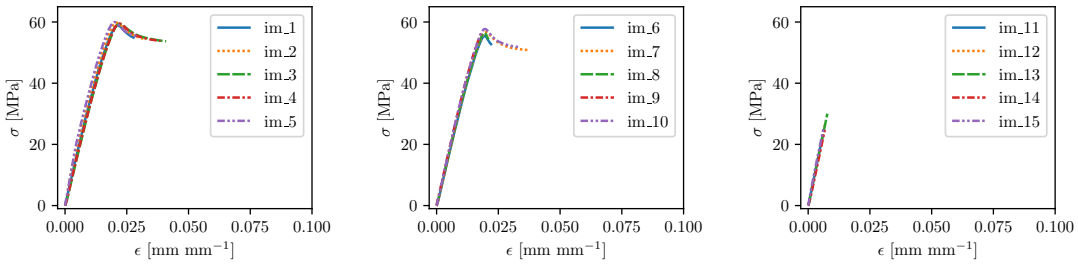

(a) 0LDH_PLA. **(b)** 2LDH_PLA. **(c)** 10LDH_PLA.

Figure E.39: The stress strain graphs of all the tensile samples made with injection moulding.